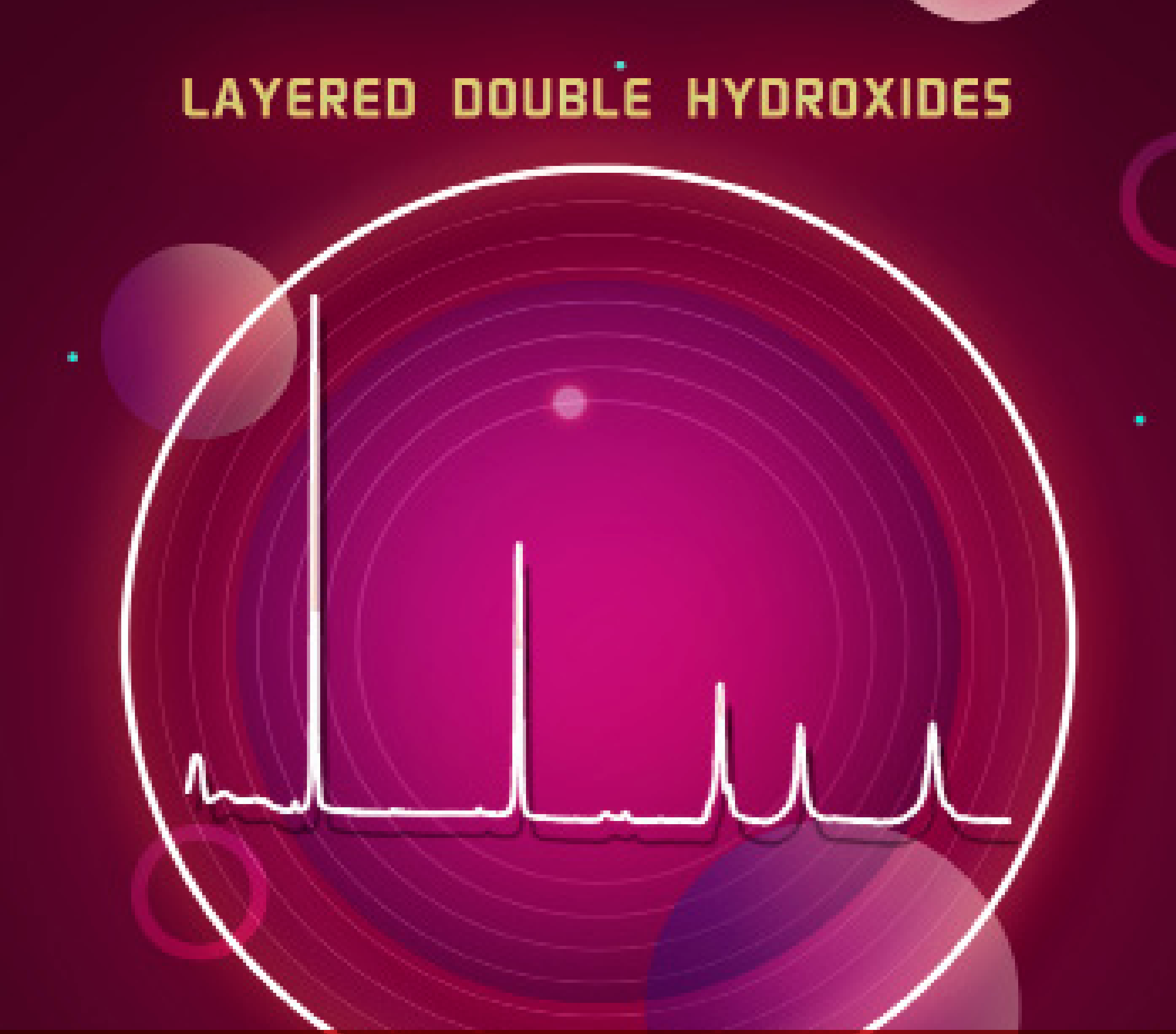

In-situ formation of Layered Double Hydroxides (LDHs) in Alkali Activated Materials (AAMs)

Tao Liu

Bouwstenen 348

In-situ formation of Layered Double Hydroxides (LDHs) in Alkali Activated Materials (AAMs)

ter verkrijging van de graad van doctor

aan de Technische Universiteit Eindhoven,

op gezag van de rector magnificus prof.dr.ir. F.P.T. Baaijens,

voor een commissie aangewezen door het College voor Promoties,

in het openbaar te verdedigen op donderdag 19 januari 2023 om 11:00 uur

door

Tao Liu

geboren te Hefei, China

Dit proefschrift is goedgekeurd door de promotoren en de samenstelling van de promotiecommissie is als volgt:

Voorzitter:	Prof. dr. ir. A.S.J. Suiker
Promotor:	Prof. dr. ir. H.J.H. Brouwers
Copromotor:	Prof. dr. ir. Qingliang Yu (Wuhan University)
Promotiecommissieleden:	Prof. dr. John Provis (University of Sheffield)
	Prof. dr. Wei Chen (Wuhan University of Technology)
	Prof. dr. Nele De Belie (Ghent University)
	Prof. dr. Angel Palomo (Spanish National Research Council | CSIC)
	Asst. Prof. dr. Juho Yliniemi (University of Oulu)
	Prof. dr. Sieger van der Laan
	Prof. dr. Emiel Hensen

In-situ formation of Layered Double Hydroxides (LDHs) in Alkali Activated Materials (AAMs)

T. Liu

Eindhoven University of Technology

January 2023

CIP-DATA LIBRARY TECHNISCHE UNIVERSITEIT EINDHOVEN

In-situ formation of Layered Double Hydroxides (LDHs) in Alkali Activated Materials (AAMs) / by Tao Liu

A catalogue record is available from the Eindhoven University of Technology Library

ISBN: 978-90-386-5652-6

Bouwstenen 348

NUR 955

Ph.D. thesis, Eindhoven University of Technology, the Netherlands

Cover design: Tao Liu

Printed by: ProefschriftMaken | | www.proefschriftmaken.nl

Het onderzoek of ontwerp dat in dit proefschrift wordt beschreven is uitgevoerd in overeenstemming met de TU/e Gedragscode Wetenschapsbeoefening.

Dedicated to my parents

献给我亲爱的父母

Preface

This thesis presents the research work performed in the group of Building Materials, Department of the Built Environment, Eindhoven University of Technology (TU/e) since 1st October 2018. This research is supported by the China Scholarship Council and the Eindhoven University of Technology.

First of all, I sincerely appreciate the opportunity offered by prof.dr.ir. H.J.H. (Jos) Brouwers (my promotor) that I can pursue my Ph.D. in the Netherlands. 4 years ago, we met each other in Wuhan for the first time. I did not speak fluent English, but we did have a pleasant talk about the future and research. With your encouragement, I started my Ph.D. without any hesitation. Your patient and passionate supervision guided me passing through the Ph.D. journey. It is always a pleasure to work under the supervision of Jos. You always gave me wise advice and guided me to a clear orientation. I learned how to manage myself in my study and further in my life.

Secondly, I am grateful to my daily supervisor prof. dr. Qingliang Yu. (Wuhan University).Thanks for all the constructive comments on my manuscripts and thesis. Especially in my first manuscript, I did not even know how to structure my results and how to extract the conclusions. Your patient and professional supervision support me during the Ph.D. journey. I cannot finish my Ph.D. without your knowledgeable suggestions. I am grateful to have your supervision in the group.

Furthermore, I sincerely thank my master's supervisor prof. Jianfeng Fan guided me in the study of civil engineering in Wuhan. You brought me into the field of doing research, which was the seed of doing doctoral research. Now the seed has been germinated. It let me see a broader world.

I also would like to express my gratitude to my promotion committee, prof. dr. John Provis (University of Sheffield), prof. dr. Wei Chen (Wuhan University of Technology), prof. dr. Nele De Belie (Ghent University), prof. dr. Angel Palomo (Spanish National Research Council | CSIC), prof. dr. Emiel Hensen (Eindhoven University of Technology), prof. dr. Sieger van der Laan (Eindhoven University of Technology), asst. prof. dr. Juho Yliniemi (University of Oulu) for accepting to be a member. Thanks for your reading and evaluation of my thesis.

This thesis cannot be finished without all the help from my colleagues. Thanks for the contributions from Ing. A.C.A Delsing and Mr. H.L.W Smulders for the tests and technical support during my research. Gang Liu and Yuxuan Chen, thanks for your help and guidance in my research and daily life. I still remember the first day in Eindhoven, Yuxuan picked me up and treated me for the first meal. Yan Luo and Xuan Ling, thanks for your help as well. We travelled together a lot for conferences and holidays. Anna, Winnie, and Jawad, thanks for your companying during Covid time as well. We spent a lot of time hanging out and having food. Florent and Katrin, thanks for the guidance in technical help. Thanks to the members of Texas poker: Peipeng, Xinglong, Xuan, Yanjie, Daoru, and Daiwei. We experienced happiness, excitement, bluff, and heart-breaking time together. Together with Yueye, Perry, Qadeer, Kinga, Kate, Hoss, Zhengyao, Xiaoxiao, Zixiao, Fan, Jia, Helong, Zhihan, Shaohua, Miruna, Ricardo, Iris, Charles, Jonathan, Naomi, Felix, Marc, Marina, Alex, Samuel, Samantha, Leila, and Beatrice. I wish you all the best in the future and have a wonderful life.

Moreover, I give my thank to my father (Guangling Liu) and mother (Ping Sheng). Thanks for bringing me into this world, growing me up, and supporting me all these years. Finally, I would like to give my sincerest appreciation to my girlfriend (Tingting Sun). Thanks for the time companying me in the Netherlands, we met each other during the pandemic time. And we shared the happiness during travel, passed all the tough times, and supported each other in a foreign country. A new life for us is coming!

Rotterdam, 23rd October 2022

Tao Liu

Contents

Chapter 1 Introduction

1.1 Background

1.1.1 Supplementary cementitious materials in alkali activation

The primary component, Portland cement, in making concrete needs large amounts of raw materials and energy. Tremendous efforts have been made to develop substitute materials that can act as new binder systems in concrete [1,2]. The use of supplementary cementitious materials (SCMs) to partially replace cement has been going on for a few decades, including fly ash (FA), ground granulated blast furnace slag (GGBS), silica fume (SF), metakaolin (MK), limestone, fine glass powder, etc [3–6].

However, SCMs cannot hydrate on their own. As a result, SCMs can only replace cement to a limited extent to assure satisfactory performance. Alkaline solution can alternatively be used to activate Si/Al-rich SCMs to create a cementless binder. These latter binders can be broadly categorized into two groups: 1) geopolymer, which has a three-dimensional silicoaluminate structure, FA (low calcium fly ash), SF, and MK are activated to create the commonly used geopolymers [7–9]. 2) High calcium alkali-activated materials (AAM), which mostly contains C−A−S−H gel. FA (Class C), GGBS, and steel slag are calcium-rich slags that are activated to create high calcium alkali activated binders [10–14].

Alternative binders undergo complex physical and chemical changes during the process of alkali activation. To broaden the application of SCMs, the fundamental analysis of raw materials is necessary to be characterized. Simultaneously, the performance of AAMs is important to investigate including chloride binding capacity, heavy metal ions leaching, efflorescence, etc [15–17]. Those properties are closely related to the reaction products of AAMs. Particularly, the secondary reaction product of NaOH activated GGBS, layered double hydroxides (LDHs), showed a superior capacity for chloride, sulfate, and heavy metal ions absorption [18]. LDHs in binders have the properties for binding heavy metal and anions in their structure. Previous studies investigated the effect of synthetic LDHs on the AAMs matrix by external addition [19,20]. The synthesis of LDHs is a complicated process, which limits the application of LDHs [21,22]. Here, we introduce the concept of in-situ formation of LDHs in AAMs. Sodium aluminate ($NaAlO_2$) activation has been proposed as a special method to achieve the promotion of the in-situ formation of LDHs in the AAMs system, enhancing the capacity of chloride, sulfate, and heavy metal ions absorption.

1.1.2 Current AAMs system

In the AAMs system, the composition of reaction products is determined by the precursors and activator. To discuss the AAMs, the chemistry of AAMs binder is essential to first classify these systems according to the types of gel that dominate the structures. Fig. 1.1 shows the process and reaction products of AAMs. The composition of reaction products will be discussed in detail.

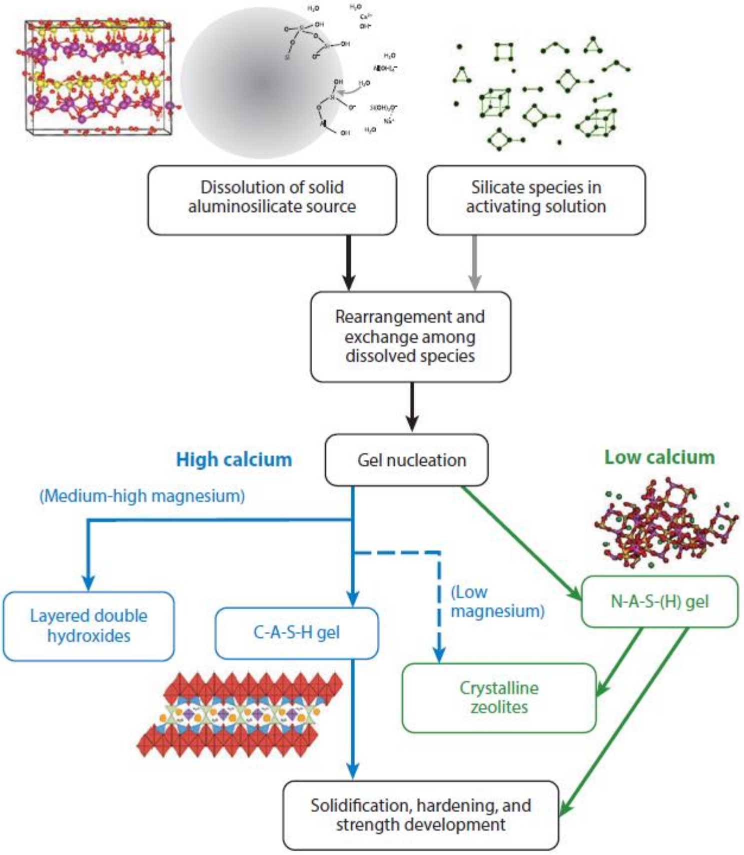

Fig. 1.1 Process and reaction products of alkaline activation of a solid aluminosilicate precursor. High-calcium systems react according to the left-hand (blue) pathway, with the nature of secondary products determined by Mg content, whereas low-calcium systems react according to the right-hand (green) pathway. For each type of precursor, hydroxide activation tends to increase the ratio of crystalline to disordered products compared with silicate activation [23].

1.1.2.1 Alkali activated ground granulated blast furnace slag

The composition of ground granulated blast furnace slag (GGBS) consists of a large amount of glassy Cao-SiO_2-Al_2O_3-MgO [24]. Nowadays, GGBS is the mainly used precursor in the AAMs system, meanwhile, an alkaline solution is needed to accelerate the hydrolysis of aluminosilicate particles [24].

Greenberg et al. [25] reported that calcium silicate hydrates (C−(A)−S−H) did not form in the solution which had a pH value lower than 9.5. Thus, the alkali activation of slag has a threshold pH value to start the reaction process and generate the C−(A)−S−H gel. The previous study [26] has reported that the pH value of the mixing solution should be higher than 11.5 to effectively activate the GGBS. Hence, three types of activators can be used to activate the GGBS: I. Alkaline hydroxides (e.g. NaOH, KOH, $Ca(OH)_2$), II. Alkaline salt (e.g. Na_2SiO_3, Na_2CO_3), and III. Blended activator (e.g. NaOH + Na_2SiO_3). The reaction products of alkali activated GGBS show different compositions that are affected by the types of activators.

Alkaline hydroxides activated GGBS

The amorphous phases of calcium silicate hydrates (C−S−H) and calcium aluminosilicate hydrates (C−A−S−H) are the main reaction products of alkaline hydroxides activated GGBS [27,28]. While, hydrotalcite, one type of Layered Double Hydroxides (LDHs), is the secondary reaction product in sodium hydroxide activated GGBS [29–31]. There are several types of Mg-Al layered double hydroxides not only hydrotalcites [32]. For example, quintinite is sometimes detected in AAMs. And Mg-Al LDHs can also be partly amorphous i.e. not detectable with XRD.

Alkaline salt activated GGBS

Normally, sodium silicate is often used as an alkaline salt to activate GGBS [33]. Moreover, the deprotonating process of sodium silicate can keep a constantly high pH environment due to its buffering effect and provide soluble silica resources during the reaction process [34]. Here, the reaction products of sodium silicate activated slags are C−(A)−S−H, hydrotalcite (at low silicate modulus), and stratlingite (at low silicate modulus) [35,36].

Recently, sodium carbonate has received great attention for activating the GGBS due to its low environmental footprint [37]. The reaction process is quite different from that of sodium silicate, since CO_3^{2-} reacts with the dissolved Ca^{2+} in GGBS to form the $CaCO_3$ precipitation and OH^-, yielding an increased pH value and then activating GGBS [38]. The dominant reaction products of sodium carbonate activated GGBS are C−(A)−S−H, calcite, hydrotalcite, and a small amount of gaylussite and akermanite [38,39].

Sodium sulfate is also another eco-friendly activator [40]. C−(A)−S−H, ettringite, and hydrotalcite can be found in the reaction products of the sodium sulfate activated GGBS [40,41].

Hybrid activator activated GGBS

The solution of sodium hydroxide and sodium silicate is widely utilized in AAMs [42]. The addition of sodium hydroxide in the solution shows the role of silicate modulus (Ms) modification [43]. The primary reaction product is C−(A)−S−H, which is the same as the sodium silicate activated slag. However, the content of hydrotalcite decreases with the increased Ms, because the soluble silicate competes with the Mg^{2+} reacting with Al, the soluble silicate will preferentially react with Al to form C−A−S−H at low MgO content AAMs matrix [43,44]. Adversely, it is reported that in the high MgO and low soluble silicate systems, Mg^{2+}

will preferentially form hydrotalcite by reacting Al with Mg until all Mg has been exhausted [45,46].

Recently, the hybrid activator of sodium carbonate and sodium hydroxide has captured attention by a large number of researchers [47]. With the increased dosage of sodium carbonate in sodium hydroxide, the relatively longer setting time, higher 28d compressive strength, and lower drying shrinkage are found. Moreover, sodium hydroxide compensates for the early strength of sodium carbonated activated GGBS [48]. Likewise, the reaction products are mainly C−(A)−S−H, hydrotalcite, calcite, and a small amount of gaylussite [48]. The reaction products of sodium carbonate and sodium silicate activated slag are C−(A)−S−H, calcite, and a small amount of chabazite [49].

In addition, sodium sulfate and sodium hydroxide activator are studied by Ye et al. [50]. C−(A)−S−H, hydrotalcite, and ettringite are the primary crystalline formation.

1.1.2.2 Alkali activated fly ash

Fly ash (FA) particles are normally glassy and spherical, which need a sufficient alkaline environment to start the hydrolysis of aluminosilicate particles and the geopolymerization [51]. FA raw materials are composed of SiO_2, Al_2O_3, Fe_2O_3, and CaO. Furthermore, FA is divided into low-calcium fly ash (LCFA) and high-calcium fly ash (HCFA) according to the calcium content [52]. Alkaline hydroxides and silicate solutions are most often utilized to activate FA [53].

Alkali activated LCFA and HCFA

Alkali activated LCFA prefers to form sodium aluminosilicate hydrates (N−A−S−H) as the primary amorphous reaction product, as well as a minority of sodalite-group and cancrinite-group crystalline phases [54–56]. Meanwhile, a small amount of quartz and mullite remains in the alkali activated FA. Here, sodalite-group and cancrinite-group crystalline phases are regarded as zeolite-like phases.

Alkali activated HCFA exhibits a different composition of the reaction products. Compared to the alkali activated LCFA, the iron-containing silicate hydrogarnet ($Ca_3AlFe(SiO_4)(OH)_8$) can be found among the reaction products. On the contrary, the zeolite-like phases develop poorly in the reaction products of alkali activated HCFA, due to the high amount of calcium participation [52].

1.1.2.3 Alkali activated metakaolin

Metakaolin (MK), calcined from natural kaolin, mainly consists of Al_2O_3 and SiO_2 [57]. The Al_2O_3 inside the MK shows high reactivity because of the thermal dehydroxylation of kaolinite. The energetic Al-O-Al bonds are easy to react in a highly alkaline environment [58]. Sodium hydroxide and sodium silicate activated MK shows the similar reaction products, to some extent, the alkali activation of MK is similar to those of LCFA geopolymers [53]. The predominant reaction products of alkali activated MK are N−A−S−H, C−(A)−S−H gel, and zeolite-like crystalline phases [59–61].

1.1.2.4 Alkali activated blended precursors

Blended matrices range from GGBS/FA [62], GGBS/MK [63], MK/FA [64] binary systems to a variety of other binary and ternary systems including silica fume [65], waste glass powder [66], red mud [67,68] and rice husk ash [69,70].

The reaction products of the blended matrices are complex, the initial compositions of the blended precursors can be changed by different mix designs. But the dominant amorphous gels are still C(N)−A−S−H, C−S−H, and the coexistence of those gels [71]. Similarly, the hybrid C(N)−A−S−H gel can also be found in the reaction products of AAMs by scanning electron microscopy-energy-dispersive X-ray spectroscopy (SEM-EDS) [71]. Moreover, the crystalline phases include hydrotalcite-like phases, zeolite-like phases, and some other amounts of crystalline phases. It is worth mentioning that the hydrotalcite-like phases and zeolite-like phases normally do not exist simultaneously.

1.1.2.5 Compositions of reaction products in different AAMs systems

The primary phases of reaction products in the main trend research are listed in Table 1.1. The primary amorphous phases and crystalline phases are picked up to present the physical and chemical chloride stabilization in the following sections.

Table 1.1 Primary phases of reaction products in different AAMs systems.

Precursors	GGBS	FA	MK	Blended precursors
Primary amorphous phases	C−A−S−H	N−A−S−H	N−A−S−H	C(N)−A−S−H
Primary crystalline phases	Hydrotalcite-like phases, Ettringite, Stratlingite, Calcite	Zeolite-like phases, Calcite	Zeolite-like phases	Hydrotalcite-like phases or Zeolite-like phases

1.1.3 $NaAlO_2$ activation

1.1.3.1 Reaction products

In this thesis, the process of sodium aluminate ($NaAlO_2$) activation has been investigated comprehensively. Unlike the current of AAMs system, the $NaAlO_2$ activation shows different reaction kinetics and reaction products compared to NaOH, Na_2SiO_3, and Na_2CO_3 activation.

Sodium aluminate activator was also investigated to generate more ettringite and calcium silicate hydrate (C−(A)−S−H) in slag and cement system [72], increasing strength. Liu et al. [18] observed that sodium aluminate activation can promote C(N)−A−S−H and in-situ formation of LDHs via elevated $Al(OH)_4^-$ in the pore solution, improving the microstructure of the activated matrix. With the increase of sodium aluminate participation, N−A−S−H gel can be found as well. Simultaneously, the zeolite formation in sodium aluminate activation has been reported [73], it is normally companied by N−A−S−H gel formation.

LDHs can be represented as $\left[M^{2+}_{(1\text{-}x)}M^{3+}_{x}(OH)_2\right](A^{n-})_{x/n}\cdot zH_2O$, where M represents a metallic skeletal ion (e.g., Mg or Al) and A^{n-} represents an interlamellar anion (e.g., SO_4^{2-} or Cl^-), where various combinations of M^{2+}/M^{3+} can be used [74]. However, their formation during the alkali activation of GGBS is rather limited. As mentioned, the sodium aluminate activator provides extra $Al(OH)_4^-$, which significantly influences the in-situ formation of LDHs. The mechanism of how the $Al(OH)_4^-$ influences in-situ synthetic LDH and gel formation in sodium aluminate activation is unknown. Furthermore, the different phase assemblages of the sodium aluminate activated matrix affect the microstructure and final performance. It is important to understand the role of sodium aluminate in activation system.

1.1.3.2 Microstructure and performance of activated matrix

The microstructure evolution is influenced by the formation of amorphous and crystalline phases. The porosity of AAMs matrices is related to primary and secondary reaction products. It is hard to make connections between porosity and reaction products. Generally, with the increasing Al participation in matrices, the C−A−S−H gel and hydrotalcites increase, and the porosity may be improved by the formation of these phases. Meanwhile, the N−A−S−H gel and zeolites favor forming in the low-calcium matrices, so the porosity can be improved by extra Al participation as well. An in-depth analysis of the $NaAlO_2$ activated matrix will be discussed in the main body of this study in terms of microstructure evolution.

As discussed in previous sections, the extra $Al(OH)_4^-$ promotes the reaction process, resulting in a denser microstructure, further enhancing strength. Besides, the promoted amorphous gels and in-situ formed LDHs improve the capacity of chloride, sulfate, and heavy metal ions absorption. A detailed description and analysis are presented in the following chapters.

1.2 Motivation and objective

Last decades, supplementary cementitious materials have been widely studied to be valorized in building materials. By introducing a strategy of alkali activation, these SCMs can be utilized as a cementless binder. As mentioned above, GGBS is used as the main precursor in this research. The promotion of LDHs, secondary reaction products of activated slag, can enhance the capacity of chloride, sulfate, and heavy metal ions absorption. The concept of in-situ formation of LDHs is investigated via sodium hydroxides, sodium silicate, and sodium aluminate activation. The $NaAlO_2$ activation is explored comprehensively to achieve the in-situ formation of LDHs. Therefore, the promotion of in-situ formed LDHs in $NaAlO_2$ activated slag can be the potential approach to mitigate the chloride penetration and leaching issue of municipal solid waste incineration bottom ash (MSWI BA). To realize all, the objective of this thesis is as follows:

- Investigating the effect of MgO, Mg-Al-NO_3 LDH and calcined LDH-CO_3 (CLDH) on chloride resistance of alkali activated fly ash and slag blends, which provides a comprehensive understanding of in-situ formed LDHs and external added LDHs on the chloride penetration in the matrix.
- Exploring the $NaAlO_2$ activation mechanism, moreover, revealing the role of Al-O tetrahedra in the in-situ formation of LDHs.
- Further exploring the $NaAlO_2$ activation mechanism via thermodynamic modelling and predicting the leaching pattern of incorporated MSWI BA in $NaAlO_2$ activated slag.
- Investigating the mechanism of MgO modified $NaAlO_2$ activated slag and MSWI BA, revealing the impact of Mg^{2+} on the in-situ formation of LDHs and leaching behavior.
- Reusing waste glass in alkali activated slag and fly ash, investigating the effect of waste glass on reaction process and chloride resistance.
- Investigating the $NaAlO_2$ activated slag and waste glass, revealing the mechanism of how $NaAlO_2$ mitigates the efflorescence behavior of the alkali activated waste glass matrix.

1.3 Outline of the thesis

This research framework is presented in Fig. 1.2. The contents of the chapters are briefly introduced in the following paragraphs.

Chapter 2 investigates the different effects of MgO, nitrate intercalated LDHs, and calcined LDH-CO_3 on the chloride resistance of the alkali activated fly ash and slag (AAFS) binder. The reaction heat flow, reaction products, pore structures, mechanical properties, and chloride resistance of AAFS incorporated with MgO, LDHs, and CLDHs are investigated. Furthermore, the mechanism to form the LDH in AAFS affected by MgO and CLDH is analyzed. Ordinary Portland Cement (OPC) based samples are also used as comparison to the AAMs samples. The respective contributions to enhance the chloride resistance of the three admixtures are evaluated.

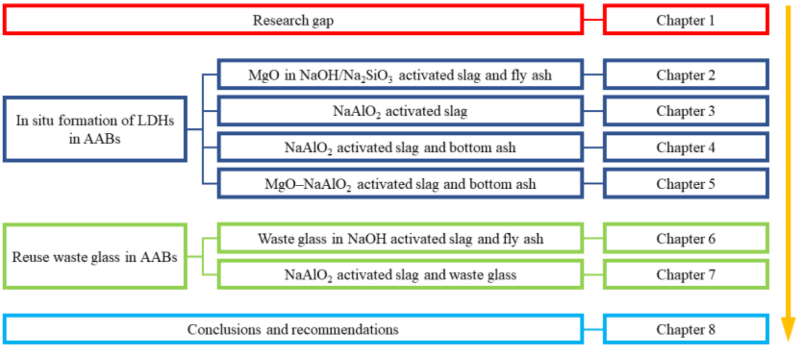

Fig. 1.2 Outline of the thesis.

Chapter 3 investigates the mechanism of how the $Al(OH)_4^-$ influences in-situ synthetic LDH and gel formation in sodium aluminate activated slag (SAAS), and the consequent chloride absorption performance. The changes in pH value and ions in the pore solution of SAAS paste were tested to reveal the behavior of $Al(OH)_4^-$ in sodium aluminate that affects the Mg-Al LDH and gel formation at different curing ages. The reaction heat flow, reaction products as well as microstructure were determined to understand the activation process. A reaction mechanism was proposed to give an insight into the promotion of in-situ formed LDH and gels by sodium aluminate activator.

Chapter 4 presents the sodium aluminate activated slag and bottom ash (SAASB) by modelled and experimental approaches. The hardened pastes were evaluated including mineralogy, thermogravimetric analysis, pore structure, mechanical property, and leaching behavior. Importantly, thermodynamic modelling of the reaction process had been simulated and validated based on the analysis of isothermal calorimetry data. Then, the prediction of heavy metal binding capacity was simulated based on the thermodynamic modelling on a time scale. The new insights are revealed in terms of thermodynamic modelling of sodium aluminate activated slag and bottom ash as well as environmental impact.

Chapter 5 reveals the influence of Mg^{2+} on LDHs and gel formation in MgO–NaAlO$_2$-activated GGBS/BA (MSAASB), with special attention to the leaching behavior. The pH and alkali-metal ions in the pore solution of the MSAASB were characterized. The reaction products and microstructures were determined, and the leaching of potentially toxic elements as well as the compressive strengths were tested. Based on the results, the influence of Mg^{2+} on the reaction products and leaching behavior is discussed. These research findings contribute to maximizing Mg–Al LDH formation in situ and its binding to leaching ions.

Chapter 6 explores the chloride transport mechanism of alkali activated slag/fly ash/waste glass blends. The reaction heat flow is determined to study the reaction kinetics, meanwhile, the reaction products are characterized. The microstructure, mechanical performance, and chloride diffusion are investigated. Furthermore, the chloride transport in the pore structure is discussed based on the experimental results. The addition of waste glass is proven to enhance the chloride resistance of AAMs.

Chapter 7 uses sodium aluminate to activate the slag and waste glass improving the resistance toward efflorescence. The sodium hydroxides and their hybrid activator were used as the control group. The reaction products of SAASG were determined by Quantitative X-ray diffraction (QXRD), thermogravimetry (TG), and Fourier Transform InfraRed spectroscopy (FTIR). The gel structure was characterized by nuclear magnetic resonance (NMR). The microstructure was assessed by Scanning electron microscopy (SEM). Importantly, the efflorescence behavior and compressive strength of paste samples were evaluated as well. A mechanism of efflorescence behavior was proposed to give insight into stabilizing Na^+ leaching by crosslinked C(N)−A−S−H formation.

Chapter 8 summarizes the important results of this research and recommends further studies.

Chapter 2 Effect of MgO, Mg-Al-NO_3 LDH and calcined LDH-CO_3 on chloride resistance of alkali activated fly ash and slag blends

The mechanism of layered double hydroxides (LDHs) formation with the addition of magnesium oxide (MgO), the LDHs reconstruction of calcined layered double hydroxides (CLDHs) and the effect of externally added synthetic LDHs in alkali-activated materials (AAMs) system are important factors influencing the chloride resistance of AAMs. The objective of this research is to investigate the different effects of MgO, Nitrate intercalated LDH (Mg-Al-NO_3 LDH) and Calcined natural LDH-CO_3 on the alkali activated fly ash and slag blends (AAFS) in terms of chloride resistance. Mg-Al-NO_3-LDH was successfully synthesized with the co-precipitation method. CLDH was obtained by thermal treating natural Mg-Al-CO_3 LDH. The reaction heat flow and reaction products of the AAFS were tested by isothermal calorimetry and X-ray diffraction (XRD), respectively. The microstructure of the AAFS was characterized by the nitrogen sorption tests (BET) and mercury intrusion porosimetry (MIP). The compressive strength of AAFS was also tested. Non-steady-state migration (NSSM) was applied to determine the chloride resistance of AAFS. Ordinary Portland Cement (OPC) samples were also studied for comparative purpose. The results of the calorimeter test showed that the MgO, Mg-Al-LDH, and CLDH delayed the time to reach the reaction peak (TRRP) for 3.9%, 11.2%, and 9.2%, respectively. The MIP results illustrated that mesopores and micropores of AAFS were refined by the three admixtures. The NSSM results indicated that CLDH can significantly improve the chloride resistance of AAFS binder compared to the samples containing MgO and Mg-Al-NO_3 LDH. The different influences of MgO, Mg-Al-NO_3 LDH and CLDH are compared in this chapter.

This chapter is partially published elsewhere:

T. Liu, Y. Chen, Q. Yu, J. Fan, H.J.H. Brouwers, Effect of MgO, Mg-Al-NO3 LDH and calcined LDH-CO3 on chloride resistance of alkali activated fly ash and slag blends. Construction and Building Materials 250 (2020). doi:10.1016/j.conbuildmat.2020.118865.

2.1 Introduction

Numerous military and civilian concrete structures exposed to the marine environment face the risk of chloride corrosion [75]. Chloride penetration into reinforced concrete can cause local destruction of the passive layer, leading to localized corrosion. Consequently, the usability and load-bearing capacity decreases, even the failure of the structure could occur. Facing a large amount of chloride ingress problems, approximately 3.4% of the global GDP ($2.5 Trillion USD) is spent each year to prevent, mitigate, and repair the infrastructure damage due to chloride-induced corrosion [76]. As we can see from Fig. 2.1, remarkable chloride ingress problems are universal worldwide [77]. The corrosion problems of offshore concrete structures lead to an urgent demand for the research about the chloride resistance of the AAMs. The effect of the alkaline environment in AAMs on passivate steel bars may be very important in improving the durability of the reinforced concrete structure. Meanwhile, the use of by-product in AAMs also meet the demand for sustainable development worldwide. To solve these issues, many methods were developed to prevent chloride penetration. Table 2.1 lists studies on chloride resistance.

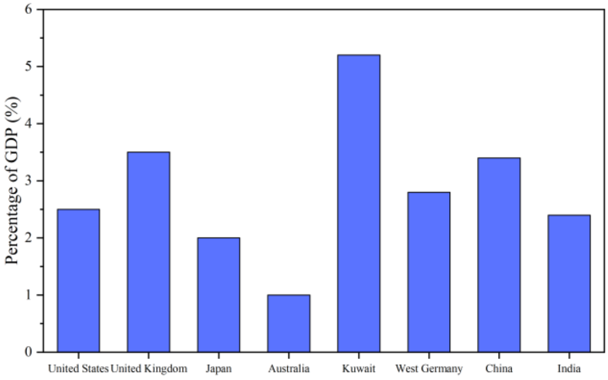

Fig. 2.1 Cost of corrosion related to GDP in different countries [77].

Recently, Layered double hydroxides (LDHs) are widely investigated for their ability to absorb undesired anions in aqueous solution [78]. LDHs are one of the primary reaction products in alkali activated slag. The skeleton of LDHs contains a divalent metal ion and a trivalent metal ion, for example, Mg^{2+} and Al^{3+} [79]. The interlayer of LDHs has the capability of binding the anions in AAMs, for instance, chloride ions and sulfate ions. The interlayer anion can exchange with other anions and the affinity order of anion is characterized by Costa [80] as:

$$CO_3^{2-} > SO_4^{2-} > OH^- > F^- > Cl^- > Br^- > NO_3^- \qquad (2\text{-}1)$$

Thus, the amount of Mg-Al-NO_3^--LDH influences the chloride resistance in the silicate matrix, because the NO_3^- can exchange the Cl^- in the chloride environment. Xu et al. [81] prepared the Mg-Al-NO_3^--LDH and Mg-Al-NO_2^--LDH by the co-precipitation method, and both Mg-Al-LDHs exhibited excellent chloride removal and corrosion inhibition capacities. Qu et al. [96] reported that the finer particle size of the Ca-Al-NO_3^--LDH enhanced the chloride resistance of the cement matrix, which is attributed to both the physical barrier effect of the increased tortuosity and chemical binding capacity of the LDHs. Regardless of the references mentioned above, the synthesis pH of LDH, flow rates, temperature, pressure conditions partly contribute to the property of the final product [97]. However, few literature reports the

Table 2.1 Durability investigations of AAMs in terms of chloride resistance.

Standards	Precursors	Activators	Admixtures	Remarks	Year	Ref.
ASTM C1202	Slag	NaOH+ $Na_2O.rSiO_3$	Phosphoric acid	Dosage of Na_2O and H_3PO_4 of additional mixture optimize the properties and durability of samples.	2012	[82]
ASTM C1202	Slag+Metakaolin	NaOH+ $Na_2O.rSiO_3$	-	Increased metakaolin contents and higher activator concentrations decrease the water sorptivity and chloride permeability.	2012	[83]
ASTM C1202	Slag	NaOH+ $Na_2O.rSiO_3$	Nano-silica, Micro-silica	The micro-silica admixture increases the chloride resistance, hut the nano-silica shows the opposite results.	2017	[84]
ASTM C1202	Slag+Fly Ash	$Na_2O.rSiO_3$	-	The chloride resistance sequence of the different precursors: Slag>OPC>Fly Ash.	2018	[85]
ASTM C1202	Slag+Fly Ash	NaOH+ $Na_2O.rSiO_3$	MgO	The increasing incorporation of MgO promotes hydrotalcite formation and chloride resistance.	2018	[86]
ASTM C1543	Slag+Fly Ash	$Na_2O.rSiO_3$	-	The surface area of production gel increases with the fly ash inclusion, and the chloride sorption is increased.	2013	[87]
ASTM C1556	Slag+Fly Ash	NaOH+ $Na_2O.rSiO_3$	-	Fly ash mortars are much more susceptible to the chloride environment than the OPC mortars.	2016	[88]
ASTM C1556	Slag+Fly Ash	NaOH+ $Na_2O.rSiO_3$ or KOH+ $Na_2O.rSiO_3$	-	High calcium content increases the chloride resistance, but the high alkali concentration has the opposite effect.	2018	[89]
ASTM C1556	Fly Ash	NaOH+ $Na_2O.rSiO_3$+ $Na_2Si_2O_5$	-	The chloride diffusion resistance of the FA-based concrete is very low.	2019	[90]
NT Build 443	Slag	NaOH+ $Na_2O.rSiO_3$	-	The relationships of chloride diffusion factors are related to water soluble chloride.	2019	[91]
NT Build 443	Slag+Fly Ash	NaOH+ $Na_2O.rSiO_3$	-	The pH value affects the chemical and physical chloride binding capacity from the long-term chloride exposure.	2019	[92]
NT Build 492	Slag	NaOH+ $Na_2O.rSiO_3$	-	The increasing Ms promotes the chloride resistance.	2013	[93]
NT Build 492	Slag	Na_2CO_3	CLDH	The CLDH admixture enhances the chloride binding capacity of the sodium carbonate activated slag	2017	[94]
NT Build 492	Slag+Fly Ash	NaOH+ $Na_2O.rSiO_3$	-	The increase of Ms and decrease of fly ash content reduce the chloride diffusion due to the optimization of microstructure.	2019	[95]

externally added synthetic LDHs in AAMs pertaining to chloride resistance [76]. Thus, there are still largely unknown areas in terms of LDHs applied in AAMs matrix to promote the chloride resistance. The influence of the synthetic and externally added LDHs in AAMs needs to be deeply investigated.

Magnesium oxide (MgO) is introduced in the AAMs to deal with the chloride ingress problem, because the MgO content in the silicate system influences the formation of LDHs in the AAMs matrices, thus improving chloride resistance [86]. High contents of MgO (higher than 8 wt.%) increase the formation of the hydrotalcite-like phase and decrease the C–S–H phase. Consequently, the chemical binding capacity increases by more LDHs content but the physical binding capacity decreases by the less C–S–H gel [98]. With the addition of MgO in AAMs, it is hard to control the content of LDHs formation, because the reaction is affected by many parameters, e.g. the two metal ions molar ratio [99]. Therefore, further investigations are needed for a desirable control of MgO content in AAMs to increase the chloride binding capacity.

The calcined layered double hydroxides (CLDHs) can be calcined from the natural hydrotalcite (Mg-Al-CO_3 LDH) and rebuild the layered double structure in the high alkaline system [100]. Sato et al. [101] investigated the effect of CLDH on the cement concrete structure, the results of the rapid chloride penetration test showed that the CLDH promoted the chloride binding capacity due to the reconstruction of a LDH-like phase in the cementitious matrix (Fig. 2.2). The utilization of the CLDH in the sodium carbonate activated slag exhibited a higher chloride resistance than the reference samples without CLDH incorporation [102]. Because CLDH rebuilds the LDH-like phase to absorb the chloride ion and increases the chemical chloride bin-ding capacity. Therefore CLDHs has the potential to act as an effective chloride

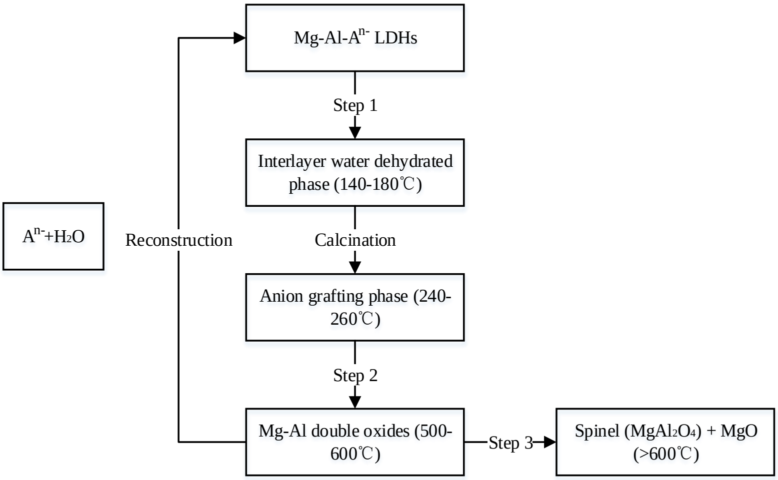

Fig. 2.2 Calcination and reconstruction of LDHs.

adsorbent in AAMs matrix. The CLDH content promotes the LDH-like phase formation, thereby affecting the chloride binding capacity of AAMs. As mentioned above, there were studies about applying CLDHs in sodium carbonate activated slag, but very limited researches about CLDHs applied in alkali activated slag and fly ash. Consequently, investigations on chloride adsorption of CLDHs are needed to understand the influence of the CLDHs dosage in alkali activated slag and fly ash.

The MgO and CLDH influence the LDH formation in AAMs, and externally added LDHs can play the role of filler and chemical absorbent in AAMs, thereby affecting the chloride resistance of AAMs. Therefore, the objective of this research is to investigate the different effects of MgO, nitrate intercalated LDHs and calcined LDH-CO_3 on chloride resistance of the AAFS binder. The reaction heat flow, reaction products, pore structures, mechanical properties and chloride resistance of alkali activated fly ash and slag incorporated with MgO, LDHs, and CLDHs are investigated. Furthermore, the mechanism to form the LDH in AAFS affected by MgO and CLDH is analyzed. The Ordinary Portland Cement (OPC) based samples are also used as the comparison to the AAMs samples. The respective contributions to enhance the chloride resistance of the three admixtures are evaluated.

2.2 Experiments

2.2.1 Starting Materials

Fly ash (FA), ground granulated blast-furnace slag (GGBS) and ENCI Portland Cement CEM I 52.5 R were utilized in this research. The chemical compositions were determined by X-ray fluorescence (XRF), as shown in Table 2.2.

Table 2.2 Chemical composition of the FA, GGBS, and Cement.

Composition	MgO	Al_2O_3	SiO_2	SO_3	K_2O	CaO	TiO_2	Fe_2O_3	Cl	LOI* （%）
FA	1.1	25.6	53.9	2.9	1.6	5.4	1.5	7.9	0.1	3.8
GGBS	9.0	13.1	31.2	5.2	0.3	39.1	1.4	0.7	0.1	1.0
Cement	1.8	3.9	16.6	4.1	0.2	69.5	0.3	3.7	0.1	0.7

*LOI = loss on ignition at 1000°C

The activator used in this research was a mixture of sodium hydroxide and sodium silicate solution. The SiO_2/ Na_2O molar ratio was 1.5. The composition of the sodium silicate is shown in Table 2.3.

Table 2.3 Chemical composition of the sodium silicate.

	SiO_2	Na_2O	H_2O
Wt. %	27.7%	8.4%	63.9%

The MgO utilized in this chapter was Magnesia 291 (provided by the MAGNESIA GERMANY) with a purity of 96%. The reactivity of the MgO was tested by the reaction time with acetic acid following [103]. The reaction time was 19.86 seconds, which was defined as a medium active magnesia. The specific surface area of the MgO was 51.39 m^2/g and Fig. 2.3 showed the crystalline pattern of MgO.

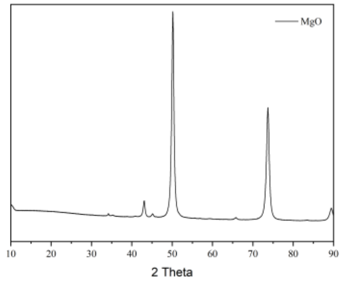

Fig. 2.3 X-ray diffractogram of MgO

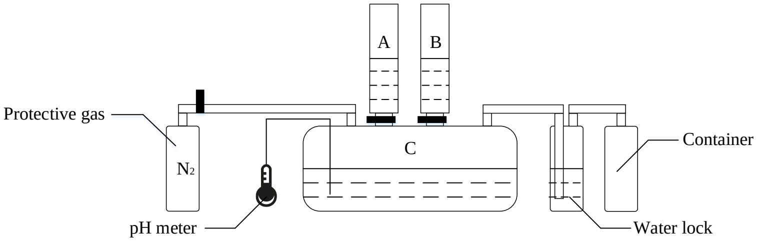

Fig. 2.4 Illustration of Mg-Al-LDHs-NO_3 synthesis.

Mg-Al-NO_3 LDH was prepared by a co-precipitation method [96]. Solution A containing Mg $(NO_3)_2 \cdot 6H_2O$ and Al $(NO_3)_3 \cdot 9H_2O$ with Mg/Al molar ratio of 3.0 ($[Mg^{2+}] + [Al^{3+}] = 1.0$ mol/L) and solution B containing 1.75 mol/L NaOH and 0.75 mol/L $NaNO_3$ was simultaneously dripped into 50 ml deionized water in a 500 mL container with magnetic stirring under N_2 atmosphere. The pH value of the solution was maintained at 11.0 ± 0.5. Afterward, the resulting suspension was aged at 65 °C for 24 h in a thermostatic bath. The final precipitate was filtered, thoroughly washed, and dried at 75 °C for 24 h. The set-up of the Mg-Al-NO_3 LDHs synthesis is shown in Fig. 2.4.

CLDH was calcined from the natural hydrotalcite (LDH-CO_3) (BeanTown Chemical) with a heating rate of 5 °C /min and kept at 550 °C for 3h. Then the material was cooled naturally in the furnace to 105 °C before it was moved to a sealed centrifuge tube and kept in a desiccator under vacuum. The characteristic peaks of the LDH and CLDH are presented in Fig. 2.5, showing the crystalline patterns of the LDH and CLDH. The feature peaks of LDH are situated at 13.6°(2 theta), while the feature peaks of the CLDH were situated at 41.2°, 51.3°, and 75.6°(2 theta). Fig. 2.5(d) illustrates that the CLDH shows the non-homogeneity state, which proves that the double layered structure collapsed to the non-rule layered structure.

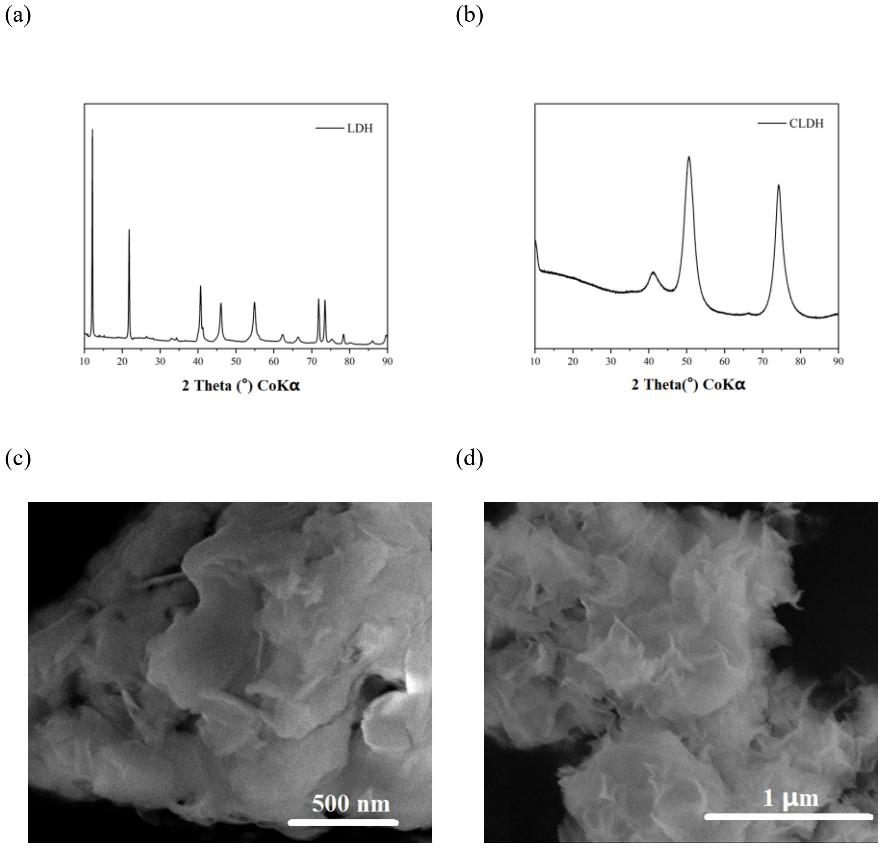

Fig. 2.5 (a) X-ray diffractogram of LDH-NO_3; (b) X-ray diffractogram of CLDH; (c) SEM of LDH NO_3; (d) SEM of CLDH.

2.2.2 Sample preparation

MgO, LDHs, and CLDHs replaced 2 wt. % and 4 wt. % of the alkali activated binder, which are described as modified samples. GGBS / FA mass ratio is 7:3 (see the sample ID in Table 2.4). The starting raw materials were mixed with the designed proportion in the mortar mixer following the preparation procedure suggested by EN 196-1 [104]. Paste samples were cast in the steel molds (40 mm × 40 mm × 40 mm) followed by the vibration. All the mortar samples were cast in the Ø 100 mm × 200 mm cylinder mold followed by the vibration.

All the samples were warped in plastic film to prevent moisture losses under 20 ℃ until the specific days for testing.

Table 2.4 Formulations of the pastes and mortars using different additions.

Sample ID	Binder						Sand	Na_2O/Binder	W/B*
	GGBS	FA	MgO	LDH(NO_3)	CLDH	Cement			
P-A0	70	30	-	-	-	-	-	7%	0.4
P-M2	68.6	29.4	2	-	-	-	-	7%	0.4
P-M4	67.2	28.8	4	-	-	-	-	7%	0.4
P-L2	68.6	29.4	-	2	-	-	-	7%	0.4
P-L4	67.2	28.8	-	4	-	-	-	7%	0.4
P-C2	68.6	29.4	-	-	2	-	-	7%	0.4
P-C4	67.2	28.8	-	-	4	-	-	7%	0.4
P-OPC	-	-	-	-	-	100	-	-	0.4
M-A0	70	30	-	-	-	-	300	7%	0.4
M-M2	68.6	29.4	2	-	-	-	300	7%	0.4
M-M4	67.2	28.8	4	-	-	-	300	7%	0.4
M-L2	68.6	29.4	-	2	-	-	300	7%	0.4
M-L4	67.2	28.8	-	4	-	-	300	7%	0.4
M-C2	68.6	29.4	-	-	2	-	300	7%	0.4
M-C4	67.2	28.8	-	-	4	-	300	7%	0.4
M-OPC	-	-	-	-	-	100	300	-	0.4

* W/B = Water/Binder mass ratio (where binder is defined as FA + GGBS + MgO/LDH/CLDH)

2.2.3 Characterization

X-ray diffractometry

X-ray diffractometry (XRD) was performed by using a Bruker D4 Phaser instrument with Co-Kα radiation (40kV, 30mA). The powdered specimens were measured with a step size of 0.05° from 5° to 80° 2θ, and a counting time of 1s/step.

Isothermal calorimetry

The heat flow of the samples by different precursors was measured by an isothermal calorimeter set at 20℃ (TAM AIR Calorimetry). It was noteworthy that the initial 4-6 minutes after mixing could not be measured due to the sample preparation procedure and the initial 0.5-1h of the heat flow data could be inaccurate because of the instability of apparatus disturbed by the loading process. The results were normalized by the mass of the solid, excluding the water amount.

Nitrogen physisorption test

The nitrogen sorption test was conducted by TriStar II 3020, Micromeritics. The pore size distribution was determined by the Barett, Jonyer, and Halenda (BJH) method [105] from the desorption branch. Before the test, paste samples were ground to powder and the samples were immersed in the 2-propanol for 24h to stop the hydration process, then dried to constant weight with liquid nitrogen at the age of 28 days.

Mercury intrusion porosimetry

The samples for the mercury intrusion porosity (MIP) analysis were selected from mortars, with the dimensions of 3-5 mm each side. The selected samples were immersed in 2-propanol for 24h to halt the hydration process and then put in the vacuum drying oven for 3 days in order to remove all the pore water. The MIP tests were conducted by using a Micromeritics Autopore 9600 Mercury Porosimeter.

Compressive strength

After 28 days of curing, the strength of the samples was determined according to EN 196-1 [104]. The samples were centered on the platens of the machine. Subsequently, the load was increased smoothly at the rate of 2400 N/s over the entire load application until the fracture load.

Non-steady-state migration experiments

The Ø 100×200 mm cylindrical mortars were used and cut into 50 ± 2mm thick slice from the central portion. The cylindrical samples were put in the vacuum container for vacuum treatment for 3 hours with the pressure in the range of 10-50 mbar (1-5kPa), and then the samples were immersed in the saturated $Ca(OH)_2$ solution for 18±2 hours. Subsequently, the non-steady-state migration (NSSM) experiments were carried out according to the NT Build 492 [106].

$AgNO_3$ was used to reveal the chloride penetration depths. The non-steady-state migration coefficient is calculated by [106]:

$$D_{nssm}=\frac{0.0239(273+T)L}{(U-2)t}\left(x_d-0.0238\sqrt{\frac{(273+T)L\cdot x_d}{U-2}}\right) \tag{2-2}$$

Where:

D_{nssm}:	non-steady-state migration coefficient, ×10^{-12} m^2/s;
U:	the absolute value of the applied voltage, V;
T:	the average value of the initial and final temperatures in the anolyte solution, °C;
L:	the thickness of the specimen, mm;
x_d:	the average value of the penetration depths, mm;
t:	test duration, hour.

The scheme of the NSSM test set up is shown in Fig. 2.6

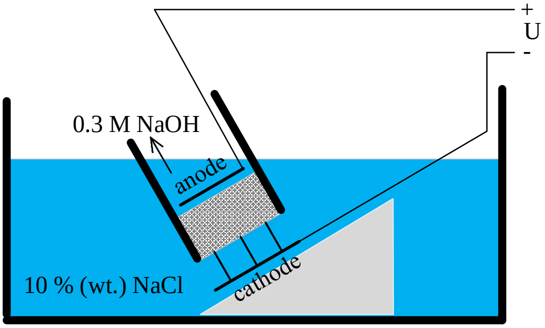

Fig. 2.6NSSM test set-up.

2.3 Results and discussion

2.3.1 Reaction kinetics

The reaction process of AAFS (shown in Fig. 2.7(a)) can be generally classified into three stages [107,108]: (a) destruction–coagulation; (b) coagulation–condensation; (c) condensation–crystallization. The normalized hydration heat flows of different samples are shown in Fig. 2.7(b). The MgO, LDHs and CLDHs addition exhibit a prolonged dormant period and the time to reach the reaction peak (TRRP) of the investigated mixture ranged from 10-15 hours (shown in Fig. 2.8).

The primary differences between OPC pastes and AAFS pastes are obvious. The normalized hydration heat peak of the AAFS binder is 75.9% smaller than that of the OPC binder, comparing to the P-OPC and the P-A0 (Fig. 2.8). It is clear from Fig. 2.8 that increasing the MgO, LDHs and CLDHs content slightly prolong the TRRP.

Due to the high MgO content in the P-M2 and P-M4 (higher than 8 wt. %), the high MgO systems can preferentially form hydrotalcite by reacting Al with Mg [98], and the hydration heat shows the prolonged TRRP. As shown in Fig. 2.7(b) and Fig. 2.8, the P-M2 and P-M4 extend the TRRP at 3.2% and 3.9% comparing to the P-A0, respectively. Firstly, MgO dissolves in the solution and releases Mg^{2+}; Then, the free Mg^{2+} reacts with the OH^- in the alkaline environment precipitating the $Mg(OH)_2$ and decreasing slightly the pH value. Consequently, the MgO addition increases the TRRP and delays the hydration process slightly. Meanwhile, the increased MgO content has a slight effect on TRRP in the high MgO (higher than 8 wt. %) and Al_2O_3 (higher than 14 wt. %) blended system [109].

The addition of LDHs in the geopolymer pastes shows a slight prolonged TRRP and decreased heat peak. The P-L2 and P-L4 exhibit the 7.2% and 11.2% delay comparing to the P-A0 reference, respectively. Firstly, the nitrate ion in the LDH releases some NO_3^-, and the OH^- in the AAFS matrix partly exchange with NO_3^-, resulting in the pH value decrease of the AAFS matrix. Thus, it delays the TRRP. Secondly, the agglomeration of LDH materials can also extend the TRRP in AAFS matrix. Therefore, the incorporation of LDH exhibit a decrease in TRRP and reaction heat peak.

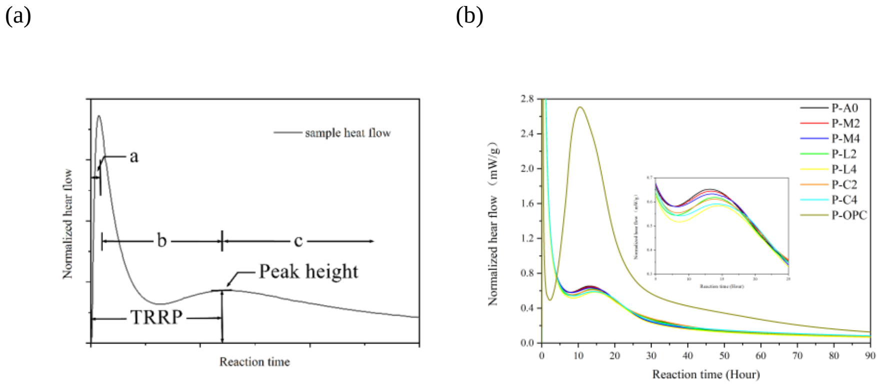

Fig. 2.7 Normalized reaction heat flow (a. hydration process of AAFS pastes; b. AAFS and OPC pastes).

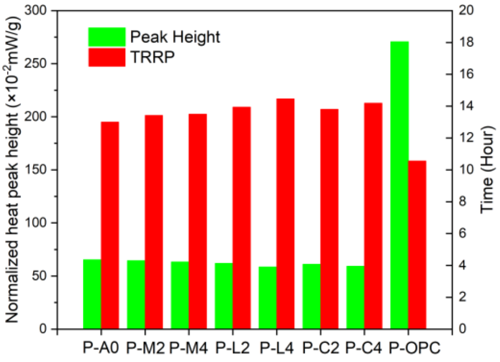

Fig. 2.8 Heat peak and TRRP of AAFS and OPC pastes.

Ke et al. [102] utilized the CLDHs to expedite the reaction kinetics of the different Na_2CO_3 activated blast furnace slags. The CLDHs was associated with the removal of dissolved CO_3^{2-} from the fresh cement, yielding a rise in the pH value, and the potential seeding effects. While the CLDHs in sodium silicate and sodium hydroxide activated fly ash and slag system demonstrate the opposite effect, the CLDHs react with OH^-, forming the LDH-OH and yielding a decrease in the pH value, consequently prolonging the TRRP. Therefore, the TRRP prolongs 0.81 hours (P-C2) and 1.19 hours (P-C4) comparing to the reference group P-A0 (shown in Fig. 2.8), which extends the TRRP 6.2% and 9.2%, respectively.

2.3.2 Reaction products

The XRD patterns of the samples show that the primary hydration products of AAFS binder are C−(A)−S−H and hydrotalcite-like phase.

Fig. 2.9(a) and (b) show the crystalline phases in all the AAFS samples exhibit the same reaction products at 3 curing days and 28 curing days, respectively. Comparing Fig. 2.9(a) and (b), the 3-day crystalline products of AAFS are practically consistent with the 28-day crystalline products. The primary AAFS crystalline products are formed in the initial 3 days. However, the OPC samples show the peak changes between 3 days and 28 days, which illustrates that the hydration still goes on after 3 days.

The main characteristic peak of hydrotalcite is identified at 13.6° from Fig. 2.9(a) and Fig. 2.9(b). However, Ke et al. [110] reported the main peak of the XRD pattern for a similar hydrotalcite-like phases after filtration was centered at 11.6°. The shift in the hydrotalcite-like peak can be attributed to the partial carbonation of the LDH.

Periclase is identified in specimens prepared with MgO addition (P-M2 and P-M4), which indicated that the MgO is not fully reacted with slag to form LDH. However, according to the previous study [86], the content of LDH formed from MgO in AAFS binder has the potential to grow over time, due to the solid state reaction of MgO in alkali activated cement.

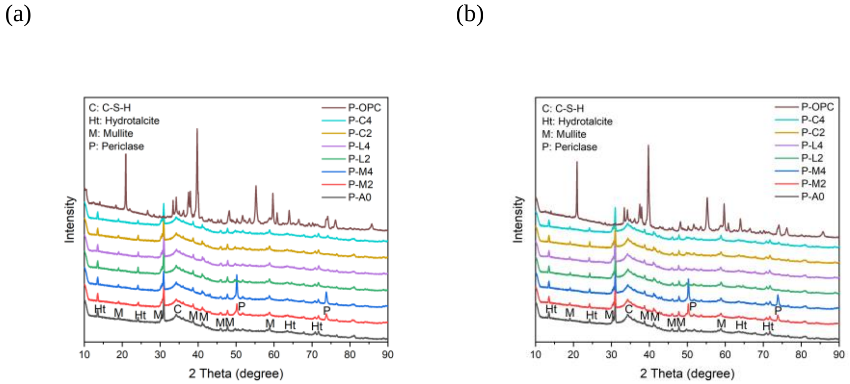

Fig. 2.9XRD patterns of AAFS and OPC pastes at (a) 3 days; (b) 28 days.

The XRD patterns of P-L2, P-L4, P-C2, and P-C4 demonstrate almost the same intensity of LDHs. The characteristic peak of the CLDH phase is not found either in 3-day or 28-day XRD patterns, while the peak of the hydrotalcite-like phase appears, proving the CLDH completes the reconstruction process in AAFS to form the LDH.

Combining Fig. 2.9(a) and Fig. 2.9(b), the MgO and CLDH participate in the LDH formation in the AAFS matrix. Meanwhile, the externally added LDH can remain in the AAFS matrix. The three admixtures show the same results in the AAFS matrix in terms of the crystalline products.

2.3.3 Pore structure

As seen in Fig. 2.10(a), the OPC pastes obtain the most mesopores (20 to 50 nm) and macropores (50 to 100 nm) and the lowest micropores. Meanwhile, the AAFS pastes are also the highest in mesopores and the lowest in micropores and macropores, as shown in Fig. 2.10(b). The amount of the mesopores is nearly the same for all the AAFS pastes, which are quite different from the mesopores in OPC pastes. OPC pastes show a larger pore size than those of AAFS pastes.

Fig. 2.10(b) shows the pore size distribution of AAFS pastes incorporating 2 wt.% and 4 wt.% MgO, LDH and CLDH. It shows the porosity slightly increases from the reference sample P-A0 to samples containing 2 wt.% and 4 wt.% MgO and CLDH. Furthermore, the porosity decreases with the LDH addition. Therefore, the pore size distribution is slightly improved by the LDH addition, and the microstructure is refined.

The pore size distribution results of mortars from the MIP measurement are shown in Fig. 2.11. It is obvious that the pore size distribution of OPC mortars mainly situates between the 10-100 nm (mesopores), which are consistent with the BJH method results shown in Fig. 2.10(a).

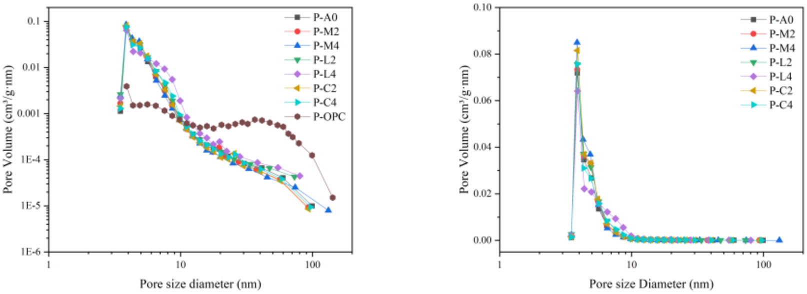
(a) (b)

Fig. 2.10 Pore size distribution of AAFS and OPC from nitrogen sorption results (a. AAFS and OPC pastes; b. AAFS without OPC pastes).

The AAFS mortars are the highest in mesopores and the lowest in macropores. As described in Fig. 2.11(b), the addition of MgO (M-M2 and M-M4) increases the total volume of the macropores comparing to the reference M-A0. However increasing the content of MgO can reduce the macropores of AAFS mortars, which forms a small amount of the $Mg(OH)_2$ to fill the pores and corresponds well with the reference [111,112].

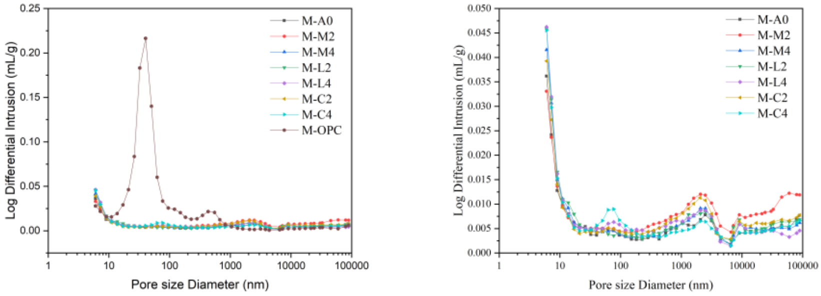
(a) (b)

Fig. 2.11 Pore size distribution of AAFS and OPC mortars from MIP results (a. AAFS and OPC mortars; b. AAFS mortars).

Fig. 2.12(a) and Fig. 2.12(b) show the cumulative porosity and the total porosity of AAFS and OPC samples. The total porosity of OPC mortars (20.01%) is much higher than the M-A0 mortars (3.969%).

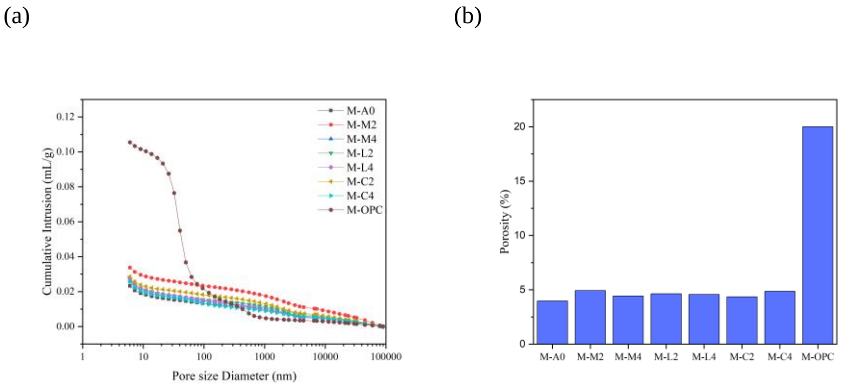

Fig. 2.12 (a) Cumulative porosity of AAFS and OPC mortars from MIP results; (b) Porosity of AAFS and OPC mortars from MIP results.

The porosity of AAFS decreases with the increasing MgO dosage, which is generally in agreement with the BJH method result (Fig. 2.10(b)). The LDH admixture in the AAFS samples also shows a slight influence on the porosity, but the 2 wt.% and 4 wt.% replacement of the fly ash and slag exhibit little difference in terms of the porosity (4.64% and 4.57%, respectively). However, comparing the porosity of P-A0, the incorporation of 2 wt.% and 4 wt.% CLDH (M-C2 and M-C4) has a positive correlation on total porosity, increasing up to 4.35% and 4.87%, respectively.

In general, the incorporation of MgO, LDH, and CLDH have slight effects on total porosity, while the unreacted MgO and small amount of the $Mg(OH)_2$ function as a filler in the AAFS matrix. The LDH and CLDH admixtures have a slight effect on the microstructures. The AAFS mortars exhibit almost the same porosity, ranging from 3.96% to 4.93%.

Combining the nitrogen sorption results and MIP measurement results, the pore size of AAFS mortars mainly range from 3-10 nm (mesopores), while the pore size of OPC mortars mainly widely situate from 10-100nm (both mesopores and macropores) The total porosity of the AAFS mortars are from 3.96% to 4.93%, while the OPC mortars is around 20.01%.

2.3.4 Compressive strength

Fig. 2.13(a) shows the compressive strength of the AAFS and OPC pastes at the curing age of 3, 7 and 28 days. Fig. 2.13(b) shows the relative strength of blended pastes at 3, 7 and 28 days compared to the AAFS (P-A0). The increasing trend of compressive strength shows that the strength of AAFS samples may continue to increase after the 28-day curing time, due to the incorporation of fly ash with a slow pozzolanic reactivity. These observed trends are related to the XRD results shown in Section 2.3.2, and also in agreement with [113,114].

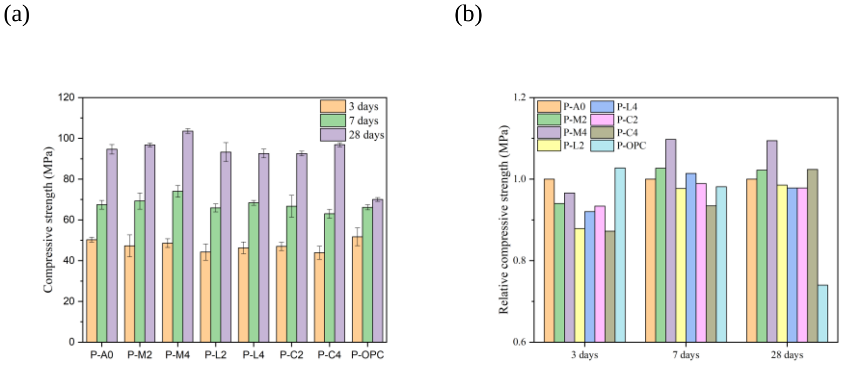

Fig. 2.13 (a) Compressive strength of AAFS and OPC pastes; (b) Relative compressive strength of AAFS and OPC pastes.

The compressive strength increases with the increasing content of the MgO of 7 and 28 days, and this agrees with previous researches [115–117]. P-M2 and P-M4 exhibit higher compressive strength than other samples, up to 96.75 MPa and 103.58 MPa at 28 days curing age, respectively. The increase in relative strength for increased MgO content is attributed to the total content of MgO. Hwang et al. [117] reported that the content of MgO at 12 wt. % (including the MgO inside binder material) in alkali activated slag showed the highest compressive strength. As the MgO dosage increased in P-M2 and P-M4, the compressive strength increases. The observed results agree with the mesopores distribution in Section 2.3.3, the increased MgO content decreases the macropores and porosity that leads to the higher compressive strength.

Increasing the dosage of LDH in AAFS shows a slight decrease in compressive strength at 28 days, compared to the reference sample (P-A0). According to [118], the strength of the concrete samples gradually decreased with the increasing content of LDH. Meanwhile, the macropores of LDH samples increased with the rising dosage of LDH in Section 2.3.3, the obtained compressive strength is consistent with these results.

The compressive strength development of CLDH addition in AAFS exhibits the same trend with LDH addition samples, namely the CLDH addition in AAFS slightly declines the compressive strength. Furthermore, P-C2 and P-C4 show the same compressive strength level with P-L2 and P-L4, at the 28 days curing age, respectively. The observed results are in agreement with [119], who reported that the CLDH content higher than 1wt. % resulted in the reduction of compressive strength.

2.3.5 Chloride migration

The results of the NSSM experiments are shown in Table 2.5 and Fig. 2.14. The OPC reference illustrates the highest coefficient D_{nssm} among all mortar specimens. Meanwhile, the AAFS reference (M-A0) also shows the highest coefficient D_{nssm} in all AAFS mortars, excluding the samples with 2 wt.% LDH replacement (M-L2). Fig. 2.14(b)shows the relationship between replacing materials content and chloride migration coefficients. With the increasing replacement content, the MgO, LDH and CLDH mortars show the decreasing trend of the coefficient. In general, the incorporation of MgO, LDH, and CLDH increases the chloride resistance of AAFS mortars.

As one can see from Fig. 2.14, the MgO admixture decreases the chloride migration coefficient. The chloride binding capacity is due to (1) the LDH phase in the AAFS [45,86,120] and (2) pore size distribution [66,121,122]. On the one hand, the XRD pattern (in Section 2.3.2) shows that the hydrotalcite phase is formed in the AAFS samples, which can increase the chloride binding capacity. The MgO is a significant resource to form the LDH, and the chloride migration coefficient proves that the MgO addition enhances the hydrotalcite formation and then promotes the chloride resistance of AAFS [86]. The results in Table 2.5 illustrates that the coefficient D_{nssm} of M-A0, M-M2, and M-M4 are 5.42, 4.68 and 4.55 $\times 10^{-12}$ m^2/s, respectively. The chloride migration coefficient declines by 13.7% (sample M-M2) and 16.1% (sample M-M4), compared to the reference sample M-A0. On the other hand, the pore size distributions have a large effect on the chloride resistance of the AAMs samples with supplementary cementitious materials (SCMs), especially the mesopores and macropores significantly affect the permeability of concrete. The relationship between microstructure and permeability is investigated by many researchers [95,123]. As we can conclude from Section 2.3.3 that the increasing MgO content leads to more LDH formation, resulting in more chloride binding. Thus, the observed results are consistent with the NSSM test.

Fig. 2.14(a) and (b) also show the nitrate intercalated LDH incorporation in the AAFS matrix in terms of the chloride resistance. Comparing M-L2 and M-L4 to M-A0, the chloride migration coefficient of M-L2 is higher than the reference M-A0 at 7.2%, while the coefficient of M-L4 is lower than the reference sample at 17.2%. The obtained results indicate that the nitrate intercalated LDH has a remarkable increase in the chloride binding capacity of AAFS. The slight increase in the M-L2 coefficient is possibly due to the high applied voltage during the NSSM test. Spiesz et al. [124] reported that the coefficient D_{nssm} was nearly 10% larger for samples under the 60V than the samples under the lower voltages (35V and 47.5V). Generally, the dosage of the nitrate intercalated LDH has a direct influence on the chloride resistance of the AAFS matrix, Fig. 2.14(b) shows that the chloride resistance of samples is sensitively related to the increasing LDH dosage.

The CLDH incorporation has the highest contribution to chloride binding capacity in the AAFS matrix as shown in Fig. 2.14(a) and (b). The coefficient of M-C2 and M-C4 is lower than M-A0 at 24.2% and 46.9%, respectively. Obviously, the CLDH illustrates the higher chloride resistance than the MgO and LDH addition. This phenomenon may be attributed to the filler effect of LDH formation from CLDH on the AAFS mortars, and the microstructures also prove that the mesopores and macropores decrease as the CLDH content increased. The CLDH also absorbing a lot more of the water in the mix and giving an effectively lower w/b ratio as it rehydrates. Meanwhile, the mesopores and macropores results are consistent with the observed chloride penetrations in the AAFS matrix. The CLDH addition in AAFS has the lowest mesopores and macropores, thus CLDH contributes to the highest chloride resistance in all the AAFS samples in this chapter.

Table 2.5 Chloride migration coefficients calculated from the NSSM test in the mortar at 28 days curing age.

Sample ID	M-A0	M-M2	M-M4	M-L2	M-L4	M-C2	M-C4	M-OPC
Chloride migration coefficient (×10^{-12} m^2/s)	5.4	4.7	4.6	5.8	4.5	4.1	2.9	7.6
Applied voltage (V)	30	24.9	15.2	20.3	30.0	20.3	30.1	25.1
Time duration (hours)	19	17	20	17	23	24	23	23.5
Thickness of sample (mm)	52.5	49	49.5	45.5	50.2	47.5	48	50
xd (mm)	10.3	7.0	5.3	7.4	10	7.2	7.0	14

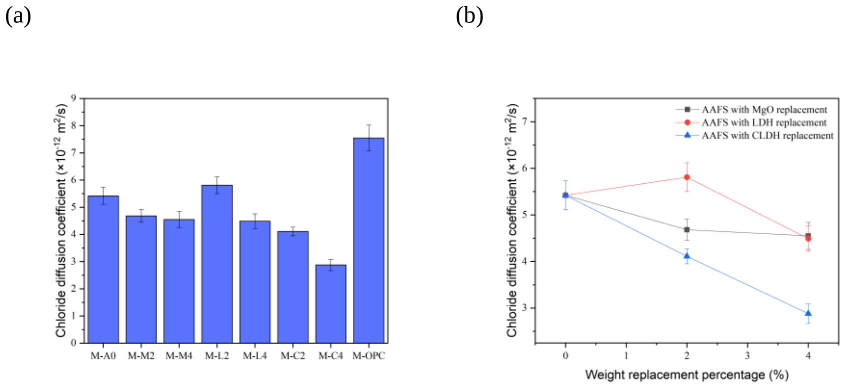

Fig. 2.14 (a) Chloride migration coefficients of AAFS and OPC mortars; (b) The relationship between replacing materials content and chloride migration coefficient.

2.4 Conclusions

In this paper, the reaction heat flow, reaction products, microstructure, compressive strength, and chloride resistance of alkali activated fly ash and slag blends with the addition of MgO, LDH and CLDH are studied. The different effects of the MgO, Mg-Al-NO_3 LDH and CLDH incorporation are evaluated. The three admixtures in AAFS are proved to enhance the mechanical property, chloride resistance, and microstructure. According to the experimental results, the following conclusions can be drawn:

- The MgO, LDH and CLDH admixtures delay the time to reach the reaction peak

(TRRP) in the AAMs matrix up to 3.9%, 11.2%, and 9.2%, respectively. The MgO admixture first forms $Mg(OH)_2$ precipitation, while the LDH-NO_3 and CLDH absorb the OH^-. Therefore, all three admixtures slightly decrease the pH value in the AAFS matrix and prolong the time to the reaction peak (TTRP).

- MgO promotes the formation of the in-situ growth of LDH phase, and the CLDH completes the LDH-reconstruction process in AAFS. Meanwhile, the externally added LDH-NO_3 remains in the AAFS matrix. The LDHs phase influenced by the three admixtures shows the partial carbonation in the AAFS matrix, and the carbonation results in the shift of LDH-NO_3 characteristic peak from 11.6° to 13.6° (2 theta).

- The microstructures of AAFS are refined by the inner filler effect with unreacted MgO and a small amount of $Mg(OH)_2$. The MgO shows the highest refinement on mesopores and macropores. While the LDH-NO_3 and CLDH admixtures have a limited effect on the microstructure.

- The increased MgO and CLDH content result in the higher compressive strength in AAFS, which is related to the mesopores refinement. While the LDH admixture shows limited influence on the compressive strength.

- MgO, LDH-NO_3, and CLDH improved the chloride resistance of the AAFS matrix. The CLDH shows the highest chloride binding capacity and enhancement.

Chapter 3 In-situ formation of layered double hydroxides (LDHs) in sodium aluminate activated slag: The role of Al-O tetrahedra

Alkali activated materials (AAMs) have gained great attention as a new low-carbon binder. However, their durability performance, e.g. chloride ingress resistance, still needs further improvement. This chapter attempts to enhance the chloride binding of AAMs by activating slag with sodium aluminate with the aim to promote the in-situ formation of layered double hydroxides (LDHs). The evolution of pH and ions in the pore solution, reaction products and microstructure were determined to investigate the dynamic activation process. Results show that the sodium aluminate stabilizes the pH environment at around 12.7 during the curing ages. The Mg-Al-LDH with higher Al-O tetrahedra (denoted as $Al(OH)_4^-$) contents is promoted, enhancing the chloride absorption capacity. A new reaction mechanism is proposed to describe the activation process. This chapter reveals that the extra $Al(OH)_4^-$ in a relatively low pH environment prevents the competition between Mg^{2+} and Si-O tetrahedra to react with $Al(OH)_4^-$, promoting the formation of LDH and C(N)−A−S−H simultaneously.

This chapter is partially published elsewhere:

T. Liu, Q. Yu, H.J.H. Brouwers, In-situ formation of layered double hydroxides (LDHs) in sodium aluminate activated slag: The role of Al-O tetrahedra. Cement and Concrete Research. 153 (2022). doi:10.1016/j.cemconres.2021.106697.

3.1 Introduction

Alkali activated materials (AAMs) have shown to be a promising alternative to Portland cement. However, its long-term performance, as well as the involved mechanisms under different exposure environments, are still not well understood. Many efforts have been spent on enhancing the chloride resistance of AAMs, but the effects are limited [76,125,126]. Besides, the high pH of AAMs also showed hazardous which limits their practical application [127]. The effect of amorphous gels and the crystalline phases in the hardened cementitious materials are investigated pertaining to chloride resistance [19,20]. Layered double hydroxides (LDHs), one of the secondary reaction products of alkali activated ground granulated blast-furnace slag (GGBS), can absorb the anions, e.g. chloride ion, in the matrix [128]. The incorporation of ex-situ synthetic LDHs in the AAMs systems has been investigated and the LDHs showed high effectiveness in terms of chloride binding [21,129]. However, external-added LDHs absorb a large amount of water during the casting, which limits the total content of external LDHs in the AAMs matrix [96]. Besides, the costly and complicated synthesis process also highly limits the external LDHs application in the AAMs matrix to tackle the chloride ingress issue [21,22]. Moreover, promoting the in-situ formation of LDHs to replace the external-added LDHs AAM has not been well addressed.

Chloride ingress is one of the most prominent issues in AAMs. The chloride resistance is influenced by chemical binding through reaction products and physical absorption via pores and reaction products [76]. From the aspect of reaction products, the incorporation of ex-situ synthetic LDHs shows a virtuous performance of chloride resistance attributed to physical absorption (major contribution) and chemical binding (minor contribution) of chloride ions [20,21,129]. Xu et al. [81] synthesized Mg-Al-NO_3-LDH and Mg-Al-NO_2-LDH, finding that the chloride binding and corrosion resistance are increased by both LDHs additions. Qu et al. [96] reported that smaller particle size of Mg-Al-NO_3-LDH improved the microstructure, meanwhile, the LDH material promoted the chemical chloride binding capacity of the matrix. Moreover, Ke et al. [130] examined the chloride removal by Mg-Al and Ca-Al LDHs in the simulated pore solution of alkali activated slag cement and found that the chloride binding was due to ion exchange and surface adsorption. At the same time, the chloride uptake was sensitive to pH change in the pore solution. Mundra et al. [131] simulated the chloride transport in AAMs and found that the Ca-Al LDH increased in the low MgO system while the Mg-Al LDH increased in the high MgO system. Both Ca-Al and Mg-Al LDH postpone the chloride ingress and increase chloride resistance. Besides, it is also worth mentioning that the Mg-Al LDH shows better chloride binding capacity than Ca-Al LDH. However considering the water absorption of LDHs during casting, the content of LDHs in the AAMs system is usually lower than 4 wt. % of binder as otherwise the large water demand would compromise other properties [21,96], which significantly limits the chloride binding capability of AAMs. Ye [22] reported the autogenous formation and the behaviors of nitrite- and nitrate-intercalated LDHs in Portland cement-metakaolin-dolomite (OPC-MK-DM) blends. While the author attempted to increase the autogenous formation of AFm (Ca–Al LDHs), the results suggested that the incorporation of NO_2^- and NO_3^- harmed the evolution of microstructure despite the NO_2^- and NO_3^- anions preferably occupied the interlayer space of LDHs phases. Also, the increase of OPC replacement ratio from 30% to 45% in the ternary OPC-MK-DM systems lowered the degree of reaction and amount of reaction products. Therefore, the amount of LDHs phases was limited. Consequently, the autogenous formation of LDHs contributed little impact to the chloride binding capacity. These studies reveal that the chemical binding of chloride ions in AAMs is intensively affected by the amount of LDHs [21,99]. Thereby, the increase of in-situ formed LDHs in the AAMs could increase the chloride binding capacity. It is thus hypothesized that the increase of in-situ synthetic LDHs has a high potential for a remarkable increase in the chloride resistance of AAMs.

The skeleton of LDHs consists of two metal ions, one is a divalent cation (e.g. Mg^{2+}), and the other one is a trivalent cation (e.g. Al^{3+}) [132]. The concentration of aluminate (one type of normal trivalent metallic ions in LDH) in the pore solution of the AAMs matrix is one of the most important factors influencing the crystallization of the LDHs [133]. Meanwhile, the condition of Mg-Al LDH crystallization requires a relatively lower pH environment (ranging from 9~11) than the normal alkali activated solution [132]. Thus, the sodium aluminate solution, in this research, is hypothetically introduced as an activator to control (1) the Al-O tetrahedra (hereafter denoted as $Al(OH)_4^-$) concentration and (2) a relatively low pH value in the pore solution of the AAM matrix to enhance the in-situ formed LDHs. Thereby, the comprehension of the mechanism of in-situ formed LDHs in AAMs is critical to understand how the sodium aluminate promotes the formation of LDHs. Moreover, the $Al(OH)_4^-$ participates in the process of gel formation. However, the mechanism of how the sodium aluminate affects the formation of calcium (sodium) aluminosilicate hydrates (C(N)−A−S−H) phases still remains poorly understood.

To discuss it further, the other physical aspects of chloride resistance, e.g. the lower porosity and more complex tortuosity of the microstructure in the AAMs matrix, in general, contribute to decreasing the chloride penetration. The complex distribution of pore diameter ranges and pore connections have a huge effect on ions' transport property [134]. Gel formation is the important factor influencing the evolution of microstructure, while the content of Si-O and Al-O tetrahedra, pH value, and other ions in the pore solution influence the gel formation. Under a given alkali content, the SiO_2 to Na_2O molar ratio improves the microstructure evolution at the early stage [135], benefiting the transport parameters and enhancing the chloride resistance of AAMs [136]. Similarly, the Al_2O_3 to Na_2O molar ratio also influences the gel formation, affecting the pore evolution [137]. The Al_2O_3 mainly comes from the solid precursors, while the proposed sodium aluminate activator providing a large amount of $Al(OH)_4^-$ could directly participate in the reaction [138]. The sodium aluminate activator was also investigated to generate more ettringite and calcium silicate hydrate (C−S−H), resulting in the strength increase [72]. The formation of more gel refines the microstructure, increasing the physical chloride binding ability. Therefore, the sodium aluminate is hypothetically an appropriate activator, as it can provide both (1) available Al-O tetrahedra and (2) a low pH environment for the LDH and gel formation, because the extra $Al(OH)_4^-$ could prevent competition between LDH and gel capturing $Al(OH)_4^-$ during the process of reaction. The mechanism of how the $Al(OH)_4^-$ in sodium aluminate activator promotes the formation of LDHs and gels remains unknown in alkali activated slag system. More specifically, there is insufficient understanding about how ions changes of pore solution explains the phases evolution and in-situ formed LDHs and gel.

This chapter investigates the mechanism of how the $Al(OH)_4^-$ influences in-situ synthetic LDH and gel formation in sodium aluminate activated slag (SAAS), and the consequent chloride absorption performance. The changes of pH value and composition in the pore solution of SAAS paste were analysed to reveal how $Al(OH)_4^-$ affects the Mg-Al LDH and gel formation at different curing ages. The reaction heat flow, reaction products as well as microstructure were determined to understand the activation process. A reaction mechanism was proposed to give an insight into the promotion of in-situ formed LDH and gels by sodium aluminate activator.

3.2 Experiment

3.2.1 Materials and sample preparations

Ground granulated blast-furnace slag (GGBS) was used in this chapter. The chemical compositions were determined by X-ray fluorescence (XRF), as shown in Table 3.1. The crystalline structure was determined by X-ray diffraction, as shown in Fig. 3.1(a). The particle size distribution (PSD) of the powder feedstocks was determined by laser granulometry, using a Master Sizer laser granulometry with an open measuring cell. The preparation of the powders was done by wet dispersion in deionized water. The particle size distribution is shown in Fig. 3.1(b), with the average particle size (d_{50}) of 16 μm.

Table 3.1 Chemical compositions and physical properties of GGBS.

Chemical composition	MgO	Al_2O_3	SiO_2	SO_3	K_2O	CaO	TiO_2	MnO	Fe_2O_3	LOI* (1000°C)	Particle density (g/cm3)	Specific surface area (m2/g)
GGBS (wt. %)	8.5	13.2	30.7	2.8	0.3	42.1	1.6	0.4	0.4	1.3	2.9	0.3

*LOI = loss on ignition at 1000 °C

The GGBS was activated by sodium hydroxides and sodium aluminate solutions, respectively (see the sample IDs in Table 3.2). The starting raw materials were mixed with the designed proportion in a Hobart mixer following the preparation procedure suggested by EN 196-1 [139]. The pastes were cast in the Ø 45 mm × 55 mm cylindrical plastic mold followed by vibration. All the pastes were sealed and cured at the ambient temperature until the specified curing ages.

The detailed information about the preparation of the used activators is presented as follows. The analytical grade sodium hydroxide pellets (99% purity) were dissolved in deionized water to prepare the sodium hydroxide (NH) solution for the Ref-NH samples, and the sodium hydroxide activator was prepared 24 hours before applications. The analytical grade sodium aluminate pellets were dissolved in deionized water to prepare the sodium aluminate (NA) solution for the NA2 to NA4 samples, while the sodium aluminate activator was prepared 6 hours before applications.

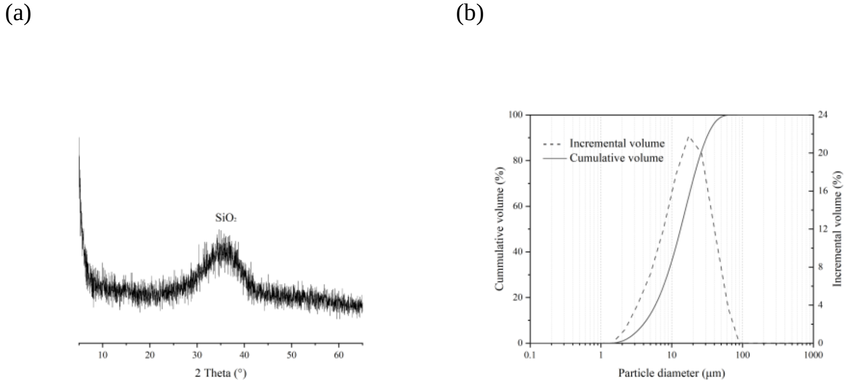

Fig. 3.1(a) X-ray diffractogram of GGBS; (b) Particle size distribution of GGBS.

Table 3.2 Formulations of the paste samples.

Sample ID	GGBS (g)	$NaAlO_2$ (wt. %)	NaOH (wt. %)	Na_2O/Binder (wt. %)	W/B*
NA2	100	5.3	-	2	0.4
NA2.5	100	6.6	-	2.5	0.4
NA3	100	7.9	-	3	0.4
NA3.5	100	9.3	-	3.5	0.4
NA4	100	10.6	-	4	0.4
Ref-NH	100	-	5.2	4	0.4

* W/B = Water/Binder mass ratio

3.2.2 Testing methods

Cold water extraction

The ground powder from pastes was utilized to measure the ions and the pH value of the pore solution by Cold water extraction (CWE) at specific curing ages (3, 7, 14, and 28 days). 50g of powder was mixed with 50g of deionized water and shaken for 5 mins (5-min leaching procedure) [140,141]. The suspension was then filtrated by a filter syringe. Previous studies showed no remarkable uptake of ions by the filter [141]. Finally, the rapid leachate was diluted 10 times with deionized water. The obtained diluted solutions were acidified with HNO_3 to prevent the precipitation, and then the solutions were analyzed for Al, Si, Mg, and other heavy metal ions using Inductively coupled plasma-optical emission spectrometry (ICP-OES). During the acidification HNO_3 process, precipitation of $Al(OH)_3$ might occur. However, when sufficient HNO_3 is applied in the ICP testing solution, the precipitation disappears. Na and Ca were analyzed by diluted solution, using Ion chromatography (IC).

Based on the IC and ICP-OES results, the content of elements was calculated as follow:

$$X = [X]_{CWE} \cdot \frac{m_{w105} + m_{add}}{m_{sample}} \tag{3-1}$$

where X is the free cation content in the samples (mmol/L). $[X]_{CWE}$ is the concentration of the element in the filtrate obtained after CWE (mmol/L), determined by IC or ICP. m_{w105} is the mass of evaporable water at 105 ℃ in the samples (see Table 3.3). m_{add} is the mass of deionized water that is added during the 5-min rapid leaching process, and m_{sample} is the mass of the sample (g).

$$\gamma[OH^-]_{CWE} = 10^{\,pH_{CWE} - 14} \tag{3-2}$$

Where pH_{CWE} is the pH value in the filtrate obtained after CWE, γ is the activity coefficient at the testing moment. $[OH^-]_{CWE}$ is the OH^- concentration calculated by the pH_{CWE} after the CWE.

$$[OH^-] = [OH^-]_{CWE} \cdot \frac{m_{w105} + m_{add}}{m_{sample}} \tag{3-3}$$

Where $[OH^-]$ is the real OH^- concentration in the pore solution of the samples. Overall, the pH value of the pore solution could be calculated with Eq.3-4, by combining the Eqs. 3-2 and 3-3.

$$pH = pH_{CWE} + \log \frac{m_{w105} + m_{add}}{m_{sample}} \tag{3-4}$$

Using the CWE method to determine the pH and ions concentration has a limitation, but it has been proved that this method could obtain a relatively good estimate to predict the state of pore solution [140].

Table 3.3 Amount of evaporable water at 105 °C (i.e. free water) in the mortar samples 28 days after casting, m_{w105} measured after oven-drying.

	Before drying (g)	After drying (g)	m_{w105} (g)	$\frac{m_{w105}+m_{add}}{m_{sample}}$
NA2	49.9	38.9	11.1	1.2
NA2.5	50.0	39.6	10.5	1.2
NA3	49.9	40.1	9.8	1.2
NA3.5	50.0	40.6	9.5	1.2
NA4	50.1	40.2	9.8	1.2
Ref-NH	50.3	40.4	9.9	1.2

The measurement accuracy of alkali metal cations (i.e. Na^+, K^+, and Ca^{2+}) using CWE has been proved in a previous study [140]. To evaluate the deviation of $Al(OH)_4^-$, $Si(OH)_4$, and Mg^{2+} concentrations by CWE, a separate 5-min leaching test of raw GGBS powder was carried out under different pH values of the alkali leaching solution. The test results are shown in Table A7. When the pH is lower than 13, the metal ions of $Al(OH)_4^-$, $Si(OH)_4$, and Mg^{2+} from GGBS will not influence the pore solution leaching results, therefore the deviation of ions' concentrations could be neglected in this chapter.

pH value of pore solution at the early stage

The pH value of the pore solution was determined by a pH meter in the slurry state of the pastes. The paste samples were cast in the plastic bottles, and the pH value of the slurry was determined at 5 minutes, 1 hour, 3 hours, 6 hours, and 24 hours.

Isothermal calorimetry

The heat flow of the samples activated by different activators was measured by isothermal calorimetry set at 20 °C (TAM AIR Calorimetry). It should be noted that the values measured during the initial 45 minutes might slightly deviate as it takes time to stabilize the inner measurement environment. The results were normalized by the mass of the solids.

X-ray diffractometry

X-ray diffractometry (XRD) was performed by using an Endeavor instrument with Co-K_α radiation (40kV, 30mA). The pressed powdered specimens were measured with a step size of 0.05° and a counting time of 1s/step, from 10° to 90° 2θ.

Thermogravimetry

The thermogravimetric (TG) test was conducted by using an STA 449 F1 instrument, at a heating rate of 10 ℃/min, to samples of ≈ 100 mg. Experiments were carried out from 40 ℃ to 1000 ℃, and during the test process, N_2 was used as the carrier gas. Before the test, the pastes were ground to powder. Then the powder samples were immersed in 2-propanol for 24 hours to stop the hydration process. Subsequently, the powder samples were dried in an oven at 60 ℃ for 3 days to remove the remaining free water and stored in the sealed plastic bag.

Fourier-transform infrared spectroscopy

Fourier-transform infrared spectroscopy (FTIR) analysis was performed using a Varian 670-IR spectrometer with a wavelength range of 400 to 4000 cm^{-1} with a resolution of 1 cm^{-1}.

Nitrogen physisorption test

The nitrogen physisorption tests were conducted by TriStar II 3020, Micromeritics. The pore size distribution was determined by the Barett, Jonyer, and Halenda (BJH) method [105] from the desorption branch. Before the test, paste samples at the age of 28 days were ground to powder and the samples were immersed in the 2-propanol for 24h to stop the reaction process, then dried to constant mass.

Chloride absorption test

An accelerated experimental approach was used to study the chloride absorption of SAAS samples. The chloride absorption tests were performed with 0.1 mol/L NaCl solution to the samples with a particle size < 4 mm at the liquid to solid ratio of 2/1. In this accelerated chloride absorption test, the contact time between the solid material and the NaCl leachate was 24 hours. 5g of paste powder and 10g of deionized water were placed in a plastic bottle, and 24-hour shaking was performed on a shaking table (which is for the leaching test) with 200 rpm. After the shaking procedure, the eluate was filtrated through a 0.45 μm filter and analyzed for remaining chloride ions in the eluate by using Ion chromatography (IC). The ion chromatography (Dionex 1100) is equipped with an ion-exchange column AS9-HS (2×250 mm). The absorbed chloride ions could be calculated by comparing the original NaCl solution.

This non-standard leaching-absorption testing method is adopted from a previous study [142]. The hydrated gels and hydrotalcite in the reaction products can absorb the chloride ion during the shaking process. The results could generally evaluate the ability of chloride absorption of paste samples.

3.3 Results analysis

3.3.1 Evolution of pore solution

3.3.1.1 Variation of pH value

Previous studies indicated the significance of the pH value of pore solution on the reaction of AAMs [143–145]. According to Paudel et al. [146], the pH value of pore solution in the AAMs decreases with the curing ages, which is attributed to the process of reaction that consumed much of OH^- in the pore solution. In this chapter, the evolution of the pH value of pore solution in the SAAS paste samples is obtained by the Cold Water Extraction (CWE) method. The sodium hydroxides activated GGBS was selected as a reference to compare with the sodium aluminate activated GGBS at the specific curing ages. Fig. 3.2 shows the pH value variation of pore solution in the SAAS paste samples at an early stage (5 mins, 1 hour, 3 hours, 6 hours, and 24 hours, by pH meter directly) and later stage (3, 7, 14, and 28 days, by CWE).

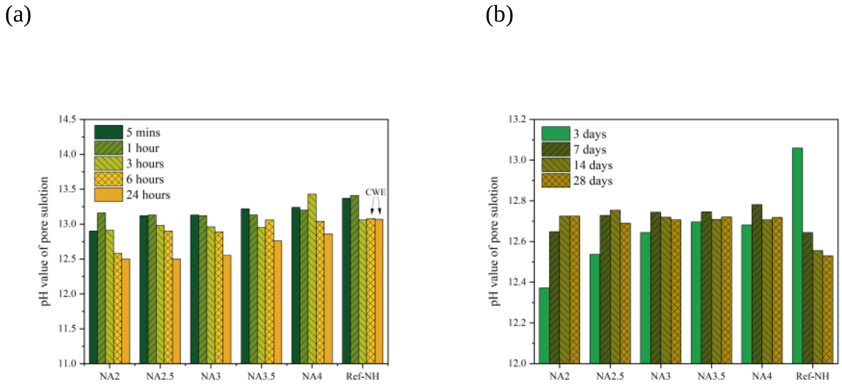

Fig. 3.2 Variation of pH value in the pore solution of AAMs: (a) Early stage; (b) After 3 days.

Fig. 3.2(a) shows that all the samples exhibit, generally, the decreasing trend of pH value during the early stage, which is due to the dissolution of slag that consumes a large amount of OH^-. The Ref-NH shows the highest pH value while NA2 is the lowest among the samples, which represents the alkalinity of the samples. The pH at 6 hours and 24 hours of Ref-NH is tested by CWE because of the fast hardening of the paste which makes it impossible to directly test its pH with the pH meter. However, the pH changes of SAAS pore solutions exhibit a more gradual decrease than the Ref-NH, especially NA3.5 and NA4.

As can be seen in Fig. 3.2(b), the Ref-NH shows the decrease of pH value along with the sample ages, ranging from 13.06 (3 days) to 12.53 (28 days). The cause of the pH decrease is that the formation of amorphous gel (C−A−S−H as mentioned in Section 3.3.3.1) and crystalline phases (Hydrotalcites and gibbsite as mentioned in Section 3.3.3.1) consumes the OH^- continually in the pore solution. However, the pH value in the pore solution of SAAS paste samples shows a different trend. After decreasing at the early age, the pH value slightly increases from the age of 3 days to the age of 7 days, and then keeps relatively stable at further curing ages, around 12.7. The $NaAlO_2$ shows buffering effect at late stages in the pore solution of SAAS samples. Thereby, the pH value of the pore solution remains at different sample ages. Furthermore, it is worth mentioning that the higher the Na_2O content in the SAAS matrix, the higher the initial pH value of the pore solution of SAAS pastes till the Na_2O content of 3.5% (i.e. NA3.5). This can be explained by the limitation of $NaAlO_2$ hydrolysis.

3.3.1.2 Variation of ions

Fig. 3.3 presents the concentrations of Al, Si, Na, Ca, and Mg (hereafter denoted as [Al], [Si], [Na], [Ca], and [Mg] respectively) in the pore solution (unit mmol/L) of SAAS pastes as the function of time at 3, 7, 14 and 28 days. The detailed pore solution data are listed in Appendix A Table A1~Table A6. It is noted that [Na] and [Ca] were determined by the IC, while the rest of the ions were determined by the ICP-OES.

There is a strong variation of [Al] during the curing ages in NA samples, while the Ref-NH maintained the [Al] stably in the entire curing period (shown in Fig. 3.3(a)). NA2 shows firstly an increasing trend of [Al] from 3 days to 7 days, then a remarkable decrease appeared after 7 days. The relatively lower pH value of pore solution in NA2 at 3 days, compared to that at the later curing period, results in the large content of unconsumed Al. In the meantime, the alkaline environment in the pore solution keeps breaking the Al-O bond from GGBS, consequently an increase in $Al(OH)_4^-$ is resulting. Subsequently, more and more $Al(OH)_4^-$ ions interact with $Si(OH)_4$ under the relatively higher pH value, compared to that at the early curing period, around 12.7, thus the [Al] declines with the curing ages. Thus NA2 shows a slow activation rate. However, unlike NA2, the [Al] keeps decreasing sharply in NA2.5, NA3, NA3.5, and NA4, attributed to the relatively higher pH values of the pore solution in these mixtures compared to that of NA2 that promotes the reaction between 3 and 7 days. However, NA2 remains insufficient pH of the pore solution in this period. According to the previous study [147], the increase of Na_2O content (NaOH activated slag) will not lead to an obvious variation of [Al] in the pore solution. On the contrary, the increase of Na_2O content in SAAS pastes directly introduces a great quantity of [Al] in the pore solution. The difference between NaOH and $NaAlO_2$ activated systems is obviously due to the diverse content of aluminate participation. At the same time, the Ref-NH shows that all the [Al], dissolved from GGBS, is under 3 mmol/L during the testing period. By the comparison of NA4 and Ref-NH, the difference of [Al] can be attributed to the extra aluminate content and pH value of the pore solution. With a higher pH environment of Ref-NH than that of NA4 before 3 days, the $Al(OH)_4^-$ is easier to be consumed to form gels (e.g. C−A−S−H gel) or crystalline phases (e.g. hydrotalcite) [148]. It is worth mentioning that the [Al] shows a similar concentration level after 28 days among the SAAS and reference samples, ranging from 2 to 3 mmol/L. This indicates that $Al(OH)_4^-$ in the pore solution is largely consumed during the activation process.

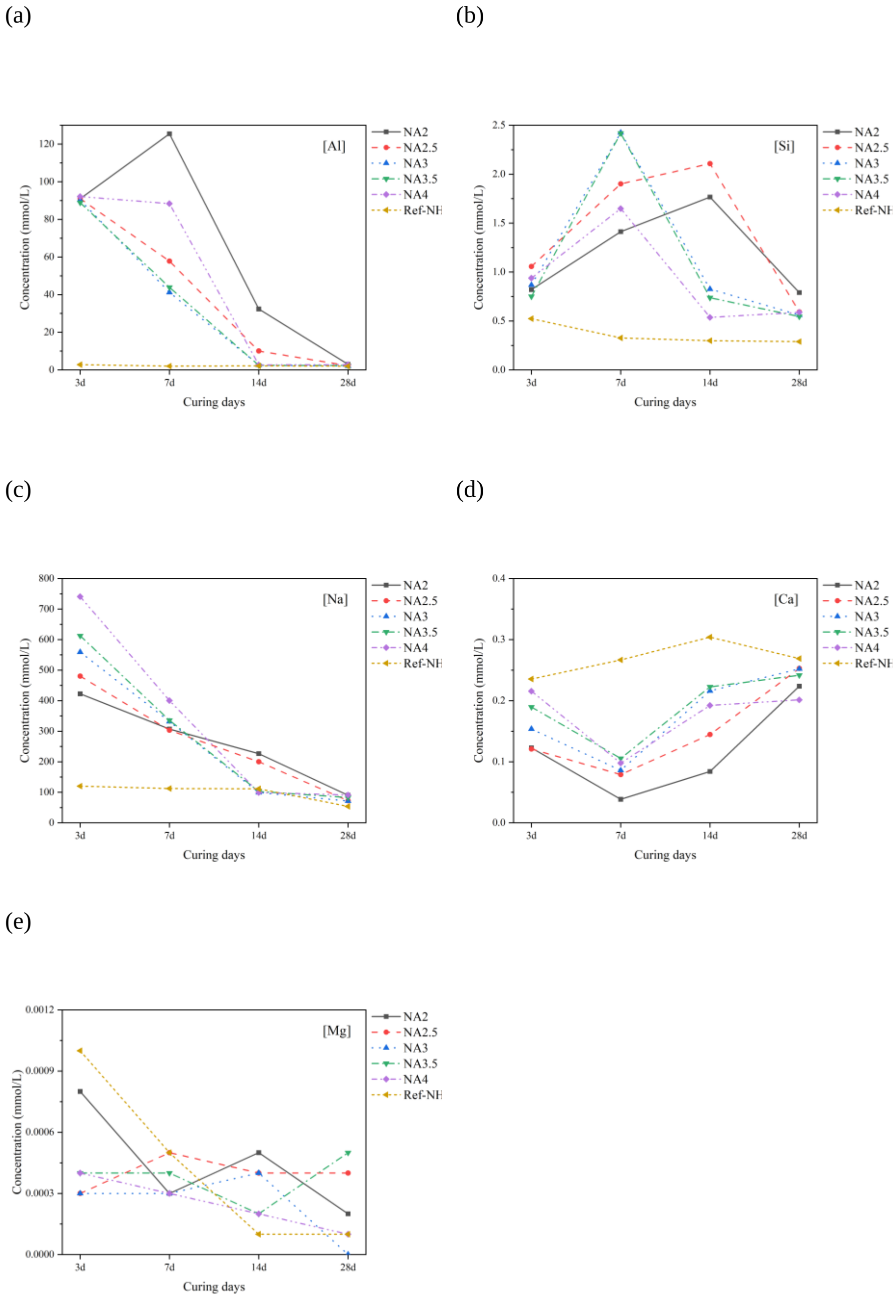

Fig. 3.3Cation variation of pore solution in SAAS at different curing times: a) [Al]; b) [Si]; c) [Na]; d) [Ca]; e) [Mg].

The [Si] of NA2 and NA2.5 shows a hill-like trend and the peaks of concentration appeared at 14 days. Likewise, the trends of [Si] in NA3, NA3.5, and NA4 are the same, whereas the peaks show at 7 days (shown in Fig. 3.3(b)). The $Si(OH)_4$ in pore solution is completely originated from the GGBS, thereby the time to the peak reflects the rate of slag dissolution and the subsequent Si-O consumption, namely the activation process. Instantaneously, the [Si] in Ref-NH shows a low concentration (< 0.53 mmol/L) during the curing period, which represents the consummation of activation before 3 days. This is attributed to the high content of Na_2O and pH value of pore solution in the NA samples that promotes gelation and crystallization.

There is a remarkable variation of [Na] during the testing period in all samples. The [Na] decreased remarkably with time among the samples (shown in Fig. 3.3(c)). For the sodium aluminate activated system, the initial period of up to 3 days shows the extensively high [Na]. Simultaneously, the [Na] increased with the increase of Na_2O content. However, comparing the NA4 with Ref-NH, the two mixtures with the equivalent Na_2O content show a huge difference of [Na]. The Na^+ is consumed largely before 3 days in Ref-NH, while the SAAS samples show a delay in the activation of Na^+ with other ions in the following period (7 days to 14 days). During 7 days to 14 days, the [Na] of SAAS decreases to the concentration around 100 mmol/L, and the [Al] declines to the concentration below 3 mmol/L, at the same time, the [Si] remains at a low concentration. The changes of these ions reflect the process of activation between Na^+, $Al(OH)_4^-$, and $Si(OH)_4$.

The [Ca] of SAAS shows a valley-like trend along with the curing time, and all the bottoms appeared at 7 days (shown in Fig. 3.3(d)). However, the [Ca] in Ref-NH increases with the curing time and reaches its peak (0.3040 mmol/L) at 14 days, and subsequently, decreases to 0.2689 mmol/L at 28 days. For SAAS samples, the Ca^{2+} is remarkably consumed under the relatively stable pH environment along with the curing time to form

Ca-based gels. Combining with [Al] and [Si], the Ca^{2+} reacts with $Al(OH)_4^-$ before 14 days tremendously, which leads to a remarkable decrease of [Al] as well. After 14 days, the $Si(OH)_4$, OH^-, and Na^+ show lower values. The combination between $Si(OH)_4$, OH^-, Na^+, and Ca^{2+} to form solid reaction products had dropped. It may lead to the compensation of Ca^{2+} under the alkali environment in the pore solution. Thereby, the valley-like trend of [Ca] appears in the pore solution, finally reaching a similar level among all samples. For the Ref-NH, the activation of Ca^{2+} is mainly concentrated before 3 days, thus the Ca^{2+} continually increases with the curing time. The low concentrations of [Al] and [Si] in Ref-NH after 3 days confirm that the activation has been transferred from a high rate of reaction to a low rate of it within the first 3 days. It may be associated with that the access of hydroxyl to the unreacted slag is inhibited by the reaction products around slag grains.

Mg^{2+} is dissolved from GGBS under the alkaline environment, and the concentration ranges from 0 to 0.0012 mmol/L (shown in Fig. 3.3(e)). The large content $Al(OH)_4^-$ reacts with Mg^{2+} preferentially to form hydrotalcite, thereby the [Mg] remains at a low concentration during the curing time. The excessive $Al(OH)_4^-$ ions in the pore solution prevent the competition between $Si(OH)_4$ and Mg^{2+} to form gels and hydrotalcite, respectively.

Overall, the [Al] shows a remarkably decreasing trend, generally, along the curing ages in the pore solution, which is associated with activation and the LDH formation process. Similarly, the [Na] declines with the curing time obviously, relating to the process of activation. The [Si] increases at early ages providing $Si(OH)_4$ and decreases after 7 days. The [Ca] decreases at the early ages reacting with dissolved $Si(OH)_4$, and rises after 7 days.

In addition, the [B], [Cu], [Fe], [Ga], [Li], [Se], and [V] showed lower than 0.2 mmol/L during the testing time, and details are shown in the Appendix A Table A1~Table A6.

3.3.2 Reaction kinetics

Fig. 3.4 shows the normalized reaction heat flow and cumulative reaction heat release of the SAAS pastes. A remarkably higher reaction heat flow and cumulative reaction heat release from the Ref-NH than the other SAAS pastes is observed. Generally, the higher the equivalent Na_2O content in the SAAS, the higher the reaction heat flow, the higher cumulative reaction heat release, and the earlier reaction heat peak could be obtained.

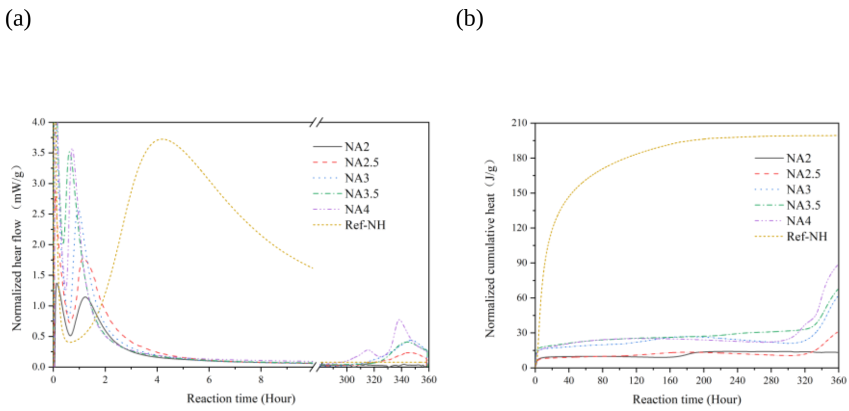

Fig. 3.4(a) Normalized reaction heat flow of SAAS; (b) Cumulative reaction heat release of SAAS.

As can be seen from Fig. 3.4(a), with the increasing equivalent Na_2O content in the SAAS, the time to the first peak is decreased. However, the NA4 exhibits a delay at the time to the first peak compared to NA3.5. From NA2 to NA3.5, the pH value of the pore solution increases with the Na_2O content at the early activation period, thus the time to the first peak decreases and the peak height raises. The first peak height of NA3.5 and NA4 are close to each other, which is in agreement with their similar pH value of pore solution. The first peak is mainly about the small amount of Calcium Aluminum Silicate Hydrate (C−A−S−H) gel and gibbsite formation (see Fig. 3.5(a)). The reason is that the pH environment around 13 (see Section 3.3.1.1) is suitable for gel formation at the beginning 6 hours. The large amount of OH^- is consumed subsequently, resulting in the pH decrease that slows down the reaction.

Moreover, the extra Al hinders the activation at the early stage [149], and the total induction period of SAAS shows around 280 hours. But the Al will be consumed after 14 days, which is also shown in Fig. 3.3, and the extra Al in NA4 could generate more zeolites and N−A−S−H gels (mix with zeolites formation). Because in this period, the Na^+ and $Al(OH)_4^-$ are consumed remarkably, thereby the long-term performance is improved by the increase of Na_2O content. Although the extra aluminate extends the induction period of SAAS, there is still a large amount of $Si(OH)_4$ in the pore solution of SAAS, thereby the entire activation process of NA2.5 -NA4 finished after 14 days, and new phases are formed in this period. Because of the low alkaline environment, the steady stage of NA2 appeared after 14 days to reach the low rate of reaction state. Combining Sections 3.3.1.1 and 3.3.1.2, a stable pH at around 12.7 and [Al] around 3 mmol/L in the pore solution represent it reaching the low rate of reaction stages of SAAS. The [Al] of Ref-NH at 3 days is 2.7838 mmol/L, so it has already finished the activation process.

Fig. 3.4(b) illustrates the trend that with a higher aluminate content in the matrix, the cumulative heat release is increased. Specifically, the comparison between Ref-NH and NA4 shows that the cumulative heat release of NA4 pastes is remarkably lower than Ref-NH. Since the content of Na_2O is the same, the difference in heat release can be attributed to the pH value of the early state in the pore solution. NA4 exhibits a relatively lower pH value than Ref-NH. So, the small amount of OH^- ions in NA4 reflects the delay in the formation of early reaction products. Thereby the reaction heat is influenced by the pH to a great extent, showing low heat release at the early state. Further, the pH value of the pore solution is affected by the concentration of $Al(OH)_4^-$ in the SAAS pastes, resulting from the hydrolysis of $NaAlO_2$, which is the resource of the alkali in the SAAS pastes at early curing age. The higher $NaAlO_2$ content, the higher pH at early stage. Simultaneously, the difference of pH leads to the different concentrations of elements in the pore solution, it may also influence the heat release of the reaction at the early stage. Overall, lower heat release of NA4 is observed than that of Ref-NH.

3.3.3 Reaction products

3.3.3.1 X-ray diffraction

Fig. 3.5(a) and (b) show the XRD patterns of the NaOH activated GGBS (reference sample) and SAAS pastes at 2 hours and 28 days, respectively. The following phases are recognized at the first 2-hour of reaction in Fig. 3.5(a): zeolite (JCPDS-ICDD 00-016-0339), gibbsite (JCPDS-ICDD 00-024-0217), and Calcite ($CaCO_3$, JCPDS-ICDD 01-086-2343). The dissolved Ca^{2+} from GGBS reacts with excessive Al from the activator to form zeolite and gibbsite, which leads to the fast coagulation of the paste samples. Along the early stage of the paste reaction, the pH environment decreases continually because of 1) the consumption of the OH^- ions in the pore solution to form zeolite and gibbsite, and 2) the dissolution of slag.

The following phases are recognized at 28 days in Fig. 3.5(b): calcium silicate hydrate (C−S−H) (Tobermorite, JCPDS-ICDD 00-006-0010), zeolite (JCPDS-ICDD 00-016-0339), hemicarboaluminate ($C\text{-}A\text{-}\bar{C}\text{-}H$) (JCPDS-ICDD 00-036-0129), zeolite A (Zeolite, JCPDS-ICDD 00-039-0222), calcite ($CaCO_3$, JCPDS-ICDD 01-086-2343), and hydrotalcite

($(Mg_{0.67}Al_{0.33}(OH)_2)(CO_3)_{0.165}(H_2O)_{0.48}$, JCPDS-ICDD 01-089-5434). The main reaction products of Ref-NH identified are C−(A)−S−H , zeolite, Calcite, and Hydrotalcite, which is in agreement with our previous study [150]. The main reaction products of SAAS pastes are zeolite, Zeolite A, hemicarboaluminate, Calcite, and Hydrotalcite. Due to the incorporation of the extra Al in the activator in NA2 ~ NA4, the activated systems favor to form zeolite instead of C−(A)−S−H with the increasing Al/Si ratio [23,151]. Meanwhile, the excessive $Al(OH)_4^-$ in the activator promotes the reaction with the dissolved $Si(OH)_4$ from slag and Na^+ in the activator, leading to the formation of more zeolites and sodium aluminum silicate hydrates (N−A−S−H) gels [152]. From the XRD results (Fig. 3.5(b)), the intensity of the zeolite peak becomes stronger when more Al is involved. At the same time, the peak intensity of zeolite and hemicarboaluminate increases with the increase of sodium aluminate content. However, the intensity of zeolites shows an increasing trend, thus the N−A−S−H gel may also increase with the increase of zeolites. While in the Ref-NH, the dissolved $Al(OH)_4^-$ is from slag, reacting with the Ca^{2+} and $Si(OH)_4$ to form C−(A)−S−H and zeolite, because Ca^{2+} has higher charges than Na^+ which is earlier to participate in the gel chain. In addition, with a higher content of sodium aluminate, the intensity of hydrotalcite shows an increasing tendency. Besides interacting with Ca, Na, and Si to form amorphous gels, Al also reacts with Mg to form extra hydrotalcite, and these two processes happen simultaneously.

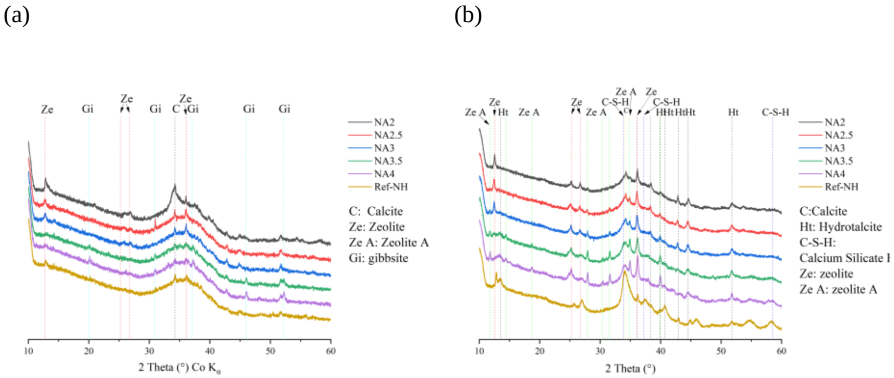

Fig. 3.5 XRD patterns of the SAAS pastes at (a)2 hours, (b) 28 days.

To conclude, the increased sodium aluminate content promotes the formation of zeolites, N−A−S−H, and hydrotalcite, but decreases the formation of zeolite. The small amount of calcite may be due to the slight carbonation of samples.

3.3.3.2 Thermogravimetric analysis

The results of thermogravimetric analysis (TGA) for the reference paste and SAAS pastes at 28-day curing time are presented in Fig. 3.6. As seen in Fig. 3.6(a), the mass of samples is continuously decreasing during the temperature range from 40 ℃ to 1000 ℃. Specifically, the main mass losses of bound water from C−(A)−S−H , C−A−S−H, and N−A−S−H gels were about 5.54%, 6.43%, 7.62%, 8.46%, 9.25%, and 8.18% in NA2 to Ref-NH, respectively, within the ranges of 100-300 ℃ [153–155]. The higher water losses in the ranges represented the higher content of gel formation, which is attributed to the higher $Al(OH)_4^-$ in the pore solution thanks to its promotion of gelation. As shown in Fig. 3.6(a) and Table 3.4, the mass losses of second-largest peaks are about 1.42%, 1.66%, 1.81%, 2.12%, 2.34%, and 2.33% in NA2 to Ref-NH, respectively, within the ranges of 300-400 ℃ [154]. While the decomposition of hydrotalcite has two steps [132], the first one (150-250°C) corresponds to the loss of the interlayer water, the second peak (250-450°C) arises from the decomposition of the hydroxide layers and carbonate anion. Thus, the decomposition of the gels may overlap the first peak of hydrotalcite decomposition. Specifically, these second-largest peaks on DTG curves (Fig. 3.6(b)) are assigned to the relative content of Mg-Al hydrotalcite decomposition. It is seen that the higher content of hydrotalcite appears with a higher aluminate content. According to Section 3.3.1.1, the pH environments of SAAS are closer than that of Ref-NH to the condition of hydrotalcite formation (pH 9~11) during the reaction period. It is worth mentioning that the main reaction period of Ref-NH is before 3 days and the pH value of the pore solution is around 13.1. While the reaction period of SAAS is between 7 days and 14 days, the pH value of the pore solution is around 12.5 ~ 12.7. Meanwhile, the excessive $Al(OH)_4^-$ interacts with the Mg^{2+} dissolved from GGBS to form more hydrotalcite. A slight content of calcite is found in all samples, which is due to the slight carbonation of the samples during the curing [156]. The TG results agree well with the observation of XRD analysis. The phases after 800 °C are caused by the recrystallization of new phases under high temperatures: 1) gehlenite (majority) is formed by the C−A−S−H under high-temperature heating [157]; 2) the small

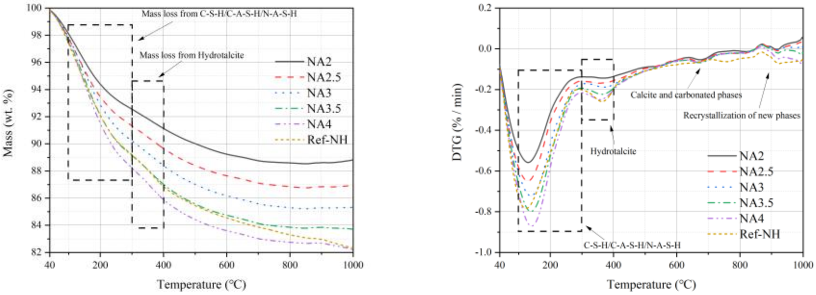
(a)

(b)

Fig. 3.6(a) Thermogravimetry (TG) curves of SAAS at 28 days; (b) Differential thermogravimetry (DTG) curves of SAAS at 28 days.

amount of Merwinite observed is originated from the activated GGBS [158]; 3) monticellite is also generated by the activated GGBS in a relatively low content [159] (see details in Fig. A1).

Table 3.4 Relatively mass losses of gel and LDHs.

Sample ID	Mass losses of gel (wt. %)	Mass losses of LDHs (wt. %)
NA2	5.5	1.4
NA2.5	6.4	1.7
NA3	7.6	1.8
NA3.5	8.5	2.1
NA4	9.3	2.3
Ref-NH	8.2	2.3

3.3.3.3 Fourier-transform infrared spectroscopy

The FTIR spectra of SAAS pastes, Ref-NH paste, and raw GGBS are presented in Fig. 3.7. The broadest peaks of SAAS pastes are located at 944 to 955 cm^{-1}, which are associated with the Si-O tetrahedra. The stretching vibrations of the Si-O tetrahedra represent the different number of bridging oxygen atoms. More specifically, the Si-O-Si bonds are due to the typical aluminosilicate chains containing C−S−H/C−A−S−H, or N−A−S−H type gels formed in the alkali activated GGBS. The reaction products tend to form Al-rich structures with the increasing aluminate content in the matrices. For all the spectra, the bands at around 1646 and 3392 cm^{-1} are attributed to the bending and stretching vibrations of bound water molecules, respectively. Similarly, the bands at around 666, 1415, and 1473 cm^{-1} in all samples are due to the presence of carbonate with different vibration modes: $\nu_2[CO_3]^{2-}$ for 666 cm^{-1}, and $\nu_2[CO_3]^{2-}$ for 1415 and 1473 cm^{-1} [160]. These carbonate phases are partly from hydrotalcite, partly from calcite, and partly from other carbonated phases, which is consistent with the XRD results (Fig. 3.5(b)).

Furthermore, a more distinctive effect of sodium aluminate on the main band shifts can be observed in the zoom-in graph of Fig. 3.7. An increase of the main band wavenumber is found in the higher sodium aluminate content in the matrices. It is known that the shifts of characteristic peaks of Si-O stretch are a notable feature of alkali activation, namely reaction, at around 950 cm^{-1} [161]. A higher aluminate content increases the amount of available $Al(OH)_4^-$ at the entire reacting period, which has a major influence on the activation process, and it is also in agreement with the dissolved Al in the pore solution presented in Section

3.3.1.2. The $Al(OH)_4^-$ in the pore solution inhibits the dissolution process of $Si(OH)_4$, but the Si-O stretch is shifted because under the relatively high pH environment, the dissolved $Si(OH)_4$ in the pore solution would react with $Al(OH)_4^-$ immediately, forming the Al-rich geopolymer. Generally, the high $Al(OH)_4^-$ in the pore solution promotes the activation process.

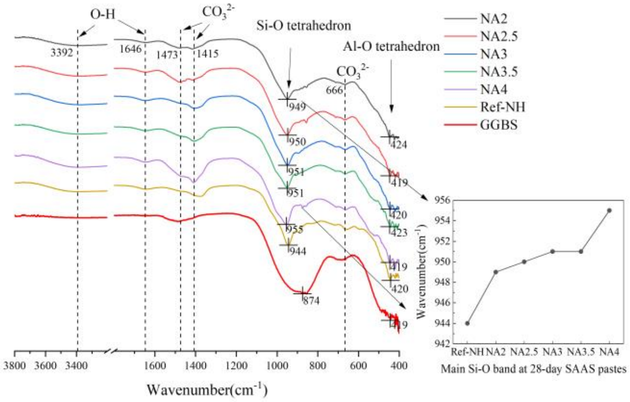

Fig. 3.7FTIR spectrum of SAAS, Ref-NH, and GGBS.

3.3.4 Microstructure

Fig. 3.8 shows the pore size distribution of SAAS samples at 28 curing days by nitrogen sorption test. From the nitrogen sorption test, the mesopore (2 – 50 nm) and partial macropore (50 ~ 200 nm) can be observed.

Fig. 3.8(a) represents the cumulative pore volume of SAAS paste samples. As can be seen, the total pore volume of samples declines with the increased content of sodium aluminate. Especially, mesopores are the primary pores in the microstructure. The NA2.5 ~ NA4 have a lower cumulative pore volume (partial mesopore ranging from 27 to 50 nm) than the Ref-HN, while the cumulative pore volume of NA2 is higher than the reference sample. For NA2.5 to NA4, the refinement of pore structure is attributed to the higher amounts of gels (C−A−S−H / N−A−S−H) filling in the capillary pores, which is also in line with the TG results. Thereby, the matrices tend to be more compacted and have a higher capacity to prevent water penetration and ion transport, e.g. chloride ion.

The pore size distribution of SAAS is illustrated in Fig. 3.8(b). Among the samples, the peaks of the void are concentrated at around 20 ~ 30 nm, namely mesopores. It is attributed to the gelation of C−A−S−H / N−A−S−H, the gel grew to intertwine and crosslinked to fill the mesopores, which results in the decrease of the volume of mesopores with the higher sodium and aluminate contents. While the NA2 has the highest peak at around 70 nm, the second peak is consistent with the other samples. From Sections 3.3.1.1 and 3.3.1.2, the low alkalinity of NA2 and slow consumption of $Al(OH)_4^-$ in the pore solution resulted in the low content of gelation, consequently, poor microstructure. The content of gel formation is relatively lower than the others, therefore increasing the total pore volume in the matrix.

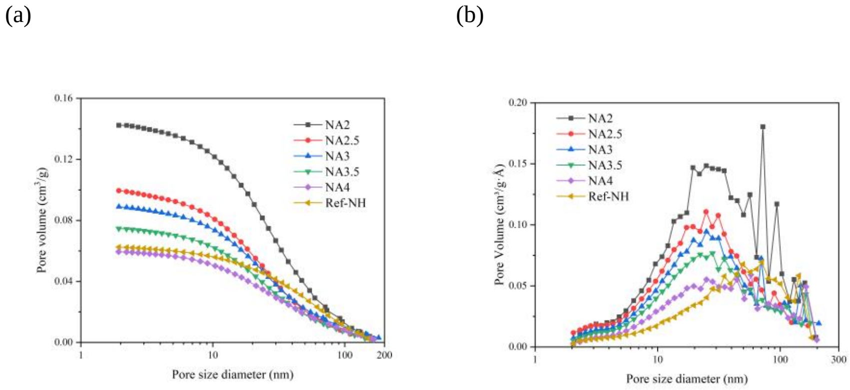

Fig. 3.8(a) BJH adsorption cumulative pore volume of SAAS at 28 days; (b) Pore size distribution of SAAS from BJH adsorption dV/dlog(w) pore volume at 28 days.

3.3.5 Chloride absorption

Fig. 3.9(a) presents the chloride concentration in the remaining solution after 24-hour contact with the SAAS pastes, and the original liquid is the 0.1 mol/L NaCl solution. Fig. 3.9(b) presents the normalized content of chloride absorption by the SAAS pastes, corresponding to the results shown in Fig. 3.9(a).

As seen in Fig. 3.9(a), all the samples show a remarkable decrease of Cl^- concentration in the remaining liquid, compared to the reference NaCl solution. Similarly, the NA3, NA3.5, and NA4 illustrate the distinctively high chloride absorption at 1.7, 1.9, and 1.9 mg chloride/g paste, respectively, with an increase up to 32%, 46.1%, and 48.4%, compared to the Ref-NH (1.3 mg chloride/g paste). Compared to NA3, the NA3.5 and NA4 have higher C−A−S−H/N−A−S−H contents, they show a noticeable increase of chloride absorption than that of NA3 up to 10.7% and 12.4%, respectively. Moreover, the content of hydrotalcite in NA4 is also higher than that of Ref-NH, which leads to a higher ability to absorb chloride ions by both ion exchange and surface stabilization. Besides, a lower content of mesopores, generally higher chloride resistance [21], therefore the lower volume of part mesopore (27 ~ 50 nm) in NA3, NA3.5, and NA4 than Ref-NH improve the chloride absorption.

However, the NA2 and NA2.5 show slightly lower chloride absorption at 1.2 and 1.2 mg chloride/g paste, respectively, both lower than the Ref-NH up to 7.7%,. Simultaneously, the content of gels and hydrotalcite of NA2 and NA2.5 are relatively lower than the Ref-NH, which decreases the chloride absorption.

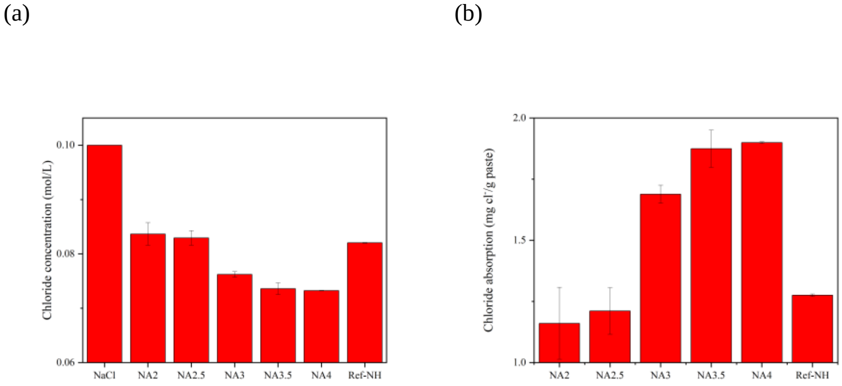

Fig. 3.9(a) Chloride concentration in the remaining solution after 24-hour shaking of the SAAS pastes; (b) Contents of chloride absorption in the SAAS pastes.

3.4 Discussions

Understanding the changes in the pore solution upon different ions and pH is critical regarding understanding the mechanisms of LDH and gel formation along the curing period. In this chapter, the role of Al(OH)$_4^-$ provided by sodium aluminate was investigated to understand how it influences the formation of in-situ formed LDH and gels. The CWE was used to determine the dynamic ion changes (including Al, Si, Na, Mg, Ca, etc.) in the pore solution.

3.4.1 Effect of Al(OH)$_4^-$ on LDH formation

3.4.1.1 Comparison of Al(OH)$_4^-$ profiles from CWE with LDH profiles from TGA

In Fig. 3.10, the Al(OH)$_4^-$ profiles determined by CWE at 3, 7, 14, and 28 curing days are compared to the LDH profiles at 28 curing days determined by TGA. The concentration of Al(OH)$_4^-$ in Ref-NH remains at a low level from 3 days to 28 days, thus the dissolved Mg^{2+} reacts with dissolved Al(OH)$_4^-$ from GGBS to form the LDH. The concentration of Al(OH)$_4^-$ in the SAAS pastes exhibits a declining trend with the curing time, especially after 14 days. With a higher content of Al(OH)$_4^-$ in the pore solution of SAAS, more LDHs are formed, which is consistent with the declining trend of Mg^{2+} concentration. It can be seen that the LDH formation is controlled by the content of available $Al(OH)_4^-$ in the pore solution. The formations of gel ($Al(OH)_4^-$ interacting with $Si(OH)_4$) and LDH ($Al(OH)_4^-$ interacting with Mg^{2+}) show no priority under the high amount of $Al(OH)_4^-$ in the pore solution. Here, the $Al(OH)_4^-$ in NA2 goes up before 7 days, which is different from the other mixes. Because the Al dissolved from slag may not be consumed under the low pH environment of the NA2 pore solution, an increase of $Al(OH)_4^-$ is observed, but the other pastes have sufficient alkalis to consume $Al(OH)_4^-$ forming LDH, zeolites, and gels.

From this aspect, the key point promoting the in-situ formed LDH is to control the competition between Mg^{2+} and $Si(OH)_4$ to react with $Al(OH)_4^-$. In Fig. 3.11, the mechanism of $NaAlO_2$ activated slag is proposed based on the dynamic $Al(OH)_4^-$ concentration in the pore solution to promote the LDH and gel formation. In the $NaAlO_2$ activated slag, the extra free $Al(OH)_4^-$ from the activator prevents the competition between Mg^{2+} and $Si(OH)_4$ reacts with $Al(OH)_4^-$ in the pore solution. Consequently, the LDH (Mg^{2+}

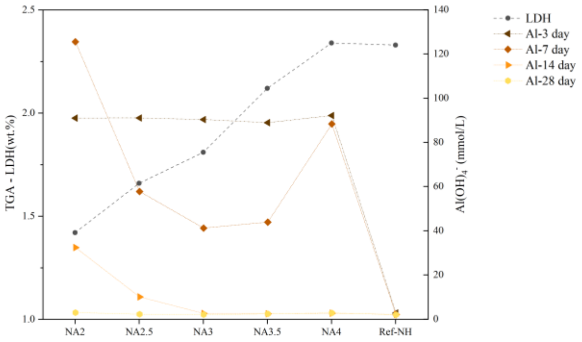

Fig. 3.10 The comparison of $Al(OH)_4^-$ profiles (3, 7, 14, 28 days) from CWE with LDH profiles (28 days) from TGA.

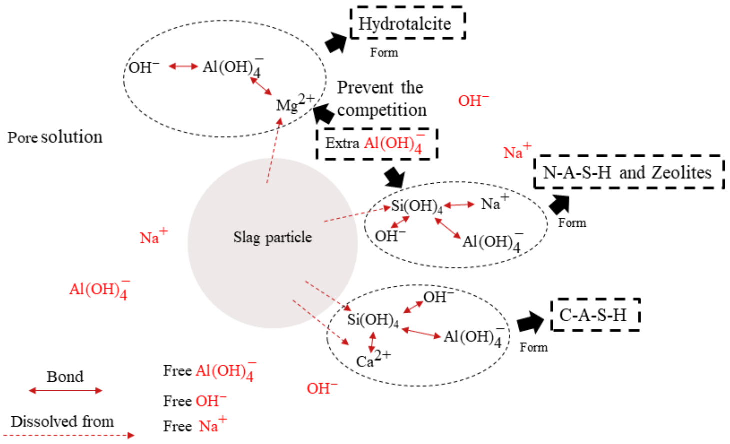

Fig. 3.11 Mechanism of $NaAlO_2$ activated slag.

reacts with $Al(OH)_4^-$) and gels ($Si(OH)_4$ reacts with $Al(OH)_4^-$) are generated simultaneously. It is shown that the high concentration of $Al(OH)_4^-$ in the pore solution avoids the competitive mechanism, in other words, to achieve the promotion of in-situ formed LDH. While in the NaOH activated slag, the $Al(OH)_4^-$ dissolves from slag, which will react with $Si(OH)_4$ and Ca^{2+} (also dissolved from slag) to form C−A−S−H, thus $Al(OH)_4^-$ might be insufficient to react with Mg^{2+} to form LDH at the same time.

3.4.1.2 Comparison of the Mg^{2+} and $Al(OH)_4^-$ profiles with pH in pore solution from CWE on LDH formation

In Fig. 3.12, the concentrations of the Mg^{2+} and $Al(OH)_4^-$ are presented with the pH value in the pore solution. The NA3.5 and NA4 show the similar pH value and the concentrations of Mg^{2+} and $Al(OH)_4^-$ at the entire curing times, while the NA4 shows that more Mg^{2+} and $Al(OH)_4^-$ have been consumed to form LDH and gels at 28 days. Moreover, NA2 has a low pH value of around 12.5, while NA4 shows a pH of about 12.7 during the entire reaction period. All the pH values are relatively lower than that of the Ref-NH at the early stage of the reaction. LDH is observed in the Ref-NH at the early state, however, the LDH in NA2 and NA4 is shown only after 14 days.

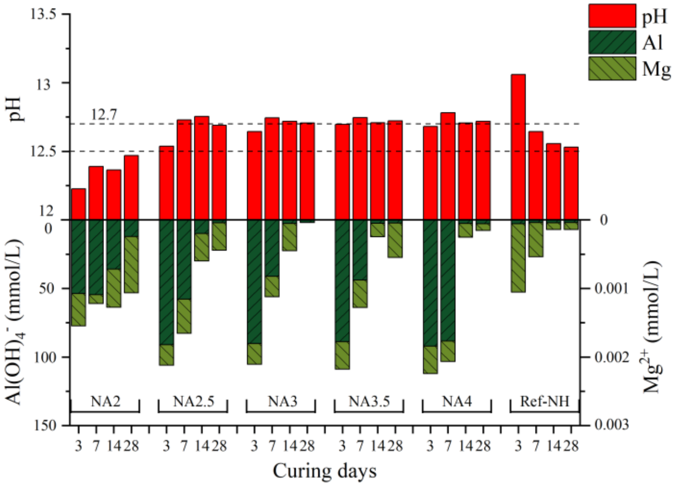

Fig. 3.12 The variation of pH, Mg^{2+} and $Al(OH)_4^-$ in the pore solution.

It should be noted that the solubility of Mg^{2+} is another primary reason for the LDH formation. When the pH of the pore solution is between 12.5 ~ 12.7, the $Al(OH)_4^-$ favors reacting with Mg^{2+} to form LDH. Thus, the pH controlling (around 12.5-12.7) is another key point to achieve the promotion of in-situ formed LDH.

To discuss it further, the Mg/Al molar ratio shows an increasing trend along with curing time in SAAS, which is attributed to the pH increase in the matrix and the available Mg^{2+} is increased and favors to form more LDH in the suitable pH environment. The in-situ formed LDH may also be influenced by the changes of the Mg/Al molar ratio in the pore solution. The extra Mg^{2+} further accelerates the LDH formation and the process of reaction in SAAS systems.

3.4.2 Effect of pH, Na^+, Ca^{2+}, $Si(OH)_4$ and $Al(OH)_4^-$ on C(N)−A−S−H formation

Fig. 3.13 represents the concentrations of Na^+, Ca^{2+}, $Si(OH)_4$, and $Al(OH)_4^-$ with pH value in the pore solution from CWE profile, comparing with C(N)−A−S−H formation from TGA results. The most obvious discrepancy is the two different competing groups of ions 1) Na^+ and Ca^{2+}, 2) $Si(OH)_4$, and $Al(OH)_4^-$. The molar ratio of Na^+/Ca^{2+} continually decreases with the curing age. Simultaneously, the molar ratio of $Si(OH)_4$/ $Al(OH)_4^-$ gradually increases to the same level at the end of curing age, around 0.15 to 0.27. Compared to the C(N)−A−S−H formation, the Al participates mostly in the reaction, and the amorphous gels increase obviously with the content of Na$^+$ and $Al(OH)_4^-$. It is worth mentioning that the pH conditions of zeolite and N−A−S−H growth ranged from 9.5 to higher than 12, therefore the pH environment of all SAAS samples is suitable for the formation of zeolite and N−A−S−H gel. Meanwhile, the stable pH values and tremendous

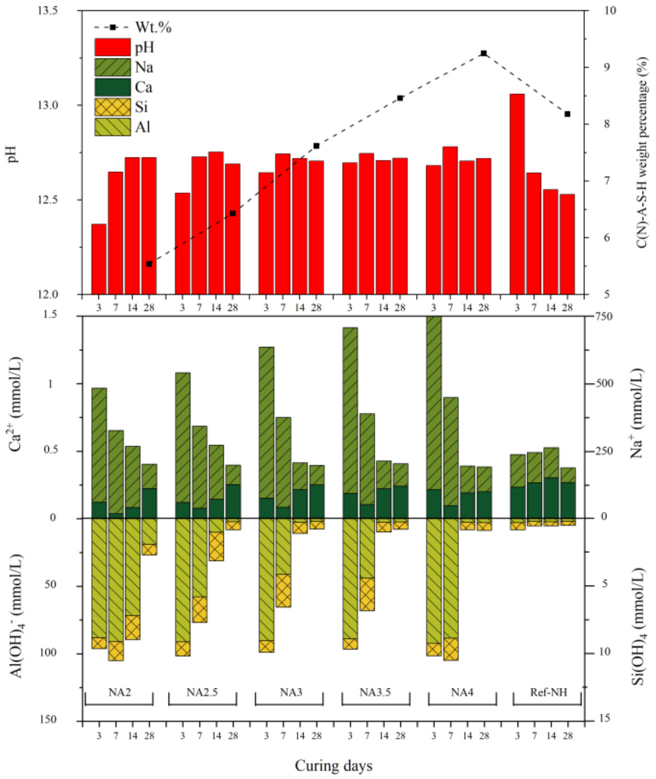

Fig. 3.13 The variation of pH, Na$^+$, Ca^{2+}, $Si(OH)_4$, and $Al(OH)_4^-$ in the pore solution and C(N)−A−S−H formation.

Na$^+$ content in SAAS samples lead to the formation of more zeolite, as observed in the XRD patterns. Among the samples, the Na$^+$/Ca^{2+} ratio and $Si(OH)_4$/ $Al(OH)_4^-$ ratio change obviously between 7 days and 14 days, which represents the formation of C(N)−A−S−H at this period in the sodium aluminate activating system. The extra Na$^+$ and $Al(OH)_4^-$, especially $Al(OH)_4^-$ ions, dominate the reaction in the entire testing age. The C−A−S−H and N−A−S−H gels are promoted by the extra available $Al(OH)_4^-$ in the pore solution to undergo the reaction of SAAS.

Moreover, when the pH environment is sufficient for the gelation, the extra Al in the pore solution inhibits the dissolved Si from GGBS, so it can postpone the partial Al reacts with Si up to 7 to 14 days, while the reaction of the sodium hydroxide system has reached the low rate of reaction before 3 days. Eventually, the ratio of $Si(OH)_4$/ $Al(OH)_4^-$ ended at around 0.25 (average results), with a low concentration of $Si(OH)_4$ (around 0.62 mmol/L) and $Al(OH)_4^-$ (around 2.49 mmol/L), which indicates it reaching a low rate of reaction.

Fig. 3.14 proposes the process of sodium aluminate activation, the pH environment of the pore solution has a significant effect on the final products. In the beginning, the pH value of the pore solution is relatively low, the Ca^{2+} is easier to keep soluble in the pore solution. Consequently, dissolved Ca^{2+} participates in the activation process with $Si(OH)_4$, $Al(OH)_4^-$, and OH^-, thus the C–A–S–H is generated. However, the amount of free Ca^{2+} declines in the pore solution when the pH rises higher than 12.5. It is associated with its pH-dependent solubility. Then the Na^+ is captured by the $Si(OH)_4$, $Al(OH)_4^-$, and OH^- forming N–A–S–H gel and zeolite. The synergistic effect of pH, Na^+ , Ca^{2+}, and $Al(OH)_4^-$, transforms the final products from C–A–S–H dominated to N–A–S–H dominated in the SAAS system. Eventually, the N–A–S–H gel and zeolite became the dominant reaction products in the SAAS system.

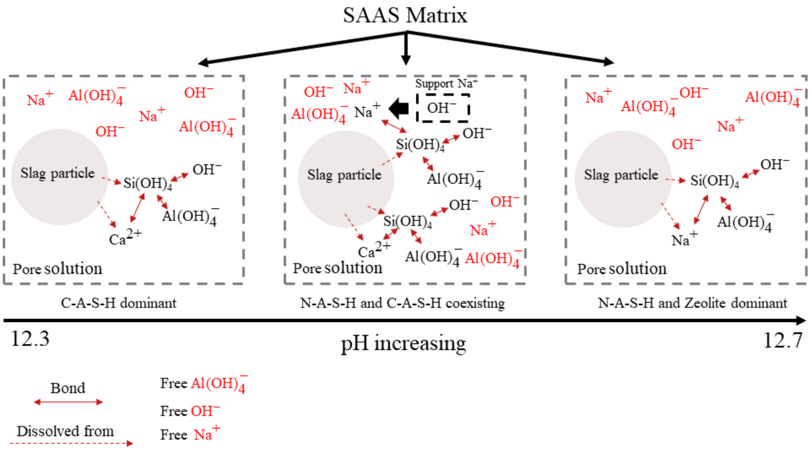

Fig. 3.14 Synergistic effect of pH, Na^+ , Ca^{2+}, $Si(OH)_4$, and $Al(OH)_4^-$ in the pore solution of SAAS.

3.5 Conclusions

This chapter attempts to deepen the understanding of sodium aluminate activated ground granulated blast-furnace slag (SAAS), with the aim of enhanced chloride absorption ability by promoting the in-situ formed LDHs through the alkali activation. This chapter shows that the sodium aluminate activator provides a relatively low pH environment and extra

$Al(OH)_4^-$, to facilitate the in-situ formation of hydrotalcites (LDHs). Moreover, the low pH activation shows the potential to tackle the issue of the high pH of the AAMs to human health which significantly limits its engineering applications. The following detailed conclusions can be drawn:

- The sodium aluminate activated slag results in the preferred in-situ formed LDHs. Simultaneously, with a higher sodium aluminate content, the content of gels in the SAAS is promoted. Thereby, the chloride binding capacity is enhanced by the promoted generation of reaction products (LDHs and gels).
- The sodium aluminate provides the extra $Al(OH)_4^-$ in the pore solution, which lessens the competition between $Si(OH)_4$, and Mg^{2+} capturing $Al(OH)_4^-$. It confirms the hypothesis of this chapter that the extra Al could promote the content of in-situ formed LDHs and gels simultaneously.
- The proposed low pH activation of SAAS between 12.5 and 12.7 is desired to promote the in-situ formation of Mg-Al LDH. Along with the curing ages, the increase of pH value in the pore solution of SAAS transfers the primary reaction products from C−A−S−H to N−A−S−H and zeolites.
- The ratio of $Si(OH)_4$/ $Al(OH)_4^-$, stabilizes at around 0.25, with a low concentration of $Si(OH)_4$ (around 0.62 mmol/L) and $Al(OH)_4^-$ (around 2.49 mmol/L), representing the SAAS reaching the low rate of reaction state.

Chapter 4 $NaAlO_2$ activated slag and MSWI bottom ash: Simulation and experimental analysis of leaching behavior

The long-term leaching behavior of municipal solid waste incineration bottom ash (MSWI BA) is one of the severe issues limiting its practical application as a secondary cementitious material. This chapter aims to investigate the influence of MSWI BA on NaAlO2 activated slag in terms of the reaction process, furthermore, to predict the leaching behavior by a novel thermodynamic model. The hardened sodium aluminate activated slag and bottom ash (SAASB) pastes were evaluated by mineralogy, microstructure, strength, and leaching analysis. The heat flow of SAASB up to 28 days was determined to investigate the reaction kinetics. Moreover, the quantification of calorimetric data was coupled with selective dissolution to obtain the reaction degree. The thermodynamic modelling was carried out, considering the raw materials chemistry and activator used. Furthermore, the heavy metal ions binding capacity of the matrices was simulated. The calorimetric results show the metastable period in the SAASB system, corresponding to the gibbsite formation. The modeled C(N)−A−S−H and hydrotalcite content decrease with the higher BA incorporation. The C(N)−A−S−H, hydrotalcite, and zeolite A (as a function of time) primarily contribute to the uptake of heavy metal ions.

The chapter is partially from the following article:

T. Liu, Y. Tang, K. Schollbach, J.L. Stapper, H.J.H. Brouwers, Q. Yu, NaAlO2 activated slag and MSWI bottom ash: Simulation and experimental analysis of leaching behavior. (In progress)

4.1 Introduction

Municipal solid waste incineration bottom ash (MSWI BA) (denoted as BA) is compositionally close to the lithosphere, therefore its reuse as a building material or for civic application is hypothesized to be compatible with geological compositions [162]. Last decade, incorporation of BA into the Ordinary Portland cement (OPC) system [163,164] or alkali activated materials (AAMs) system [162,165] were investigated. However, BA is regarded as one problematic residue due to its leaching issue of various heavy metal ions [166]. It may result in serious harm to both human health [167] and water supplies [168]. To date, the utilization of BA remains a severe leaching issue as a building material [169].

In BA blended OPC or AAMs matrix, the hydration products, e.g. amorphous gels (C−S−H/C(N)−A−S−H) and layered double hydroxides (LDHs), can physically or chemically absorb heavy metal ions [162,164,165]. The framework structure of amorphous gels acquires a net negative charge. It is balanced by the cations (e.g. Ca^{2+}) which can be replaced by heavy metal ions, e.g. Cs^{+}. Besides, the amorphous gels can also physically absorb heavy metal ions by surface absorption [164]. Likewise, LDHs have been observed to possess superior heavy metal binding capacity by surface absorption [20]. Simultaneously, the interlayer sites of LDHs can be occupied by anions (e.g. $Cl^{-}$and SO_4^{2-}), resulting in a high chemical binding capacity of LDHs [170]. However, the high pH of the pore solution is well known in both OPC and AAMs systems. Some metal species in some heavy metal ions display an oxyanionic leaching pattern. High pH of the pore solution leads to higher leaching of these ions, for instance, Mo tend to leach out in a high alkaline environment [171]. To realize the objectives above, the promotion of gels and LDHs formation by using sodium aluminate as activator has been proposed [18]. Sodium aluminate was reported as a relatively low pH activator properly providing the extra Al−O tetrahedra (denoted as $Al(OH)_4^-$) to increase the in-situ formation of gels and LDHs [18]. Chen et al. [172] reported that extra $Al(OH)_4^-$ from sodium aluminate activator led to the inhibition of the early-phase hydration reaction, consequently, a delay in setting time could result. Moreover, Phair et al. [173] reported that the utilization of sodium aluminate activation promoted either 4- or 6-coordinate Al depending on the $[OH^-]/[Al]$ confirming by ^{27}Al NMR. It resulted in equivalent or greater strength to that obtained with sodium silicate in fly ash-based geopolymer. Even though, the reaction process of sodium aluminate activation still lacks sufficient investigations. Moreover, understanding the reaction processes requires knowledge of thermodynamics, as it offers an estimation of the reaction process and phase assemblage during the reaction.

The thermodynamic modelling of NaOH, Na_2SiO_3, and Na_2CO_3 activated slag has been developed recently [174,175]. To explicitly account for the structurally integrated Al and Na into C−S−H, Myers et al. [175] suggested a calcium-alkali aluminosilicate hydrate ideal solid solution model (CNASH_ss) for the first time. Then they used it to predict the chemistry of C(N)−A−S−H in alkali-activated slag. Several researchers also applied the CNASH_ss model to predict alkali activated slag via different activator types [174,176,177]. The primary reaction products of $NaAlO_2$ activated slag were reported as C(N)−A−S−H gels [18], thus the CNASH_ss model would be suitable for the modelling of $NaAlO_2$ activation. However, the $NaAlO_2$ activator has never been investigated by thermodynamic modelling, which limits the

$NaAlO_2$ application. To study the reaction process of $NaAlO_2$, it is necessary to establish the thermodynamic modelling of $NaAlO_2$ activation. Zuo et al. [174] reported that the quantified reaction kinetics of NaOH activation to establish the modelling. More importantly, the thermodynamic modelling of $NaAlO_2$ activated materials should be further utilized to predict its long-term performance (e.g. leaching issue). Liu et al. [178] investigated the solidification of phosphogypsum using cemented paste backfill via experimental and numerical simulation. The simulated leaching profiles of phosphorus was revealed in terms of different pH environment. Besides, the leaching behavior and long-term environmental impact of cement-solidified municipal solid waste incineration fly ash were investigated under acid rain scenarios [179]. The different control mechanisms of heavy metal ions were established. However, there is no literature about the heavy metal ions binding capacity as a function of the reaction process by using modelling of $NaAlO_2$ activation. The use of modelling results can give a long-term perspective on the reaction product assemblages, further influencing the leaching behavior. Therefore, coupling thermodynamic modelling and experimental analysis of $NaAlO_2$ activation are urgent to be investigated. Furthermore, the analysis of modelling results to predict the long-term leaching behavior is vital to be explored innovatively.

The study of sodium aluminate activated slag and bottom ash (SAASB) had thoroughly been investigated both in modelled and experimental approaches. The hardened pastes were evaluated including mineralogy, thermogravimetric analysis, pore structure, mechanical property, and leaching behavior. Importantly, thermodynamic modelling of the reaction process had been simulated and validated based on the analysis of isothermal calorimetry data. Then, the prediction of heavy metal binding capacity was simulated based on the thermodynamic modelling in a time scale. The new insights are revealed in terms of thermodynamic modelling of sodium aluminate activated slag and bottom ash as well as environmental impact.

4.2 Experiments and methods

4.2.1 Characterization of GGBS and MSWI BA

Ground granulated blast-furnace slag (GGBS) and municipal solid waste incineration bottom ash (MSWI BA) (denoted as BA) were used in this chapter. The chemical compositions of GGBS and BA were determined by X-ray fluorescence (XRF), as shown in Table 4.1. The particle size distribution (PSD) of GGBS and BA was determined by laser granulometry, coupled with Master Sizer laser granulometry with an open measuring cell. The raw GGBS and BA powder was dispersed in deionized water. The PSD results of GGBS and BA are illustrated in Fig. 4.1(a) with the median sizes (d_{50}) of 13.32 μm and 12.05 μm, respectively.

Municipal solid waste incineration bottom ash (MSWI BA) is a primary residue during the incineration process of municipal solid waste. MSWIBA is compositionally close to the lithosphere. The crystalline phases of GGBS and BA were determined by X-ray diffraction, and the quantitative phase composition of GGBS and BA was determined by Rietveld analysis performed with the TOPAS software, version 4.2 from Bruker [180], as shown in Fig. 4.1(b) and (c). It can be seen from Fig. 4.1(c) that small amounts of calcite and gehlenite also present in GGBS, and 6 wt.% quartz, 6 wt.% diopside, and some other crystalline phases in BA. The detailed compositions are presented in Table 4.2.

Table 4.1 Chemical compositions and physical properties of GGBS and MSWI BA.

Chemical composition	GGBS (wt.%)	MSWI BA (wt.%)	Chemical composition	GGBS (wt.%)	MSWI BA (wt.%)
Na_2O	-	5.9	CaO	37.2	16.8
MgO	8.9	1.9	TiO_2	1.4	-
Al_2O_3	13.0	8.6	Fe_2O_3	0.7	12.6
SiO_2	34.2	50.1	Cl	0.1	0.4
P_2O_5	-	0.5	Other	0.2	1.6
SO_3	4.1	0.6	LOI* (1000℃)	1.323	5.382
K_2O	0.3	1.1	Particle density (g/cm^3)	2.947	2.512

*LOI = Loss on ignition at 1000℃

To further characterize the property of raw materials, the FTIR and TG-DTG analyses had been performed. Fig. 4.1(d) shows the FTIR of GGBS and BA. The bands at around 874 cm^{-1} and 1487 cm^{-1} in the slag are due to the small amount of calcite [18]. The O−H stretching at 3371 cm^{-1} is shown in both solid materials, corresponding to water [181]. The bond of absorbed water also shows at 1631 cm^{-1} in BA. Similarly, the vibration at 1437 cm^{-1} is due to calcite in the bottom ash. The bottom ash exhibits bridge Si−O bonds at 778 cm^{-1}, 796 cm^{-1}, and 1011 cm^{-1}, respectively. Those bonds are mainly from akermanite, quartz, and glass phases [182].

It can be seen from Fig. 4.1(e) and (f), that there is around 1% of mass loss from GGBS mainly due to the loss of moisture and a small amount of calcite. A slight peak at around 650 °C can be observed in Fig. 4.1(f). The mass loss of TGA is in line with the loss on ignition (LOI). In the meantime, the mass loss of BA occurs between 0 and 500 °C and is consistent with the loss of moisture water and residual organic compositions, e.g. cellulose, within this temperature range [183]. The peak of mass loss at around 650 °C is due to the decomposition of calcium carbonates [184]. The mass loss of TG is slightly lower than the LOI of BA. It may due to oxidation reactions (organic matter) [185].

Table 4.3 presents the leaching of potentially toxic elements (PTEs), sulfates, and chlorides from the raw GGBS and MSWI BA in order to estimate the potential environmental impact of the studied materials from their activated matrix. The limits are established by Dutch Soil Quality Regulation [186] regarding the acceptance of emission requirements for inorganic

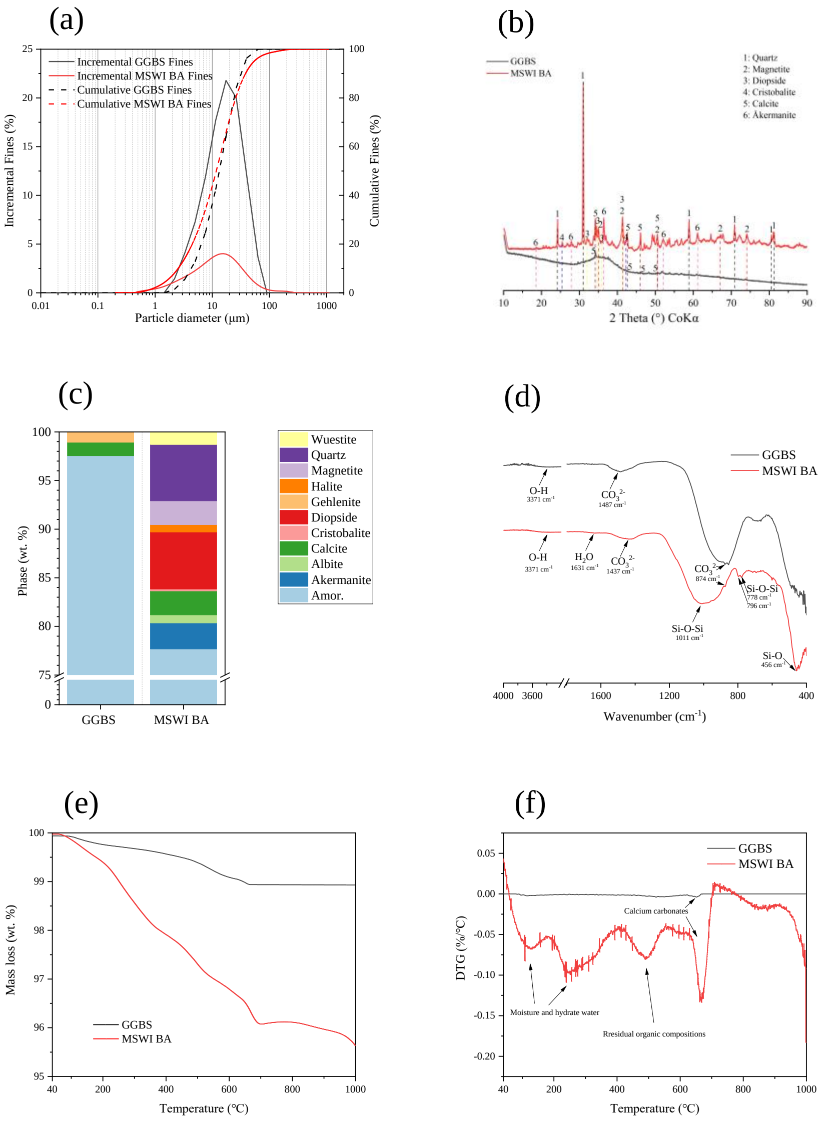

Fig. 4.1 (a) Particle size distributions of GGBS and BA; (b) XRD patterns of GGBS and BA; (c) Quantification of GGBS and BA; (d)FTIR of GGBS and BA; (e) TG of GGBS and BA; (f) DTG of GGBS and BA.

Table 4.2 Compositions of raw materials.

Mineral compound	Chemical formula	GGBS (wt.%)	MSWI BA (wt.%)	#PDF-reference
Amorphous contents	-	97.5	77.7	-
Akermanite	$Ca_2Mg(Si_2O_7)$	0.0	2.7	01-083-1815
Albite	$NaAlSi_3O_8$	0.0	0.8	00-003-0451
Calcite	$CaCO_3$	1.4	2.5	01-072-1937
Cristobalite	SiO_2	0.0	0.2	01-077-1317
Diopside	$CaMgSi_2O_6$	0.0	5.9	01-071-1495
Gehlenite	$Ca_2Al(Al,Si)_2O_7$	1.1	0.0	00-025-0123
Halite	NaCl	0.0	0.7	00-001-0993
Magnetite	Fe_3O_4	0.0	2.5	03-065-3107
Quartz	SiO_2	0.0	5.8	01-083-0539

Table 4.3 Leaching of raw GGBS and MSWI BA (Limits from Dutch Soil Quality Decree [186]).

Elements (mg/L)	GGBS	MSWI BA	Limit	Elements (mg/L)	GGBS	MSWI BA	Limit
Al	1.985	42.810	-	Mo	0.007	0.732	1
B	0.058	0.815	-	Ni	0.000	0.009	0.44
Ba	0.075	0.138	22	Sb	0.006	0.401	0.32
Cr	0.030	0.036	0.63	Sr	1.317	1.170	-
Cu	0.002	1.083	0.9	V	0.017	0.003	1.8
Fe	0.015	0.000	-	Cl^-	36.2	3354.4	616
Li	0.120	0.175	-	SO_4^{2-}	155	7303.3	1730
Mg	0.056	0.393	-	pH*	11.68	11.41	-

*pH is the pH of the leachate

parameters. The values for GGBS are well below the limit for PTEs, sulfates, and chlorides. However, the leaching of BA shows that Cu, Sb, Cl^-, and SO_4^{2-} are above the legislation limit.

Meanwhile, the leaching of Mo in BA is close to the limit. Specifically, sorption or precipitation regulates the fate of Cu and Mo in leachate. Through sorption and precipitation, it joins up with calcareous compounds [187,188]. The solubility of Sb shows the oxyanionic pattern and increases with the pH of the aqueous environment [189]. Meanwhile, the leaching of Cl^- and SO_4^{2-} is less pH dependent relating to their availability in the raw materials [190].

4.2.2 Sample preparation

The paste samples were mixed with different GGBS / BA mass ratios. Samples with added BA relative to binder (GGBA+BA) of 5, 10, 15, 20, and 25 wt.% were prepared (denoted as BA0, BA5, BA10, BA15, BA20, and BA25). The alkali activator with equivalent 3 wt.% Na_2O was prepared by stirring the specific amount of sodium aluminate powder in deionized water. The sodium aluminate activator was prepared 6 hours before the pastes mixing. The detailed mix design of the pastes is listed in Table 4.4. In order to evaluate the mechanical properties of SAASB, standard mortar samples were cast with a binder (GGBS+BA) to sand mass ratio of 1/3 [191].

All the samples were warped in plastic film to prevent moisture losses under 20 ℃ until the specific days for testing.

Table 4.4 Mix design of the pastes.

Sample ID	w/b*	$NaAlO_2$ (wt.%)	Equivalent Na_2O (wt.%)	GGBS (wt.%)	BA (wt.%)
BA0	0.5	7.9	3	100	0
BA5				95	5
BA10				90	10
BA15				85	15
BA20				80	20
BA25				75	25

*w/b = water to binder (GGBS + BA) mass ratio

4.2.3 Methods

X-ray diffractometry

X-ray diffractometry (XRD) was performed by using the Bruker D4 Phaser instrument with Co-Kα radiation (40kV, 30mA). The pressed powdered specimens were measured with a step size of 0.05° and a counting time of 1s/step, from 10° to 90° 2θ.

Quantification of X-ray diffractometry

Quantification of X-ray diffractometry (QXRD) was prepared by adding an internal standard (Si powder), which was obtained from Siltronix, France. In the XRD sample, 10 wt.% internal standard was added in the paste samples. Then, the mixed paste sample was milled by the ball mill at level 3 speed for 15 mins. For the quantification of mineral phases in the samples, Rietveld analysis was performed with the TOPAS software, version 4.2 from Bruker [180].

Fourier-transform infrared spectroscopy

Fourier-transform infrared spectroscopy (FTIR) analysis was performed by using a Varian 670-IR spectrometer with a wavelength range of 400 to 4000 cm^{-1} with a resolution of 1 cm^{-1}.

Thermogravimetry

The thermogravimetric (TG) test was conducted by using the STA 449 F1 instrument, at a heating rate of 10 ℃/min, with a sample weight of ≈ 100 mg. The 7-day and 28-day paste samples were used for TG tests. Experiments were carried out from 40 ℃ to 1000 ℃, during the test process, N_2 gas was used as the protection gas.

Nitrogen physisorption test

The nitrogen physisorption tests were conducted with a TriStar II 3020, Micromeritics. The pore size distribution was carried out by the Barett, Jonyer, and Halenda (BJH) method from the absorption branch [21]. Before the test, the 28-day paste samples were ground to powder and the samples were immersed in the 2-propanol for 24h to stop the hydration process, then dried to constant mass under 60 ℃ for 3 days.

Mechanical testing

After 28 days of curing, the compressive strength of the samples was determined according to EN 196-1 [191]. The sample size is 40×40×160 mm. The samples were centered on the platens of the machine. Subsequently, the load was increased smoothly at the rate of 2400 N/s over the entire load application until the fracture load.

After 28 days of curing, the flexural strength of the samples was also determined according to EN 196-1. The prism was placed in the testing machine with one side face on the supporting rollers and with its longitudinal axis normal to the supports. The distance between supports was 100 mm ± 0.5 mm. The load was applied vertically by means of the loading roller to the opposite side face of the prism, at the same time the load was increased smoothly at the rate of 50 ± 10 N/s until fracture.

Isothermal calorimetry

The heat flow of the samples by different mixes was measured by isothermal calorimetry set at 20 ℃ (TAM AIR Calorimetry) for 28 days. The results were normalized by the mass of the total solid and solution.

Selective dissolution

The selective dissolution method was applied to analyze the reaction degree of SAASB pastes. The paste samples were ground and then dissolved in salicylic acid (5 Vol%) in ethanol. 1 g of 28-day powder was added to 250 mL of salicylic acid solution. The suspension was stirred for 2 hours and filtered by using a 2 μm filter paper. The insoluble residues were washed by the ethanol until the neutral pH is reached, then dried to the constant mass. All the 28-day powdered samples were treated by the same way to obtain the final reaction degree of samples.

Selective dissolutions were repeated 3 times for each mix. The salicylic acid desolves the structure of C(N)−A−S−H gels and other reacted phases, leaving only the unreacted precursors (insoluble residue).

Quantification of reaction degree

Alkali-activated slag undergoes multiple distinct reaction phases that are regulated by diverse reaction mechanisms, similar to the hydration of Portland cement. Initial dissolution, induction, acceleration/deceleration, and stable periods are all common parts of the reaction process of alkali-activated slag. However, the sodium aluminate ($NaAlO_2$) activation has a unique metastable state. This will be discussed in the Reaction kinetics section. In the different reaction stages of sodium aluminate activation, the Ginstling-Brounshtein equation can be used to quantify the reaction kinetics as follow [192].

$$kt = 1-\frac{2}{3}\alpha-(1-\alpha)^{\frac{2}{3}} \tag{4-1}$$

Where k is the apparent diffusion coefficient; t is the reaction time; α is the reaction degree of the reactant at time t.

The calorimetric responses of sodium aluminate activated GGBS and BA can be described by coupled reaction degree of two reactants as follow.

$$\alpha = P\alpha_1+(1-P)\alpha_2 \tag{4-2}$$

Where α_1 and α_2 are the reaction degrees of GGBS and BA at time t, respectively; P is the weight percentage of GGBS in the matrix.

However, the heat release from the calorimeter exhibits different mechanism-controlled reaction kinetics from the diffusion controlled reaction kinetic. To describe the reaction process of sodium aluminate activated GGBS and BA, a reaction grade N was introduced into the Ginstling-Brounshtein equation. Then this empirical equation can be expressed as follows:

$$kt = [1-\frac{2}{3}\alpha-(1-\alpha)^{\frac{2}{3}}]^{N} \tag{4-3}$$

Where k is the diffusion coefficient of SAASB. Then the linear forms are:

$$\frac{1}{N}\ln k + \frac{1}{N}\ln t = \ln\left[1-\frac{2}{3}\alpha-(1-\alpha)^{\frac{2}{3}}\right] \tag{4-4}$$

Thermodynamic modelling

The CNASH model proposed by Myers et al. [175] was used in the chapter to simulate the main reaction product of $NaAlO_2$ activated GGBS/BA. In the calculations of Myers et al., Fe was neglected due to low content in the slag. In this chapter, a small amount of ferro-glaucophane (iron-containing phase) was observed originating from Fe in the raw BA. It was applied in thermodynamic modelling. Simultaneously, the dawsonite was also detected in the drying sample after hydration stoppage. So, the dawsonite was also introduced in the modelling part. Further discussion will be presented in Section 4.3.3.

The phase compositions as determined in XRD (dawsonite, zeolite A, and ferro glaucophane) are introduced in the modelling. The thermodynamic properties of these end members are needed to supplement the database of C(N)−A−S−H by Myers et al. [175]. Table 4.5 presents the thermodynamic properties of the end members used in the modelling simulations.

The thermodynamic modelling for BA0 ~ BA25 was carried out in O_2 (1g) and CO_2 (1g) atmosphere at 20 ℃, 1 bar using GEM-Selektor V3 (https://gems.web.psi.ch/). The thermodynamic database as described in [196], is based on an updated version of CEMDATA 18.1. The GEM-Selektor was used for thermodynamical simulation of alkali activated slag, and the findings were in good agreement with the experimental data. In the $NaAlO_2$ activated slag system, the effect of bottom ash may therefore be further examined.

In thermodynamic modelling, the dissolution of slag was assumed that SiO_2, CaO, Al_2O_3, MgO, Fe_2O_3, H_2S, and K_2O were employed in normalized amounts without TiO_2 and Cl. Because the amounts of TiO_2 and Cl are very limited. Similarly, the Na_2O, SiO_2, CaO,

Al_2O_3, MgO, Fe_2O_3, H_2S, and K_2O were employed in normalized amounts of bottom ash without P_2O_5 and Cl.

Table 4.5 Thermodynamic properties of the end members were used in the thermodynamic modelling simulations. The reference state is 298.15 K and 1 bar.

End member	V^0 [cm^3/mol]	$\Delta_f G^0$ [kJ/mol]	$\Delta_f H^0$ [kJ/mol]	S^0 [J/mol]	C_p^0 [J/mol]	Ref
5CA	57.3	−2491	−2293	163	177	[175]
INFCA	59.3	-2551	-2343	154	181	[175]
5CNA	64.5	−2569	−2382	195	176	[175]
INFCNA	69.3	−2667	−2474	198	180	[175]
INFCN	71.1	−2642	−2452	186	184	[175]
T2C	80.6	−2721	−2465	167	237	[175]
T5C	79.3	−2780	−2517	160	234	[175]
TobH	85.0	−2831	−2560	153	231	[175]
M4A-OH-LDH	21.9	-6358	-7160	549	648	[175]
M6A-OH-LDH	30.5	-8023	-9007	675	803	[175]
M8A-OH-LDH	39.2	-9687	-10853	801	958	[175]
$NaAlCO_3(OH)_2$ (Dawsonite)	58.5	-1786	-1964	132	142	[193]
Zeolite 4A	3913.6	-18716	-197840	35810	12490	[194]
Ferro glaucophane	272.5	-220.5	-320.7	541.2	643.9	[195]

One-stage batch leaching test

The batch leaching tests were performed with demineralized water on material with a particle size < 4 mm and at the L/S-ratio of 10 l/kg (EN12457 part 2) [197]. In both the one-stage batch leaching tests, the contact time between the solid material and the leachate was 24 hours. After the leaching test, the eluate was filtered through a 0.45 μm filter and analyzed for a wide range of parameters.

For each test material, 20 eluates were obtained. In total 60 eluates were analyzed for a broad spectrum of the parameter using inductively coupled plasma-optical emission spectrometry (ICP-OES). All the eluates were analyzed for Ca, K, Na, Ba, Mg, As, Cd, Cr, Cu, Ni, Pb, Zn, Al, and Mo. The Cl and SO_4 were analyzed by Ion Chromatography (IC)

4.3 Results and discussion

4.3.1 Evaluation of hardened pastes

4.3.1.1 X-ray diffraction

Fig. 4.2 presents the XRD patterns and phase assemblages of SAASB samples cured for 7 and 28 days, with different proportions of BA. It can be seen in Fig. 4.2(a), that the reaction products are not obvious at 7 days. The presence of gibbsite is mainly due to the extra $Al(OH)_4^-$ (from activator). Combined with Fig. 4.2(c), the gibbsite content decreases with the increase of BA incorporation. However, the meionite ($Ca_4Al_6Si_6O_{24}CO_3$ #PDF 00-014-0191) and dawsonite ($NaAlCO_3(OH)_2$ #PDF 00-014-0191) gradually increase with the BA contents in the matrix. Because the carbonate ions are mainly from BA, which can promote the formations of meionite and dawsonite in an Al-rich alkaline environment [198,199]. Nevertheless, it should be noted that there is also a possibility that the dawsonite is formed during the drying process of hydration stoppage [193]. Because the elevated temperature and free CO_2 in the drying oven can transfer gibbsite to dawsonite. This will be further explained in section 4.3.3. Simultaneously, the increase of BA quantity in BA0 ~ BA25 leads to the rising contents of akermanite ($Ca_2Mg[Si_2O_7]$), calcite ($CaCO_3$), and magnetite (Fe_3O_4), and quartz (SiO_2) in the activated matrix. These are all from unreacted BA phases The wuestite from raw BA powder only has a very small proportion in the activated matrices, which can be neglected.

Fig. 4.2(b) illustrates the reaction products of SAASB at 28 days. The assemblage of the phases at 28 days is exhibited in Fig. 4.2(d). The presence of zeolite A ($Na_{12}Al_{12}Si_{12}O_{48}$ $27H_2O$ #PDF 00-011-0590) indicates that the large amounts of Na^+ and $Al(OH)_4^-$ from activator react with $Si(OH)_4$ dissolved from GGBS. As shown in Fig. 4.2(d), zeolite A is slightly promoted by the incorporation of BA in the matrix. The higher Al/Si ratio in the matrix increases the zeolite A formation [200]. The Al is mainly from $NaAlO_2$ activator and the Si mainly dissolving from slag. So, the higher BA (less Si from slag) relatively increases the Al/Si ration in the pore solution. The hydrotalcite ($Mg_6Al_2CO_3(OH)_{16}$ $4H_2O$ #PDF 00-014-0191) declines with the higher incorporation of BA. The more Mg^{2+} dissolved from slag particles reacts with extra $Al(OH)_4^-$ (from activator), the more hydrotalcite can be generated. Besides, the content of ferro-glaucophane ($Na_2Fe_3Al_2Si_8O_{22}(OH)_2$) increases with the BA additions. It is due to the iron rich content in the BA, participating in the reaction process. Only small amounts of ferro-glaucophane can be observed lower than 0.3 wt.% among the pastes. In addition, the calcite ($CaCO_3$) is from both GGBS and BA, while the quartz (SiO_2), magnetite (Fe_3O_4), and akermanite ($Ca_2Mg[Si_2O_7]$) are from BA as mentioned above. These phases increase with the BA proportions in the matrix as well.

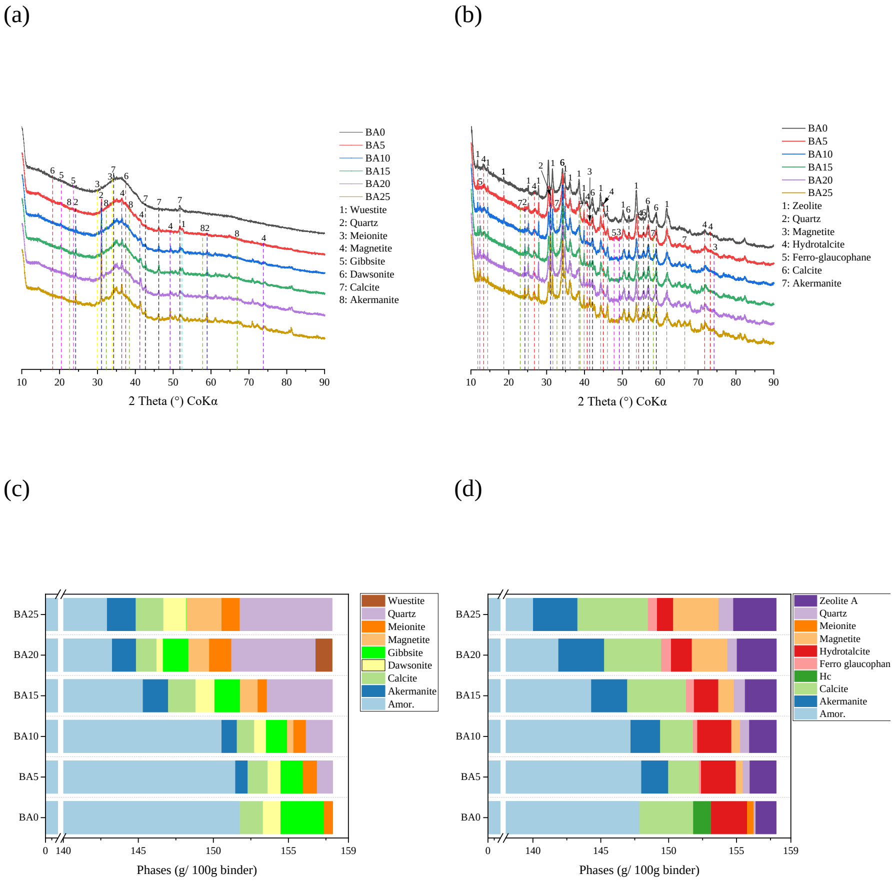

Fig. 4.2 XRD pattern of SAASB at (a)7 days and (b)28 days. The quantitative XRD results of SAASB at (c)7 days and (d)28 days.

4.3.1.2 Thermogravimetric analysis

The results of thermogravimetric analysis (TGA) for the BA pastes at 7- and 28-day are illustrated in Fig. 4.3 ranging from 40 to 1000 ℃. The mass loss of SAASB at 7 days in Fig. 4.3(a) and (b) shows that a higher content of BA leads to a higher moisture loss water in BA ranging from 40 ~ 200 ℃ [183]. Because the BA stays unreacted in the initial 7 days. The second largest peaks within 200 ~ 400 ℃ are attributed to dawsonite and gibbsite at 7 days. The broad peak of dawsonite shows at 320 ℃ [201–203]. At the same time, the decomposed peak of the gibbsite appears at around 300 ℃ [204]. The gibbsite is formed because of extra aluminate from the activator. The higher content of BA in the SAASB results in elevated content of organic matter at around 500 ℃ as well [183]. The thermally decomposed peak of calcium carbonates exhibits at 700 and 800 ℃ [18]. Those calcium carbonates mainly originate from raw BA materials. Generally, those results are in line with QXRD at 7 days.

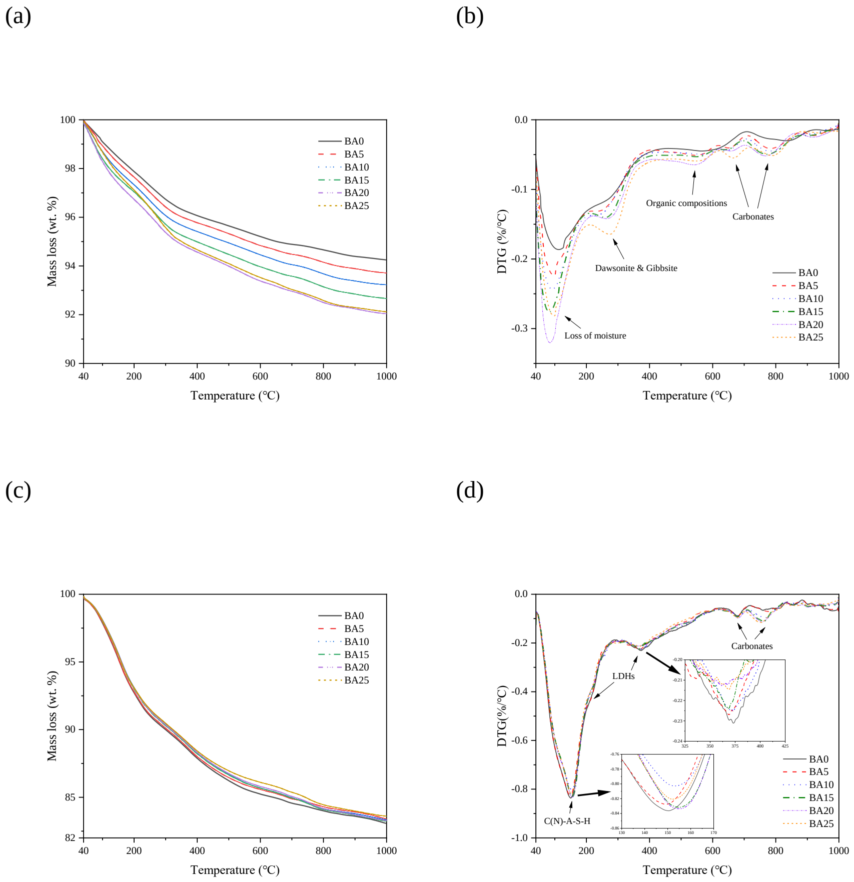

Fig. 4.3 Mass loss of SAASB at (a) 7; (c) 28 days. DTG of SAASB at (b) 7; (d) 28 days.

It can be seen from Fig. 4.3(c) and (d) that the decomposition of gels at 28 days within 100 ~ 300 ℃. Simultaneously, the decomposition of zeolite A is overlapped by the decomposition of C(N)−A−S−H ranging from 100 to 300 ℃. It is worth noting that with the higher content of zeolite A in the matrix from BA0 to BA25, the first peak shifts to a slightly higher temperature. It is in line with the QXRD results at 28 days. The distinct peaks of hydrotalcite, namely layered double hydroxides (LDHs), can be observed. The first peak of

LDHs shows at around 250 °C representing the first decomposition of bound water in the LDHs. The second peak of LDHs shows at around 380 °C representing the decomposition of anions in the interlayer. The hydrotalcite content declines with elevated BA incorporation in SAASB. It is because that a lower slag content leads to less Mg^{2+} dissolution in the pore solution. Therefore, less hydrotalcite can be formed. Furthermore, it can be seen from Fig. 4.3(d) that the second peak of LDHs shifts to the lower temperature with the higher BA incorporation. It is associated with a slightly different ratio of OH^-/CO_3^{2-} in the interlayer of LDHs [205]. LDHs with a higher ratio of OH^-/CO_3^{2-} tends to decompose at a lower temperature. So, there are more OH^- intercalated LDHs with the higher BA incorporation. Because BA particle are less reactive than slag particle in the alkaline environment. The higher BA in the SAASB consumes less OH^- to dissolve the slag particle. Consequently, more OH^- can participate in the LDHs formation.

4.3.1.3 Pore structure

Fig. 4.4 shows the pore size distribution of SAASB pastes at 28 curing days by nitrogen sorption test. From the nitrogen sorption test, the curves show that the pores distribute in the range of 2-200 nm, which consists of the gel pores (< 10 nm) and capillary pores (> 10 nm) [206].

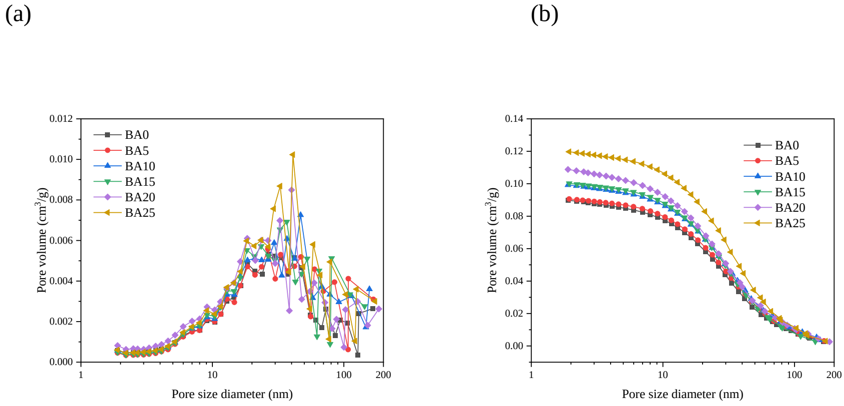

Fig. 4.4 Pore size distribution of SAASB pastes at 28 days (a) Incremental volume; (b) Cumulative volume.

Fig. 4.4(a) illustrates the incremental pore volume of SAASB pastes. There are two hump peaks of the pore at 6 and 9 nm among SAASB samples. It is associated with the intrinsic pores of C(N)−A−S−H gels. Their pore volume increases with the BA content in the matrix. Because less gel formation leads to higher pore volume, which is in line with the TGA results in Section 4.3.1.2. Also, there is a broad peak centered at 40 nm among SAASB samples, spanning the range from 10 to 50 nm. It is due to the overlapping of C(N)−A−S−H gels resulting in a porous network at capillary pores scale [207]. The volume of capillary pores increases with an elevated BA content owing to less gel growing to intertwine and getting crosslinked to fill the capillary pores [207].

Fig. 4.4(b) exhibits the cumulative pore volume of SAASB pastes. The cumulative volume of BA0 shows the lowest pore volume, and the pore volume increases with higher BA content (shown in Table 4.6). It is related to the reaction products of C(N)−A−S−H gels as mentioned above. It is consistent with variations of amorphous content in QXRD and TGA (Section 4.3.1.1). Simultaneously, the average pore diameter increases with BA content as well (shown in Table 4.6). Because the lower C(N)−A−S−H gel formation leads to a larger porosity by gel overlapping at capillary pores scale within higher BA matrices as mentioned above.

Table 4.6 The average pore diameters and total pore volumes (between 1.7 ~ 300 nm) of the samples.

Samples	Average pore diameter (nm)	Total pore volume (cm^3/g)
BA0	16.1	0.09
BA5	17.0	0.09
BA10	17.8	0.10
BA15	18.2	0.10
BA20	18.6	0.11
BA25	19.6	0.12

4.3.1.4 Mechanical property

Fig. 4.5 illustrates the compressive and flexural strengths of SAASB mortars at 7, 28, and 56 days. It is obvious to see that the elevated BA proportions result in the lower compressive and flexural strengths of mortars. For the BA0 sample, the compressive strength is 2.7 ± 0.1 MPa at 7 days, and it increases to 32.1 ± 1.7 MPa and 38.8 ± 0.4 MPa at 28 days and 56 days, respectively. The flexural strength is 0.6 ± 0.1 MPa at 7 days, and it increases to 4.7 ± 0.1 MPa and 5.7 ± 0.1 MPa at 28 days and 56 days, respectively. The dramatic increases (from 7 to 28 days) of mechanical properties are due to the formation of C(N)−A−S−H gels at around 20 days developing a dense microstructure. After 28 days, the reaction of the sample turns to a stable reaction stage, so less development of mechanical property can be observed. For BA5 ~ BA25 samples, the development of mechanical property shows the same trend as BA0. Besides, the mechanical properties decline with higher BA incorporation. Because the BA incorporation decreases the final amorphous gel formation (in line with TGA and modelling results) leading to less refined microstructure (in line with N_2 sorption results).

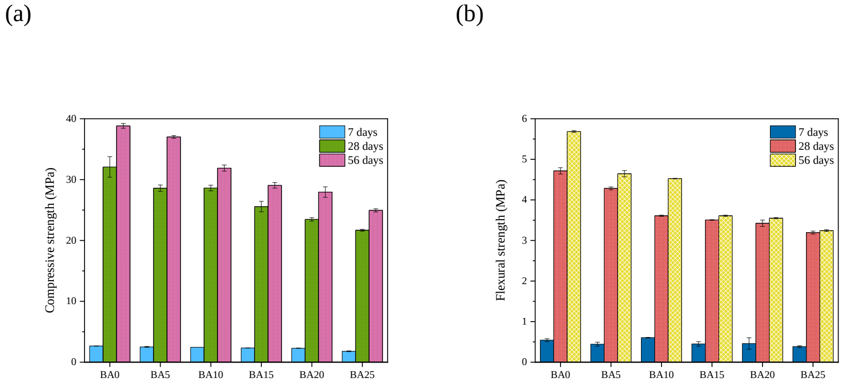

Fig. 4.5 Mechanical properties of SAASB mortars at specific curing days (a) compressive strength; (b) flexural strength.

4.3.1.5 Leaching behavior

Table 4.7 shows the PTEs, sulfates, and chlorides from the SAASB pastes are lower than the limits. The limits are established by Dutch Soil Quality Regulation [186] as mentioned in Section 4.2.1 about the approval of the inorganic parameters' emission standards.

It can be seen from Section 4.2.1 that the components in the BA above the limits are Cu, Sb, Cl^-, and SO_4^{2-}. However, the leaching of Cu and Sb in all SAASB pastes are lower than the limits. The leaching of Cu and Sb increase with the higher BA input in the SAASB pastes. The input waste BA are the main factor influencing the leaching of Cu and Sb. On the other hand, the C(N)−A−S−H gels content has the ability to bind heavy metals [208]. From the TGA and modelling results, the gel formation from BA0~BA25 shows a declining trend. Thus, the heavy metal binding capacity decreases with the BA incorporation. Besides, the LDHs formation can bind heavy metal ions as well [209].

The leaching of Cl^- and SO_4^{2-} show a similar trend with Cu and Sb. They are lower than the limits but increase with BA proportions in the matrix. The leaching patterns of Cl^- and SO_4^{2-} are governed by the solubility control mechanism [210]. Thus, the available Cl^- and SO_4^{2-} will leach in the aqueous environment along with the gradient of concentration which is less pH dependent [210].

Table 4.7 28 days leaching of SAASB.

Elements (mg/L)	BA0	BA5	BA10	BA15	BA20	BA25	Limit
Al	36.923	38.761	45.445	47.186	7.364	33.604	-
B	0.676	0.770	0.878	0.872	0.955	1.050	-
Ba	0.003	0.003	0.005	0.006	0.003	0.003	22
Cu	0.000	0.021	0.057	0.061	0.054	0.132	0.9
Fe	0.109	0.162	0.225	0.248	0.040	0.186	-
Ga	0.046	0.049	0.054	0.056	0.011	0.048	-
Li	0.057	0.059	0.051	0.048	0.043	0.040	-
Mg	0.017	0.009	0.010	0.008	0.007	0.004	-
Mo	0.010	0.054	0.107	0.109	0.161	0.254	1
Sb	0.001	0.002	0.005	0.013	0.018	0.022	0.32
Se	0.090	0.074	0.071	0.032	0.032	0.069	0.15
Sr	0.114	0.102	0.095	0.089	0.075	0.055	-
V	0.112	0.102	0.115	0.122	0.040	0.140	1.8
Zn	0.001	0.002	0.009	0.011	0.003	0.002	4.5
Cl-	26.7	31.7	41.2	49.7	49.8	63.3	616
SO2-4	274	308	337	341	352	393	1730

To compare the 28-day leaching results and prediction by thermodynamic modelling, the following calculation can be performed. First of all, the elements input from SAASB pastes should be determined. As mentioned, the exact amount of PTEs, sulfates, and chlorides inputs from the raw GGBS and MSWI BA can be calculated based on the leaching of raw materials (shown in Table B4). The Cu, Mo, Sb, sulfates, and chlorides are selected because their leaching results are close or higher than the legislation limit. Then, these elements and ions in the SAASB pastes can be calculated as follow:

$$\mathrm{Ele}_{\mathrm{Binder}} = \mathrm{Ele}_{\mathrm{GGBS}} \cdot \frac{M_{\mathrm{GGBS}}}{M_{\mathrm{GGBS+BA+water+NaAlO_2}}} + \mathrm{Ele}_{\mathrm{BA}} \cdot \frac{M_{\mathrm{BA}}}{M_{\mathrm{GGBS+BA+water+NaAlO_2}}} \qquad (4\text{-}5)$$

Where Ele_{Binder} is the toxic elements input from SAASB pastes; Ele_{GGBS} and Ele_{BA} are the elements input from raw GGBS and BA, respectively. M_{GGBS} , M_{BA} , and $M_{GGBS+BA+water+NaAlO_2}$ are the weight percentages of GGBS, BA, and SAASB pastes, respectively. The toxic elements input in SAASB are calculated listing in Table 4.8.

Table 4.8 Elements (Cu, Mo, Sb, Cl^-, SO_4^{2-}) can be leached out from SAASB. (mg/ g paste).

Elements input from SAASB (mg/g paste)	BA0	BA5	BA10	BA15	BA20	BA25
Cu	0.00001	0.00035	0.00070	0.00104	0.00138	0.00172
Mo	0.00004	0.00027	0.00050	0.00073	0.00096	0.00119
Sb	0.00004	0.00016	0.00029	0.00041	0.00054	0.00066
Cl-	0.22921	1.27972	2.33023	3.38074	4.43125	5.48175
SO_4^{2-}	0.98143	3.24451	5.50759	7.77067	10.03375	12.29683

Table 4.9 Comparison between 28 days leaching of SAASB and modelled prediction.

Elements (mg/L)	BA0		BA5		BA10		BA15		BA20		BA25	
	Exp.*	Pre.**	Exp.	Pre.	Exp.	Pre.	Exp.	Pre.	Exp.	Pre.	Exp.	Pre.
Cu	0	0	0.021	0	0.057	0	0.061	0	0.054	0	0.132	0
Mo	0.010	0	0.054	0	0.107	0	0.109	0	0.161	0	0.254	0
Sb	0.001	0	0.002	0	0.005	0	0.013	0	0.018	0	0.022	0
Cl^-	26.7	0	31.7	0	41.2	108	49.7	226	49.8	310	63.3	432
SO_4^{2-}	274	0	308	0	337	0	341	116	352	221	393	549

Exp.* = experiment results

Pre.** = modelled prediction results

Combining the leaching data in Table 4.8 with the 28-day absorption capacity prediction from Fig. 4.11 in Section 4.3.3.2, the leaching results by modelled prediction can be calculated as follow:

$$\text{Leaching}_{\text{Prediction}} = \left(\text{Ele}_{\text{Binder}} - \text{Ele}_{\text{absorption}} \times 1000\right) \div 0.01 \tag{4-6}$$

Where the $\text{Leaching}_{\text{Prediction}}$ is the final leaching results of modelled prediction (mg/L). $\text{Ele}_{\text{Binder}}$ is the toxic elements input from 28-day SAASB pastes (mg/ g paste). $\text{Ele}_{\text{absorption}}$ is the 28-day absorption capacity of toxic elements (g/g paste) by the calculation of modelled prediction in Fig. 4.11. The 0.01 in the equation represents 0.01 L of water when doing the leaching test. It is worth noting that the leaching test is performed by 1g SAASB paste and 10 g deionized water as mentioned in Section 4.2.3. The detailed validation of the modelling is discussed in Section 4.3.3.

The comparison between 28-day leaching of SAASB and modelled prediction are listed in Table 4.9. From the comparison, all the leaching predictions of toxic elements are close to the experimental results, and the errors are within 1 order of magnitude as well.

4.3.2 Reaction kinetics

4.3.2.1 Isothermal calorimetry analysis

Previous studies reported the reaction heat flow of sodium hydroxides activated slag intensively [21], the induction period finished within the initial 10 hours. The acceleration and deceleration periods were associated with a high heat release from the nucleation, growth, and precipitation of the reaction products [211]. While the sodium aluminate activated slag showed a long induction time due to the relatively lower pH value compared to sodium hydroxides [18]. In this chapter, different percentages of BA replaced the GGBS in the matrix, to investigate the role of MSWI BA in terms of reaction kinetics using isothermal calorimetry. Fig. 4.6 illustrates the 28-day normalized reaction heat flow, cumulative reaction heat release, time to reach the second exothermic peak (T_{SP}), second peak height (SPH), and the time to reach the third exothermic peak (T_{TP}), and the third peak height (TPH).

As can be seen in Fig. 4.6(a), all the T_{SP} and T_{TP} show the obvious retardation, also, the SPHs and TPHs decrease remarkably with the higher substitution of BA in the SAASB system. The **initial dissolution (I)** time was associated with the heat released during the initial 1h, which was due to the dissolution of GGBS. The higher BA contents postpone the initial dissolution time. The **metastable period (II)** appears between 1 to 10h among the samples. Fig. 4.6(a) illustrates that the higher BA contents lead to the delay of T_{SP}. The SPH is associated with gibbsite formation, which is a metastable phase [18,212]. The gibbsite will be incorporated into phases like C(N)−A−S−H, zeolite, LDHs, etc. during the further reaction process. The metastable period is a unique reaction period differing from the other activators, e.g. sodium hydroxides, and sodium silicate. Subsequently, the duration of the **induction period (III)** is longer than 461.98 hours. In this period, the high aqueous Al in the pore solution hinders the dissolution of Si from GGBS. Thus, the geopolymerization process delays reflect in Fig. 4.6(b). The normalized cumulative heat release stays at a low value (< 40 J/g) before 450 hours among the SAASB samples. In the meantime, the gel layer (from the reaction between aluminates and silicates) wraps the GGBS and BA grains resulting in the barrier between the anhydrous and aqueous phases. The higher additions of BA postpone the induction times because the finer BA grains adhere to the surface of GGBS grains, obstructing the contact between activator and amorphous oxides.

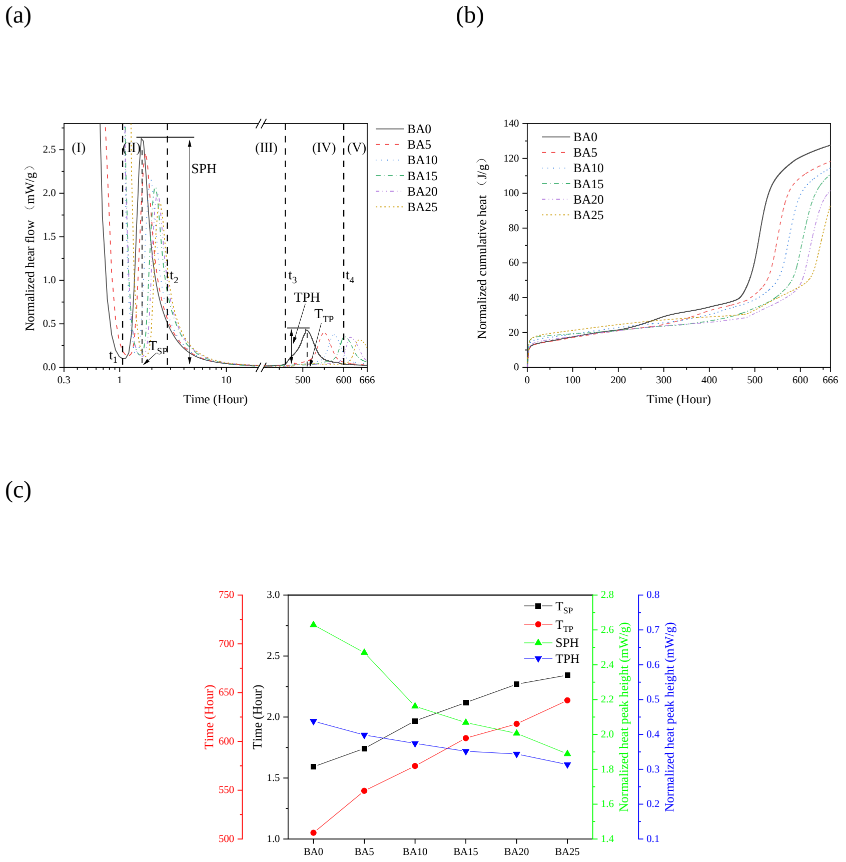

Fig. 4.6 (a) Normalized reaction heat flow of SAASB; (b) Normalized cumulative heat of SAASB; (c) T_{SP}, T_{TP}, SPH, and TPH of SAASB. the evolution area and the representative vertical dividing lines are shown for BA0.

The induction stage is followed by the **acceleration/deceleration period (IV)**, ranging from 461.98 to 734.71* hours (* is by linear fitting) among the SAASB pastes. The t_4 of BA20 and BA25 is linear fitting by BA content and evolution time (shown in Table 4.11). The T_{TP} and TPH of samples appear in this period. The T_{TP} of BA0 to BA25 are 506h, 549h, 574h, 603h, 618h, 642h, and later than 666h, respectively. The BA25 shows a 26.8% delay of T_{TP}, which is due to the large content of BA. The BA has relatively lower reactivity than GGBS, the dissolved ions from BA are slower than that from GGBS, thereby it causes a long delay in terms of T_{SP}. The remarkable decrease in TPH is also attributed to the higher BA content, the GGBS provides the main reaction heat release, thus lower proportions of GGBS lead to lower TPHs. Meanwhile, the pore structure mainly evolves in this period, improving the mechanical properties [213]. Thus, the earlier this period starts, the improved mechanical properties can be obtained. It is in line with Section 4.3.1.4. The **stable reaction period (V)** is the slow reaction stage showing after 550.99 hours among samples. And the starting time of a stable reaction period is delayed by elevated BA participation as well. The gradual reduction of heat release represents the reaction process converts to the slow-reaction-rate stage.

4.3.2.2 Quantification of reaction degree of $NaAlO_2$ activated slag

Based on the cumulative heat release, the reaction degree of SAASB can be calculated as follow.

$$\alpha(t)=\frac{Q(t)}{Q_{max}} \tag{4-7}$$

Where Q(t) is the cumulative heat release at time t, and Q_{max} is the total heat release. Combining the selective dissolution and calorimeter heat release at 28 days yielded the total heat release. Table 4.10 presents the computed outcomes. In comparison to the previously published value of 461 J/g slag [214], the computed total heat release is lower. The relatively low heat release by $NaAlO_2$ activation have also been reported elsewhere [18].

Table 4.10 The residue and reaction degree of SAASB at 28 days. The cumulative heat release at 28 days and total heat release of SAASB.

Sample	Residue (g)	α	Q (J/g binder)	Qmax (J/g binder)
BA0	0.69	0.31	127.7	413.2
BA5	0.69	0.31	118.3	384.0
BA10	0.72	0.28	114.6	407.7
BA15	0.75	0.25	111.0	438.9
BA20	0.75	0.25	101.8	405.5
BA25	0.76	0.24	93.6	393.3

The reaction degrees of SAASB are illustrated in Fig. 4.7. It suggests a fast reaction process after 400 hours among all samples. It will be further discussed in Section 4.3.3.

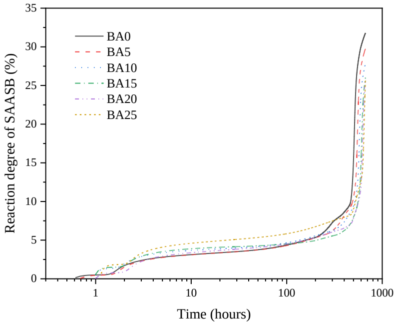

Fig. 4.7 Reaction degree of SAASB as a function of time. The curves were calculated by cumulative heat release and Eq. (4-7).

The heat evolution rate curve has indicated five reaction stages as discussed in Fig. 4.6 in Section 4.3.2.1. As seen in Fig. 4.8, the linear relationships between $\ln\left[1\text{-}2\alpha/3\text{-}(1\text{-}\alpha)^{2/3}\right]$ and $\ln t$ are regressed at each reaction stage. The slope and intercept of linear regression represent 1/N and $1/N \ln k$, respectively. For each reaction stage, the reaction grade (N) and reaction rate parameter (k) are calculated as listed in Table 4.11.

Subsequently, the reaction degree of GGBS and BA need to be computed by coupling with the calorimeter results. The reaction degree of slag (α_1) at initial dissolution, metastable stable period, and induction period can be calculated by coupling with the second peak height (SPH) of samples and BA0 (pure slag system) as follow:

$$\alpha_1 = \frac{\alpha}{P} \cdot \frac{\mathrm{SPH}_{\mathrm{BA\ sample}}}{\mathrm{SPH}_{\mathrm{BA0}}} \tag{4-8}$$

Where P is the percentage of slag in the matrix, the $\mathrm{SPH}_{\mathrm{BA\ sample}}$ is the second peak height of BA samples, and $\mathrm{SPH}_{\mathrm{BA0}}$ is the second peak height of BA0. Then the reaction degree of BA (α_2) can be calculated by Eq. 4-2.

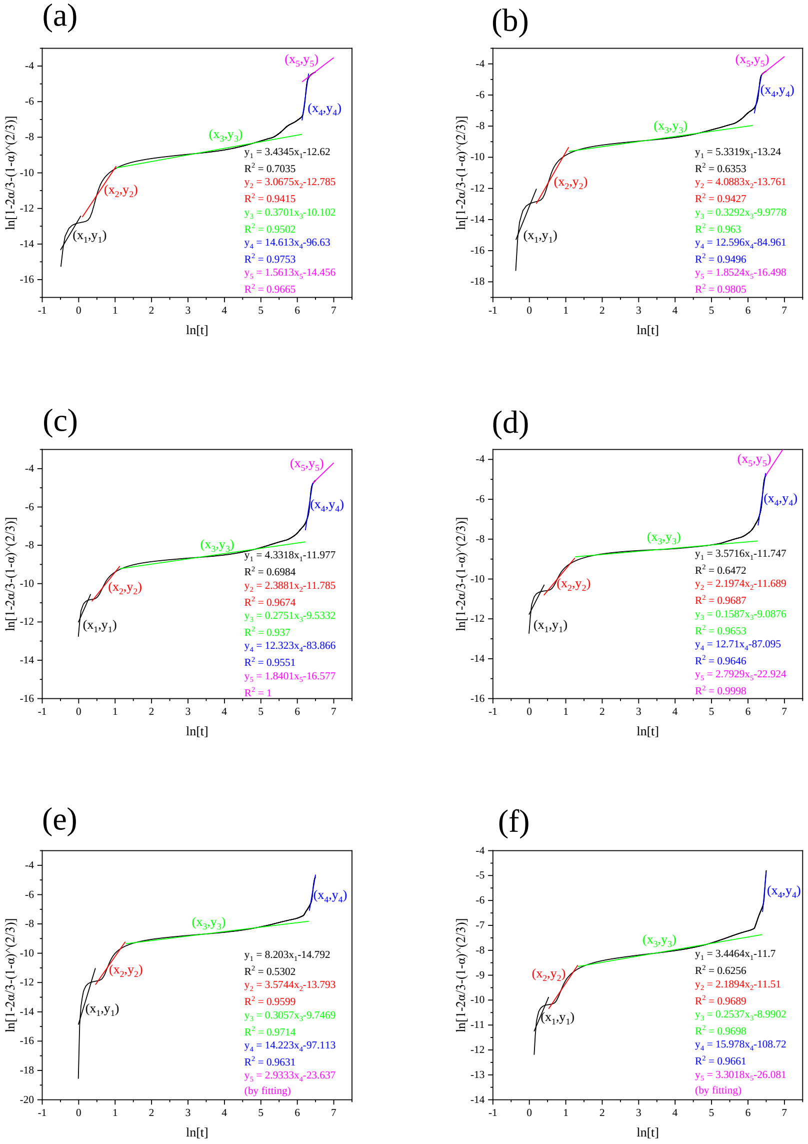

Fig. 4.8 Linear fits applied to ln[1-2α-(1- α)$^{2/3}$] versus ln$t$ for SAASB. (x_1,y_1), (x_2,y_2), (x_3,y_3), (x_4,y_4), and (x_5,y_5) represent initial dissolution period, metastable period, induction period, acceleration/deceleration period, and stable reaction period, respectively. The fittings of BA20 and BA25 at the stable stage are shown in Appendix Fig. B1 and Table B3.

At the same time, the reaction degree of slag (α_1) at acceleration/deceleration period and stable reaction period can be calculated by coupling with the third peak height (TPH) of samples and BA0 (pure slag system) by Eq.4-7:

$$\alpha_1 = \frac{\alpha}{P} \cdot \frac{TPH_{BA\ sample}}{TPH_{BA0}} \tag{4-9}$$

Where P is the percentage of slag in the matrix, the $TPH_{BA\ sample}$ is the third peak height of BA samples, and TPH_{BA0} is the third peak height of BA0. Then the reaction degree of BA (α_2) at stable reaction period can be calculated by Eq. 4-2.

Table 4.11 Evolution time (t), reaction grade (N) and reaction rate parameter (k) of SAASB.

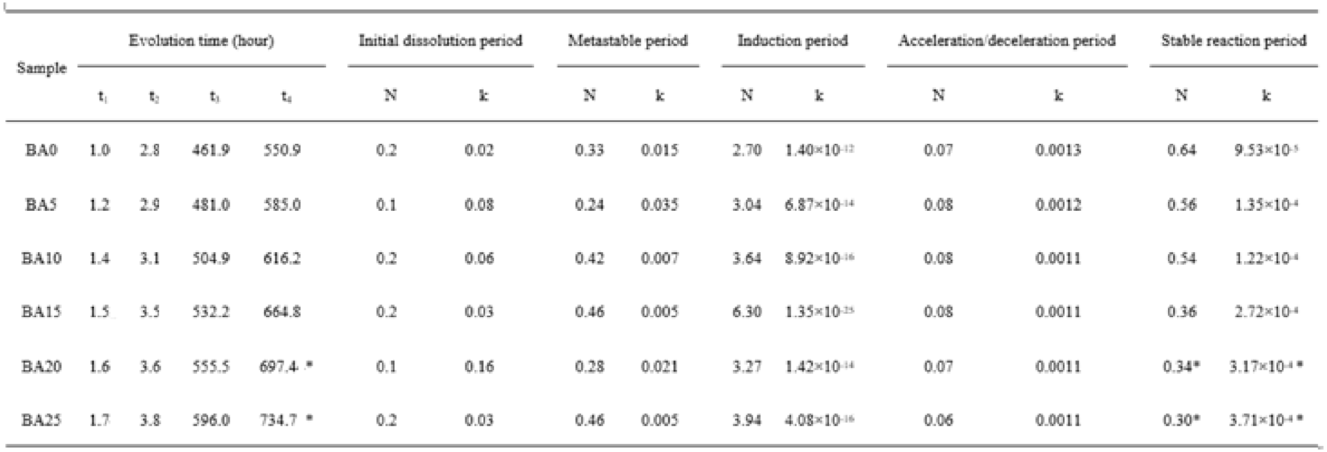

Sample	Evolution time (hour)				Initial dissolution period		Metastable period		Induction period		Acceleration/deceleration period		Stable reaction period	
	t_1	t_2	t_3	t_4	N	k	N	k	N	k	N	k	N	k
BA0	1.0	2.8	461.9	550.9	0.2	0.02	0.33	0.015	2.70	1.40×10^{-12}	0.07	0.0013	0.64	9.53×10^{-5}
BA5	1.2	2.9	481.0	585.0	0.1	0.08	0.24	0.035	3.04	6.87×10^{-14}	0.08	0.0012	0.56	1.35×10^{-4}
BA10	1.4	3.1	504.9	616.2	0.2	0.06	0.42	0.007	3.64	8.92×10^{-16}	0.08	0.0011	0.54	1.22×10^{-4}
BA15	1.5	3.5	532.2	664.8	0.2	0.03	0.46	0.005	6.30	1.35×10^{-25}	0.08	0.0011	0.36	2.72×10^{-4}
BA20	1.6	3.6	555.5	697.4 *	0.1	0.16	0.28	0.021	3.27	1.42×10^{-14}	0.07	0.0011	0.34*	3.17×10^{-4} *
BA25	1.7	3.8	596.0	734.7 *	0.2	0.03	0.46	0.005	3.94	4.08×10^{-16}	0.06	0.0011	0.30*	3.71×10^{-4} *

*The data is calculated by linear fitting. The fitting calculation is shown in Appendix Fig. B1 and Table B3.

4.3.3 Thermodynamic modelling

4.3.3.1 Modelled reaction process as a function of time

Fig. 4.9 exhibits the modelled reaction process of SAASB as a function of time analyzing the influence of BA on the chemical and mineralogical composition assemblages. It can be seen that a dramatic increase of reaction products appears around 20 days among the samples, which is assigned to the acceleration/deceleration period of $NaAlO_2$ activation. During the period, the anhydrous phases of SAASB are progressively consumed and C(N)−A−S−H gel, hydrotalcite, and zeolite are the main reaction phases formed. Notably, no dawsonite phase forms along the reaction process. The calculation of Gibbs free energy implies that the Na and Al are taken by the formation of zeolite A. It may be assumed that a large amount of dawsonite is formed during the hydration stoppage process. It is transferred from the gibbsite combined with CO_2 in the drying oven [193].

Notably, no C(N)−A−S−H gel is detected by TGA at 7 days, but it exists in the samples at 28 days, in conformity with the modelling results presented in Fig. 4.9. Simultaneously, the formation of C(N)−A−S−H gel decreases with the BA incorporation at 28-day modelling results. Because the higher BA replacement decreases the reaction rate as proved in heat release flow.

Fig. 4.10(a) plots the modelled amounts of hydrotalcite with QXRD results as a function of time. For 7-day SAASB pastes, there is a small amount of hydrotalcite formation in the modelled results. However, no hydrotalcite is detected by XRD at 7 days. It is probably that the low content of hydrotalcite in samples is too weak to be detected. Notably, hydrotalcite is clearly evident by XRD at 28 days, and the comparisons show good agreements between the modelled results and measured ones at 28 days. The hydrotalcite formation slightly decreases with the increased BA content. It is associated with relatively lower dissolved Mg^{2+} from slag resulting in less hydrotalcite formation.

Similarly, Fig. 4.10(b) illustrates the modelled amounts of zeolite A with QXRD results as a function of time. The comparisons show that modelled results are higher than the measured ones at 7 and 28 days. For 7 days, a limited amount of zeolite A is observed in XRD, while no zeolite A is fitted in QXRD. However, the modelled results illustrate around 2 wt.% of zeolite A among the samples. Because the reprecipitated Al layer on the slag or BA surface postpones $Al(OH)_4^-$ (from activator) reacting with $Si(OH)_4$ (from GGBS). This is not considered in the modelling simulation. Consequently, the reaction process of modelling simulation is slightly faster than the reality. Thus, the content of zeolite A is slightly overestimated in the modelling simulation. Also, the 28-day comparison shows a similar trend, the modelled results are slightly higher than the measured ones. However, the higher percentages of BA in the activated matrix promote the zeolite A formation as predicted in the modelling simulation. It is in line with the QXRD results.

Regarding gibbsite formation in QXRD results, the content of dawsonite has been converted to the same molar weight of gibbsite. Because the dawsonite is transferred from the gibbsite at early reaction age (before acceleration/ deacceleration period) during the hydration stoppage process. Fig. 4.10(c) shows the modelled amounts of zeolite A with QXRD results as

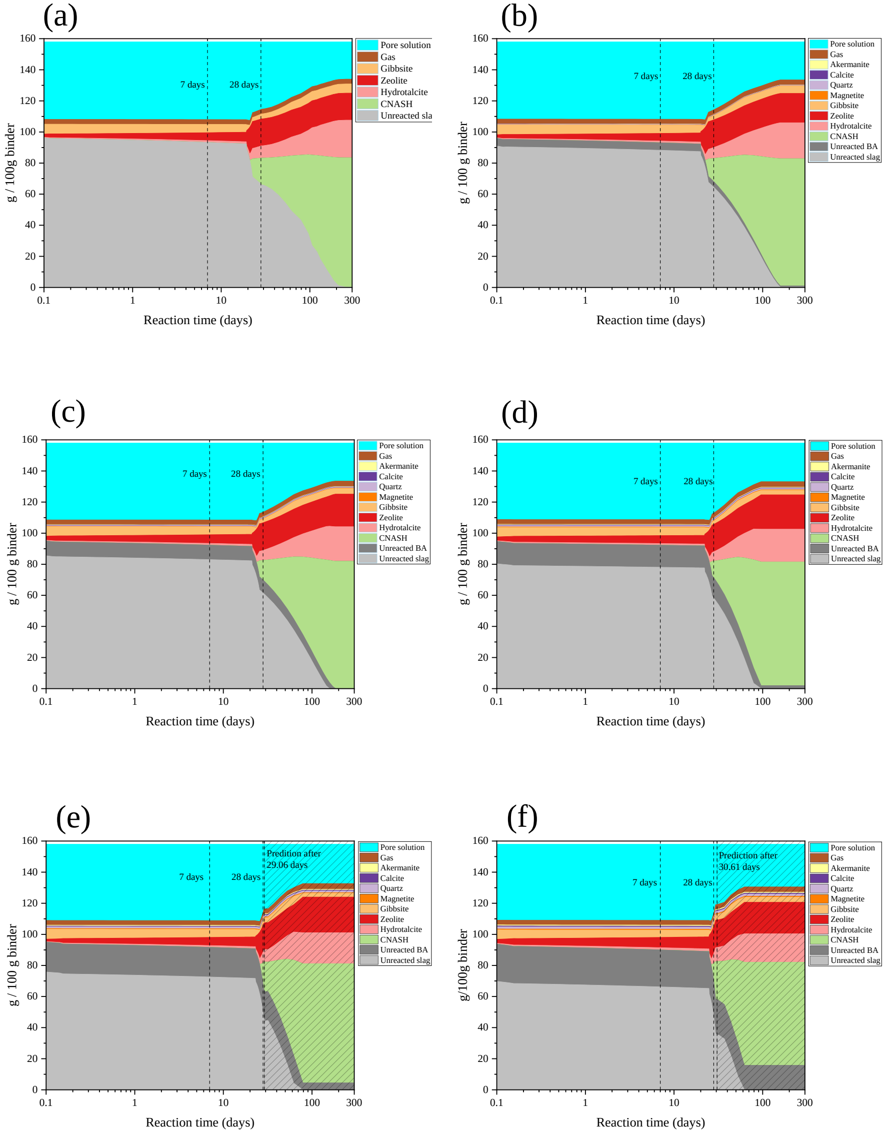

Fig. 4.9 Thermodynamic modelling of SAASB (a) BA0; (b) BA5; (c) BA10; (d) BA15; (e) BA20; (f) BA25. The predictions in BA20 and BA25 are originated from the fittings in Table 4.11 in terms of stable reaction period.

a function of time. As mentioned above, the reprecipitated Al layer on the slag or GGBS surface will not participate in the early reaction process. Thereby, less available Al in the real experiment decreases the total gibbsite formation compared to the modelled results at 7 and 28 days. For the 7-day comparison, the higher content of gibbsite formation shows in lower BA replacement samples both in the modelled results and measured ones. The elevated BA replacement slightly decreases the pH value of pore solution, then less gibbsite formation can be observed. It is in line with the leaching pH of raw materials, the pH of GGBS leachate is higher than that of BA. For 28-day comparisons, the modelled results are lower than 1wt.% and no gibbsite is identified in QXRD results. A large amount of gibbsite redissolves to $Al(OH)_4^-$ and reacts with $Si(OH)_4$, Ca^{2+}, and Na^+ to form C(N)−A−S−H. At the same time, hydrotalcite and zeolite formation also consume the redissolved $Al(OH)_4^-$ from gibbsite.

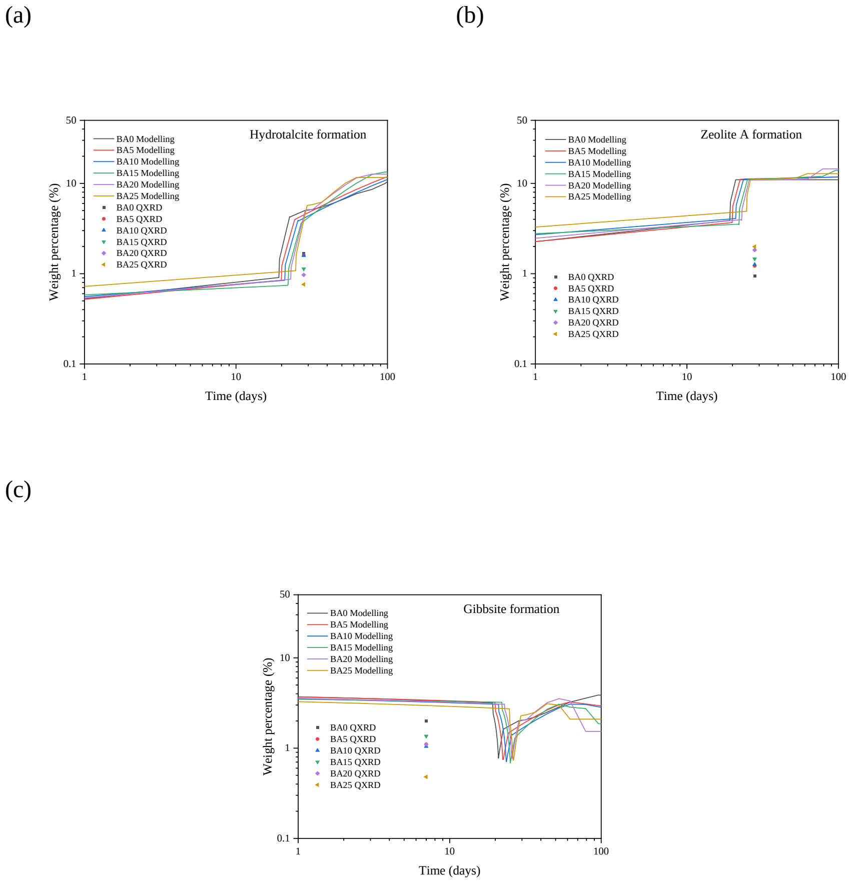

Fig. 4.10 Comparison between thermodynamic modelling and QXRD results.

4.3.3.2 Prediction of heavy metal ions binding capacity as a function of time

Based on the leaching of raw materials, the exact amount of PTEs, sulfates, and chlorides inputs from the raw GGBS and MSWI BA can be calculated (shown in Table B4). Only Cu, Mo, Sb, sulfates, and chlorides are selected. Because these ions are higher or closer to the legislation limits as described in Section 4.2.1. Three phases (C(N)−A−S−H, hydrotalcite, and zeolite A) in our study can efficiently absorb PTEs, chlorides, and sulfates. The leaching prediction of SAASB is based on the immobilizing capacity of the phases. The elements (Cu, Mo, Sb, Cl^-, SO_4^{2-}) can be immobilized by different phases are listed in Table 4.12. But limited literature about the exact uptake of chloride and sulfate ions is available.

Table 4.12 Elements (Cu, Mo, Sb, Cl^-, SO_4^{2-}) can be immobilized by different phases.

	C(N)−A−S−H	Ref	Hydrotalcite	Ref	Zeolite A	Ref
Cu	8.9~10.7 wt.%	[215]	10.8 wt%	[216]	34.2 wt.%	[217]
Mo	-	[218,219]	0.9 wt%	[220]	1.8 wt. %	[221]
Sb	0.03 wt.%	[222]	0.9~1.8 wt.%	[223]	0.6 wt.%	[224]
Cl^-	0.1~1 wt.%.	[225,226]	2.0 wt.%	[227]	-	-
SO_4^{2-}	3.4 wt.%	[226]	9.3~13.5 wt.%	[228]	-	-

Fig. 4.11 illustrates the PTEs, sulfates, and chlorides binding capacity per gram SAASB pastes by thermodynamic modelling as a function of time. In general, the predicted binding capacity grows with the formation of reaction products in line with the curing ages. Meanwhile, the absorption capacity reaches earlier to its maximum value with the increasing content of BA in the SAASB pastes. It is associated with the consumption of GGBS in the activation process [163]. The lower GGBS dosage leads to a low rate of the reaction at the early stage. Simultaneously, BA contributes limited reaction product formation at the final state due to its low reactivity.

As can be seen, the uptake of Cu shows the highest efficiency along with the curing ages in all scenarios. At the beginning 20-day curing period (Fig. 4.11), the limited uptake of Cu is due to the low C(N)−A−S−H and zeolite A formation. Notably, the zeolite A primarily contributes the Cu absorption by modelling prediction. Because the cage of zeolite A can absorb Cu ion significantly [229]. The remarkable increase of Cu absorption capacity shows after the acceleration/deceleration period. It is associated with the elevated C(N)−A−S−H gel formation. The C(N)−A−S−H gels mainly take charge of the Cu absorption in the long-term reaction stage. Besides, the higher slag content (BA0~BA25) in the matrix promotes the formation of C(N)−A−S−H gels. Thus, the higher Cu absorption capacity can be observed with higher slag participation.

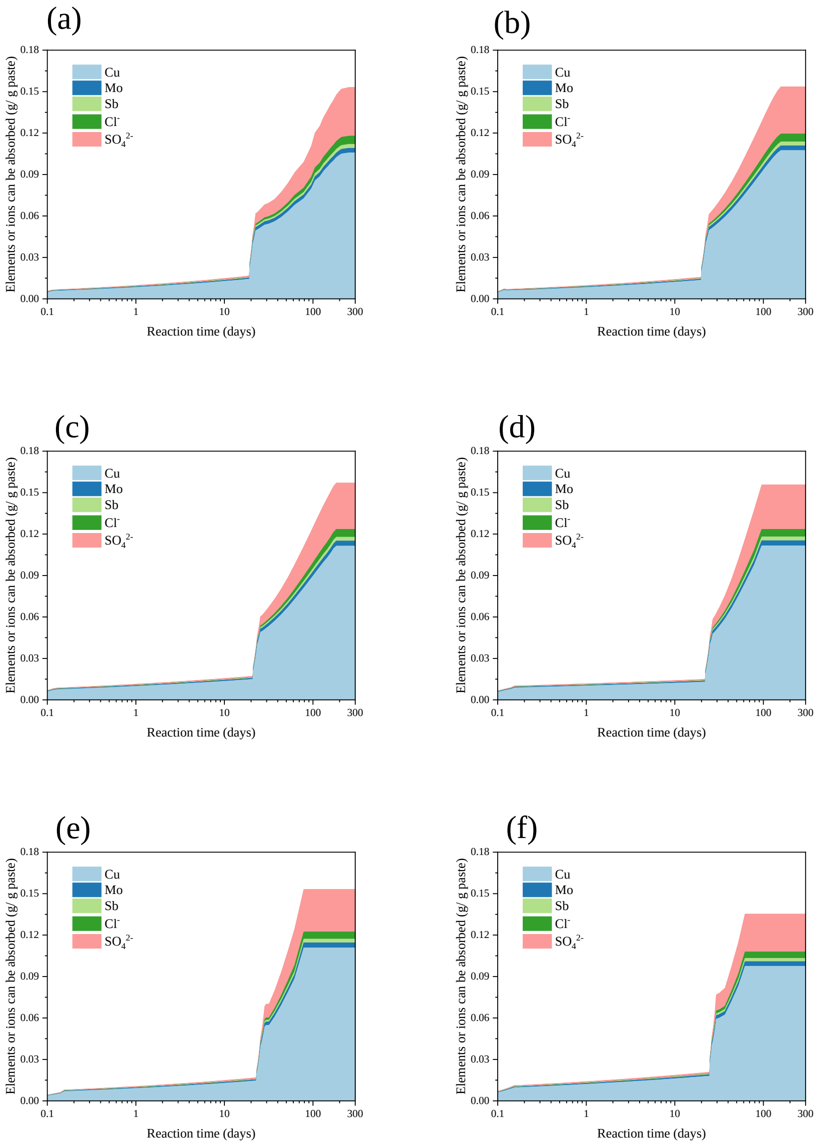

Fig. 4.11 PTEs, sulfates, and chlorides binding capacity of per gram paste by thermodynamic modelling as a function of time (a) BA0; (b) BA5; (c) BA10; (d) BA15; (e) BA20; (f) BA25.

The Sb absorption by SAASB pastes also exhibit satisfactory performance as a function of time. The higher slag content shows higher Sb uptake, which is associated with higher hydrotalcite formation. Because hydrotalcite performs as the primary Sb uptake phase [223]. The Sb absorption capacity also increases with the hydrotalcite formation along the curing ages.

The sulfates and chlorides absorption by SAASB pastes also exhibit increasing trend as a function of time. The BA0 shows the highest sulfates and chlorides absorption capacity among the SAASB pastes. Because the highest content of hydrotalcite can physically and chemically absorb sulfates and chlorides ions in BA0 [18]. The C(N)−A−S−H gel formation, increasing with curing ages, also marginally contributes to the physical absorption of sulfates and chlorides ions.

Limited Mo absorption can be observed in all cases (shown Fig. 4.11). The leaching of Mo is more sensitive to the pH environment than the formation of reaction products [210]. Simultaneously, the leaching of Mo is related to the precipitation of $CaMoO_4$ [230]. Thus, the amount of available Ca^{2+} is important to influence the Mo precipitation as well.

4.4 Conclusions

This paper provides a thorough analysis of sodium aluminate activated slag MWSI bottom ash (SAASB). The waste solids are characterized. The impact of bottom ash on early age reaction, gel chemistry, and microstructure are identified. Moreover, the thermodynamic modelling of SAASB is conducted by coupling colorimeter and selective dissolution. Based on the findings, the following conclusions can be drawn:

- Higher bottom ash content promotes the zeolite A formation in SAASB because of the increased Al/Si ratio in the matrix. While hydrotalcite formation decreases with increased bottom ash incorporations due to less Mg^{2+} in the pore solution. The reaction study by calorimeter reveals the metastable period of SAASB. It is associated with gibbsite formation, a metastable phase, at a very early reaction stage. It can be detected at 7 days but disappears after 28 days. Simultaneously, the bottom ash delays the reaction process of SAASB.
- Bottom ash negatively influences the development of microstructure, which is associated with less C(N)−A−S−H formation. This results in the decreased strength of the matrix.
- The heavy metal leaching complies with Dutch legislation, demonstrating the feasibility of utilizing $NaAlO_2$ activation of slag and bottom ash. The leaching prediction of toxic elements are close to the experimental results, and the error are within 1 order of magnitude.
- Compared to experimental results, the thermodynamic modelling results slightly overestimate the phase content but within 1 order of magnitude. The predicted heavy metal ions binding capacity of the matrix shows that the uptake of Cu is related to C(N)−A−S−H formation, while the binding capacity of Sb, sulfates, and chlorides increases with the hydrotalcite formation along the curing ages.

Chapter 5 In-situ formation of layered double hydroxides in MgO–$NaAlO_2$-activated GGBS/MSWI BA: Impact of Mg^{2+} on reaction mechanism and leaching behavior

Leaching problems of municipal solid waste incineration bottom-ash (MSWI BA) have been extensively reported in the literature. The outstanding heavy-metal-ion binding capacity of layered double hydroxides (LDHs) can potentially address this problem. This chapter aimed to investigate the in-situ formation of Mg–Al LDHs in MgO–$NaAlO_2$-activated ground granulated blast-furnace slag (GGBS) and BA blends, and the evolution of pH, ions, reaction products, microstructure, strength, and leaching behavior were characterized. The results indicate that the formation of Mg–Al LDHs is promoted using a higher MgO/NaAlO2 molar ratio, which improves the heavy-metal-ion binding capacity. $Al(OH)_4^-$ reacts with extra Mg^{2+} ions rather than Ca^{2+} ions to preferentially form Mg–Al LDHs over Ca–Al LDHs. Meanwhile, the extra Mg^{2+} ions snatch the $Al(OH)_4^-$ from Na^+, increasing the Mg–Al LDH content and reducing the zeolite content. Moreover, the in-situ-formed LDHs absorbed more SO_4^{2-} than Cl^-.

The chapter is partially from the following article:

T. Liu, S. Li, Y. Chen, H.J.H. Brouwers, Q. Yu, In-situ formation of LDHs in MgO-NaAlO2 activated GGBS / MSWI BA : The impact of Mg2+ on reaction mechanism and leaching behavior. (Submitted).

5.1 Introduction

Municipal solid waste (MSW) is produced in vast quantities worldwide, and incineration reduces the volume of MSW by up to 90%. However, this process results in a problematic residue, municipal solid waste incinerated bottom ash (MSWI BA) [231]. MSWI BA (denoted hereafter as BA for simplicity) is mainly composed of Ca, Si, and Al [232]. Previous studies have demonstrated the potential of BA as a supplementary cementitious material [162]. However, various mobile species may leach out during BA utilization, for example, antimony (Sb), copper (Cu), molybdenum (Mo), chloride (Cl^{-}), and sulfate (SO_4^{2-}), thereby contaminating the environment [233]. The reaction products of alkali-activated materials (AAMs) and C–S–H gels have active sites to absorb heavy-metal ions [234], potentially making them useful for immobilizing heavy-metal ions using BA as a partial precursor. However, these gels have shown limited capacity to bind heavy metal ions [235].

Layered double hydroxides (LDHs), which are secondary reaction products of alkali-activated ground granulated blast-furnace slag (GGBS) [236], have been demonstrated to possess superior heavy-metal binding capacity [20]. LDHs can be represented as $\left[M^{2+}_{(1\text{-}x)}M^{3+}_{x}(OH)_2\right](A^{n-})_{x/n}\cdot zH_2O$, where M represents a metallic skeletal ion (e.g., Mg or Al) and A^{n-} represents an interlamellar anion (e.g., SO_4^{2-} or Cl^{-}), where various combinations of M^{2+}/M^{3+} can be used [74]. However, their formation during the alkali activation of GGBS is rather limited. Enhancing LDH formation in the matrix is a promising method for tackling the leaching of harmful BA elements in AAMs [237]. The physical surface adsorption of LDHs mainly accounts for its binding capacity [20]. In addition, the hydroxyl groups on the surface of LDHs contribute to the coordination of heavy-metal ions [170]. Furthermore, heavy-metal ions such as Cu^{2+} and Cr^{3+} can intercalate into the framework of LDHs by replacing Mg^{2+} and Al^{3+} [237]. Xu et al. [81] synthesized and applied Mg–Al–NO_3 and Mg–Al–NO_2 LDH to AAMs and observed an increase in the chloride binding capacity. However, the high water absorption of LDHs during casting affects their dosage in cementitious matrices [96,238]. Thus, the in-situ generation of LDHs in alkali-activated GGBS/BA binders is preferred. Yang et al. [20] used calcined dolomite in sodium-carbonate-activated GGBS to promote the formation of hydrotalcite-like phases, which exhibited a potentially high ion-binding capacity. Ye et al. [22] investigated the autogenous formation of nitrite- and nitrate-intercalated LDHs. However, the final cementitious matrix appeared to contribute little to the chloride binding. Liu et al. [18] observed that sodium aluminate activation can promote the in-situ formation of LDHs, improving the ion-binding capacity of the activated matrix. However, they also observed a relatively slow reaction rate of sodium aluminate activation at an early age, which is in line with the results of previous studies [72,239]. The low-pH environment causes a relatively low activating efficiency of $NaAlO_2$, especially at an early age.

The pH of the environment strongly influences the reaction rate. It has also been reported that the high-pH environment of AAMs facilitates the leaching of heavy-metal ions. Most metal species in BA (e.g., Cu, Zn, and Pb) follow a cationic leaching pattern, and increasing the pH of the solution leads to a decrease in the concentration of leached elements [240]. However, some heavy-metal ions show an oxyanionic leaching pattern; for example, high concentrations of Mo are reached under highly alkaline conditions [171]. At the same time, the leaching of Cl^- and SO_4^{2-} is less pH-dependent, and the released amounts are mainly availability-controlled [241]. Thus, it can be hypothesized that the relatively low pH of AAMs can alleviate the heavy-metal leaching issue [240]. Therefore, activators with a relatively low pH can promote the formation of Mg–Al LDHs and reduce leaching issues in AAMs. Here, sodium aluminate was introduced as an activator to provide a low-pH environment for the pore solution. The extra available Al–O tetrahedra (denoted as $Al(OH)_4^-$) from sodium aluminate are believed to promote the formation of gels and Mg–Al LDHs [18]. However, Chen et al. [172] reported that although a sodium aluminate activator provided extra $Al(OH)_4^-$ ions, they were coated on the surface of the slag particles. This inhibited the early-phase hydration reaction, prolonging the setting time but promoting the formation of highly crosslinked gels in the late phase of the hydration reaction, resulting in an improved compressive strength at this stage. Yliniemi et al. [242] investigated the influence of activator type, including sodium aluminate, on the reaction kinetics, setting time, and compressive strength of alkali-activated mineral wool. Sodium aluminate exhibited lower alkalinity than sodium hydroxide and took several days to initiate the reaction, although it produced a high compressive strength after 28 days of curing. Therefore, mitigation methods are required.

To realize all the aforementioned objectives, that is, (1) the promotion of LDH formation in situ, (2) the need for a low-pH environment, and (3) addressing the slow setting of sodium aluminate activation, MgO is a promising additive for the alkali activation of GGBS/BA. First, it is a divalent cation for Mg–Al LDH formation. Moreover, it can maintain the low-pH environment of the pore solution. More importantly, it can promote the early-stage strength of sodium-aluminate-activated GGBS/BA (SAASB) [243]. More hydrotalcite could be produced by increasing the MgO content. Furthermore, sufficient Mg^{2+} and $Al(OH)_4^-$ (the trivalent cation of Mg–Al LDHs) and their ratios are important for the formation of LDHs [46]. However, the presence of extra Mg^{2+} affects the dissolution of the slag particles and results in various reaction products [244]. The variation in dissolved ions from the precursors in the pore solution is important for understanding the reaction mechanism [245–247]. In addition, the microstructure of the matrix is influenced by the MgO content, which purportedly decreases the formation of C–A–S–H products with higher Al uptake, high chain length, and a lower degree of crosslinking at a later age. These reactions and microstructural developments rely greatly on the evolution of the pore solution. However, studies examining the pore-solution composition in AAMs have rarely been reported and are rarely reported for alkali-activated slag blended with bottom ash [245,247,248]. Moreover, studies investigating the effects of Mg^{2+} (from MgO addition) on the reaction and further leaching behavior lack a comprehensive understanding of the MgO–$NaAlO_2$-activated matrix.

This chapter aims to reveal the influence of Mg^{2+} on LDHs and gel formation in MgO–$NaAlO_2$-activated GGBS/BA (MSAASB), with special attention to the leaching behavior. The pH and alkali-metal ions in the pore solution of the MSAASB were characterized. The reaction products and microstructures were determined, and the leaching of potentially toxic elements as well as the compressive strengths were tested. Based on the results, the influence of Mg^{2+} on the reaction products and leaching behavior is discussed. These research findings contribute to maximizing Mg–Al LDH formation in situ and its binding to leaching ions.

5.2 Methods

5.2.1 Raw materials and sample preparation

GGBS and MSWI BA (simplified as BA in the text) were used in this chapter. The chemical compositions of GGBS and BA were determined using X-ray fluorescence (XRF) spectroscopy, as shown in Table 5.1. Magnesia 291 (96% purity, Magnesia, Germany) was used in this chapter. The reactivity of MgO was assessed based on its reaction time with acetic acid [103]. Since the reaction time was 18.95 s, it was classified as medium-active magnesia. The BET specific surface area of MgO was 50.41 m^2/g. The crystalline structures of GGBS, BA, and MgO were determined using X-ray diffraction, as shown in Fig. 5.1(a), (b), and (c), respectively.

Table 5.1 Chemical compositions and physical properties of GGBS and MSWI BA.

Chemical composition	GGBS (wt%)	MSWI BA (wt%)	Chemical composition	GGBS (wt%)	MSWI BA (wt%)
Na_2O	-	5.9	NiO	-	0.1
MgO	9.0	1.9	CuO	-	0.3
Al_2O_3	13.0	8.6	ZnO	-	0.5
SiO_2	31.0	50.1	SeO_2	-	-
P_2O_5	-	0.5	SrO	0.1	0.1
SO_3	5.1	0.6	ZrO_2	-	0.1
K_2O	0.3	1.1	Ag_2O	0.2	-
CaO	38.8	16.8	Eu_2O_3	-	0.1
TiO_2	1.4	-	PbO	-	0.1
V_2O_5	0.1	0.2	Cl	0.1	0.4
Cr_2O_3	0.1	0.1	LOI* (1000℃)	1.3	5.4
MnO	0.3	0.2	Particle density (g/cm^3)	2.9	2.5
Fe_2O_3	0.7	12.6	-	-	-

*LOI = Loss on ignition at 1000℃

The particle-size distributions (PSD) of the powder feedstocks were determined by laser granulometry using a Master Sizer laser granulometer with an open measuring cell. The powders were prepared by wet dispersion in ethanol. The PSD of GGBS, BA, and MgO are shown in Fig. 5.1(d), with median particle sizes (d_{50}) of 11.8, 11.5, and 9.4 μm, respectively.

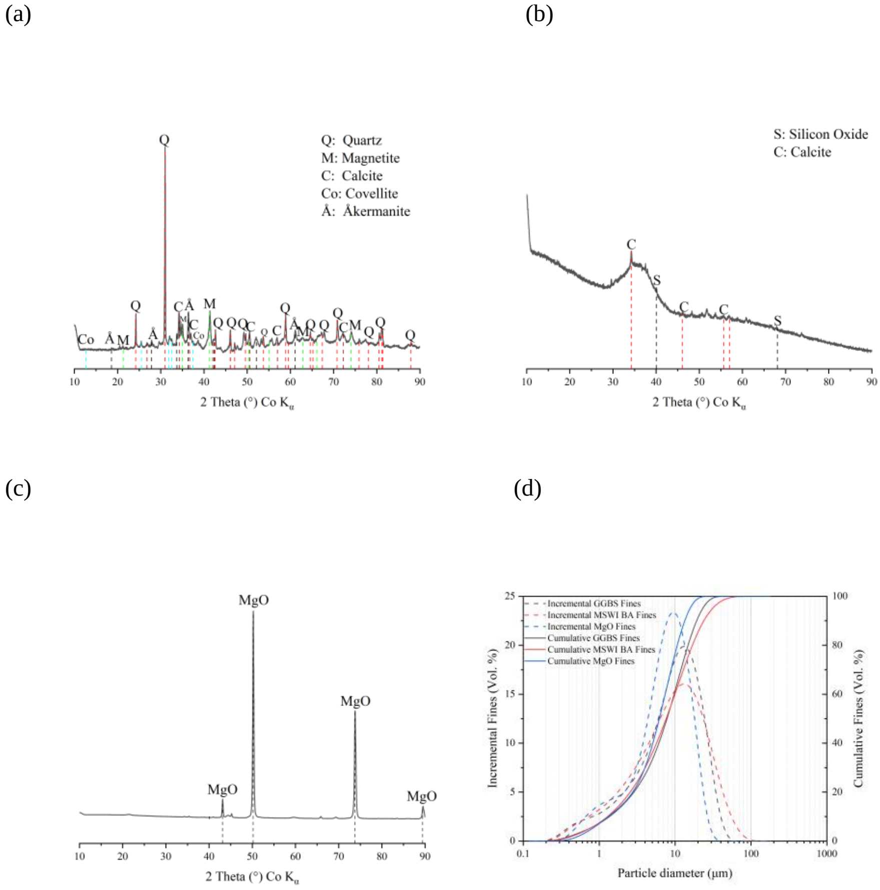

Fig. 5.1 XRD patterns of (a) MSWI BA; (b) GGBS; and (c) MgO; (d) Particle size distributions of GGBS, MSWI BA, and MgO.

GGBS and BA were mixed in a 9:1 (GGBS:BA) mass ratio as the solid precursor, which was activated by hydroxide and sodium aluminate solutions (see the sample IDs in Table 5.2). The raw starting materials were mixed in the designated proportion in a Hobart mixer following the preparation procedure suggested by EN 196-1 [249]. The pastes were cast in a Ø 45 mm × 55 mm cylindrical plastic mold and then subjected to vibration. All the pastes were sealed and cured at room temperature (20 ℃) until the specified curing ages. The mortars were produced by adding a (GGBS + BA)/sand mixture in a ratio of 1:3 by mass. The mortar samples for mechanical testing were cast in a 40 mm × 40 mm × 160 mm prism mold and then subjected to vibration as EN 196-1 [250].

The activators used in this chapter were sodium hydroxide or sodium aluminate. Analytical grade sodium-hydroxide pellets (99% purity) were dissolved in deionized water to prepare a solution for the sodium hydroxides activated samples, and the sodium-hydroxide activator was prepared 24 h before application. Analytical grade sodium-aluminate pellets were dissolved in deionized water to prepare solutions for the NA and MA samples, while the sodium aluminate activator was prepared 6 h before application. The additional MgO was calculated based on the aluminate in the activator, where MA0.5, 1, 2, and 4 indicate $MgO/NaAlO_2$ molar ratios of 0.5, 1, 2, and 4, respectively.

Table 5.2 Mix design of the pastes.

Sample ID	w/b ratio*	$NaAlO_2$ (g)	NaOH (g)	MgO (g)	Equivalent Na_2O	GGBS (g)	BA (g)
NH	0.5	-	3.9	-	3	90	10
NA	0.5	7.9	-	-	3	90	10
MA0.5	0.5	7.9	-	1.9	3	90	10
MA1	0.5	7.9	-	3.9	3	90	10
MA2	0.5	7.9	-	7.7	3	90	10
MA4	0.5	7.9	-	15.5	3	90	10

*w/b = water-to-binder mass ratio

Binder mass= GGBS + BA

5.2.2 Experimental programs

5.2.2.1 Cold water extraction

The paste powder was used to measure the cations and pH values of the pore solution by cold water extraction (CWE). First, 25 g of powder was mixed with 50 g of deionized water and shaken for 5 min (5 min leaching procedure). The suspension was filtered through a filter syringe. Previous studies have shown no remarkable uptake of ions by filter [140,141]. Finally, the rapid leachate was diluted 10-fold with deionized water. The 25 g diluted solutions were acidified with HNO_3 to prevent precipitation, and the solutions were analyzed for Na, Ca, Si, Al, Mg, Fe, and other heavy-metal ions using inductively coupled plasma optical-emission spectrometry (ICP-OES).

Based on the ICP-OES results, the free cation content and pH value of the pore solution were calculated as follows:

$$X = [X]_{CWE} \cdot \frac{m_{105}+m_{add}}{m_{sample}} \tag{5-1}$$

$$pH = pH_{CWE} + \log\frac{m_{w105}+m_{add}}{m_{sample}} \tag{5-2}$$

where X is the free cation content of the pore solution of the sample (mmol/L); $[X]_{CWE}$ is the concentration of the element in the filtrate obtained after CWE (mmol/L), as determined by ion chromatography (IC) or ICP; m_{105} is the mass of evaporable water at 105 ℃ in the samples (Table 5.3); m_{add} is the mass of deionized water added during the 5 min rapid-leaching process; m_{sample} is the total weight of the sample (g); and pH_{CWE} is the pH of the filtrate obtained after the CWE. Detailed derivations of Eqs. 5-1 and 5-2 can be found in Ref. [18].

The CWE technique has a restriction when used to measure pH and ions concentration, however it has been demonstrated that this approach can get a reasonably accurate estimate of composition of the pore solution. The Na^+, K^+, Ca^{2+}, Mg^{2+}, $Al(OH)_4^-$, and $Si(OH)_4$ had been proved in the previous studies [18,140].

Table 5.3 Amount of evaporable water at 105 °C or free water in the paste samples after casting for 28 days.

	Before drying (g)	After drying (g)	m_{105} (g)*	$\frac{m_{105}+m_{add}}{m_{sample}}$
NH	25.1	18.6	6.5	2.3
NA	25.0	18.9	6.1	2.2
MA0.5	25.3	19.1	6.2	2.2
MA1	25	19.1	5.9	2.2
MA2	25	19.4	5.6	2.2
MA4	25.1	20.1	5.0	2.2

*The m_{105} value was measured after oven-drying.

5.2.2.2 X-ray diffraction

X-ray diffraction (XRD) was performed using a Bruker D4 Phaser instrument emitting Co-K_α radiation (40 kV, 30 mA). The pressed, powdered specimens were measured with a step size of 0.05° and counting time of 1 s/step. The 2θ range was 10–90°.

5.2.2.3 Quantification of X-ray diffraction

Quantification of X-ray diffraction (QXRD) was performed by adding an internal standard (10 wt% Si powder; Siltronix, France) to the paste samples. Then, the mixed paste samples were milled using the XRD mill at level 3 speed for 15 min. For the quantification of mineral phases in the samples, Rietveld analysis was performed using TOPAS software (version 4.2, Bruker) [180].

5.2.2.4 Thermogravimetry

Thermogravimetric (TG) tests were performed on ≈100 mg samples by using an STA 449 F1 instrument at a heating rate of 10 ℃/min. Experiments were carried out from 40 ℃ to 800 ℃, in which N_2 was used as the carrier gas.

5.2.2.5 Nitrogen physisorption test

Nitrogen physisorption tests were conducted using a TriStar II 3020 (Micromeritics). The pore size distribution was carried out using the Barett, Jonyer, and Halenda (BJH) method [105] from the desorption branch. Before the test, the paste samples were ground into powder, immersed in 2-propanol for 24 h to stop the hydration process, and then dried to constant mass at 60 ℃ for 3 d.

5.2.2.6 SEM mapping and image analysis

SEM mapping

The morphologies of the mortar samples at day 28 were analyzed using scanning electron microscopy (SEM). The gold-coated specimens were measured under high vacuum at an accelerating voltage of 15 kV. The SEM instrument was equipped with a secondary electron detector (SED) and energy-dispersive spectrometer (EDS). The SED images were obtained simultaneously with the EDS mapping. The distributions of Si, Al, O, Na, Ca, Mg, and C were determined using EDS mapping.

After the SED and EDS mapping images were obtained, a series of image analyses was performed. This was divided into two major steps: interfacial transition zone (ITZ) determination and quantitative analysis.

ITZ determination

The grayscale is the essential difference in the image that allows the aggregates, pores, and reaction products to be distinguished. A typical SEM image of the mortar sample is shown in Fig. 5.2a). To distinguish the paste matrix and aggregates, the boundary pixels of the aggregates were delineated and labelled (Fig. 5.2b)). Subsequently, the aggregate zone was removed, and strip delineations were added in 5 μm increments from the aggregate boundary to 20 μm. The grayscale of Fig. 5.2c) was counted, and the overflow point was determined by fitting the trends of the grayscale counts (shown in Fig. 5.2f)). The pores region and reaction product region can be identified in Fig. 5.2f). The fitting lines are selected by the edge of pore region and the region between pore and reaction product region in the histogram. The overflow point represents the pore threshold in the paste matrix. Then, the porosities of the entire paste matrix and strip matrices were calculated. When the porosity of the strip part is close to that of the entire paste matrix, the ITZ can be determined. For example, the porosity of Part 4 in Fig. 5.2h) was close to the entire paste matrix, and the porosity of Part 3 is larger than that of Part 4. The ITZ was then confined to strip parts 1, 2, and 3. This method is recommended in the previous studies as well [251,252].

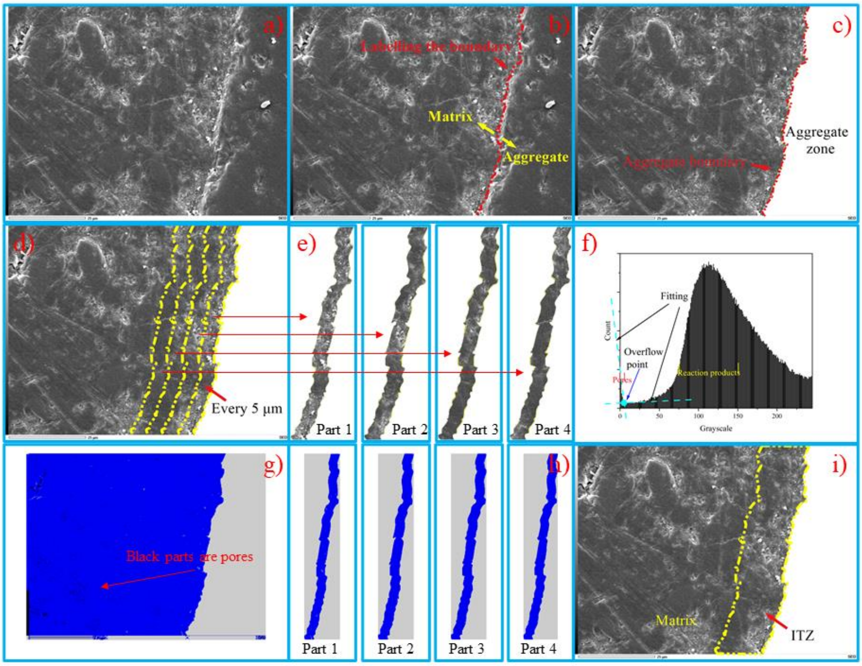

Fig. 5.2 Schematic diagram for the aggregate boundary delineation and quantitative analysis to determine the ITZ (sample aged for 28 days).

Quantitative analysis of SEM mapping in ITZ

The elemental distributions of Si, Al, O, Na, Ca, Mg, and C were then quantified in the ITZ of each matrix. The MATLAB code for color-proportion determination is provided in the Supplementary Material (code 2). The Si/Al, Mg/Al, and Ca/Al atomic ratios were calculated, and the porosities of the ITZ and matrix were determined.

5.2.2.7 One-stage batch-leaching test

Batch-leaching tests were performed by subjecting a material with a particle size of <4 mm and L/S ratio of 10 L/kg to demineralized water (EN12457 part 2 [197]). During the one-stage batch-leaching tests, the contact time between the solid material and the leachate was 24 h. After the leaching test, the eluate was filtered through a 0.45 μm filter and further analyzed.

In each test, the material was analyzed for a broad spectrum of parameters using ICP-OES. All eluates were analyzed for Ba, Cr, Cu, Mo, Ni, Se, Sb, V, and Zn. Cl^- and SO_4^{2-} were analyzed using ion chromatography (IC).

5.2.2.8 Mechanical testing

After curing for 28 d, the compressive strength of the mortar samples was determined according to EN 196-1 [249]. The samples were centered on the plates of the machine. Subsequently, the load was increased smoothly at the rate of 2400 N/s over the entire load application until the fracture load.

5.3 Results

5.3.1 pH and composition of pore solution

Fig. 5.3 presents the changes in the pH value and ion concentration with respect to Al, Si, Mg, Na, and Ca (hereafter denoted as [Al], [Si], [Mg], [Na], and [Ca], respectively) in the pore solution of the paste samples at specific curing times of 3, 7, 14, and 28 d. Detailed pore-solution data are listed in the Appendix C. The pore solution was dominated by $Al(OH)_4^-$ and Na^+ions, whereas much lower concentrations of $Si(OH)_4$, Mg^{2+}, and Ca^{2+} were observed.

Fig. 5.3(a) illustrates that only the pH of the NH sample exhibits a distinctive decreasing trend with increasing curing age, while the NA and MA samples show stable pH values between 12.80 and 12.95 among the curing ages. The pH decrease in the NH sample was attributed to the consumption of OH^- by the formation of gels and crystalline phases. However, in the sodium-aluminate-activated matrix, sodium aluminate shows a pH-buffering effect, and the aluminate continually compensates for OH^- upon the formation of gels and crystalline phases; consequently, the pH remains at ≈12.9. MA1, MA2, and MA4 showed a very slight decrease in pH during the first seven days. Subsequently, the continuous hydrolysis of MgO in the pore solution provides Mg^{2+}, promoting the formation of hydrotalcite (Ht). This process was also beneficial for maintaining the pH of the pore solution. Noticeably, with an increase in the $MgO/NaAlO_2$ molar ratio, the rate of decrease in pH before the 7 d mark increased because the extra MgO accelerated geopolymerization and Ht formation [238].

Among the NA and MA samples, a dramatic decrease in [Al] was detected in the pore solution with increasing curing time, whereas the NH sample showed a remarkably low [Al] in the pore solution after three days (Fig. 5.3(b). The concentration of $Al(OH)_4^-$ showed an obvious declining trend with increasing $MgO/NaAlO_2$ molar ratio. This can be explained by the fact that extra Mg^{2+} can react with $Al(OH)_4^-$ to form more LDHs. In the sodium-hydroxide-activated system, [Al] remains stable at a low value of ≈2.12 mmol/L after 3 d, which is attributed to the intense reaction process within the first 3 d. Low concentrations of available $Al(OH)_4^-$, $Si(OH)_4$, and Na^+ and relatively low-pH environments (compared with the initial pH) indicate a low rate of the reaction process [18]. In the sodium-aluminate-activated system, the NA sample showed the highest [Al] after 3 d. $Al(OH)_4^-$ in the pore solution reacts with $Si(OH)_4$, Mg^{2+}, and Ca^{2+} dissolved from the GGBS. It should be emphasized that the extra $Al(OH)_4^-$ hampers the dissolution of $Si(OH)_4$ from the raw materials [253]. The dissolved $Si(OH)_4$ (from the slag) and extra $Al(OH)_4^-$ ions (from the activator) re-adsorb Ca^{2+} (from the slag) at an early stage, reprecipitating on the surface of the raw materials. The reprecipitated layer was deposited on the grains of the raw materials, delaying further dissolution of the raw materials at an early stage. This resulted in a large amount of $Al(OH)_4^-$ remaining in the pore solution. MA0.5 and MA1 exhibited a similar trend to that of NA, where [Al] tended to decrease with increasing MgO content. LDHs were formed in the reactions of Mg^{2+} (produced in the hydrolysis of MgO) with $Al(OH)_4^-$ (provided by the activator). The reactions of NA, MA0.5, and MA1 were complete after 14 d. In addition, the [Al] in MA2 indicates that the geopolymerization process finishes between days 7 and 14. Moreover, the reaction of MA4 is even faster than that of MA2, as reflected by the complete consumption of [Al] within 3–7 d. The completion of the MA reaction process can be deduced from the decrease in [Al] to ≈2 mmol/L. Meanwhile, the higher $MgO/NaAlO_2$ molar ratio accelerated the consumption of $Al(OH)_4^-$ in the pore solution to form more gels and LDHs.

[Si] varies widely among the samples subjected to different curing times (Fig. 5.3(c)). The [Si] remained low in the NH sample with increasing curing time, which is consistent with the change in [Al]. This confirms the low reaction rate. The [Si] in NA, MA0.5, and MA1 illustrate the hill-like trend with curing time; the [Si] reached a maximum at 7 d and decreased to a low value after 14 d. The large amounts of $Si(OH)_4$ were consumed between days 7 and 14. This represents a high rate of geopolymerization in $NaAlO_2$-activated materials. For MA2, [Si] decreased dramatically between days 3 and 14. In addition, the [Si] of MA4 decreased as a function of curing time up to 28 d. The decrease in [Si] in MA2 and MA4 occurred earlier than that in the other samples, which is due to the extra MgO in the matrix. As mentioned above, an excessive $Al(OH)_4^-$ content results in a reprecipitated layer. This obstructs the dissolution of $Si(OH)_4$ originating from the GGBS. However, the extra MgO can react with the extra $Al(OH)_4^-$ ions to form hydrotalcite, mitigating the obstruction of $Si(OH)_4$ dissolution. Therefore, the addition of MgO accelerated the geopolymerization process and hydrotalcite formation during the first 7 d. Meanwhile, MA4 exhibits more obvious [Si] changes in the pore solution over days 3 to 7 than does MA2 during the same timeframe. The noticeably declined pH of MA4 indicates higher reaction rates than those of MA2 during this period.

Fig. 5.3(d) illustrates the changes in [Mg] as a function of the curing age. MA2 and MA4 showed a remarkable increase before 14 d, followed by a dramatic decrease after 14 d. The other samples exhibited a slight decrease with curing time. NH shows stable [Mg] after 3 d, which is in agreement with the changes in [Al] and [Si]. The [Mg] of NA, MA0.5, and MA1 generally decreased with curing time owing to continuous geopolymerization when the Mg^{2+} is consumed to form LDHs, particularly after 14 d. Meanwhile, MA2 showed a high rate of reaction between days 7 and 14. Large amounts of hydrotalcite were generated in the reaction between $Al(OH)_4^-$ and Mg^{2+} during this period. Similarly, MA4 exhibited a high rate of reaction between days 3 and 7 owing to hydrotalcite formation, which occurred earlier than for MA2. A higher MgO content accelerated hydrotalcite formation, which is in line with the XRD quantification in Section 5.3.2.1. The increases in [Mg] in MA2 (after 7 d) and MA4 (after 3 d) were due to the dissolution of MgO. The reaction process consumes large amounts of OH^-; therefore, more MgO dissolves in the pore solution to maintain the pH of the environment [254,255].

A significant decrease in [Na] during the curing of the NA and MA samples was observed, while [Na] remained relatively stable in the mixed NH during the curing period (shown in Fig. 5.3(e)). NA, MA0.5, and MA1 showed similar declining trends with increasing curing time. In addition, the higher the $MgO/NaAlO_2$ molar ratio, the lower the [Na]. Moreover, the [Na] in MA2 and MA4 decreased faster than that in NA, MA0.5, and MA1. This indicates that Mg^{2+} accelerated gel formation to consume excessive Na^+ in the pore solution. In addition, the Na^+ in the pore solution of MSAASB showed a variation similar to that of $Al(OH)_4^-$, which may prove the formation of N–A–S–H during the curing period.

Fig. 5.3(f) shows that during the curing period, the [Ca] of MSAASB continued to increase at a low concentration (below 0.3 mmol/L), while [Ca] in NH remained relatively stable (around 0.25 mmol/L). For the MA pastes, the increase in the $MgO/NaAlO_2$ molar ratio slightly increased [Ca] in the pore solution. MgO addition maintained the pH of the pore solution; consequently, Ca^{2+} from GGBS can be dissolved under a stable pH environment of the pore solution. Therefore, it increased with the curing age.

Overall, [Al] and [Na] in the pore solution show a remarkable decrease with increasing curing age, which is due to the formation of zeolite and N–A–S–H gels. [Si] decreases with a higher $MgO/NaAlO_2$ molar ratio during curing, reflecting the consumption of $Si(OH)_4$ during the geopolymerization process. Most importantly, the higher MgO content compensates for Mg^{2+} in the pore solution, which accelerates the formation of gels and hydrotalcite. Furthermore, the hydrolysis of the extra MgO maintains the pH environment, which facilitates the dissolution of Ca^{2+} from the GGBS, leading to an increase in [Ca] with curing age.

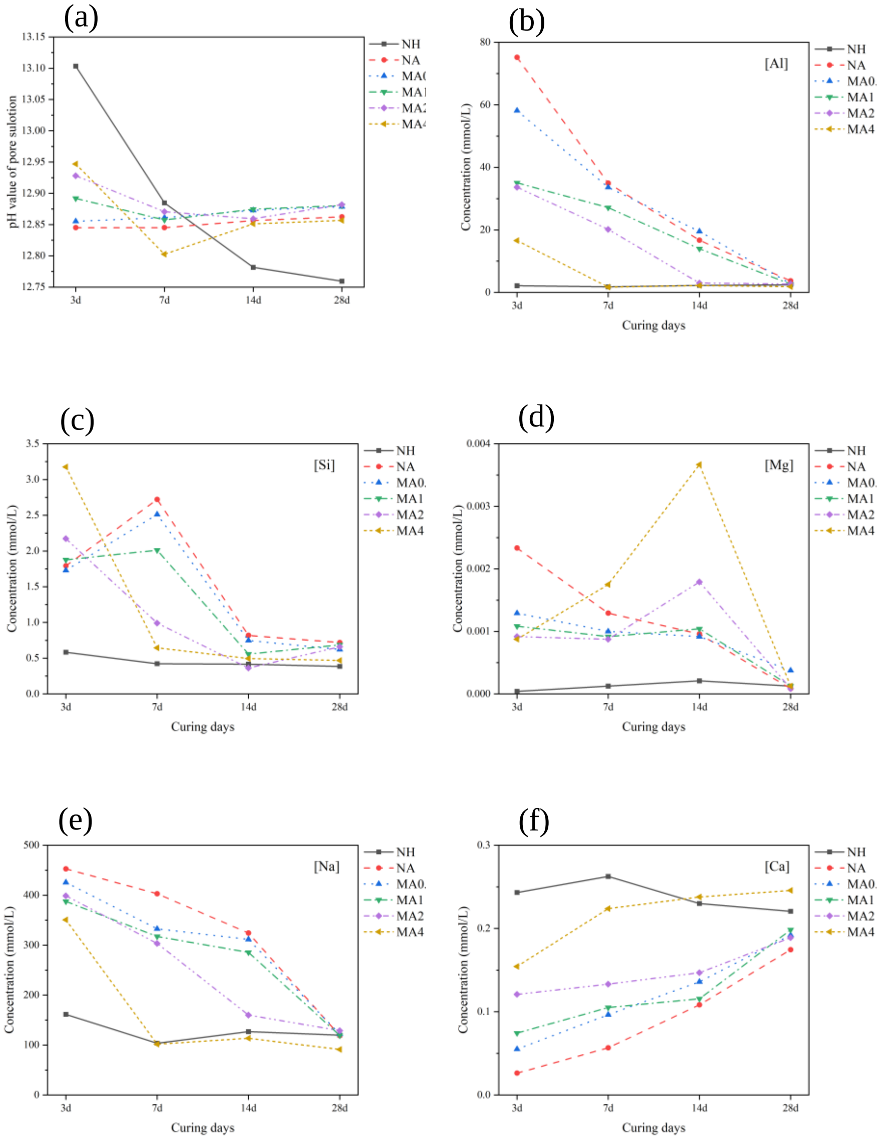

Fig. 5.3pH and ion-concentration changes of MSAASB pore solution at different curing days: (a) pH, (b) [Al], (c) [Si], (d) [Mg], (e) [Na], and (f) [Ca].

5.3.2 Phase evolution of activated pastes

5.3.2.1 X-ray diffraction

The XRD patterns of the 7- and 28-day NaOH-activated slag, SAASB (without MgO addition), and MA paste samples are presented in Fig. 5.4(a) and (b). The content of calcium silicate hydrate (C–S–H, PDF 00-033-0306), calcium aluminum oxide carbonate hydrate (hemi-carboaluminate, denoted as Hc) ($Ca_4Al_2(OH)_{12}[OH(CO_3)_{0.5}]\cdot5.5H_2O$, PDF 00-041-0221), and hydrotalcite (denoted as Ht) ($(Mg_6Al_3)CO_3(OH)_{16}\cdot4H_2O$, PDF 00-014-0191) varied significantly. Quartz (PDF 01-079-1906), akermanite (PDF 01-089-0951), magnetite (PDF 01-089-0951), and calcite (PDF 01-086-2340) from the BA remained relatively unchanged during the curing period.

The reaction products of the paste at 7 d were highly consistent with those of the 28-day pastes. A large amount of Mg–Al LDHs and smaller amounts of Zeolite A (sodium aluminum silicate hydrate; $Na_{96}Al_{96}Si_{96}O_{384}$ $216H_2O$, PDF 00-039-0222), and Hc were the distinct reaction products of SAASB during the initial 7 d. small amount of zeolite A increased with curing time up to 28 d, while a small amount of C–A–S–H also appeared in the reaction products. This is attributed to the dissolved Ca^{2+} derived from GGBS, which then interacts with $Al(OH)_4^-$ and $Si(OH)_4$ in the pore solution to form C–(A)–S–H under a suitable pH environment. In decreasing order, C–S–H, Ht, Hc, and a small amount of zeolite were the primary reaction products of MA at days 7 and 28. The Ht content (Mg–Al LDHs) increased with a higher $MgO/NaAlO_2$ molar ratio. This was associated with the MgO dissolved in the pore solution, and the sufficient Mg^{2+} and extra $Al(OH)_4^-$ (from the activator) accelerated the formation of Mg–Al LDHs. It is worth mentioning that a small amount of Hc (Ca–Al LDHs) was generated after curing for 7 d, while an increasing $MgO/NaAlO_2$ molar ratio hindered the generation of Hc. The solubility of Ht is lower than that of Hc in an aqueous environment [205,256]. Simultaneously, Mg^{2+} can directly dissolve from the extra MgO, whereas Ca^{2+} originates only from the dissolution of slag particles. Mg^{2+} in the pore solution can reach a higher concentration faster than Ca^{2+}; therefore, the precipitation of Ht was easier than that of Hc with higher MgO incorporation. The intensity of the zeolite peak decreases remarkably with an increase in the $MgO/NaAlO_2$ molar ratio in the matrix. The $Al(OH)_4^-$ is prone to react with additional Mg^{2+} instead of Na^+, generating Mg–Al LDHs rather than zeolites. This can also be explained by the fact that low concentrations of [Al] and [Si] are not beneficial to enhancing the crystallinity of sodium aluminosilicate hydrate [257] (here, zeolite).

Fig. 5.5 shows the quantification of XRD analysis at days 7 and 28 (details are shown in Table C6 and Table C7). It is noteworthy that the amorphous component is composed of C–S–H and C(N)–A–S–H [18]. At day 7, approximately 1.5 wt% Ht was present in the NH paste, while 1.1, 1.1, 1.3, 1.7, and 2.5 wt% Ht existed in the NA, MA0.5, MA1, MA2, and MA4 pastes, respectively. At day 28, 1.7, 1.6, 1.8, 2.1, 2.3, and 3 wt% Ht was detected in the NH, NA, MA0.5, MA1, MA2, and MA4 pastes, respectively. Compared with the Ht content in NH at 28 d, the NA, MA0.5, MA1, MA2, and MA4 pastes showed Ht increases of up to −5.9, 5.9, 23.5, 35.3, and 76.5%, respectively. With curing age, Ht increased only slightly in MA0.5 but remarkably in MA1, MA2, and MA4. The elevated content of MgO significantly promoted Ht formation owing to the extra supply of Mg^{2+}, which is beneficial for reacting with $Al(OH)_4^-$, forming more Ht. This result is in agreement with that of a previous study [258].

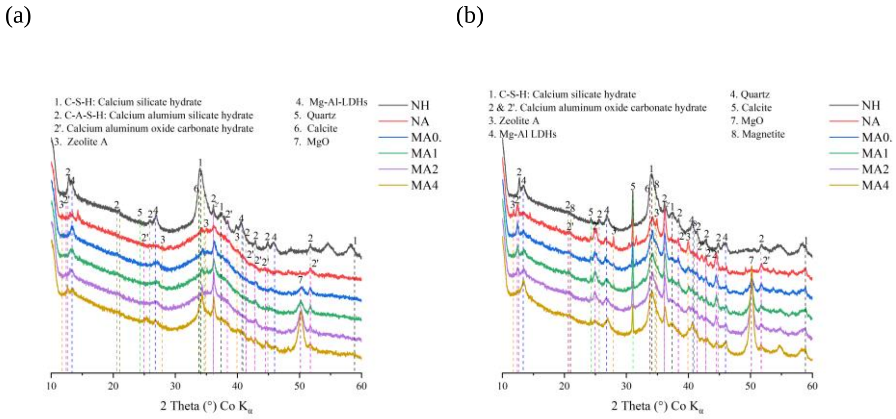

Fig. 5.4 XRD patterns of MSAASB at (a) 7 and (b) 28 d.

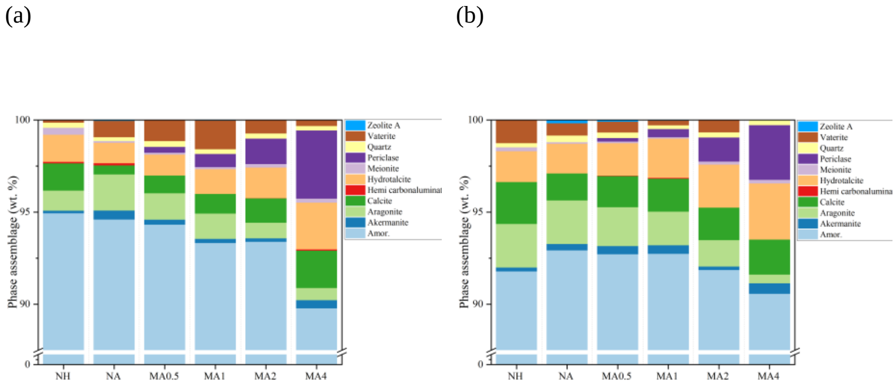

Fig. 5.5 Quantification of XRD of MSAASB at (a) day 7 and (b) day 28.

Small amounts (0.04 wt%) of zeolite A formed in the NA samples at day 7 and reached 0.16 wt% at day 28. This increase is ascribed to more $Al(OH)_4^-$ and $Si(OH)_4$ reacting with Na^+ and OH^- ions. At day 7, MA0.5 and MA1 both contained 0.02 wt% zeolite A, which remained in very low proportions at day 28. No zeolite A was observed in the NH, MA2, and MA4 pastes at any testing age. It was concluded that MgO in the activating system inhibits the growth of zeolite A.

Calcite, aragonite, and vaterite are three polymorphic forms of calcium carbonate. The calcium-carbonate content of the samples range from 2.7 to 4 wt% at day 7. The calcium carbonate partly originates from raw BA materials and partly from the carbonation of the samples. At day 28, the amount of calcium carbonate in the samples is in the range of 3.1~5.9 wt%. The slight increase was caused by carbonation.

5.3.2.2 Thermogravimetric analysis

Fig. 5.6 illustrates the thermogravimetric (TG) curves and the first derivative of the thermogravimetric curves (DTG) as a function of temperature (40 °C to 1000 °C) for the different pastes at days 7 and 28. Table 5.4 shows the relatively mass losses of gel and LDHs.

For the 7-day pastes, the mass loss and DTG changes of NH and MA4, as presented in Fig. 5.6(a) and (b), respectively, are the most obvious among the paste samples. The mass losses of NH and MA4 at 100~300 °C were approximately 6.1 and 7.6 wt%, respectively. This was associated with the decomposition of the C(N)–(A)–S–H gels [184]. It is notable that the decomposition of Hc [259,260] (at ≈150 °C) and the first-step decomposition of Ht [261] (150~250 °C) occur in the same temperature range of the gels. Also, zeolite A decomposes from 40 °C up to 200 °C [262], which is overlapped by the decomposition of the gels. The NA, MA0.5, MA1, and MA2 samples exhibited mass losses of 5.6, 5.5, 5.8, and 5.6 wt% (100~300 °C), respectively. This was mainly associated with the decomposition of bound water in the gels. Simultaneously, small amounts of mass loss result from the decomposition of Hc and zeolite A, along with the first mass loss of Ht, which are also reflected by the XRD patterns and quantification of XRD at day 7. Notably, the increase in the MgO/$NaAlO_2$ molar ratio contributed to the higher content of gels and Ht (100~300 °C). Most of the mass was lost from gels and Ht because extra Mg^{2+} ions accelerated their formation, which is in agreement with the QXRD results. There is only one distinct peak between 365 and 430 °C, which is assigned to Mg–Al LDHs [263]. Therefore, this peak was selected to represent the relative contents of Mg–Al LDHs. The weight losses in this temperature range were 1.3, 0.9, 1.1, 1.2, 1.5, and 2.1 wt% for NH, NA, MA0.5, MA1, MA2, and MA4, respectively. The higher mass losses can be attributed to the higher Ht contents. The extra Mg^{2+} (from MgO incorporation) and $Al(OH)_4^-$ (from the activator) are synergistically beneficial for the generation of Ht. Calcium carbonate, which was derived from the raw BA precursors and carbonated pastes in the form of calcite or other polymorphs, decomposes from 500 °C to 750 °C [154].

Fig. 5.6(c) and (d) illustrate the mass loss and DTG of the 28-day pastes. At temperatures between 100 and 300 °C, the paste samples NH, NA, MA0.5, MA1, MA2, and MA4 underwent mass losses of 7.2, 7.6, 7.8, 8.3, 8.5, and 9.2 wt%, respectively. The Hc and zeolite A contents decrease with a higher MgO/$NaAlO_2$ ratio; the larger mass losses are mainly in the form of bound water in the C(N)–(A)–S–H gels. Combined with the quantification of the XRD results, the formation of Hc and zeolite A was limited to lower than 0.6 wt% between days 7 and 28, while the generation of amorphous gels was appreciably promoted. It can be seen that all the sodium-aluminate-activated pastes exhibited lower contents of the reaction products at 100~300 ℃) than the sodium-hydroxide-activated binder at 7 days. Simultaneously, the amount of Mg–Al LDHs lost during the second-peak range in the samples were 1.3, 1.3, 1.4, 1.6, 1.9, and 2.2 wt% for NH, NA, MA0.5, MA1, MA2,

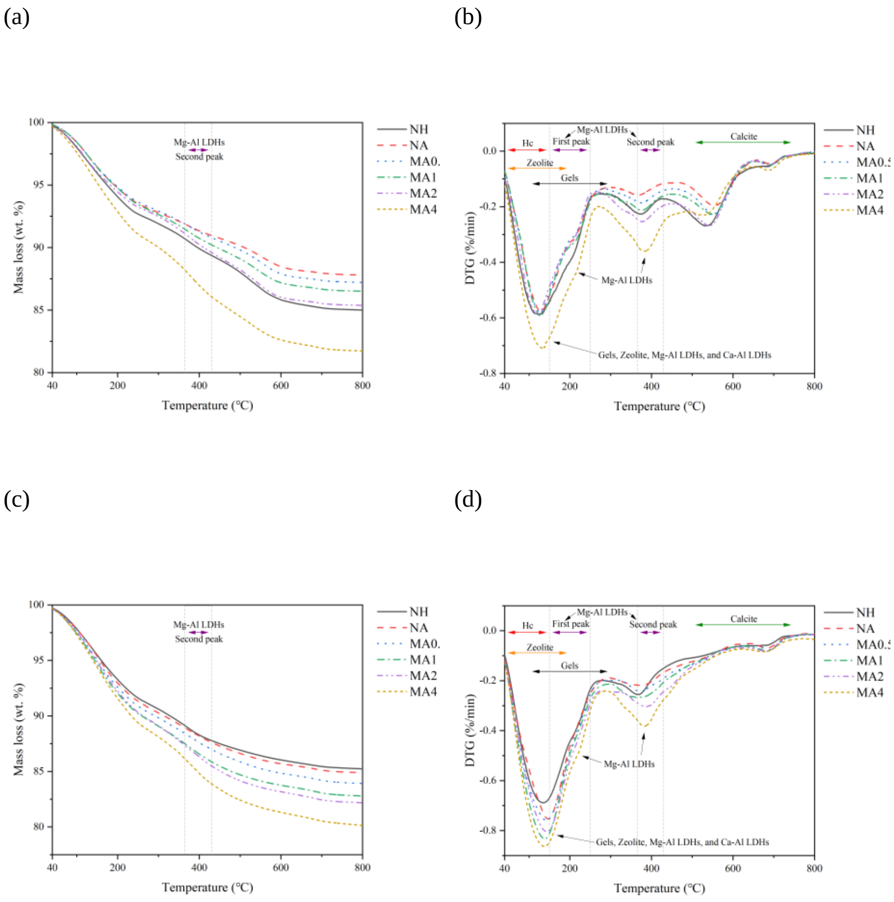

Fig. 5.6Mass loss of MSAASB at (a) day 7 and (c) day 28. b–d) TGA pattern of MSAASB at (b) day 7 and (d) day 28.

and MA4, respectively. Compared with the NH reference samples, the changes in the Mg–Al LDH contents were 0, 7.7, 23.1, 46.5, and 69.2% for NA, MA0.5, MA1, MA2, and MA4, respectively. These results are generally in line with the QXRD results presented in Section 5.3.2.1. The elevated mass losses are associated with higher Mg^{2+} and $Al(OH)_4^-$ concentrations, which are beneficial for Ht formation. Furthermore, the alkaline environment in the pore solution maintained suitable conditions for the extra Mg^{2+} and $Al(OH)_4^-$ to react with OH^- and CO_3^{2-} to produce more Mg–Al LDHs during curing. For the decomposition of calcium carbonate, two peaks at 550 °C and 700 °C are shown for the 7-day pastes, indicating the coexistence of amorphous and crystalline phases. However, the 550 °C peaks were not observed in the 28-day pastes. The high content of amorphous calcium carbonates in the MSAASB pastes at day 7 is associated with the stabilizing effect of MgO [264]. The less stable form of calcium carbonate tends to transform into a more stable form with increasing curing time [265,266]. This is in line with the QXRD results, where more calcite and aragonite were generated between days 7 and 28. Correspondingly, less vaterite was observed with increasing curing age.

Table 5.4 Relatively mass losses of gel and LDHs.

Sample ID	Mass losses of gel (wt. %)		Mass losses of LDHs (wt. %)	
	7 days	28 days	7 days	28 days
NH	6.1	7.2	1.3	1.3
NA	5.6	7.6	0.9	1.3
MA0.5	5.5	7.8	1.1	1.4
MA1	5.8	8.3	1.2	1.6
MA2	5.6	8.5	1.5	1.9
MA4	7.6	9.2	2.1	2.2

5.3.3 Pore structure

5.3.3.1 Nitrogen physisorption of activated pastes

The pore size distribution of the pastes at day 28, as determined by the nitrogen physisorption test, is shown in Fig. 5.7. Mesopores (2–50 nm) and partial macropores (50–200 nm) were also observed.

Fig. 5.7(a) exhibits the pore size distribution of the paste samples. As can be seen, there is a declining trend with increasing $MgO/NaAlO_2$ molar ratio. The peaks corresponding of the pore size of the NA paste were concentrated at ≈20 nm and ≈40 nm, which were also the largest pore voids among the samples. It is clear that lower pore volumes were associated with higher MgO additions. In particular, the incremental pore volume of MA4 is distinctively lower than that of the NH reference paste. This may be because the high MgO content promotes the formation of gels and Ht-like phases. The increased gel content and Ht-like phases refined the pore structure of the matrices. Furthermore, the microstructure is refined by the evolution of phases during the curing period [267]. Additionally, the microstructural refinement can be attributed to the filler effect of the extra-fine MgO powder.

The cumulative pore volumes of the samples is illustrated in Fig. 5.7(b). With a higher MgO/$NaAlO_2$ molar ratio, a lower cumulative pore volume was obtained. In particular, the cumulative pore volume of sodium-aluminate-activated binders was lower than that of the NH reference pastes after 40 nm. Notably, the cumulative pore volume of MA4 was lower than that of NH for all pore-width ranges. The high bulk MgO content resulted in a significant improvement in the microstructure of the sodium-aluminate-activated binders. Sufficient $Al(OH)_4^-$ and Mg^{2+} ions facilitated the generation of gels and Ht-like phases. Meanwhile, the relatively low-pH environment (≈12.8 according to Section 5.3.1) is also suitable for the reaction of the amorphous and crystalline phases.

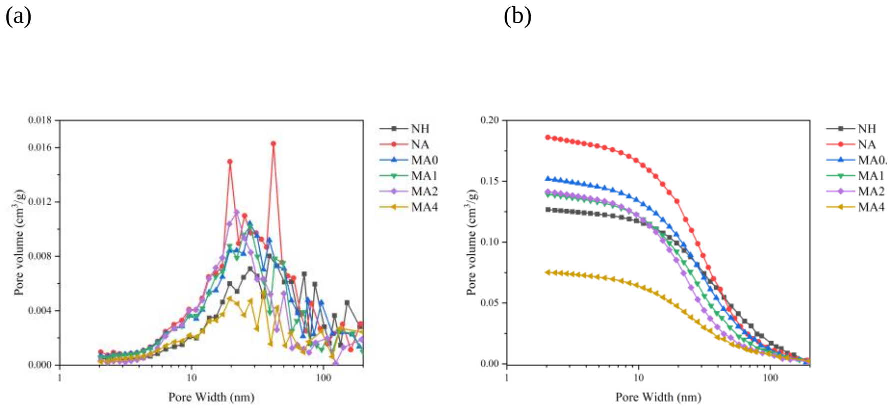

Fig. 5.7 Pore size distribution at day 28: (a) incremental volume and (b) cumulative volume.

5.3.3.2 SEM-EDS mapping of activated mortars

The scanning electron microscopy–energy dispersive spectroscopy (SEM-EDS) maps of the 28-day MSAASB mortars are presented in Fig. 5.8 to further illustrate the effect of MgO on the microstructure, especially the ITZs. Elemental quantification of silicon (Si), sodium (Na), oxygen (O), aluminum (Al), calcium (Ca), magnesium (Mg), and carbon (C) is also presented. The quantitative maps show the differences in the distribution of elements over the SEM mapping graphs.

The most uniform distribution of Na was observed over the particle areas of the samples. Similarly, Si also spreads relatively uniformly over the particle areas, and the sand area is reflected by the high concentrations of Si. The ITZs, which are marked in the graphs (determined from Fig. C1), are affected by the reaction products and their distribution. Specifically, for NA, MA0.5, MA1, MA2, and MA4, the concentrations of Al and Ca increased at the ITZs with an increase in the MgO/$NaAlO_2$ molar ratio. This is attributed to the dissolved Ca^{2+} and $Si(OH)_4$ from GGBS reacting with $Al(OH)_4^-$ (from the activator) to form gels at

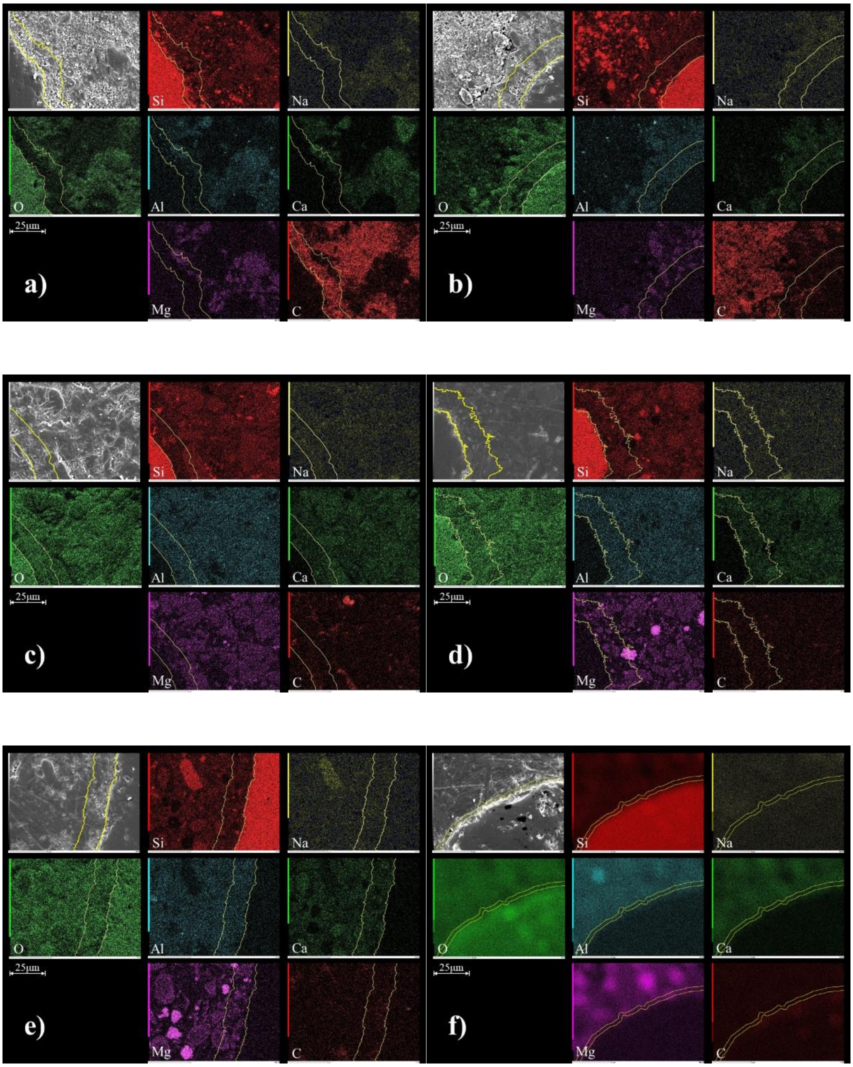

Fig. 5.8 SEM mapping of MSAASB mortars at day 28: a) NH, b) NA, c) MA0.5, d) MA1, e) MA2, and f) MA4.

different curing ages. The geopolymerization process was accelerated by the high concentrations of Mg^{2+} (from additional MgO) in relatively low pH activation system [268,269]. Consequently, the porosity and pore size decreased steadily, which is in agreement with the results presented in Section 5.3.3.1. In addition, the Mg and Al distributions of the MA strongly overlap, which is ascribed to the Mg–Al LDHs. This overlap decreases closer to the aggregate borders. It is noticeable that the ITZ in MA4 exhibits the lowest width among the mortars. The higher the MgO incorporation in the matrix, the more the reaction products fill the pores and cracks; consequently, a denser matrix can be obtained. This is consistent with the QXRD and TG results.

To further investigate this phenomenon, Fig. 5.9 illustrates the Mg/Al, Si/Al, and Ca/Al molar ratios in the ITZs and the porosities of the ITZs and the matrix. It can be seen that MA4 (with the highest Mg/Al ratio) possesses the lowest porosity among the mortar samples. The porosities of the ITZs and the matrices of the activated mortars decreased with an increase in $MgO/NaAlO_2$ ratios. A higher Mg/Al ratio indicates a greater possibility of Mg–Al LDH formation. More free Mg^{2+} ions in the ITZs promoted the formation of Mg–Al LDHs to fill the pores and cracks, which improved the microstructure of the matrix [270]. In addition, the Si/Al ratio increased with the Mg/Al ratio owing to the acceleration of the reaction by the extra Mg^{2+} in the pore solution. In addition, the Ca/Al ratio increased with increasing MgO incorporation. Simultaneously, these trends were also in line with that of the compressive strength, as presented in Section 5.3.5.

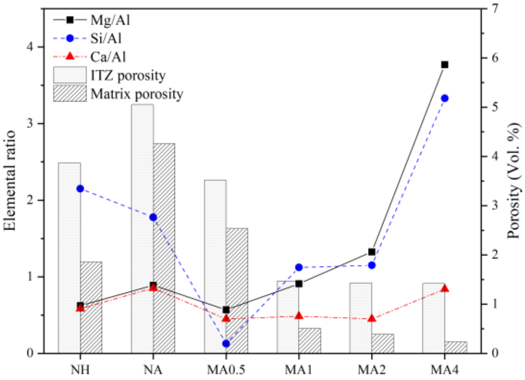

Fig. 5.9 Mg/Al, Si/Al, and Ca/Al molar ratio in ITZs and the porosities of the ITZs and matrices.

5.3.4 Leaching of potentially toxic elements

The initial hazard of the powdered raw materials was evaluated using EN 12457–2. Table 5.5 summarizes the leaching values of raw powdered GGBS and MSWI BA, and the limits were established by the Dutch Soil Quality Regulation (SQR) [271] regarding the acceptable emissions for inorganic species. In the raw GGBS particles, all the metal contents were significantly lower than their corresponding legal values, demonstrating that GGBS can be used directly without potential toxicity issues. However, the contents of Cu, Sb, Cl^-, SO_4^{2-} of MSWI BA were significantly higher than their legal values.

Table 5.6 presents the leached elemental concentration values of the sodium-hydroxide-activated slag paste, sodium-aluminate-activated slag paste, and MA pastes. The alkali-activated GGBS/MSWI BA blends considerably decreased the heavy-metal ion leaching concentration as well as the concentrations of chloride and sulfate ions. The contaminants were highly immobilized by these amorphous gels and crystalline LDHs. In the NH samples, all the ions in the leachate were far below their legal limits. However, high concentrations of Se were observed, which were very close to the legal threshold. This is due to the high pH of the pore solution, which results in a high mobility of Se [272]. Once the sodium aluminate activator was applied, the concentration of Se was significantly reduced by up to 56.03% in MA4 compared to NH. This is attributed to the additional formation of Ht in the MgO–$NaAlO_2$-activated matrix, which led to intense Se absorption [273]. The concentration of Ba declined dramatically, that is, by more than 10-fold. Ba forms insoluble carbonate and sulfate compounds, the high sulfate from BA extremely influences the leaching of Ba. At the same time, the stable pH environment of MSAASB with curing age is beneficial for gel and Ht formation; The elevated gels and Ht formation can effectively immobilize Ba ions, resulting in a lower leaching concentration [274]. In contrast to the leaching ions of raw powdered BA, distinct decreases in Mo, Cl^-, and SO_4^{2-} leaching were observed (Fig. 5.10). Moreover, the concentrations of Mo and SO_4^{2-} decreased with increasing MgO/$NaAlO_2$ ratio in the MSAASB samples. On the one hand, the leaching of Mo oxyanions is assumed to be controlled by the

Table 5.5 Leaching concentration of raw GGBS and MSWI BA (mg/L).

E/I*	GGBS	MSWI BA	Limit	E/I	GGBS	MSWI BA	Limit
Ba	0.075	0.138	22	Sb	0.006	0.401	0.16
Cr	0.030	0.036	0.63	V	0.017	0.003	1.8
Cu	0.002	1.083	0.9	Zn	UDL**	UDL	4.5
Mo	0.007	0.732	1	Cl^-	36.2	3354.4	616
Ni	UDL*	0.009	0.44	SO_4^{2-}	155	7303.3	1730
Se	0.020	0.013	0.15	pH***	11.74	11.40	-

* E/I = Elements or ions

** UDL = Under detection limit

*** pH = pH of leachate

dissolution of Ca-containing minerals [188,230], which is related to the solubility of $CaMoO_4$. Thus, a lower pH environment of the pore solution is beneficial for controlling the leaching of Mo, as a lower pH results in a higher concentration of Ca^{2+}. Meanwhile, a higher concentration of Ca^{2+} ions existed in the pore solution of the larger MgO matrix, as described in Section 5.3.1. Therefore, the high $MgO/NaAlO_2$ ratio favourably reduces the leaching of Mo. In addition, SO_4^{2-} leaching is also influenced by Ca^{2+} derived from the precipitation of anhydrite ($CaSO_4$) or gypsum ($CaSO_4 \cdot 2H_2O$) [272].

Table 5.6 28-day leaching concentrations (mg/L) in MSAASB.

E/I*	NH	NA	MA0.5	MA1	MA2	MA4	Limit
Ba	0.025	0.002	0.002	0.002	0.004	0.011	22
Cr	UDL**	UDL	UDL	UDL	UDL	UDL	0.63
Cu	UDL	UDL	UDL	UDL	UDL	UDL	0.9
Mo	0.077	0.140	0.125	0.109	0.110	0.034	1
Ni	UDL	UDL	UDL	UDL	UDL	UDL	0.44
Se	0.116	0.066	0.054	0.064	0.073	0.051	0.15
Sb	UDL	UDL	UDL	UDL	UDL	UDL	0.16
V	0.089	0.138	0.122	0.107	0.113	0.042	1.8
Zn	UDL	UDL	UDL	UDL	UDL	UDL	4.5
Cl^-	37.802	31.943	33.041	34.275	35.469	44.102	616
SO_4^{2-}	335.589	359.052	274.089	267.540	220.945	166.845	1730
pH***	12.27	12.17	12.35	12.35	12.30	12.36	-

* E/I = Elements or ions

** UDL = Under detection limit

*** pH = pH of leachate

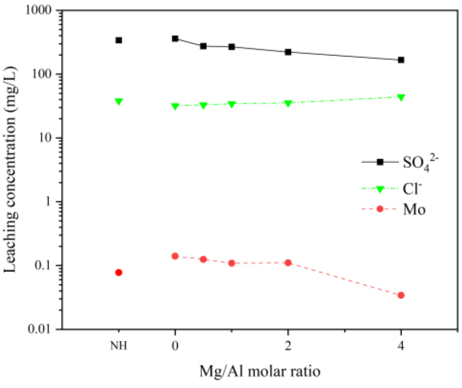

Fig. 5.10 Effect of MgO/NaAlO2 molar ratio on leaching concentrations of SO_4^{2-}, Cl^-, and Mo.

A small proportion (10 wt%) of effective BA content in the binders resulted in low-level leaching of potentially toxic elements via the dilution effect. Therefore, a correction calculation should be performed to account for the leaching contribution of BA. Thus, the coefficient of the dilution effect was used to calculate the final leaching value contributed by BA, as follows:

$$C_{Dilution} = BA / (GGBS + BA + MgO + Water + Activator) \qquad (5\text{-}3)$$

Where $C_{Dilution}$ is the coefficient of the dilution effect, and the unit of all materials is wt%.

Table 5.7 lists the leaching elemental concentration values after correcting the dilution effect as well as the $C_{Dilution}$ values. The results were calculated using the following equation:

$$Con_{BA} = \frac{\text{PTEs concentration}}{C_{Dilution}} \qquad (5\text{-}4)$$

Where Con_{BA} is the leaching value contributed by BA in each paste at day 28, and the leaching concentration refers to that of the potentially toxic elements from the paste samples, as listed in Table 5.6.

Table 5.7 28-day leaching concentrations (mg/L) of MSAASB contributed by BA.

E/I*	Raw BA leaching	NH	NA	MA0.5	MA1	MA2	MA4
Ba	0.138	0.385	0.032	0.032	0.032	0.067	0.190
Cr	0.036	UDL	UDL	UDL	UDL	UDL	UDL
Cu	1.083	UDL	UDL	UDL	UDL	UDL	UDL
Mo	0.732	1.185	2.222	1.984	1.758	1.833	0.586
Ni	0.009	UDL	UDL	UDL	UDL	UDL	UDL
Se	0.013	1.785	1.048	0.857	1.032	1.217	0.879
Sb	0.401	UDL	UDL	UDL	UDL	UDL	UDL
V	0.003	1.369	2.190	1.937	1.726	1.883	0.724
Zn	UDL	UDL	UDL	UDL	UDL	UDL	UDL
Cl^-	3354.4	581.569	507.032	524.460	552.823	591.150	760.379
SO_4^{2-}	7303.3	5162.908	5699.238	4350.619	4315.161	3682.417	2876.638
$C_{Dilution}$	-	0.065	0.063	0.063	0.062	0.060	0.058

* E/I = Elements or ions

** UDL = Under detection limit

As shown in Table 5.7, the leaching of Mo in the NH sample was similar to that of the raw BA. The hydrated gels can absorb some of the Mo ions; however, the high alkalinity of NH results in high leaching of Mo. However, the leaching of Mo decreases with higher MgO content within the MA samples, which is attributed to the enhanced Ca^{2+} generation. Compared with raw BA, the leaching of Cl^- and SO_4^{2-} significantly declined among the samples, which was associated with the absorption of the gels and LDHs. Compared with the NH samples, a higher MgO addition caused a rise in Cl^- leaching and a reduction in SO_4^{2-} leaching in the MA samples. This was attributed to the higher selectivity of LDHs for SO_4^{2-} ions rather than Cl^- ions in the same pore solution. In addition, Se has a higher leaching potential in MSAASB than in the raw BA. The alkalinity of the activated samples increased Se leaching.

5.3.5 Compressive strength

The 3-, 7-, 14-, and 28-day compressive strength of the mortars and the effect of the MgO/NaAlO$_2$ molar ratio on the compressive strength are presented in Fig. 5.11. The NH samples exhibited a compressive strength of 12.22 ± 0.14 MPa on day 3 and up to 21.16 ± 0.96 MPa on day 28 (as shown in Fig. 5.11(a)). However, the NA samples possessed very low strength (<1.88 ± 0.31 MPa) before 14 d. The low content of the reaction products (especially the amorphous gels, as described in Section 5.3.2.2) resulted in a less dense matrix. Nevertheless, comparable strengths of up to 20.75 ± 1.27 MPa were observed on day 28. Large amounts of reaction products were generated in order to develop strength during curing. In addition, the strength increased remarkably between days 14 and 28 in the MA0.5 and MA1 samples. MA0.5 and MA1 show low strengths of ≈2.46 ± 0.08 MPa and ≈6.92 ± 0.31 MPa at day 14, respectively, but high strengths of up to 27.73 ± 1.79 MPa and 29.66 ± 1.76 MPa at day 28, respectively. Additional MgO has also been reported to promote the strength of the alkali-activated matrix [238,275]. This is attributed to the additional MgO accelerating the formation of Ht and Hc gels. Compared with NA, MA0.5 and MA1 exhibited increases of 33.64% and 42.94%, respectively. In addition, at day 28, MA2 and MA4 exhibit the highest strengths of 36.88 ± 1.97 MPa and 37.05 ± 1.46 MPa. In contrast with those of NA, growth rates of 77.73% and 78.55% were obtained for MA2 and MA4, respectively. It should be noted that a higher MgO content improves strength development. The strength developments of MA2 and MA4 are in accordance with the generation of the reaction products (Section 5.3.2). Simultaneously, the strength of the matrices was also in line with the N_2 sorption test and porosity results obtained from SEM-EDS mapping (Section 5.3.3). A higher MgO content leads to a lower porosity, resulting in enhanced ITZs and increased strength.

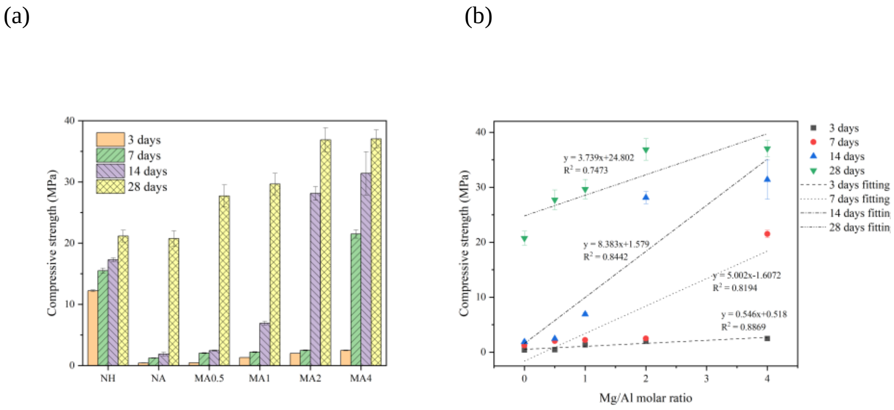

Fig. 5.11 (a) Compressive strength of MSAASB mortars on specific curing days, and (b) the effect of MgO/$NaAlO_2$ molar ratio on compressive strength (excluding the NH sample).

As can be seen from Fig. 5.11(b), the increase in the MgO/$NaAlO_2$ molar ratio strongly promoted the compressive strength before day 14. The acceleration rate of the MgO/$NaAlO_2$ molar ratio on the strength development exhibited a downward trend after 14 d. With the increase in MgO/$NaAlO_2$ molar ratio, the strength increased from 20.75 ± 1.27 MPa to 37.05 ± 1.46 MPa at day 28 in sodium-aluminate-activated matrices.

5.4 Discussion

5.4.1 Impact of Mg^{2+} on reaction products

Knowing the changes in the ions in the pore solution are critical for understanding the formation mechanism of Mg–Al LDHs. The role of Mg^{2+} in the added MgO was investigated in order to understand the sodium-aluminate activation system. The ion concentration of the pore solutions was used along with XRD, QXRD and TGA to provide an in-depth understanding of the in-situ formation of Mg–Al LDHs. A comprehensive comparison of the concentration changes of Na^+, Ca^{2+}, Mg^{2+}, $Al(OH)_4^-$ from CWE (3, 7, 14, and 28 d) using the Mg–Al LDHs profiles from XRD and QXRD (days 7 and 28) is shown in Fig. 5.12.

5.4.1.1 Competition between Mg–Al LDH and Ca–Al LDH formation

The Mg^{2+}/ $Al(OH)_4^-$ molar ratio increased, while the Ca^{2+}/ $Al(OH)_4^-$ molar ratio decreased with a higher $MgO/NaAlO_2$ molar ratio with increasing curing time in the pore solution of the MSAASB pastes (shown in Fig. 5.12). Simultaneously, the XRD and QXRD results at days 7 and 28 demonstrated a significant increase in Mg–Al LDH formation (Ht) with a higher $MgO/NaAlO_2$ molar ratio. Meanwhile, reduced formation of Ca–Al LDHs (Hc) was observed with the increase in MgO addition. Fig. 5.13 shows the dominant mechanism of the extra Mg^{2+} ions on the reaction products of the Mg–Al and Ca–Al LDHs in the sodium-aluminate activation system. The pH environment of the pore solution in the $MgO–NaAlO_2$-activated matrix is stable at ≈12.9 during the curing period. The additional MgO provides sufficient Mg^{2+} in the pore solution; therefore, $Al(OH)_4^-$ favors combination with Mg^{2+} over Ca^{2+} to form Mg–Al LDHs instead of Ca–Al LDHs. Since the solubility product constant of Mg–Al LDHs ($K_{SP} = 10^{-66.58}$ [205]) is much lower than that of Ca–Al LDHs ($K_{SP} = 10^{-29.35}$ [256]), the precipitation of Mg–Al LDHs is easier than that of Ca–Al LDHs in the high-Mg/Ca environment in the Al-rich pore solution. Simultaneously, the saturation of Mg–Al LDHs occurs earlier in an aqueous environment with a higher [Mg] in the pore solution, leading to more precipitation of Mg–Al LDHs. In addition, no evidence of M-S-H was detected in the XRD pattern. This is in line with the results of a previous study that demonstrated the absence of Mg-rich silicate gels (e.g. M-S-H) in high-Mg and high-Al systems [276]. Consequently, the increase in Ca^{2+} concentration after 7 d is due to the suitable pH environment in the pore solution dissolving from the slag particles. Mostly, Ca^{2+} participates in the formation of C–S–H and C–A–S–H gels, while Mg^{2+} is barely incorporated into the silicate gels. Therefore, Mg–Al LDHs tend to be the main secondary reaction products instead of Ca–Al LDHs owing to the increased MgO content.

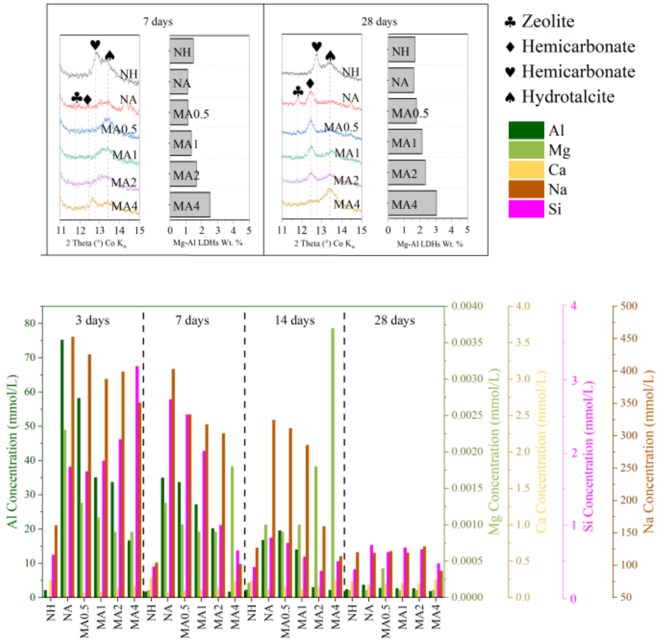

Fig. 5.12 Mg–Al and Ca–Al LDH formation.

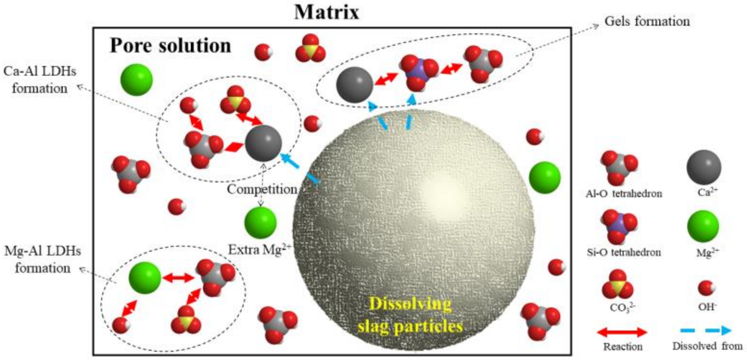

Fig. 5.13 Competition between Mg–Al and Ca–Al LDH formation.

5.4.1.2 Competition between Mg–Al LDH and zeolite formation

Fig. 5.12 also shows the changes in the $Mg^{2+}/Si(OH)_4$ ratio with different $Mg^{2+}/Al(OH)_4^-$ molar ratios. The higher the MgO incorporation, the higher the Mg^{2+}/Na^+ ratio in the pore solution before day 14. However, more Mg^{2+} ions were consumed after 14 d. During this period (14–28 d), most of Mg–Al LDHs were generated, as shown in the TGA patterns. Meanwhile, the presence of zeolite in the XRD patterns increased in the NA samples with curing time. However, the intensity of the zeolite peak decreased with an increase in the $MgO/NaAlO_2$ molar ratio of the raw materials. This is due to the increasing generation of Mg–Al LDHs. In addition, a large amount of Na^+ was consumed to form more N–A–S–H gels after 28 d; therefore, Na^+ decreased with the curing age.

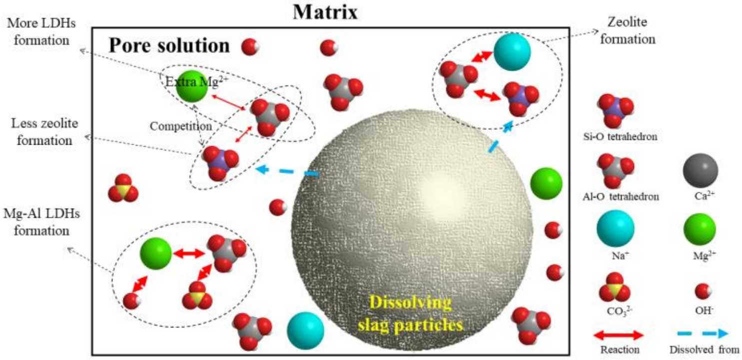

Fig. 5.14 Competition between Mg–Al LDHs and zeolite formation.

The effect of additional Mg^{2+} on the reaction mechanism for the formation of Mg–Al LDHs and zeolites is presented in Fig. 5.14. During curing, Mg^{2+} maintained a high concentration in the pore solution. The available $Al(OH)_4^-$ bonds with Mg^{2+} to form Mg–Al LDHs in a suitably alkaline environment. Less $Si(OH)_4$ reacts with $Al(OH)_4^-$ and Na^+ to form zeolite owing to more $Si(OH)_4$ forming C(N)–A–S–H gels. Consequently, the extra Mg^{2+} from the added MgO wins the competition against Na^+ in the pore solution. Eventually, the pore solution contains low concentrations of $Al(OH)_4^-$ and $Si(OH)_4$. Meanwhile, the low ion concentrations (i.e., [Al] and [Si]) lead to the low crystallinity of sodium aluminosilicate hydrate [257]. The decrease in zeolite formation can be attributed to the low concentrations of $Al(OH)_4^-$ and $Si(OH)_4$. Therefore, amorphous C(N)–A–S–H gels (low-crystallinity reaction products) can be generated by the extra Na^+ reacting with $Al(OH)_4^-$ and $Si(OH)_4$ at late curing ages. Therefore, C(N)–A–S–H is an alternative reaction product to zeolite in a high-MgO-activated system. Simultaneously, the hump in the XRD pattern (Fig. 5.12) represents C(N)–A–S–H-type gels rather than zeolite at day 28.

5.4.2 Impact of Mg^{2+} on toxic element binding by in-situ-formed LDHs

In this chapter, a one-stage batch leaching test was utilized to investigate the impact of MgO dosage on the leaching behavior of MSAASB pastes. It was found that the leaching concentrations of Mo and SO_4^{2-} were mitigated, whereas those of Cl^- slightly increased with higher MgO content in the sodium-aluminate-activated matrix. The effect of Mg^{2+} on the stabilization of MoO_4^{2-}, Cl^-, and SO_4^{2-} from BA in MgO–$NaAlO_2$-activated slag is shown in Fig. 5.15. The higher Mg^{2+} concentration (from extra MgO incorporation) maintained the pH of the pore solution. Therefore, a stable pH environment promoted the dissolution of Ca^{2+} from GGBS during curing (Fig. 5.12). Simultaneously, the extra Mg^{2+} reacts with $Al(OH)_4^-$ to form Mg–Al LDHs, and less Ca^{2+} reacts with $Al(OH)_4^-$, as discussed above. Therefore, more Ca^{2+} was available in the pore solution. Furthermore, higher [Ca] led to the immobilization of MoO_4^{2-} ions via the formation of $CaMoO_4$. Therefore, it is believed that an increase in Mg^{2+} in the pore solution is beneficial for the immobilization of Mo in Ca-rich precursors.

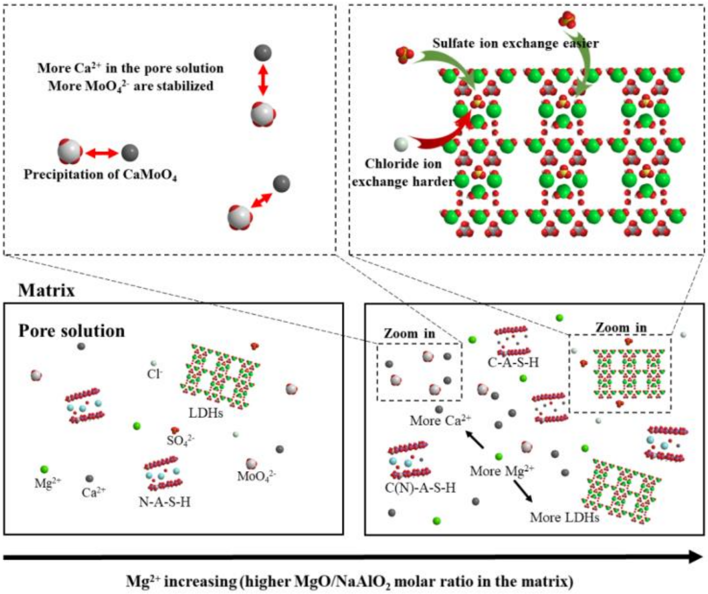

Fig. 5.15 Impact of Mg^{2+} on leaching of MoO_4^{2-}, Cl^-, and SO_4^{2-} from BA in MgO–$NaAlO_2$-activated slag.

At the same time, the extra Mg^{2+} creates more in-situ formation of LDHs in the matrix, which affects the leaching behavior of Cl^- and SO_4^{2-}. The affinity of LDHs for SO_4^{2-} is higher than their affinity for Cl^{-}, so the higher Mg^{2+} concentration results in extra LDH formation; consequently, larger amounts of SO_4^{2-} can be stabilized by the ion exchange of extra in-situ-formed LDHs. However, less Cl^{-} can be stabilized by the ion exchange of LDHs because more SO_4^{2-} occupies the interlayer sites instead of Cl^{-}. Although our hypothesis is statistically supported by the promotion of LDHs formed as a result of MgO–$NaAlO_2$ activation, the leaching of Cl^{-} is higher than that of NH with high MgO incorporation (MgO/$NaAlO_2$ molar ratio > 2). It is noteworthy that MA1 exhibits improved leaching of ions, including Cl^{-} and SO_4^{2-}, and better mechanical properties than NH. Future work should therefore control the MgO/$NaAlO_2$ molar ratio in the sodium-aluminate-activated system to control the in-situ-formed LDHs. Furthermore, this can improve both Cl^{-} and SO_4^{2-} leaching behaviors. In addition, the incorporation of Mg^{2+} promoted the formation of C(N)–A–S–H in the matrix, which also contributed to the higher surface absorption of toxic elements.

5.5 Conclusions

With this chapter, it is attempted to understand the effect of the MgO/$NaAlO_2$ molar ratio on MSAASB, with the objective of improving the heavy-metal binding capacity of in-situ-formed LDHs. The investigation showed that MgO incorporation maintains the low-pH environment of the pore solution. The additional Mg^{2+} (from MgO powder) and $Al(OH)_4^{-}$ ions (from the $NaAlO_2$ activator) synergistically promoted the formation of Mg–Al LDHs. From the results and discussion presented above, the following conclusions can be drawn.

- MSAASB showed a significant amount of Mg–Al LDH formation reaching 2.61 wt% (ref. sample is 1.6 wt%) at day 28. Meanwhile, the higher MgO/$NaAlO_2$ molar ratio accelerates the formation of Mg–Al LDHs and gels under relatively low-pH environments (12.80~12.95). Higher MgO incorporation transfers the secondary reaction products from Ca–Al LDHs and zeolite to Mg–Al LDHs.
- The microstructure was evidently improved by higher incorporation of MgO. An MgO/$NaAlO_2$ ratio of 4 resulted in the lowest porosity and best mechanical properties. Moreover, the rate of strength growth was accelerated by a higher MgO/$NaAlO_2$ ratio.
- The additional MgO provides extra Mg^{2+}, promoting the reaction between Mg^{2+} and $Al(OH)_4^{-}$, reducing the reaction between Ca^{2+} and $Al(OH)_4^{-}$. Meanwhile, less $Al(OH)_4^{-}$ reacts with Na^{+}, resulting in less zeolite formation. Mg–Al LDHs tend to be the predominant LDHs (rather than Ca–Al LDHs) in the sodium-aluminate-activated system. Furthermore, zeolite production is impeded by an aqueous environment rich in Mg^{2+}.
- Heavy-metal leaching was significantly decreased by the incorporation of MgO. A lower leachable Mo concentration was obtained owing to the increased formation of $CaMoO_4$. The leaching of SO_4^{2-} decreased dramatically, and the in-situ-formed LDHs absorbed more SO_4^{2-} than Cl^{-} with elevated MgO addition, owing to the high affinity of LDHs for SO_4^{2-}.

Chapter 6 Utilization of waste glass in alkali activated slag/fly ash blends: reaction process, microstructure, and chloride diffusion behavior

This chapter aims to investigate the chloride diffusion behavior of alkali activated slag and fly ash blends with different contents of waste glass powder (GP) addition. The reaction heat flow of alkali activated slag / fly ash / waste glass is characterized. The reaction products are determined by X-ray diffraction (XRD) and thermogravimetric analysis (TGA). N_2 adsorption analysis (BET) is used to evaluate the microstructure of samples. The accelerated chloride penetration test (ACPT) is applied to study the chloride resistance of the AAMs. Subsequently, the leaching test of chloride penetrated samples are conducted and ion chromatography (IC) is utilized to measure the chloride content in the samples. According to the BET results, the total volume of mesopores decreases with increasing GP content. The results of ACPT show that the increasing GP in AAMs shows an enhancement of chloride resistance.

This chapter is partially published elsewhere:

T. Liu, Q. Yu, H.J.H. Brouwers, Utilization of waste glass in alkali activated slag/fly ash blends: reaction process, microstructure, and chloride diffusion behavior, Journal of Sustainable Cement-Based Materials. doi: 10.1080/21650373.2022.2082577.

6.1 Introduction

Alkali activated materials (AAMs) are regarded as potential alternatives to substitute ordinary Portland cement (OPC) due to their sustainability and high resistance to chemical attacks [277]. In the past decades, the utilization of ground granulated blast-furnace slag (GGBS) and fly ash (FA) showed tangible value towards environmental concerns as the replacement of cement [278]. Meanwhile, waste glass powder (GP) was generated in large amounts worldwide [279]. However, the low recycling rate of GP led to the large amount of GP disposed into landfills [280]. The alkali activation of GP showed a promising opportunity in previous studies [280,281]. Moreover, alkali activated GGBS, FA, and GP have been intensively investigated [66,282]. The reaction process, mechanical properties, and shrinkage of alkali activated GGBS/FA/GP have been determined [283–285]. While long-term durability is important to evaluate the performance of building materials, especially the resistance to chloride penetration [286]. The mechanism of alkali activated slag/fly ash with the blending of additional GP is still insufficient in terms of chloride transport, it limits the application of waste glass in AAMs.

Chloride resistance is one of the critical properties for cementitious and alkali activated materials, since chloride penetration may result in the corrosion of steel bar [287–289]. The microstructure influences the chloride ion diffusion process in the matrix, for example, the chloride transport route and chloride absorption of micropores in the materials [290]. Liu et al. [66] investigated the chloride binding capacity of high volume waste glass in cement-based blends. The chloride migration coefficient decreases with higher waste glass content, resulting in enhanced chloride resistance. Puertas et al. [291] used waste glass as an activator to prepare alkali activated slag, the results showed that the strength and microstructure were comparable to $NaOH/Na_2CO_3$ activated slag. A small amount of waste glass particles incorporation yielded the dense microstructure of concrete by the gel formation of waste glass activation [292]. The participation of waste glass powder refines the microstructure, subsequently, enhances the mechanical performance and durability of cementitious materials. However, because of limited investigations in the mechanism of long-term durability in terms of the GP addition, especially the chloride transport mechanism of GP blended AAM binders is still not clear.

The wide range in the pore size distribution of AAMs is an important feature to evaluate the porosity and tortuosity [293,294]. Furthermore, the pore structure strongly influences chloride transport in the matrix. Previous studies have summarized how the waste glass influences the reaction process and, subsequently, the microstructure. The Krstulovic-Dabic model was used to describe the influence of waste glass powder on hydration kinetics including the nucleation and crystal growth (NG), interactions at phase boundary (I), and diffusion (D) [295]. The NG process guarantees the early development of microstructure while the I and D process supplies the subsequent microstructure evolution [296]. Briefly, hydration behavior is the key factor of microstructural development.

The major compositions of waste glass are Na_2O, CaO, and reactive SiO_2 [291,297]. The additional reactive SiO_2 resources in waste glass has the potential to promote gel formation and improve the microstructure. Consequently, the mechanical properties and chloride resistance can be improved [298]. Puertas et al. [299] reported that the major reaction products of activated waste glass are Si-high, Al- and Ca low gels. The calcium aluminosilicate hydrates (C−A−S−H), and sodium aluminosilicate hydrates (N−A−S−H) predominated the gel formation in the alkali activated waste glass matrix. The calcium aluminosilicate hydrates (C−(A)−S−H) grew on the surface of some crystals showing the homogenous status [300]. Meanwhile, the fan-like texture of the gel was about 3 nm or lower in their dimension. The evolution of microstructure was influenced by the formation of reaction products, especially on the mesopores (2 ~ 50 nm) scale [300]. Overall, hydration products, reaction processes, and microstructure should be profoundly investigated to discuss the mechanism of chloride transport in alkali activated slag/fly ash incorporating GP. Since these important parameters influence the chloride transport and lacks in-depth investigation.

This chapter aims to investigate the chloride transport mechanism of alkali activated slag/fly ash/waste glass blends. The reaction heat flow is determined to study the reaction kinetics, meanwhile, the reaction products are characterized. The microstructure and chloride diffusion are investigated. Furthermore, the chloride transport in the pore structure is discussed based on the experimental results. The addition of waste glass is proved to enhance the chloride resistance of AAMs.

6.2 Materials and methods

6.2.1 Starting materials

Ground granulated blast-furnace slag (GGBS), fly ash (FA), and waste glass powder (GP) were utilized in this chapter. The mixed color glass fractions were collected by a glass recycling plant and ground into GP by ball milling. The chemical compositions were determined by X-ray fluorescence (XRF), as shown in Table 6.1. The X-ray diffraction graphs of GGBS, FA, and GP utilized in this chapter are shown in Fig. 6.1.

The particle size distribution (PSD) of the powder feedstocks were determined by laser granulometry, using Master Sizer laser granulometer with an open measuring cell. The preparation of the powders was done by wet dispersion in deionized water. The particle size distribution of GGBS, FA, and GP are shown in Fig. 6.1(d). The D_{50} particle sizes of GGBS, FA, and GP are 16 μm, 27 μm, and 28 μm, respectively.

The activator used in this chapter was the 4 mol/L sodium hydroxide solution. The analytical grade sodium hydroxide pellets (99% purity) were dissolved in deionized water. And the activator was prepared 24 hours before it was used to cast pastes and mortars.

Table 6.1 Chemical composition and physical properties of waste glass, GGBS, and Fly ash.

Chemical composition	GP (wt. %)	GGBS (wt. %)	FA (wt. %)
Na_2O	14.7	/	/
MgO	1.3	8.6	1.1
Al_2O_3	1.9	13.3	27.2
SiO_2	68.7	29.6	51.8
SO_3	0.1	2.7	1.1
K_2O	0.7	0.4	1.9
CaO	12.0	43.0	5.9
TiO_2	0.1	1.5	1.8
MnO	/	0.4	0.1
Fe_2O_3	0.4	0.4	8.3
P_2O_5	/	/	0.9
Cl	0.1	/	/
LOI* (1000℃)	1.36	1.25	2.24
Specific density (g/cm^3)	2.52	2.96	2.38
BET Specific surface area (m^2/g)	0.99	0.37	0.82

*LOI = loss on ignition at 1000 °C

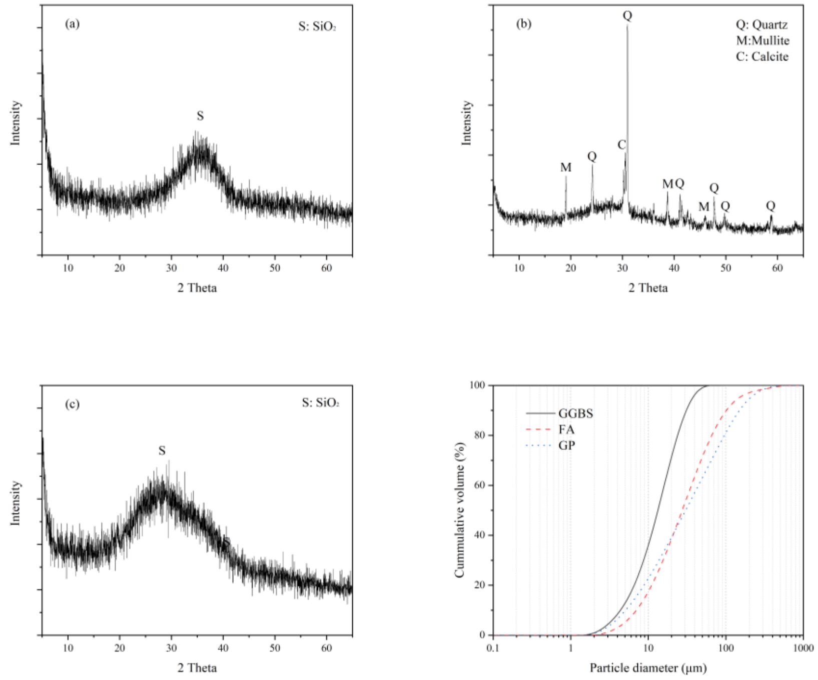

Fig. 6.1X-ray diffractogram of (a) GGBS; (b) FA; (c) GP; (d)The particle size distribution of GGBS, FA, and GP.

6.2.2 Sample preparations

The GGBS / FA weight ratio of AAM is 7:3, while the waste glass powder (GP) replaces the fly ash in AAMs from 10 wt. % to 30 wt. % (see the sample IDs in Table 6.2), so the GGBS / (FA + GP) weight ratio is constantly 7:3. The starting raw materials were mixed with the designed proportion in the concrete mixer following the preparation procedure suggested by EN 196-1 [104]. The mortars were produced by adding sand, and (GGBS + FA + GP) / Sand = 1/3. Mortar samples for mechanical testing were cast in the 40 mm × 40 mm × 160 mm prism mold followed by the vibration. While the mortar samples for chloride diffusion were cast in Ø 100 mm × 200 mm cylinder mold followed by the vibration. After 24 hours, the pastes and mortars were unmolded and were sealed by plastic cover. Then, samples were warped in plastic film to prevent moisture losses in the ambient temperature (20℃) until the age of 28 days. The chemical composition of different sample binders can be calculated, and the Al/Si, Na/Si, and Na/Al molar ratios of Ref, GP10, GP20, and GP30 are presented in Table 6.3.

Table 6.2 Formulations of the mortar samples.

Sample	L/S ratio*	NaOH (mol/L)	GGBS (wt. %)	FA (wt. %)	GP (wt. %)
Ref	0.4	4	70	30	0
GP10	0.4	4	70	20	10
GP20	0.4	4	70	10	20
GP30	0.4	4	70	0	30

*L/S ratio = liquid to solid ratio

Solid = Weight (GGBS + FA + GP)

Table 6.3 The elemental molar ratio of samples (without activator).

Sample	Al/Si	Na/Si	Ca/Si	Na/Al	Mg/Al
Ref	0.3	0	0.9	0	0.9
GP10	0.2	0.1	0.9	0.3	1.1
GP20	0.2	0.1	0.9	0.8	1.3
GP30	0.1	0.2	0.9	1.5	1.7

6.2.3 Testing methods

Isothermal calorimetry

The heat flow of the samples with different precursors was measured by isothermal calorimetry set at 20℃ (TAM AIR Calorimetry). It was noteworthy that the initial 45 minutes after mixing could not be measured due to the sample preparation procedure and deviation. The results were normalized by the mass of the solids.

X-ray diffractometry

X-ray diffractometry (XRD) was performed by using the Bruker D4 Phaser instrument with Co-Kα radiation (40kV, 30mA). The pressed powdered specimens were measured with a step size of 0.05° and a counting time of 1s/step, from 10° to 90° 2θ.

Thermogravimetry

The Thermogravimetric (TG) test was conducted by using the STA 449 F1 instrument, at a heating rate of 10 ℃/min, to samples of ≈ 100 mg. Experiments were carried out from 40 ℃ to 1000 ℃, during the test process, the gas N_2 was used as the carrier gas.

Nitrogen adsorption test

The nitrogen sorption tests were conducted by TriStar II 3020, Micromeritics. The pore size distribution was carried out by the Barrett, Joyner, and Halenda (BJH) method [105] from the desorption branch. Before the test, 28-day paste samples were ground to powder and the samples were immersed in the 2-propanol for 24h to stop the hydration process, then dried to constant mass at 60℃ for 3 days in the drying oven.

Accelerated chloride penetration test

The Ø 100 mm × 200 mm cylinder mortars were cast and cut into 100 ± 2mm thick slices. The accelerated chloride penetration test (ACPT) procedure was followed by NT Build 443 [301]. The cylinder mortars were sealed by the paraffin wax on the side and bottom surfaces, and the top surface was not sealed for exposure to the NaCl solution. An aqueous NaCl solution was prepared with a concentration of 165 g ± 1 g NaCl per dm^3 solution. The temperature of the water bath was 21-25 °C with a target average temperature of 23 °C. The container was completely filled with the exposed liquid and closed tightly. The exposure lasted for 5 weeks, and the container was shaken once a week. The cylinder mortars and NaCl solution containers are shown in Fig. 6.2.

Fig. 6.2 Accelerated chloride penetration test: (a) AAM samples; (b) Immersed set-up.

The apparent chloride diffusion was obtained by fitting as follow.

$$C(x,t)=C_s-(C_s-C_i)\cdot\mathrm{erf}\left(\frac{x}{\sqrt{4\cdot D_e\cdot t}}\right) \tag{6-1}$$

Where $C(x,t)$ is the chloride concentration, measured at the depth x, at the exposure time t in mass %. C_s is the boundary condition at the exposed surface in mass %. C_i is the initial chloride concentration measured on the concrete slice at time t = 0 in mass %. X is the depth below the exposed surface in m. D_e is the effective chloride transport coefficient in m^2/s. t is the exposure time in second. Erf is the error function defined as follow.

$$\mathrm{erf}(z)=\frac{2}{\sqrt{\pi}}\int_0^z \exp(-u^2)du \tag{6-2}$$

Leaching - Ion Chromatography

The chloride content of samples after ACPT was determined by combining leaching and ion chromatography (IC) tests. The powder samples were drilled after ACPT by depth from 1 ~ 5 cm, and the thickness of every layer was 1 cm. The leaching tests were performed with demineralized water on materials with a particle size < 4 mm and at a liquid to solid ratio of 2/l. The process of one batch leaching test was followed by EN 12457 part 1 [302]. In the leaching step, the contact time was 24 hours. After the leaching test, the leachate of the solution was filtrated through a 0.45 μm filter.

The concentration of chloride in powder samples was analyzed by ion chromatography (Dionex 1100) equipped with an ion-exchange column AS9-HS (2×250 mm). The leachate of the solution was used to determine the chloride ion concentration. The accuracy of chloride determination by the leaching-Ion Chromatography method had been proved by a previous study [303].

6.3 Results and discussion

6.3.1 Reaction kinetics

The typical reactions stages of AAMs are a) destruction-coagulation, b) coagulation-condensation and c) condensation-crystallization [106]. The first reaction heat peak corresponds to a) destruction-coagulation, while the second peak corresponds to b) coagulation-condensation. The time to reach the reaction peak (TRRP) is defined as the time to reach the second heat peak, and it is the gelation process in AAM systems. The normalized reaction heat flow by mass, normalized peak intensity by mass, and TRRP of AAMs are shown in Fig. 6.3. With a higher content of waste glass powder replacement, the reaction heat peak height is slightly increasing, while the TRRP decreases.

Fig. 6.3(a) and Fig. 6.3(b) show that the normalized reaction heat heights of the AAM pastes are close to each other. The slight differences can be seen from Fig. 6.3(b). The waste glass-based binder (GP30) takes a shorter TRRP by 0.2h than the reference paste. The high amount of fly ash can reduce the Ca^{2+} ions in the pore structure of the system, thereby prolonging the induction period [297,304]. Oppositely, the reactive SiO_2 in waste glass powder increases the total content of SiO_2 in the matrix, thus the dissolution process of Si-O and Al-O tetrahedrons in waste glass-based blends could be faster than the fly ash-based blends [305]. Furthermore, the normalized peak height is also increased by the increasing content of waste glass powder replacement. The decreasing reactive Na/Si molar ratio and increasing Na/Al molar ratio both influence the total peak height positively. While, the slight differences are due to the physical effect of GP particle size, which influences the dissolution of reactive SiO_2 in waste glass powder [306,307].

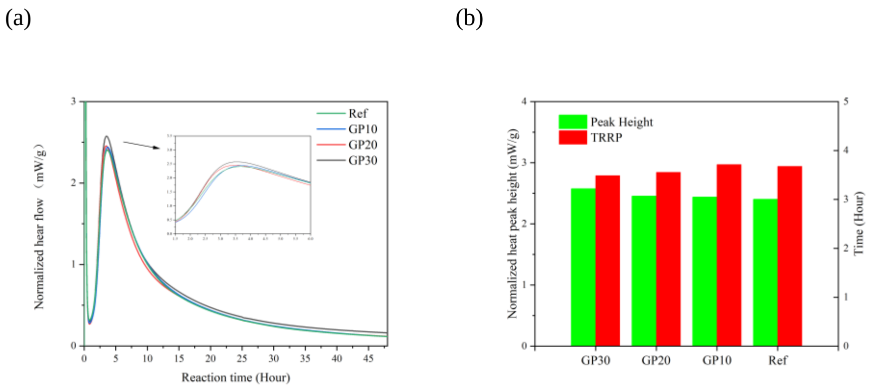

Fig. 6.3(a) Normalized heat evolutions of paste mixtures by sample mass; (b) Normalized peak height by sample mass and time to reach the reaction peak.

6.3.2 Reaction products

6.3.2.1 X-ray diffraction

The XRD pattern is presented to investigate the effect of GP additions in GGBS / FA based matrices. The reaction products of specimens after 28 curing days are presented in the X-ray diffraction patterns (Fig. 6.4).

In all AAM samples, the Calcium silicate hydrates (C−S−H) is predominantly amorphous gel. The intensity of C−(A)−S−H is similar among the AAM samples, which can be explained by the fact that the large proportions of GGBS predominate the alkali activation process. The characteristic peak of C−(A)−S−H is found at 33.9°, corresponding to (PDF# 00-006-0010). The C−(A)−S−H is the reaction product of alkali activated GGBS dominated matrices, which is in agreement with previous studies [238,282]. The lack of Al resource from the precursors drives the reaction products a silicon-high gel [308].

For the secondary reaction product of alkali activated GGBS, the characteristic peak of hydrotalcite (Mg-Al layered double hydroxides) is observed at 13.360°[238], which is consistent with (PDF# 00-014-0191). Hydrotalcite is found in all AAM samples, and the intensity of hydrotalcite is constant with diverse GP content in pastes. The dilutions of FA and GP shows similar results, thus the additional Si-O tetrahedral from GP has little impact on the 28-day paste samples in terms of hydrotalcite formation. The reaction process is predominated by GGBS, and the hydrotalcite is provided by the alkali activation of GGBS. Thereby, the additional reactive Si from GP has limited effect on hydrotalcite content.

The Calcium Aluminum Oxide Carbonate Hydroxide Hydrate (PDF# 00-041-0221) is denoted as Calcium hemicarboaluminate (Hc) [154]. The Calcium hemicarboaluminate is observed within all pastes. The hydroxides-activated slag favors forming the crystalline phase calcium hemicarboaluminate and hydrotalcite together [154]. Because the Al-rich slag provides a suitable environment for calcium hemicarboaluminate formation [309].

Calcite (PDF# 01-086-2343) is attributed to the carbonation of pastes. The calcite formation is not influenced by the GP content in the matrix. Meanwhile, the quartz and mullite gradually disappear with the higher replacement of GP in the matrix since the quartz and mullite are mainly provided by the FA.

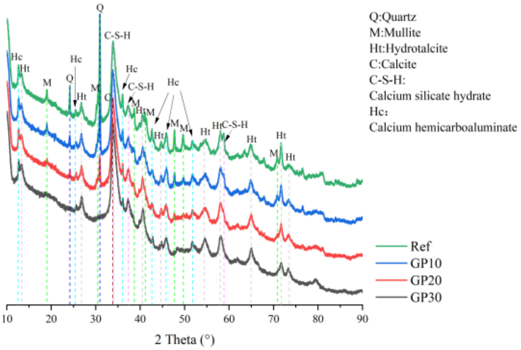

Fig. 6.4 XRD pattern of GGBS/FA paste mixtures with different GP replacement at 28 days.

6.3.2.2 Thermogravimetric analysis

The thermogravimetric (TG) and differential thermogravimetric (DTG) curves of the paste samples at 28 days are presented in Fig. 6.5. The samples show significant mass loss (Fig. 6.5 (a)) from 40 ℃ to 1000 ℃. The mass loss is attributed to the decomposition of C−(A)−S−H gels, hydrotalcite, and calcite (from carbonation). With higher GP content, the total mass loss reaches a higher value attributed to more hydrate formation. As shown in Section 6.3.2.1, the low-reactivity crystalline content (quartz and mullite) decreases with higher incorporation of GP, thus the reaction mass loss shows the highest in GP30 and the lowest in Ref.

Fig. 6.5(b) shows the differential thermogravimetric (DTG) curves of 28-day paste mixtures. Most of the mass loss of the samples is around 100 ℃ to 300 ℃. It is due to the mass loss of free water and the decomposition of C−(A)−S−H gel ranging from 100 ℃ to 300 ℃ [310]. Hydrotalcite is also found among all samples around 380 ℃ [311]. On contrary, previous studies show that with a higher content of GP in the AAMs, the hydrotalcite phase disappears gradually. However, the fineness of GP in the AAM samples performs a significant role in this chapter. Normally, the granulation of GP material reaches below 5 μm, and the raw material shows a distinct diverse property [312,313]. The extra Si-O tetrahedral may dissolve in pore solution at a very early reaction period. The extra Si-O tetrahedral consume a large quantity of Al in pore solution, then the small amount of Al interacts with Mg^{2+} forming hydrotalcite (low content) [18]. However, the median particle size of GP in this chapter is 28 μm. The large amounts of coarse GP particles are difficult to dissolve in the pore solution at early reaction time, the insufficient Si-O tetrahedral reacts with Al, thus the hydrotalcite still survives in the matrix. Besides, the predominant GGBS content controls the hydrotalcite formation. Thereby, the hydrotalcite content shows similar content among the samples. The calcite phase is observed at around 650 ℃ and 750 ℃ [310], the AAM pastes are easy to face the carbonation issue because of their high pH pore solution [314].

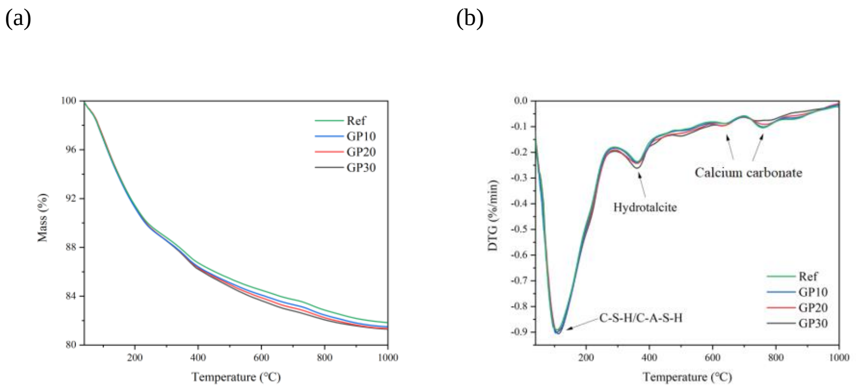

Fig. 6.5(a) Thermogravimetry (TG) curves of paste mixtures at 28 days; (b) Differential thermogravimetry (DTG) curves of paste mixtures at 28 days.

6.3.3 Microstructure

The pore size distribution of AAM samples is presented in Fig. 6.6(a), and the cumulative pore volume is presented in Fig. 6.6(b), by using N_2 adsorption testing. The pore structure is divided by the pore size: micropores (< 2 nm), mesopores (2 ~ 50 nm), macropores (50 ~ 7500nm) and megapores (> 7500 nm) [315]. In Fig. 6.6, all the paste samples show similar trends, i.e. with a higher dosage of GP, the entire matrix tends to form a denser and more homogeneous system.

As seen in Fig. 6.6(a), the paste samples obtain the most mesopores, concentrating on 4 nm. The higher content of GP addition significantly helps to decrease the pore volume. This is consistent with XRD and TG results because the outer-product pores of C−(A)−S−H normally concentrate on 3 ~ 5 nm [300,316], the more gelation in the matrices, the more pores appear at this range. The gelation of C−(A)−S−H fills the large mesopores of the matrix, while the dissolution of hollow FA makes more pores from precursor exposure [317]. The fewer FA contents, the denser microstructure with higher GP contents. Thus, the porosity of AAM samples decreases with the GP addition.

Among the samples, the second peak concentrates around 40 ~ 50 nm, at the end of the mesopores size range. Previous studies [95,123] demonstrate that the mesopores are important while parameters influencing the water penetration and ion transport in the matrix. From Fig. 6.6(a), the second pore-concentration peak also decreases with the content of GP additions. Likewise, the total mesopores decrease. Therefore, it can be concluded that the microstructure is refined with a higher content of GP samples.

The difference in the cumulative pore volume of AAM samples is illustrated in Fig. 6.6(b). The refinement of mesopores is shown distinctly with the GP addition. The higher GP content decreases the cumulative pore volume. First, the reactive GP promotes the gelation in the matrix, the pore is filled with gel products and the pore structure is refined. Simultaneously, the unreacted GP participates in the late reaction process, which means more gels will form in the later age of samples [310]. Thereby, the volume of pores will be gradually filled by the late formation of gels, and the matrix tends to become denser and has a higher capacity to prevent water penetration and ion transport.

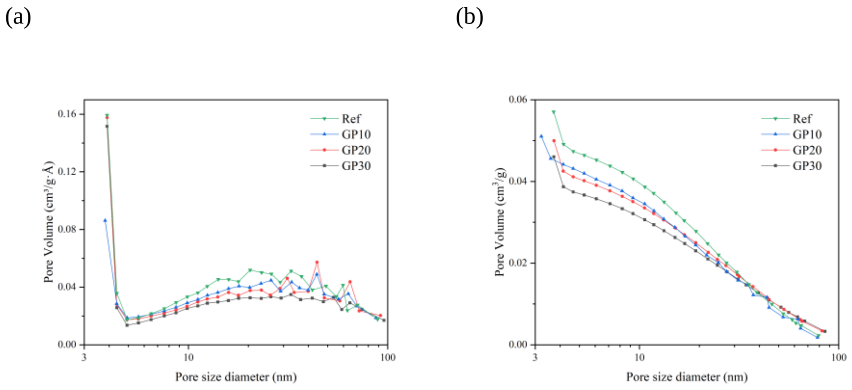

Fig. 6.6 (a) The pore size distribution of AAM pastes; (b) Cumulative pore volume of AAM pastes.

6.3.4 Chloride diffusion

Table 6.4 shows the results of chloride ions immobilized in the AAM mortars after an accelerated chloride penetration test (5 weeks immersion of sodium chloride solution). The results show that chloride content decreases dramatically with the depth of samples. Simultaneously, the chloride ion content decreases with the GP incorporation.

Table 6.4 Chloride leaching results of AAM mortars in different depths to exposure surface (unit: mg/mL).

Depth	GP30		GP20		GP10		Ref	
	Cl content	Std Dev*	Cl content	Std Dev	Cl content	Std Dev	Cl content	Std Dev
1 cm	241.2	0.8	288.0	0.9	286.9	1.7	259.8	1.2
2 cm	13.2	0.3	20.8	0.7	26.1	0.1	32.3	0.4
3 cm	12.4	0.3	16.5	0.4	15.3	0.1	19.9	0.3
4 cm	9.5	0.3	13.1	0.2	12.2	0.3	23.0	0.3
5 cm	8.4	0.1	9.6	0.3	11.4	0.1	10.1	0.0

*Std Dev: Standard Deviation

In Fig. 6.7, the chloride concentration at different drilled depths is presented. The non-linear regression curves are presented as well. Among all mortar samples, the GP30 shows the highest chloride resistance. With the higher replacement of FA by GP, the mortar samples show lower chloride mass concentration in the samples. Meanwhile, along with the depth of mortar samples, the chloride concentration shows lower with higher GP content in AAMs. The GP30 shows the lowest chloride concentration at 48.2%, 2.6%, 2.5%, 1.9% and 1.7% mass per 0.001 gram dry samples in 1 to 5 cm, respectively. While the Ref has 52%, 6.4%, 4%, 4.6% and 2% mass per 0.001 gram dry samples in 1 to 5 cm, respectively. Comparing the GP30 and Ref samples, the chloride concentration decrease by 7.3%, 59.4%, 37.5%, 58.7% and 15% from 1 to 5 cm depths, respectively. Simultaneously, the GP10 and GP20 show the approximately linear interpolation between GP30 and Ref samples (a few points present discrete features). The chloride resistance becomes higher with the increasing GP replacement in AAM mortars. Like previous studies, the chloride binding capacity is attributed to the binding of gels and hydrotalcite in this investigation [318].

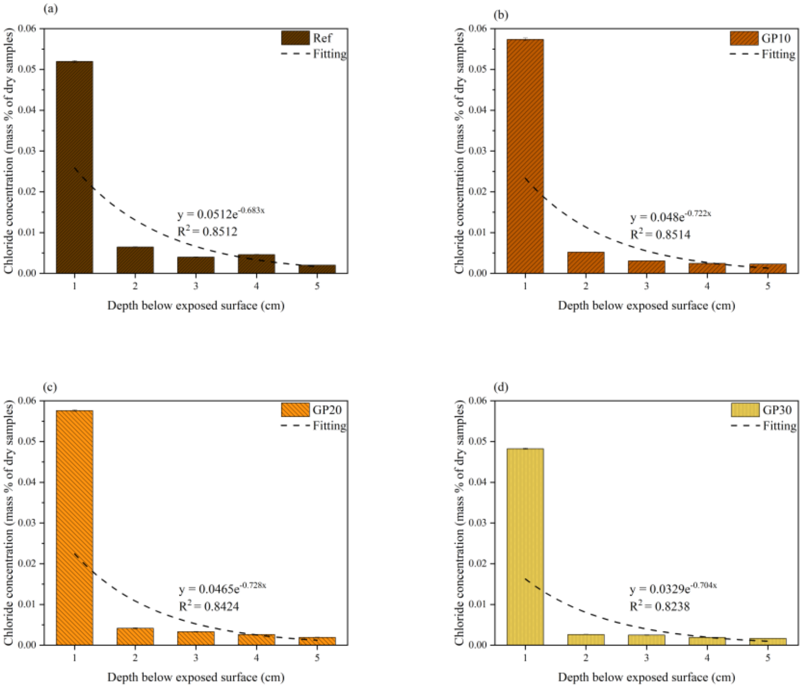

Fig. 6.7 Chloride penetration of AAMs mortars (a) Ref; (b) GP10; (c) GP20; (d) GP30.

Table 6.5 Apparent chloride diffusion coefficients of AAMs mortars.

Sample ID	D_e ($\times 10^{-12}$ m^2/s)	C_s (mass %$_{00}$)	C_i (mass %$_{000}$)	SSE*100000*
Ref	28.3	5.1	0	5.2
GP10	25.4	4.8	0.1	4.4
GP20	22.4	4.7	0.2	4.9
GP30	20.4	3.3	0.3	3.2

* Sum of square errors

Table 6.5 summarizes the parameters for calculating the apparent chloride diffusion D_e coefficient according to NT Build 443 [301]. The results show that as the GP content increased, the chloride diffusion coefficient decreased. Compared GP30 with the Ref sample, the higher

GP contents contribute to the hydration of AAMs, therefore, more gel formation leads to a denser pore structure. At the same time, fly ash based geopolymers had been proved low in chloride binding capacity [319]. Thus, more FA content results in a higher chloride diffusion coefficient of the Ref sample.

Furthermore, the physical chloride absorption is mainly attributed to C−(A)−S−H gels in the matrix. First, with more gelation, the matrix becomes denser. The micropores locate at 3 ~ 5 nm which is influenced by the gel formation [300,316]. Concurrently, the results of BET show that, with higher GP content, the matrix favors to form more gels and becomes much denser. The denser matrix may be due to more gelation and the use of GP with smaller particles (verification is supported by Fig. 6.1). The majority of pores in the matrix are mesopores, and mesopores govern the chloride transport in the matrix [238,320]. Thus, the chloride concentration becomes lower in high GP replacement mortars, because of the lower content of mesopores. Moreover, the tortuosity becomes more complicated with higher substitution of GP. As shown in Fig. 6.8, chloride transport is influenced by the hydration of GP. When the chloride ion contacts the GP hydrates surface, the transport route is affected by the gels, and chloride transport along with the surface of hydrated GP, and it takes a longer time to penetrate the matrix. While the hydrated FA exposes the hollow structure and cracking leading to an easier chloride transport state [321,322]. The high mesopores and high level of pore network interconnectivity (because of FA cracking) also lead to a high chloride transport in the FA-based matrix [66,319]. Relatively, the chloride resistance of higher GP samples is more effective than the FA-based ones. Thereby, the chloride resistance increases with higher GP content.

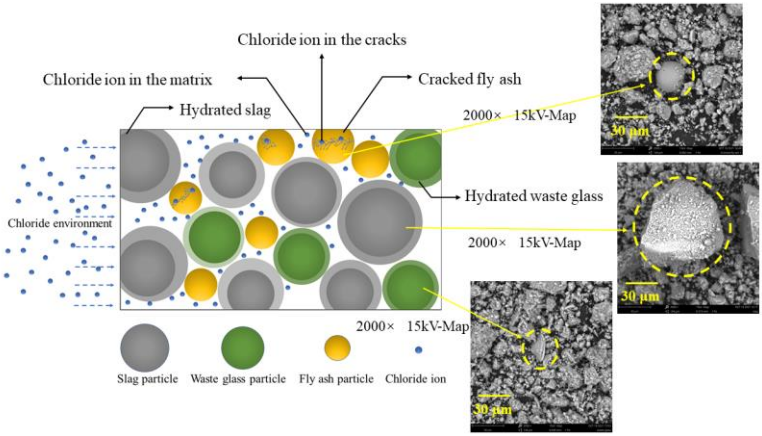

Fig. 6.8 Influence of GGBS, FA, and GP on chloride transport in AAM mortars.

The chemical absorption in the alkali activated system is normally attributed to the hydrotalcite [96,323] and ettringite [324] phases, in other words, layer double hydroxides phases, which can chemically absorb the chloride ion in the interlayer space. Among the AAM mortars, the hydrotalcite phase is clearly identified in XRD, which partly contributes to chloride ion immobilization. The hydrotalcite content shows similar among different mortars, but GP30 exhibits the highest chloride resistance. Because the hydrotalcite just contributes partly to the chloride binding capacity of the matrix. Thus, the physical chloride absorption predominates the chloride resistance in AAM mortars.

6.4 Conclusions

In this chapter, the influences of GP addition on the chloride diffusion behavior of alkali activated GGBS / FA are discussed. With higher GP substitutions in alkali activated GGBS / FA, the reaction kinetics and reaction products are determined. Furthermore, the microstructure and chloride resistance are investigated. Based on the experimental results, the following conclusions can be drawn:

- With a higher content of waste glass powder in alkali activated GGBS / FA, the intensity of the reaction heat peak is increasing, however, the time to reach the reaction peak (TRRP) decreases. The GP addition accelerates the early reaction process of alkali activated GGBS / FA.
- The C−(A)−S−H gels and hydrotalcite are observed among all the AAM samples. The hydrotalcite is still produced in the environment of extra reactive SiO_2 provided by GP, although the available Al content will be interreacted more with the extra Si-O tetrahedrons and less with Mg^{2+}. The crystalline carbonated phases reduce with higher GP content.
- Combining the GP in GGBS and FA matrix, a lower volume of pores is obtained in paste samples, which is attributed to the promotion of C−(A)−S−H formation.
- The incorporation of waste glass powder in alkali activated GGBS / FA promotes the chloride resistance of the matrix. Waste glass powder containing the AAM matrix shows both physical and chemical absorption of chloride ions, attributed to mesopores improvement and hydrotalcite phase.

Chapter 7 Reaction, microstructure, and efflorescence behavior of $NaOH/NaAlO_2$ activated slag and wastes glass: The transformation from C−S−H to C(N)−A−S−H

The efflorescence behavior is an intractable issue of alkali activated waste glass (AAWG), which is due to the vulnerable reaction products of AAWG facing carbonation and weathering. This chapter investigates that sodium aluminate activated slag and waste glass (SAASG) transfers the primary reaction product to C(N)−A−S−H possessing a high efflorescence-resistance. The reaction products of SAASG were identified to investigate the phase assemblages at different curing ages. The gel structure was characterized by ^{29}Si and ^{27}Al nuclear magnetic resonance (NMR). The microstructure was determined by scanning electron microscopy (SEM). Moreover, the efflorescence behavior and strength were evaluated as well. The results indicate that resistance towards efflorescence of SAASG was enhanced by sodium aluminate. Because sodium aluminate promotes C(N)−A−S−H formation, which captures more free Na^+ in the pore solution leading to limited Na^+ leaching, consequently higher resistance towards efflorescence.

The chapter is partially from the following article:

T. Liu, Y. Chen, G. Liu, B. Yuan, W. Zhuang, H.J.H. Brouwers, Q. Yu, Reaction, microstructure, and efflorescence behavior of NaOH / $NaAlO_2$ activated slag and wastes glass: The transformation from C−S−H to C(N)−A−S–H. (Internal revision)

7.1 Introduction

Waste glass (WG) is a typical inorganic solid waste material derived from both daily living and industrial production [325,326]. Nevertheless, there is very limited glass trash that is recycled or used, landfill is the primary method of WG treatment worldwide [327]. Currently, the utilization of waste glasses for the manufacture of alkali activated materials (AAMs) has been confirmed which might increase the recycling or reuse rate [328–330]. The suitability of using waste glass to replace common precursors such as fly ash and slag has been developed [331,332]. However, the performance durability of resulting AAMs with waste glasses is affected by different parameters, which have not yet been evaluated systematically [333]. For instance, the efflorescence of alkali activated waste glass (AAWG) becomes an intractable problem particularly when the materials are exposed to the humid environment due to the high concentration of free alkalis in AAWG [334,335].

Capillary motion causes the pore solution to move through the concrete and evaporate from its surface, leaving the concrete's surface richer in the alkali cations that were in the pore solution. The leached alkali cations react with atmospheric CO_2, causing the formation of white carbonate surface deposits known as efflorescence [336]. It may ruin the perception of color and the appreciation of concrete buildings [337]. Cyr et al. [338] reported that the high dosage of alkalis and low content of aluminum in glass cullet was the main reason for the high extent of efflorescence. The main hydration products of AAWG are mostly Si-high, Al- and Ca-low gels [332]. The hydrolytic stability of silicate gels in AAWG is poor, and attributed to easy depolymerization of the Si-high, Al- and Ca-low gels caused by the removal of bound water [339]. Consequently, AAWG is weak to prevent the occurrence of efflorescence. To improve the resistance of efflorescence, Al-rich and Ca-rich materials, e.g. slag, were applied in the AAWG matrix to enhance the stability of Si-rich gels [336]. Previous studies also reported a significant strength increase in slag incorporation in AAWG as compared to using only waste glass as a precursor [339,340]. The stable calcium/sodium aluminosilicate hydrates (C(N)−A−S−H) were generated by combining glass powder and slag as sources of Ca and Al to enhance the strength development. Vafaei et al. [341] attempted to use reactive alumina by incorporating calcium aluminate cement to modify the waste glass geopolymer. The formation of sodium aluminosilicate hydrates (N−A−S−H) resulted in improved resistance toward efflorescence. However, excess sodium oxide remaining unreacted in the materials and activator could particularly suffer unsightly efflorescence caused by mobile alkalis [342]. Relatively weak binding of Na in the geopolymer structure results in the tendency of efflorescence because Na^+ is easy to move within the pores solution and penetrate to the surface of the matrix. Thus, large content of Na bonded by C(N)−A−S−H gels can be a feasible way to enhance the efflorescence resistance of AAWG, less free Na^+ can move to the surface of the matrix in the humid environment.

To discuss it further, the formation of C(N)−A−S−H influences the evolution of microstructure, subsequently, affects the resistance of efflorescence and the mechanical properties. The changes in Al/Si and Al/Na ratios play important roles in the generation of reaction products. The C(N)−A−S−H gel formation has two stages, gel 1 and gel 2 [343]. At the gel 1 stage, the Al-O bond is weaker than the Si-O bond, so the Al-O tetrahedra (denoted as $Al(OH)_4^-$) are rich in the pore solution, thereby the high degree of Al-O-Si bond appears in the gel 1 stage, and a high Al/Si ratio promotes this phenomenon. Subsequently, the gel 2 stage involves more Si-O tetrahedra (denoted as $Si(OH)_4$) interaction into the chain of the C(N)−A−S−H. A higher Al/Si ratio can promote the C(N)−A−S−H formation in the matrix. Besides, the higher Al/Na ratio in the system increases the Si-Al chain interacting with Na to form C(N)−A−S−H in the geopolymer products [300]. Liu et al. reported that sodium aluminate activator could provide extra $Al(OH)_4^-$ promoting the C(N)−A−S−H formation in the activated slag matrix [18]. The sodium aluminate is preferably an activator to supplement Al resource in the waste glass matrix promoting the C(N)−A−S−H formation. No literature reports the property of sodium aluminate activated waste glass (SAAG). The sodium aluminate activator can provide the $Al(OH)_4^-$ in the pore solution compensating Al resource to waste glass. However, the utilization of sodium aluminate activator changes the Al/Si and Al/Na ratios, which influences the C(N)−A−S−H formation significantly in the matrix. The incorporation of $Al(OH)_4^-$ into a silicate chain could lead to the remarkable transformation of the gel structure [344]. Simultaneously, the synergetic influence of slag and waste glass on gel formation is still missing as well. Therefore, the gel structure in sodium aluminate activation remains unknown aspects. It is urgent to investigate its mechanism in terms of sodium aluminate activated slag and waste glass (SAASG).

To improve the resistance towards efflorescence of alkali activated slag and waste glass, the sodium aluminate was used to activate the precursors for the first time, and the sodium hydroxides and their hybrid activator were used as the control group. The reaction products of SAASG were determined by Quantitative X-ray diffraction (QXRD), thermogravimetry (TG), and Fourier-transform infra-red spectroscopy (FTIR). The gel structure was characterized by nuclear magnetic resonance (NMR). The microstructure was assessed by Scanning electron microscopy (SEM). Importantly, the efflorescence behavior and compressive strength of paste samples were evaluated as well. A mechanism of efflorescence behavior was proposed to give insight into stabilizing Na^+ leaching by crosslinked C(N)−A−S−H formation.

7.2 Methodology

7.2.1 Materials

Ground granulated blast-furnace slag and waste glass were utilized in this chapter. Notably, the waste glass pellets were provided by Maltha, Netherlands. The received waste glass pellets were ground in a disk mill for 5 mins to achieve the desired particle size. Fig. 7.1(a) shows that the slag and waste glass are mainly composed of amorphous phases. The slag contains a small amount of calcite and the waste glass contains a small amount of aluminum iron. Fig. 7.1(b) also indicates the stretching of carbonate in slag at 1488 and 1419 cm^{-1}. The stretching of Si-O-Si can be observed at 986 cm^{-1} in waste glass. The laser particle size analyzer (Mastersizer 2000, Malvern Instruments, UK) was used to determine the particle size distribution (PSD) of raw materials (as shown in Fig. 7.1(c)). The median particle size (d_{50}) of slag and waste glass powder were 12.743 and 27.194 μm, respectively. X-ray fluorescence spectrometry (XRF, PANalytical Epsilon 3) was used to examine the chemical composition of slag and waste glass powder (as shown in Table 7.1). The specific density, specific surface area, and loss on ignition of slag and waste glass were also determined as shown in Table 7.1.

Table 7.1 Chemical composition (wt.%), specific density, specific surface area, and loss on ignition of slag and waste glass.

Chemical composition	GGBS (wt. %)	Waste glass (wt. %)
Na_2O	/	10.2
MgO	8.6	1.1
Al_2O_3	13.3	1.8
SiO_2	29.7	71.3
SO_3	2.7	/
K_2O	/	0.8
CaO	43.0	13.6
TiO_2	1.5	/
Fe_2O_3	/	0.6
Cl	0.1	0.1
Others	1.2	0.4
LOI* (1000°C)	-0.910	0.281
Specific density (g/cm^3)	2.8	2.4
Specific surface area (m^2/g)	1.668	0.607

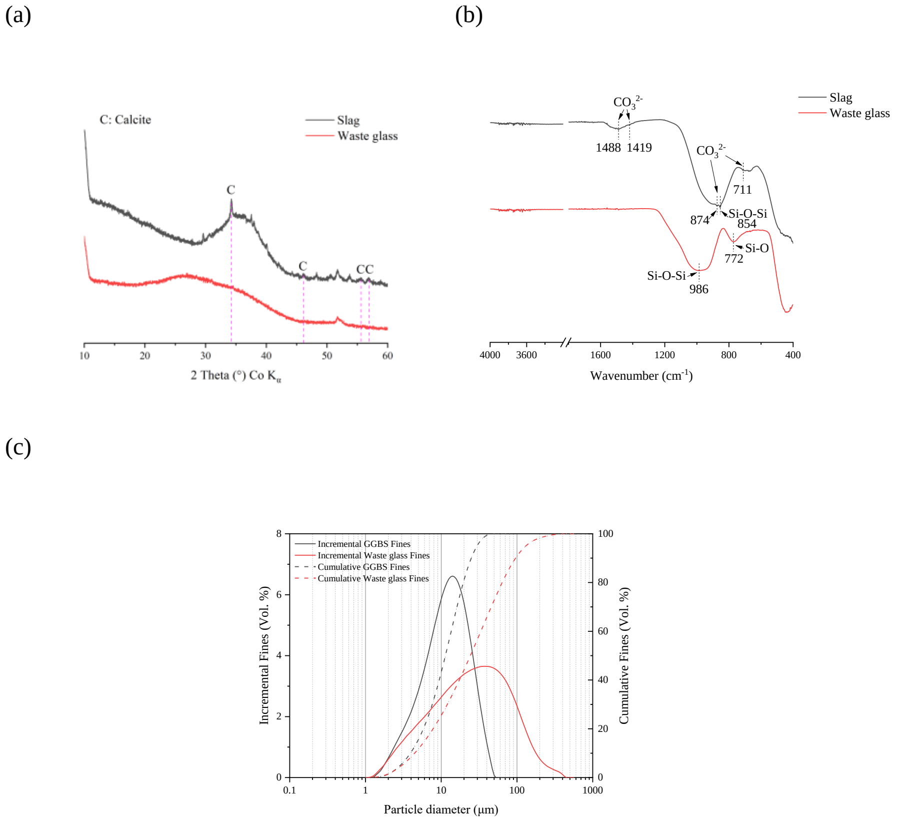

Fig. 7.1 Properties of slag and waste glass: (a) XRD; (b) FTIR; (c) PSD.

7.2.2 Mix design

The slag and waste glass were mixed in a 1:9 (slag: waste glass) mass ratio as the solid precursor, which was activated by sodium hydroxide (NH), sodium aluminate (NA), and their hybrid (NHNA) solutions. Simultaneously, the equivalent Na_2O contents vary from 3 to 5 wt.% (see the sample IDs in Table 7.2). Each SAASG blend was stirred for 10 min during the mixing to confirm the uniformity of the pastes. The fresh SAASG pastes were poured into the plastic cubic molds with a dimension of 4cm×4cm×4cm and then sealed by plastic membranes. In the first stage, all the samples were cured at room temperature (20 ℃). After 24 h, the samples were cured at 75℃ for 24 h. Then, after thermal curing for 24 h, all the samples were demolded and continued to cure in the laboratory environment (air curing) in the room with stable temperature (20 ℃) and 60% humidity.

The activators used in this chapter were sodium hydroxide, sodium aluminate, and their mixture (hybrid activator). Analytical grade sodium-hydroxide pellets and sodium aluminate pellets were dissolved in deionized water (separately or together) to prepare activators 6 h before application. The hybrid activator of sodium hydroxide and sodium aluminate was in different aluminate modulus (Al_2O_3/Na_2O) from 0 to 1.

Table 7.2 Mix design of paste samples.

Sample	w/b*	$NaAlO_2$	NaOH	Na_2O (wt. %)	Al_2O_3/Na_2O (In activator)	Glass Powder (wt. %)	Slag(wt. %)
NA3	0.4	7.9	/	3	1	90	10
NA4	0.4	10.6	/	4	1	90	10
NA5	0.4	13.2	/	5	1	90	10
NHNA3	0.4	3.9	1.9	3	0.5	90	10
NHNA4	0.4	5.3	2.6	4	0.5	90	10
NHNA5	0.4	6.6	3.2	5	0.5	90	10
NH3	0.4	/	3.9	3	0	90	10
NH4	0.4	/	5.2	4	0	90	10
NH5	0.4	/	6.5	5	0	90	10

*w/b = water to binder ratio in mass

7.2.3 Test methods

7.2.3.1 Quantitative X-ray diffraction

X-ray diffraction (XRD) was performed using a Bruker D4 Phaser instrument emitting Co-K_α radiation (40 kV, 30 mA). The crushed, powdered SAASG pastes were measured with a step size of 0.05° and a counting time of 1 s/step. The 2θ range was 10–90°. For the quantitative X-ray diffraction (QXRD) study, all the paste was ground by ball milling at level 3 speed for 15 min before the test. The silicon powder (10 wt%, Siltronix, France) was added as an internal standard to the paste samples. For the quantification of mineral phases in the samples, Rietveld analysis was performed using TOPAS software (version 4.2, Bruker). All the quantitative XRD analysis are generated by TOPAS. Before the test, the paste samples were ground into powder, immersed in 2-propanol for 24 h to stop the hydration process, and then dried to constant mass at 60 ℃ for 3 d.

7.2.3.2 Thermogravimetry

Thermogravimetry (TG) tests were performed on ≈100 mg crushed, powdered paste samples by using an STA 449 F1 instrument at a heating rate of 10 ℃/min. Notably, the aluminum crucible lid had to be used in case the boiling of the waste glass powder occurred under the thermal conditions of measurement. Experiments were carried out from 40 ℃ to 1000 ℃, in which N_2 was used as the carrier gas. The same hydration stoppage treatment was performed before the test as well.

7.2.3.3 Fourier-transform infrared spectroscopy

Fourier-transform infrared spectroscopy (FTIR) analysis was performed using a Varian 670-IR spectrometer with a wavelength range of 400 to 4000 cm^{-1} with a resolution of 1 cm^{-1}. The powdered samples were prepared after hydration stoppage treatment, which is the same as the last test.

7.2.3.4 Nuclear magnetic resonance

The solid-state magic angle spinning nuclear magnetic resonance (MAS NMR) (JNM-ECZ600R) measurements were obtained at a 14.01T magnet and a resonance frequency of 99 MHz for ^{29}Si and 132 MHz for ^{27}Al. The ^{29}Si MAS NMR spectra were recorded using a 4 mm CPMAS probe head and a 4 mm zirconia rotor by employing a spinning speed of 12 kHz, a 4 μs excitation pulse, and a 20 s relaxation delay. The solid-state ^{27}Al MAS NMR spectra were recorded using a 2.5 mm CPMAS probe head and a 2.5 mm zirconia rotor spinning at a speed of 12 kHz, a 1 μs excitation pulse, and a 0.5 s relaxation delay.

The deconvolution of the ^{29}Si MAS NMR spectra was carried out using Origin 2022. The multipeak fit was used to calculate the area of each peak of silicon and aluminum state that exists in the spectra with Gaussian function according to the literature [345,346]. The cumulative integrated percentage of each silicon and aluminum in SAASG was obtained to calculate the mean chain length (MCL) and Al-Si substitution of C(N)−A−S−H [347].

^{29}Si MAS NMR has revealed important information regarding C(N)−A−S−H formation in the hydrated matrix. Resonances from the Q^1, Q^2, and $Q^2(1Al)$ sites, which constitute the silicate chains in the C(N)−A−S−H gel, have been seen using ^{29}Si MAS NMR [348,349]. The mean chain length (MCL) of non-crosslinked C(N)−A−S−H gel can be calculated by using equation (1), while the MCL of crosslinked C(N)−A−S−H gel can be calculated by using equation (2). The Al-Si substitution in the tetrahedral chains can be obtained from the intensities of the Q^1, $Q^{2,}$ and $Q^2(1Al)$ resonances (equation (3)), as reported by Richardson et al. [350,351].

$$\mathrm{MCL_{nc}} = \frac{2\left[Q^1+Q^2+\frac{3}{2}Q^2(1Al)\right]}{Q^1} \tag{7-1}$$

$$\mathrm{MCL_c} = \frac{4\left[\mathrm{Q^1+Q^2+Q^2(1Al)+Q^3+2Q^3(1Al)}\right]}{\mathrm{Q^1}} \tag{7-2}$$

$$\frac{\mathrm{Al[IV]}}{\mathrm{Si}} = \frac{\frac{1}{2}\mathrm{Q^2(1Al)}}{\mathrm{Q^1+Q^2+Q^2(1Al)}} \tag{7-3}$$

7.2.3.5 Scanning electron microscopy / Energy dispersive spectroscopy

After the compressive strength tests of samples at 3 and 28 days, the fragments of each paste sample were collected. The microstructure of the selected samples was examined by scanning electron microscopy (SEM). The composition of the gels was determined by an energy dispersive spectroscopy (EDS) instrument based on the SEM graphs. The clusters of Si-Al-Ca-Na were normalized to obtain the quaternary phase (Si-Al-Ca-Na) diagrams. Then the composition of C(N)−A−S−H can be examined.

7.2.3.6 Efflorescence testing

7.2.3.6.1 Visual efflorescence testing

To qualitatively investigate the efflorescence behavior, the 3-day cured Ø2cm×5cm cylinder pastes were placed in transparent plastic petri dishes. The petri dishes were filled with deionized water every day to keep the level at 1cm in height. The deionized water could accelerate the leaching of Na^+ aggravating the efflorescence behavior. The evolution of visual efflorescence was recorded in time. The results of the visual efflorescence test were obtained qualitatively by visual comparison of the samples.

7.2.3.6.2 Quantitative efflorescence testing

To quantitatively evaluate the efflorescence for each sample, the experiment were followed with a leaching test. The crushed fragments of all the geopolymer pastes after 28 and 56 days of curing were collected and pass a No. 200 sieve to minimize the influence of particle size. 1.00 g of each geopolymer powder will be added to 100 ml of deionized water. The solutions were stirred for 30 min and kept at ambient temperature for 24 h to allow the full leaching of free alkali from the geopolymer paste. Then the leachates were placed in the oven after the filtration to allow the evaporation of water. The mass of soluble salts was measured to evaluate the extent of efflorescence as follow [336]:

$$\mathrm{E(wt.\ \%)} = \frac{\mathrm{m_d}}{\mathrm{1\ g\ (geopolymer\ powder)}} \times 100\% \tag{7-4}$$

Where E(wt. %) is the extent of efflorescence, m_d is the mass of dissoluble salts in 1g of geopolymer powder.

7.2.3.7 Compressive strength

After 3- and 28-day air curing, all the cubic SAASG pastes were tested for compressive strength by a constant loading rate of 2400 N/s until the fracture load. The strength value of each mix was recorded by the average of 3 samples.

7.3 Results

7.3.1 Reaction products

7.3.1.1 Quantitative X-ray diffraction

Fig. 7.2 illustrates the XRD patterns and their quantitative analysis of AASG at 3 and 28 days. Most of the amorphous weight percentages are disordered C(N)−A−S−H. And there is a large difference in crystalline phase assemblages between sodium aluminate (mainly form zeolite A), sodium hydroxide (mainly form natrite), and hybrid activator (mainly form zeolite Na-P_1)activated slag and waste glass either at 3 or 28 days. It is interesting that katoite formation only appears in the samples with $NaAlO_2$ participation, which is due to available $Al(OH)_4^-$ from $NaAlO_2$. Similarly, the hydrotalcite is only observed in the samples with NaOH participation, it is owing to Mg^{2+} dissolution from slag under the high pH pore solution. Detailed description as follow.

For sodium aluminate activated slag and waste glass (NA samples), there is a significant increase of zeolite A (ICDD00-039-0222, $Na_{96}Al_{96}Si_{96}O_{384}\cdot 216H_2O$) from 3 to 28 days. It is associated with the extra $Al(OH)_4^-$ (from $NaAlO_2$ activator) promoting the zeolite formation [18]. There is no presence of zeolite Na-P_1 (ICDD:00-039-0219, $Na_6Al_6Si_{10}O_{32}\cdot 12H_2O$) at 3 days but it appears a limited amount at 28 days in NA4 and NA5 samples. It is due to the higher alkalinity of the NA4 and NA5 activator. Nevertheless, zeolite A is still the secondary reaction product in NA4 and NA5. The higher alkalinity favors formatting zeolite Na-P_1 rather than zeolite A. Similarly, another zeolite formation (ICDD: 00-031-1271, $1.08Na_2O\cdot Al_2O_3\cdot 1.68SiO_2\cdot 1.8H_2O$) is obtained in NA4 and NA5 with a small amount but absence in NA3. Those zeolite phases are normally formed with calcium sodium aluminosilicate hydrates (C(N)−A−S−H) together in the $NaAlO_2$ activation system [18]. Thus, the C(N)−A−S−H is another reaction product in NA samples. The presence of katoite (ICDD: 01-077-1713, $Ca_{2.93}Al_{1.97}(Si_{.64}O_{2.56})(OH)_{9.44}$) in NA samples is due to the participation of slag from the precursors. The dissolved Ca^{2+} (from slag) reacts with $Al(OH)_4^-$ leading to the formation of katoite. Moreover, elevated alkalinity (NA3 to NA5) promotes the dissolution of Ca^{2+} resulting in higher katoite formation either at 3 or 28 days.

For sodium hydroxides activated slag and waste glass (NH samples), the natrite (ICDD: 00-037-0451 Na_2CO_3) formation increases with higher alkalinity from NH3 to NH5, which is also the primary crystalline phase either in 3 or 28 days. The presence of calcite (ICDD: 01-086-2341, $CaCO_3$) and hydrotalcite (ICDD: 00-014-0191, $Mg_6Al_2CO_3(OH)_{16}\cdot 4H_2O$) are due to the dissolution of Ca^{2+} and Mg^{2+} from slag. They also increase with the elevated equivalent Na_2O content. Because the higher alkalinity promotes the dissolution of Ca^{2+} and Mg^{2+}. In the meantime, no magnesite (ICDD: 01-086-2348 $MgCO_3$) is detected at 3 days but observed at

28 days. The hydrotalcite formation mainly consumes the dissolved Mg^{2+} at the early reaction process, so no magnesite formation at 3 days. With the air curing ages, more available Mg^{2+} from slag reacts with CO_2 forming magnesite at the late reaction process.

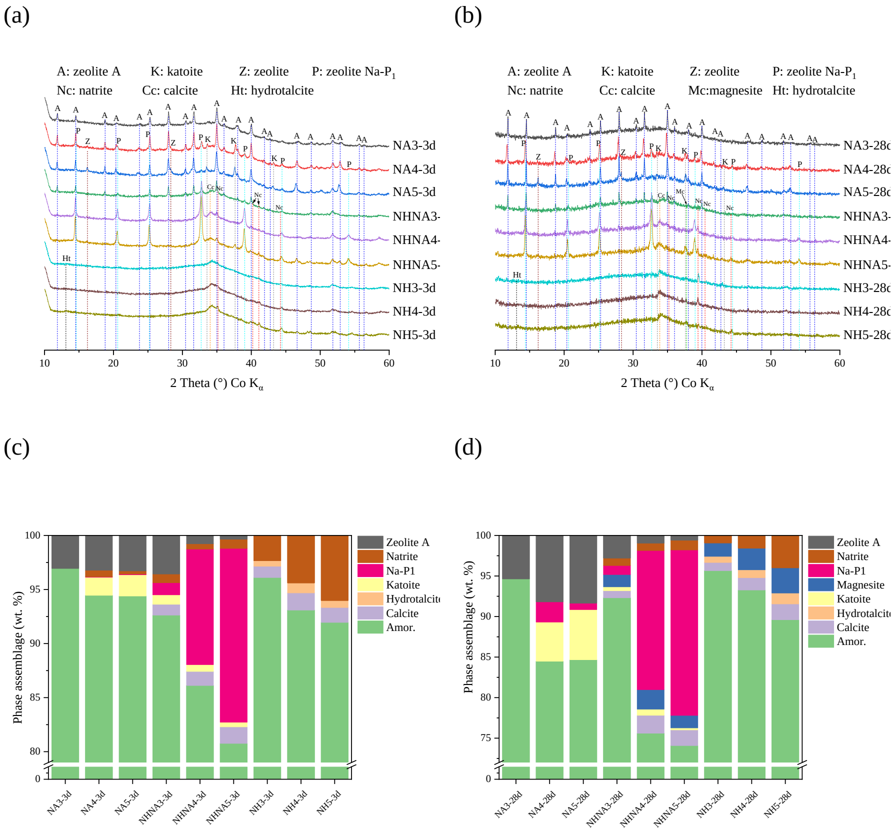

Fig. 7.2 SAASG pastes XRD at (a) 3 days; (b) 28 days; QXRD at (c) 3 days; (d) 28 days.

For hybrid activator activated slag and waste glass (NHNA samples), there is a large amount of zeolite Na-P_1 (ICDD: 00-039-0219, $Na_6Al_6Si_{10}O_{32}\cdot 12H_2O$) generation from 3 to 28 days. However, NHNA3 shows that zeolite A is the primary crystalline phase, which is different from NHNA4 and NHNA5. The reason is because of the elevated pH environment transfers the zeolite A to zeolite Na-P_1 formation. Besides, the elevated pH environment results in the increase of calcite and magnesite generation from 3 to 28 days by comparing NHNA3 ~ NHNA5.

Overall, the primary reaction products of the NA and NHNA sample are zeolite and C(N)−A−S−H gels. However, the products of NH samples are sodium/magnesium carbonate and Si-high, Al- and Ca-low gel under air curing conditions. As a consequence, the NH sample is easy to be carbonated, facing efflorescence issues [352].

7.3.1.2 Thermogravimetry

The thermogravimetry (TG) and differential thermograms (DTG) curves of the SAASG pastes, as a function of different curing ages (3 and 28 days), are presented in Fig. 7.3. For 3-day curing pastes (Fig. 7.3(a)), the first large peak of DTG of NA samples is due to the loss of moisture water (40~100℃) [326], decomposition of C(N)−A−S−H (100~300℃) [18], and the zeolite A (40~200℃) [262]. As can be seen, the mass losses in this temperature range increase with the elevated equivalent Na_2O content, and the mass losses in NA3~5 are 9.5, 9.6, and 10.6 wt.%, respectively. The difference is mainly from the decomposition of C(N)−A−S−H because the zeolite A contents in NA pastes are like each other as mentioned in QXRD results. The reason is that higher $NaAlO_2$ in the matrix provides more Al-O tetrahedra in the pore solution, which promotes the formation of C(N)−A−S−H gels [18]. The second peak of DTG at around 400℃ in NA samples is owing to the decomposition of katoite. The increased alkalinity from NA3 to NA5 leads to more dissolved Ca^{2+}, consequently, more katoite (Ca&Al-rich hydrogarnet) is formed. For NHNA samples at 3 days, the largest decomposition peak in DTG is derived by the loss of moisture water (40~100℃) [326], decomposition of C(N)−A−S−H (100~300℃) [18], the zeolite A (40~200℃) [262], and zeolite Na-P_1 (25~400℃) [353]. It is quite similar to NA samples at 3 days. Because these hydrated phases are promoted by the $NaAlO_2$ activator. However, the NaOH participation results in the reduction of zeolite A formation but an increase of zeolite Na-P_1. Thus, the primary mass losses (first decomposition peak) in NHNA4 and NHNA5 samples are from zeolite Na-P_1. It is in good agreement with QXRD results. A small amount of katoite decomposes at around 400℃ in NHNA samples as well. Interestingly, the decomposition of calcite ($CaCO_3$) at around 700℃ [354] and natrite (Na_2CO_3) at around 850℃ [355] are observed. This is due to the NaOH

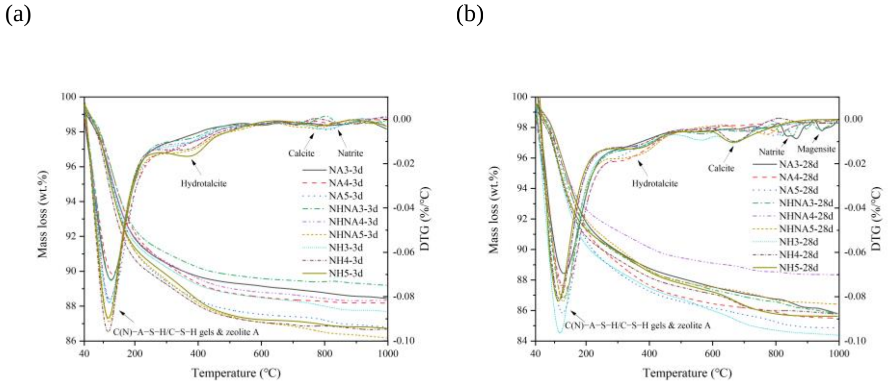

Fig. 7.3TG and DTG of SAASG at (a) 3 days; (b) 28 days.

activator rising the pH environment of the samples. It leads to the samples being vulnerable for carbonation. For NH samples at 3 days, the largest peak of DTG is mainly associated with the loss of moisture water (40~100℃) [326], decomposition of C−S−H gels, and the first decomposition peak of hydrotalcite (150~250℃) [132]. At the same time, the second decomposition peak of hydrotalcite is shown at around 400℃ as well [132]. It is typical hydrated phases from NaOH activated slag [21]. The elevated alkalinity of NH samples also leads to slightly higher amount of hydrotalcite formation. It is owing to more dissolved Mg^{2+} and $Al(OH)_4^-$ from slag forming more hydrotalcite. Besides, a small amount of calcite decomposes at around 700℃ in NH samples [354]. At the same time, a small amount of natrite decomposes at around 850℃ [355]. Those carbonated phases, which confirm by QXRD as well, originating from the carbonation during the air-curing condition.

Fig. 7.3(b) exhibits TG and DTG curves at 28 days, the NA3~5 samples show 10.1, 10.9, and 11.5 wt.% mass losses (40 ~ 300℃), respectively. The mass losses, like 3-day NA samples, include the loss of moisture water, decomposition of C(N)−A−S−H, zeolite A, and a small amount of zeolite Na-P_1. Compared to 3-day NA pastes, the increase in mass losses is associated with the elevated formation of C(N)−A−S−H and zeolite A. In addition, a typical katoite peak at around 400℃ appears in 28-day NA samples instead of 3-day NA samples. It is on account of the increase of dissolved Ca^{2+} from slag after 3 curing days. Then the raised Ca^{2+} reacts with $Al(OH)_4^-$ promoting katoite generation. It is in good agreement with QXRD results as well. For 28-day NHNA pastes, there is a large amount of C(N)−A−S−H and zeolite Na-P_1 decomposition, as well as a small amount of zeolite A decomposition before 300℃. It is similar to 3-day NHNA pastes. However, the decomposed peaks of calcite and magnesite can be observed at around 700 and 900℃, respectively. It is related to the carbonation of NHNA samples. Besides, the largest decomposed peak of 28-day NH pastes is linked with C−S−H gels. Furthermore, the decomposition of calcite and natrite can be obtained at 700 and 850℃. It is also associated with the severe carbonation of NH samples.

Particularly, comparing NA, NHNA, and NH samples, the carbonated phases (calcite, natrite, and magnesite) decrease with aluminate modulus regardless of curing ages. The aluminate contributes to the formation of Al-rich zeolite and C(N)−A−S−H gels, resulting in the less available Na^+, and Ca^{2+} forming natrite and calcite. In other words, the aluminate modulus increases the capacity of carbonation resistance among the samples.

7.3.1.3 Fourier-transform infrared spectroscopy

Fig. 7.4 illustrates the FTIR spectra of SAASG pastes at 3 and 28 days. As can be seen from Fig. 7.4(a), the main peaks in all samples at 971 cm^{-1} are assigned to the asymmetrical stretching vibration of Si−O−Al at 3 days. It corresponds to the degree of reaction [356]. All the pastes show the same degree of geopolymerization, it is due to the dissolved $Al(OH)_4^-$ at the early reaction stage by slag incorporation. It indicates that C(N)−A−S−H formation appears in all pastes. Simultaneously, the band at 778 cm^{-1} is associated with the symmetric stretching vibrations of Si−O−Si bridges from C(N)−A−S−H gels as well [357]. Similarly, a band at 664 cm^{-1} attributed to the symmetrical stretching of Si−O−T bonds is identified in the spectra of all samples [358]. It is also due to the C(N)−A−S−H gels in all samples. The peaks at 1432 and 880 cm^{-1} are associated with the stretching vibrations of CO_3^{2-} [359]. The intensity of CO_3^{2-}

stretching peaks are more obvious in NH and NHNA samples, while the NA samples show thinner humps at these ranges. It is owing to more carbonated phases in NH and NHNA samples than that in NA samples. It is in good agreement with QXRD and TG results at 3 days. Particularly, the peaks in NA samples at 552 cm^{-1} are attributed to the 8Si-D4R unit of zeolite A, which is the ring vibrations of the zeolite A structure [360,361]. This peak also shows a weak stretching vibration in NHNA3 pastes, because a small amount of zeolite A is observed in NHNA3 from XRD patterns. However, there is no presence of this peak in other NHNA and NH samples. It is due to the rather low content or absence of zeolite A in those samples, which is in line with XRD patterns as well. Besides, the stretch at 607 cm^{-1} in NHNA4 and NHNA5 is due to Si–O in bending modes from the zeolite Na-P$_1$ [362,363]. It is the primary zeolite formation in these specimens as described in XRD patterns. The peaks at 3392 and 1646 cm^{-1} are due to the stretching vibration of O−H from bound water molecules of the samples [18].

For 28-day FTIR spectra in Fig. 7.4(b), a distinctive bending and shifting vibration of Si−O−Al from C(N)−A−S−H formation at around 972 ~ 979 cm^{-1}. The degree of geopolymerization increases with curing ages. The NA3 pastes show the highest wavenumber (979 cm^{-1}) in this range, representing the highest degree of geopolymerization among specimens. At the same time, the wavenumbers in NA3 (979 cm^{-1}), NA4 (975 cm^{-1}), and NA5 (972 cm^{-1}) decrease with the higher equivalent Na$_2$O content. Similarly, the degree of geopolymerization in NHNA samples reduces with higher equivalent Na$_2$O content. The peaks of the Si−O−Al bond in NH samples are at the same position (972 cm^{-1}). Moreover, the decrease of wavenumbers represents that less Al participates in C(N)−A−S−H formation with higher equivalent Na$_2$O content. Because the higher pH of the activator is beneficial to the dissolution of Si(OH)$_4$ into the pore solution. More Si(OH)$_4$ can be doped by the silicate chain, thus a lower degree of geopolymerization is observed. Similarly, with 3-day samples, the peaks at 778 and 664 cm^{-1}, Si−O−Si bonds, and Si−O−T bonds from C(N)−A−S−H gels remain unchanged along with the curing ages. In addition, the bands at 1448 (v_3), 1392 (v_3), and 870

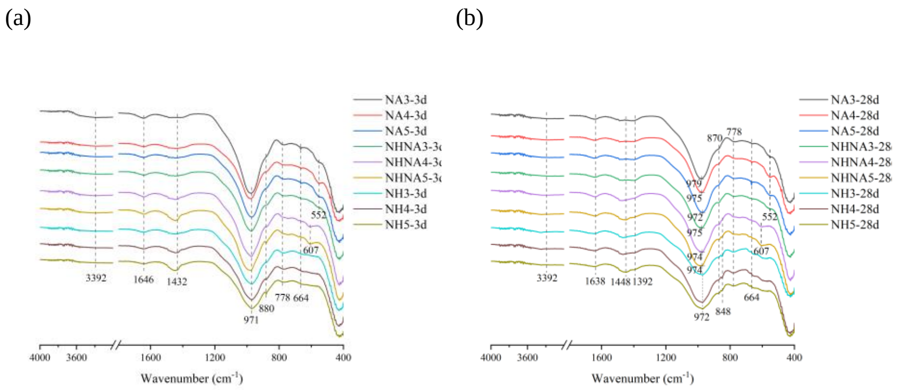

Fig. 7.4 (a) 3-day and (b) 28-day FTIR spectrum of SAASG.

cm^{-1} (v_2) are due to the presence of carbonate phases with different vibration modes [359]. These carbonate phases are from natrite and calcite, which is consistent with the XRD results. Especially, a band at 848 cm^{-1} in NHNA4, NHNA5, and all NH samples can be observed at 28-curing days. It is owing to CO_3^{2-} stretching vibration of magnesite [364]. It is also in line with XRD results. The bands at 552 cm^{-1} assigned to the 8Si-D4R unit from zeolite A remain unchanged in NA3, NA4, NA5, and NHNA3. Meanwhile, the bands at 607 cm^{-1} from zeolite Na-P$_1$ also remain unchanged in NHNA4 and NHNA5. Also, the peaks at 3392 and 1638 cm^{-1} due to the stretching vibration of bound water molecules keep constant along the curing ages.

7.3.2 Gel structure

7.3.2.1 ^{29}Si MAS NMR

The ^{29}Si MAS NMR data of raw materials are shown in Fig. 7.5, and the parameters of their deconvolution fitting curves are listed in Table 7.3. The ^{29}Si MAS NMR data of anhydrous slag illustrate a single broad resonance with a maximum intensity at around −74.5 ppm (Fig. 7.5(a)). It represents a wide distribution of Si environments and chemical shifts of raw slag, which is compatible with the material's weakly crystalline nature as shown by XRD. According to a previous study, the signal is associated with Q^0 units at −74 ppm [365,366]. The ^{29}Si MAS NMR data of anhydrous waste glass also shows a single broad resonance with a maximum intensity at around −92.5 ppm (Fig. 7.5(b)). It represents a wide distribution of Si environments and chemical shifts of raw waste glass as well. According to the literature, the signal is associated with Q^1 units at −82.5 ppm, Q^2 units at −90 ppm, Q^3 units at −96 ppm, and Q^4 units at −103 ppm [346,367–369].

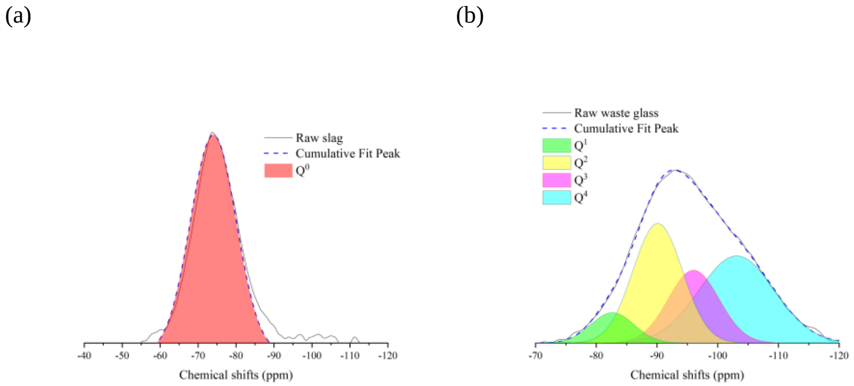

Fig. 7.5 ^{29}Si MAS NMR of raw materials (a) slag; (b) waste glass.

The ^{29}Si MAS NMR analysis of SAASG pastes at 3 and 28 days are shown in Fig. 7.6, and the parameters of their deconvolution fitting curves are listed in Table 7.4. Regardless of curing ages, the primary peaks are at −91 ppm for the Q^2(0Al) unit in NA and NHNA samples, and −90.1 ppm for the Q^2(0Al) unit in NH samples. Those peaks are attributed to the C(N)−A−S−H gels in NA and NHNA samples [347,366], and C−S−H gels in NH samples [346]. Notably, the sharp peaks at −89.1 ppm are assigned to the Q^4(4Al) unit of zeolite A in NA and NHNA samples [370]. However, no typical peak of the Q^4(4Al) unit can be observed in NH samples. Because the extra $Al(OH)_4^-$ promotes the zeolite A formation in NA and NHNA samples, but not enough $Al(OH)_4^-$ in NH samples results in the absence of zeolite A. Generally, more Q^2 and Q^3) silicate species mean a better solubility of slag and waste glass in the SAASG pore solution, which may further lead to different geopolymerization processes in the matrix.

Table 7.3 ^{29}Si MAS NMR of raw materials.

Sample		Q^0	Q^1	Q^2	Q^3	Q^4
Slag	Pos. (ppm)	-74	/	/	/	/
	Width*	14.2	/	/	/	/
	Integral (%)	100	/	/	/	/
Waste glass	Pos. (ppm)	/	-82.5	-90	-96	-103
	Width	/	8.4	9.6	9.9	14.6
	Integral (%)	/	7.5	33.8	21.2	37.5

*Width = Full width at half maximum

For NA3 paste from 3 to 28 days, Q^2 and Q^3 are mostly the silicate species as shown in Fig. 7.6(a) and (b). The peak of Q^2(0Al) silicate is the highest at −91 ppm, and the peak of Q^2(1Al) silicate also shows a high intensity. Q^2(0Al) and Q^2(1Al) silicate species are the characteristic peaks of C(N)−A−S−H [347,366]. The high intensity of Q^2(1Al) silicate represents a large amount of $Al(OH)_4^-$ replace $Si(OH)_4$ in the bridging site of C−S−H forming C−A−S−H [371]. Simultaneously, the partial replacement of Ca^{2+} by Na^+ leads to the formation of C(N)−A−S−H gels [18]. Besides, the decrease of Q^2(0Al) and Q^2(1Al) silicate species from 3 to 28 days is due to lower silicate MCL_{nc} of C(N)−A−S−H gels along the curing period as shown in Table 7.5. The decrease of MCL_{nc} of C(N)−A−S−H gels is due to the elevated incorporation of Ca^{2+} from slag and waste glass into gel formation [358]. The peak at −82.5 ppm increases with curing ages, which is associated with a higher amount of chain-end Q^1 silicate specie in C(N)−A−S−H gels [347]. It is also associated with higher incorporation of Ca^{2+}, which leads to more chain-end Q^1 silicate species [372]. The resonance at −95.7 ppm is due to the Q^3(0Al) site [373], which is attributed to the crosslinked C(N)−A−S−H gel formation in the paste. It is highly related to the MCL_c of C(N)−A−S−H gels. As can be seen from Table 7.5, the MCL_c of C(N)−A−S−H gels with decreases with curing ages. It is also higher Ca^{2+}

incorporation in C(N)−A−S−H gels, leading to a lower MCL_c. No detection of Q^0 site in NA3 compared to raw materials represents Q^0 silicate transforming to Q^1 or Q^2.

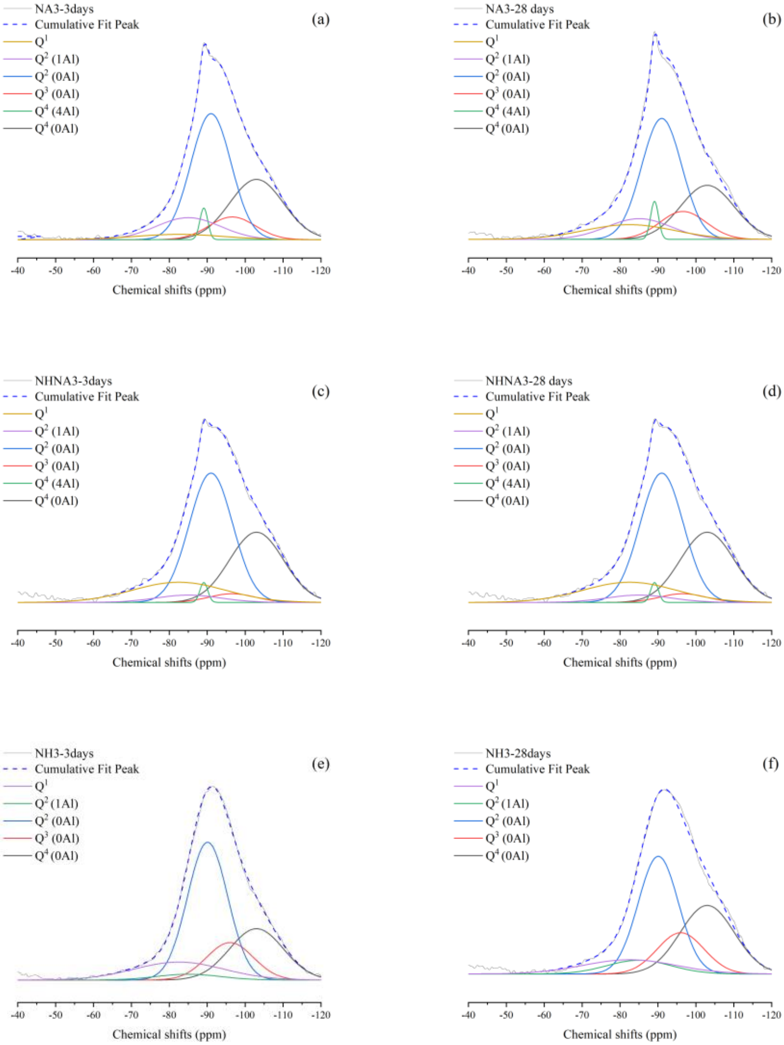

Fig. 7.6 ^{29}Si MAS NMR of SAASG at 3 and 28 days.

There is no obvious difference between NHNA3-3days and NHNA3-28 days in terms of the silicate species group (Fig. 7.6(c) and (d)). Simultaneously, NHNA samples show the same chemical shift position as NA samples. It represents that the $NaAlO_2$ activator leads to a large quantity of C(N)−A−S−H gel formation in a low-Ca, high-Al environment [347]. Notably, the MCL_{nc} and MCL_c of NHNA3-28 days pastes are lower than that of NA3-28 days pastes up to 29.3% and 33.1%, respectively. It is associated with the high pH of the activator in NHNA samples. Because the higher pH value decreases the Al uptake by C−S−H forming longer-MCL C(N)−A−S−H gels [344].

Table 7.4 ^{29}Si MAS NMR of paste samples.

Sample		Q^1	Q^2 (1Al)	Q^2 (0Al)	Q^3 (0Al)	Q^4 (4Al)	Q^4 (0Al)
NA3-3 days	Pos. (ppm)	-82.5	-85	-91	-96.6	-89.1	-103
	Width	28	20	12.5	14.5	2.5	16.8
	Integral(%)	6.9	12.3	42.1	8.3	2.2	28.1
NA3-28 days	Pos. (ppm)	-82.5	-85	-91	-96.6	-89.1	-103
	Width	28	20	12.5	14.5	2.5	16.8
	Integral(%)	11.1	11.1	40.5	10.8	2.5	24.14
NHNA3-3 days	Pos. (ppm)	-82.5	-85	-91	-96.6	-89.1	-103
	Width	29	20	13.5	14.5	2.5	16.8
	Integral(%)	15.3	3.8	45.6	3.3	1.3	30.6
NHNA3-28 days	Pos. (ppm)	-82.5	-85	-91	-96.6	-89.1	-103
	Width	29	20	13.5	14.5	2.5	16.8
	Integral(%)	15.3	3.8	45.7	3.3	1.3	30.6
NH3-3 days	Pos. (ppm)	-82.5	-85	-90.1	-96	/	-103
	Width	29	20	12.5	14.5	/	16.8
	Integral(%)	14.4	2.1	46.1	14.5	/	22.9
NH3-28 days	Pos. (ppm)	-82.5	-85	-90.1	-96	/	-103
	Width	29	20	13.5	14.5	/	16.8
	Integral(%)	14.5	3.1	37.7	15.3	/	29.3

The NH3-3 days and NH3-28 days paste exhibit typical C−S−H gel structure shown in Fig. 7.6(e) and (f), which is different from $NaAlO_2$-activated matrix. The resonances at −90.1 ppm show the highest intensity up to 46.06% and 37.74% at 3 and 28 days, respectively. Those characteristic resonances are associated with the Q^2(0Al) site from C−S−H gels in the matrix. Similarly, the signals of the Q^1(0Al) site at −82.5 ppm and Q^3(0Al) site at −96 ppm are also from the reflection of C−S−H gels. The peak at −85 ppm is associated with a small amount of C−A−S−H gel formation [371]. As can be seen from Table 7.5, a slight decrease in MCL can be observed during the curing days. It is due to more dissolved Ca^{2+} incorporation lessening the MCL of C−S−H gels as well. The MCL_{nc} of NH samples is lower than that of NA and NHNA samples. It is due to the absence of Al in NH samples leading to a lower MCL of C−(A)−S−H gels. This is also reported by previous studies [344,374]. There are no $Q^m(nAl)$ silicate species detected in NH samples confirming the major reaction products of C−S−H gels as well.

Overall, the NA samples show a high extent of crosslinked formation, while the C(N)−A−S−H gels in NHNA samples exhibit a lower extent of the crosslinked structure. The NH samples illustrate the typical C−S−H gel formation, and its MCL is significantly lower than that of C(N)−A−S−H gels in NA samples. It confirms that the $NaAlO_2$ activation transfer the hydrated gels from C−S−H to C(N)−A−S−H without NaOH participation.

Table 7.5 Mean chain length and Al-Si substitution of C(N)−A−S−H gel.

Groups	MCL_{nc}	MCL_c	Al-Si substitution
NA3-3 days	19.4	40.1	0.1
NA3-28 days	12.3	26.6	0.08
NHNA3-3 days	8.7	17.8	0.03
NHNA3-28 days	8.7	17.8	0.03
NH3-3 days	8.8	21.4	0.02
NH3-28 days	7.8	19.5	0.03

7.3.2.2 ^{27}Al MAS NMR

The ^{27}Al MAS NMR data of raw materials are shown in Fig. 7.7, and the parameters of their deconvolution fitting curves are listed in Table 7.6. The ^{27}Al MAS NMR data of anhydrous slag illustrate a broad resonance at around 65 ppm (Fig. 7.7(a)). It represents a Al[IV] site in the raw slag [375]. The resonance with a weak intensity at 10.3 ppm represents a Al[VI] site in the raw slag, which is similar to a previous study [369]. The ^{27}Al MAS NMR data of anhydrous waste glass exhibits a broad resonance at around 57.5 ppm (Fig. 7.7(b)), corresponding to Al[IV] site in the raw waste glass.

Three distinct Al environments (Al[IV], Al[V], and Al[VI]) of SAASG pastes at day 3 and 28 are detected in the ^{27}Al MAS NMR analysis (Fig. 7.8) at 52~75 ppm, 39.8 ppm, and 5~15 ppm, respectively [376]. The parameters of their deconvolution fitting curves are listed in Table 7.7. The profile of the NMR spectra shows similarities between NA and NHNA samples including 4 Al[IV] sites at 75 (q^2[I]), 67 (q^2[II]), 59.4 (Al[IV]-2), and 57.5 (Al[IV]-1) ppm, which is consistent with the dissolution of raw materials and the formation of aluminosilicate reaction products (zeolite and C(N)−A−S−H gels). The presence of Al[V] corresponds to the crosslinked C(N)−A−S−H gels structure as reported in the previous studies [377,378]. While Al[VI] represents different reaction products varying in NA and NH samples, corresponding to zeolite [379] or hydrotalcite [376], respectively. Particularly, the NA samples have a significantly high zeolite A peak while the NHNA samples show lower zeolite A intensities. It is due to that the solo $NaAlO_2$ activator promotes the Al species in the zeolite A formation.

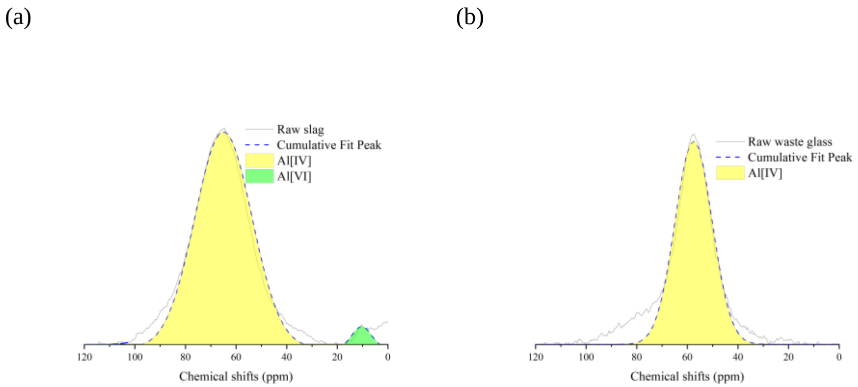

Fig. 7.7 ^{27}Al MAS NMR of raw materials (a) slag; (b) waste glass.

Fig. 7.8(a) and (b) show the ^{27}Al MAS NMR analysis of the NA3 sample from 3 to 28 days. The q^2 aluminate species at 75 and 67 ppm are assigned to two different local environments q^2[I] and q^2[II], respectively. Meanwhile, the resonance at 57.5 ppm is assigned to Al[IV]-1 site. These locations have been attributed by previous investigations to Al replaced into paired tetrahedra in C(N)−A−S−H gels [380]. The deconvolutions also show high intensity at 62 ppm corresponding to q3, which means high levels of cross-linking in the C(N)−A−S−H gels structure. It is also in agreement with the ^{29}Si MAS NMR analysis. Typically, the Al[IV]-2 aluminate species at 59.4 ppm are associated with tetrahedral Al in zeolite A [381]. Simultaneously, the q^2[I] peak at 10.5 ppm is from the octahedral Al zeolite A [379]. The q^2[II] aluminate species (octahedrally coordinated Al) at 14.7 ppm increases with curing ages shown in Table 7.7. It represents that the tetrahedrally coordinated Al of zeolite A transfers to octahedrally coordinated Al [382]. It is due to the change in the Al chemistry of the activated system. The decrease of pH environment in the pore solution leads to more presence of octahedrally coordinated Al, leading to more octahedrally coordinated Al in zeolite A formation. The q^4 sites at 52.5 ppm are expected given the assignment of $Q^4(4Al)$ owing to the zeolite A formation as well [376].

Table 7.6 ^{27}Al MAS NMR of raw materials.

Sample		Al[IV]	Al[VI]
Slag	Pos. (ppm)	65	10.3
	Width*	26.5	9.0
	Integral (%)	96.7	3.3
Waste glass	Pos. (ppm)	57.5	/
	Width	17.2	/
	Integral (%)	100	/

The NHNA3 samples show a limited increase of 2 Al[IV] sites (75, and 67 ppm) from 3d- to 28d-curing days (Fig. 7.8(c) and (d)), representing a similar level of cross-linking in the C(N)−A−S−H gels. It is in line with ^{29}Si MAS NMR results. It is worth mentioning that the slight increase of Al[VI] aluminate species at 5.6 ppm suggests the existence of a third aluminate hydrate (TAH) [383]. It is intimately associated with the formation of C−S−H gels [378]. Because the participation of NaOH promotes the formation of the C−S−H gel.

Besides, the Al chemistry in NH3 at 3 and 28 days shows the highest resonance at 57.5 ppm corresponding to C−S−H gels (and a small number of C−A−S−H gels) as shown in Fig. 7.8(e) and (f). Meanwhile, the TAH site (in NH samples) at 5.6 ppm shows the highest intensity among the SAASG samples. As mentioned above, it is intimately related to the formation of the C−S−H gel. It suggests that the C−S−H is the primary gel type in NH samples. In addition, the resonances at 14.7 and 10.5 ppm are assigned to HT[II] and HT[I] sites, relating to the formation of hydrotalcite [376]. The remarkable decrease of HT[II] and HT[I] sites is associated with the transformation of the hydrotalcite phase into TAH during the curing ages. It is similar to the previous study [383].

In summary, based on the ^{29}Si and ^{27}Al MAS NMR results, the $NaAlO_2$ activator significantly contributes to higher Al substitution for Si transferring the primary gel formation from C−S−H to C(N)−A−S−H. Simultaneously, the Al participation increases the mean chain length of gels, and more crosslinked gel structures can be obtained.

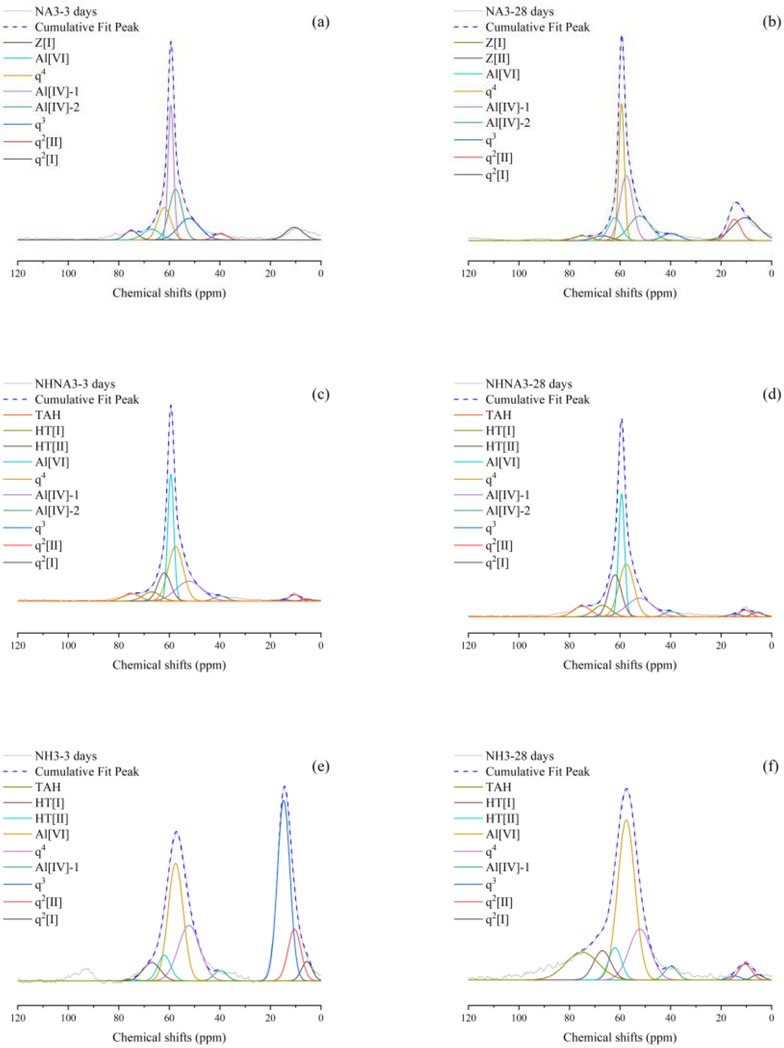

Fig. 7.8 ^{27}Al MAS NMR of SAASG at 3 and 28 days.

Table 7.7 ^{27}Al MAS NMR of paste samples.

Sample		q^2[I]	q^2[II]	q^3	Al[IV]-2	Al[IV]-1	q^4	Al[V]	Z[II]/HT[II]	Z[I]/HT[I]	TAH
NA3-3 days	Pos. (ppm)	75	67	62	59.4	57.5	52.2	39.8	/	10.5	/
	Width	6	8	6	2.6	6	10	6	/	8	/
	Integral(%)	4.1	6.3	14.5	26.1	22.6	16	2.9	/	7.5	/
NA3-28 days	Pos. (ppm)	75	67	62	59.4	57.5	52.2	39.8	14.7	10.5	/
	Width	8	8	6	2.6	6	10	8	5.8	12	/
	Integral(%)	2.3	2.4	8.3	21.5	23.5	14.8	3.4	7.4	16.3	/
NHNA3-3 days	Pos. (ppm)	75	67	62	59.4	57.5	52.2	39.8	14.7	10.5	5.6
	Width	8	8	6	2.8	7	12	6	5.8	5	5
	Integral(%)	4.4	5.4	12.5	26.3	28.1	17.6	2.3	0.5	2.3	0.7
NHNA3-28 days	Pos. (ppm)	75	67	62	59.4	57.5	52.2	39.8	14.7	10.5	5.6
	Width	8	8	6	2.8	7	12	6	5.8	5	5
	Integral(%)	5.9	6.2	17.1	23.4	25.4	15.3	2.2	1	2.3	1.5
NH3-3 days	Pos. (ppm)	75	67	62	/	57.5	52.2	39.8	14.7	10.5	5.6
	Width	6	8	6	/	7	10	6	5.8	6	5
	Integral(%)	0.2	4.6	4.8	/	25.7	17.4	1.9	32.7	9.7	3
NH3-28 days	Pos. (ppm)	75	67	62	/	57.5	52.2	39.8	14.7	10.5	5.6
	Width	15	8	6	/	8	10	6	5.8	6	5
	Integral(%)	13.6	8.2	6.8	/	44.7	17.8	2.8	0.8	3.3	1.9

7.3.3 Characterization of microstructure and mineralogy

Fig. 7.9 and Fig. 7.10 show the SEM micrographs of SAASG pastes at 3 and 28 days, respectively. The $Si(OH)_4$ and $Al(OH)_4^-$ species are released into the pore solution and produced the aluminosilicate gels when the slag and waste glass are in contact with the alkaline solutions [384]. As shown in Fig. 7.9 and Fig. 7.10, the unreacted slag and waste glass particles are bonded by the C(N)−A−S−H gels. The micro cracking increases with the elevated equivalent Na_2O content because the high alkalinity of the matrix leads to a higher risk of efflorescence. The higher extent of carbonation results in loose microstructure, namely more micro cracking. Notably, the NA pastes show the most condensed microstructure among the samples. Because the $NaAlO_2$ activator promotes the extra $Al(OH)_4^-$ species participating in the C(N)−A−S−H gels. It leads to a more condensed microstructure of the matrix. Meanwhile, the formation of C(N)−A−S−H gels reduces the risk of efflorescence. Less calcite, natrite, and magnesite form during the air curing period. While the formation of these phases leads to a loose microstructure. Besides, the increase of micro cracking along the curing ages is also related to the higher content of carbonated phases. It is in line with the XRD results.

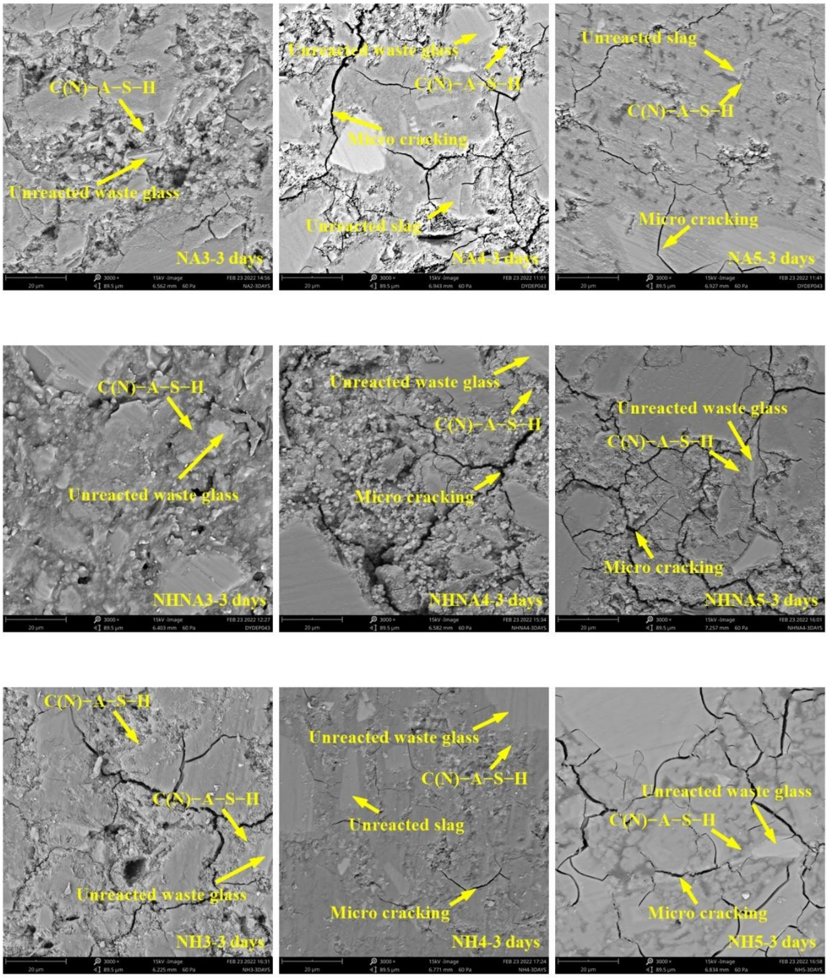

Fig. 7.9 SEM micrographs of SAASG at 3 days.

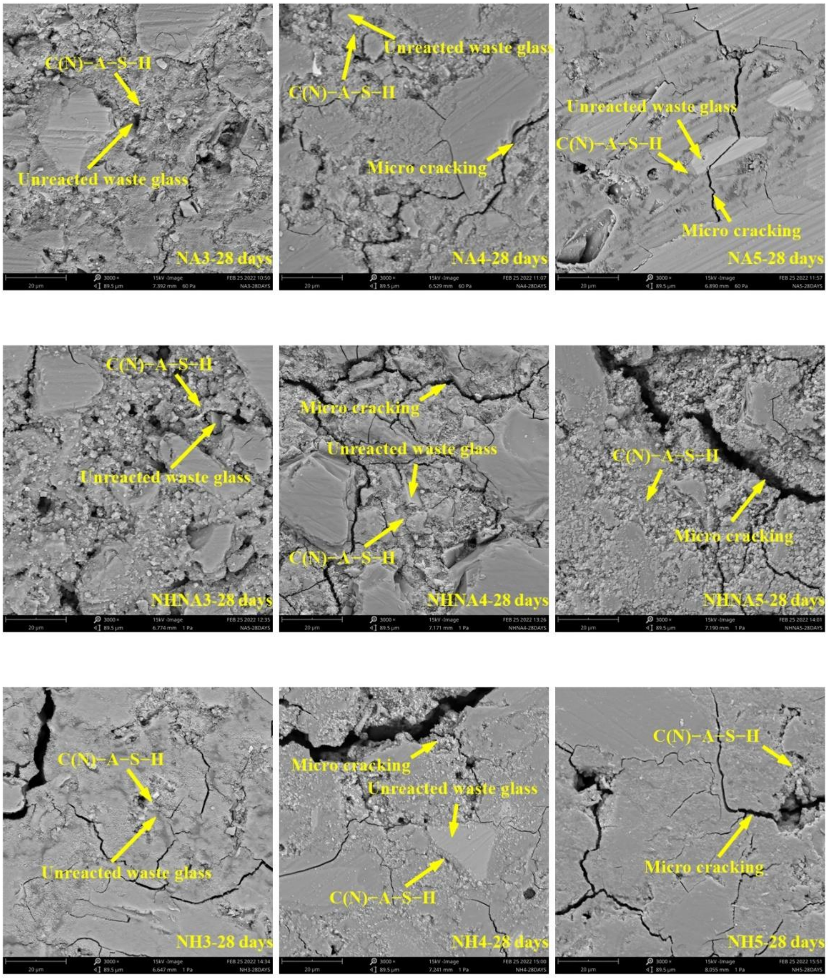

Fig. 7.10 SEM micrographs of SAASG at 28 days.

Fig. 7.11 and Fig. 7.12 illustrate the quaternary elements (Si-Al-Ca-Na) diagrams and their projection maps of SAASG in molar ratio at 3 and 28 days, respectively. As shown in Fig. 7.11, the calcium-poor C(N)−A−S−H gels can be observed among the samples at 3 curing days. Because the waste glass lacks calcium content, the Ca^{2+} can only dissolve from slag. The limited

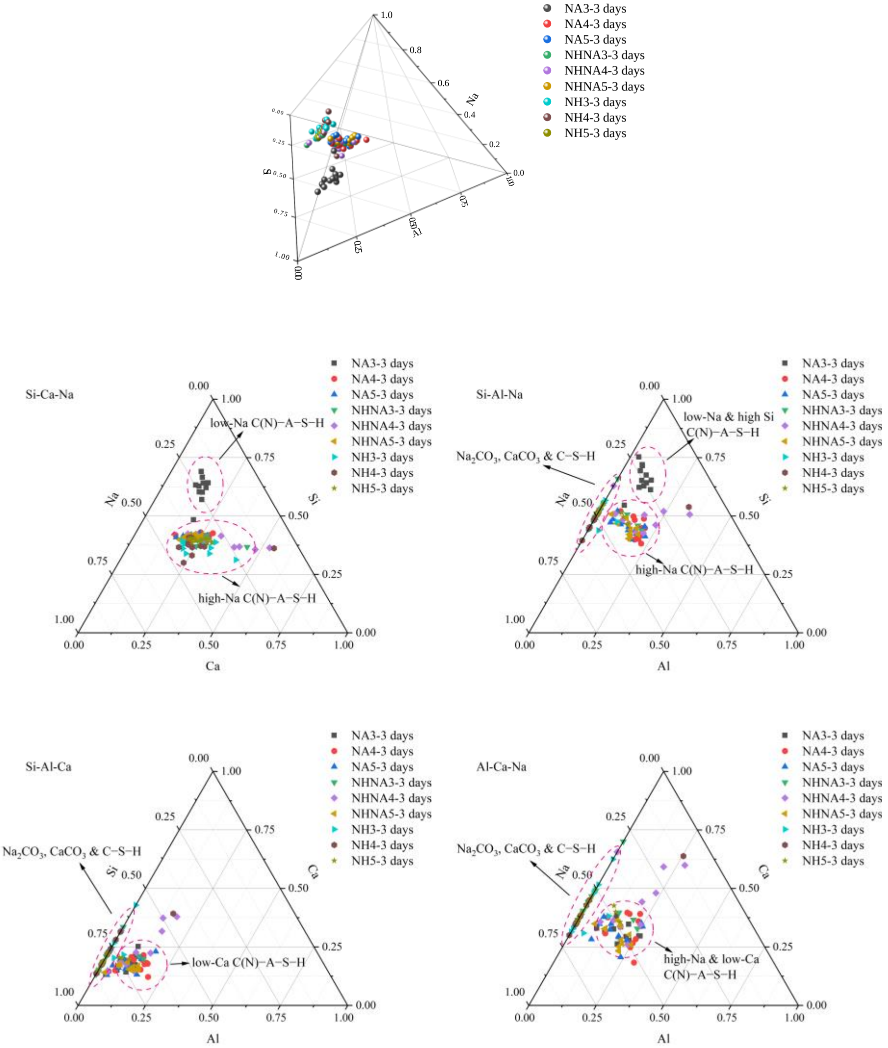

Fig. 7.11 Quaternary elements (Si-Al-Ca-Na) diagrams and its projection maps of activated slag and waste glass powder in molar ratio at 3 days.

Ca^{2+} dissolving from slag leads to the formation of calcium-poor C(N)−A−S−H gels. The C(N)−A−S−H gels in NA and NHNA samples show a low Al content. Because only limited Al can replace Si sites to form geopolymers [385,386]. While in NH samples, a small amount of Al can be found in C(N)−A−S−H gels, the primary reaction products are Na_2CO_3, $CaCO_3$, and C−S−H gels. It is due to limited Al resources from slag (without $NaAlO_2$ supplement). The reaction products of the NH samples are easier to face efflorescence, so more Na_2CO_3, and

$CaCO_3$ can be observed. It is worth mentioning that the sodium-poor and silicate-rich C(N)−A−S−H gels can be observed in the NA3 sample. The low alkalinity and relatively low sodium aluminate in NA3 result in less sodium and high silicate participation in the formation of C(N)−A−S−H gels.

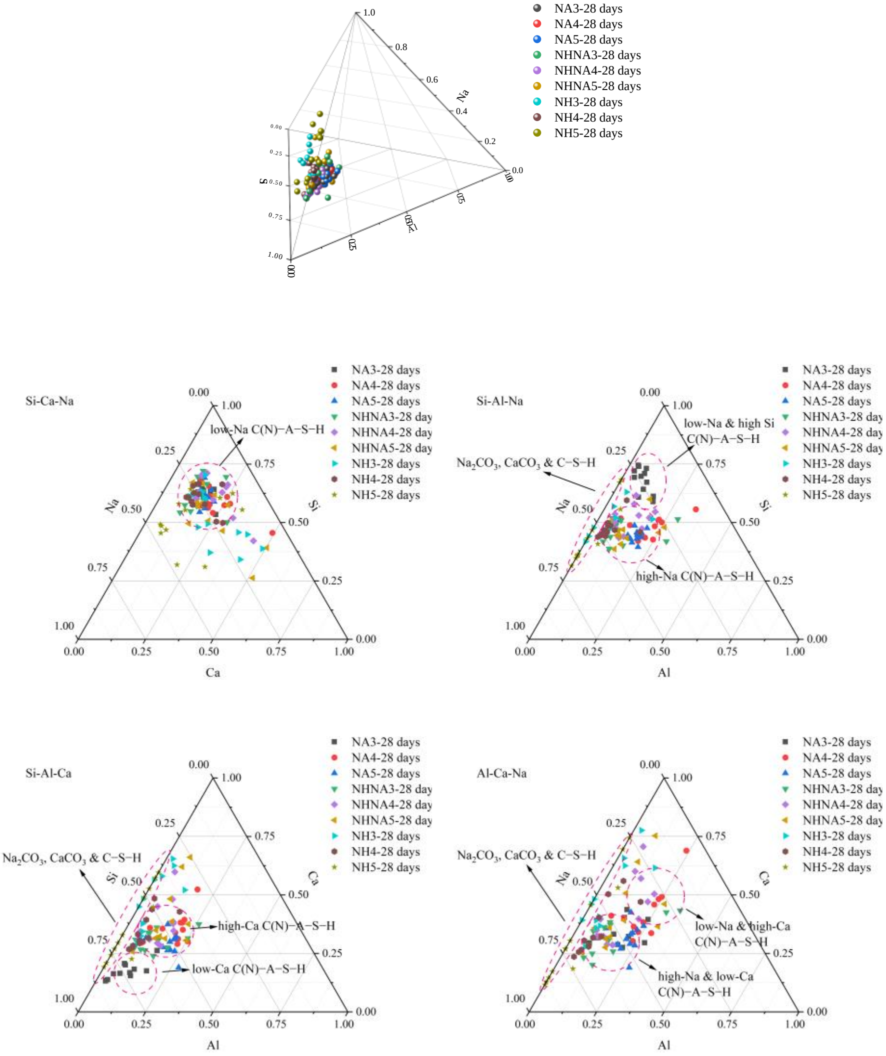

Fig. 7.12 Quaternary elements (Si-Al-Ca-Na) diagrams and its projection maps of activated slag and waste glass powder in molar ratio at 28 days.

It can be seen from Fig. 7.12, the reaction products in NA and NHNA samples at 28 days become calcium-rich, silicate-rich, and sodium-rich C(N)−A−S−H gels. With the curing ages, more and more $Si(OH)_4$ and Ca^{2+} dissolve from waste glass and slag reacting with $Al(OH)_4^-$ from $NaAlO_2$ activator to form the C(N)−A−S−H gels. The higher calcium in the geopolymers leads to lower silicate chain length [300,387,388]. It is also consistent with the NMR results. The NH samples remain in a large quantity of Na_2CO_3, $CaCO_3$, and C−S−H gels at 28 days. Some scatter with low Al content in NH samples represent low content of C(N)−A−S−H gels in NH samples. It is also in line with the NMR results.

7.3.4 Efflorescence testing

7.3.4.1 Visual efflorescence test

Fig. 7.13 exhibits that NA3-56 days clearly shows the lowest extent of efflorescence, while NH5-56 days shows the highest extent of efflorescence among the SAASG pastes at 56 days. The visual efflorescence of each paste as a function of curing ages is presented in Fig. D1.

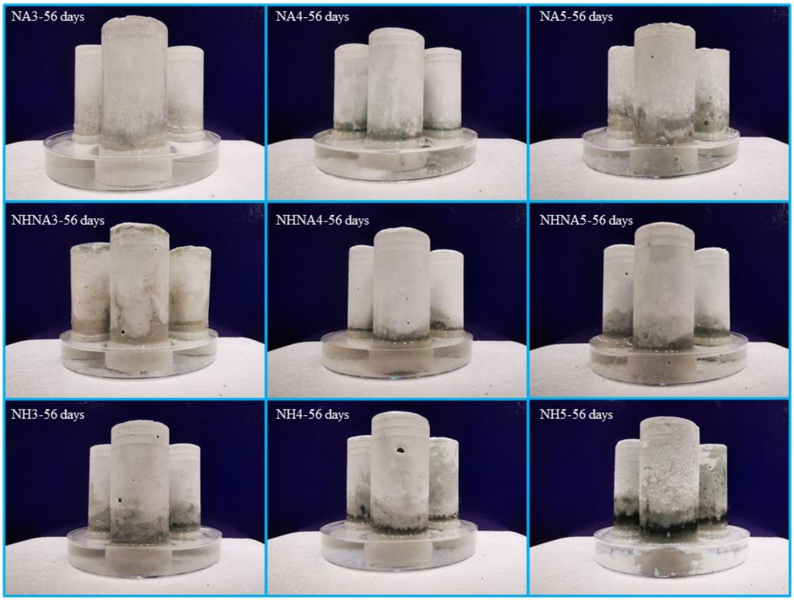

Fig. 7.13 Visual efflorescence testing SAASG pastes at 56 days.

The extent of visual efflorescence increases with the higher equivalent Na_2O content. It is associated with a higher pH environment of the pastes. Compared to NA samples, the NH samples show a more intensive efflorescence. It is associated with the leaching of Na^+ from the matrix. The NH samples possess more free Na^+ ions than the NA samples. The presence of extra $Al(OH)_4^-$ (in NA samples) from $NaAlO_2$ reduces the extent of efflorescence by forming more C(N)−A−S−H gels. It can bond more free Na^+ ions than that NH samples. Besides, NA3 shows the lowest extent of efflorescence because the primary reaction product of NA3 is Na-rich C(N)−A−S−H gels. It leads to more free Na^+ ions participating in the C(N)−A−S−H gel formation. Less Na^+ ions can leach out from the matrix during the visual efflorescence test process.

7.3.4.2 Quantitative efflorescence test

Fig. 7.14 shows a quantitative efflorescence test of SAASG pastes at 28- and 56-day air curing process. The statistics are generally in agreement with the levels of visible efflorescence in Fig. 7.13. As can be seen from Fig. 7.14, the pastes show a higher extent of alkali leaching with higher equivalent Na_2O content. This is in keeping with the well-established tendency in the pore solution chemistry as a function of alkali concentration, where increasing Na_2O content results in more alkaline pore solutions [336,389]. Subsequently, more free Na^+ ions can be diffused during the efflorescence process. At the same time, the higher Na_2O concentration also increases the dealumination of Al in C(N)−A−S−H gels [390]. Thus, it leads to a higher extent of efflorescence. In addition, NA3 samples show the lowest extent of efflorescence among the samples, indicating the lowest tendency towards efflorescence. The low alkali concentration of NA3 among the samples provides the lowest free alkali ions in the pore solution. Simultaneously, the extra $Al(OH)_4^-$ transfer the reaction products from C−S−H to C(N)−A−S−H gels. The C(N)−A−S−H gels have stronger resistance towards efflorescence than C−S−H gels [391]. However, the hybrid activator group (NHNA5) shows an even higher extent of efflorescence when Na_2O is 5 wt.%. And it shows more micro cracks with the lowest

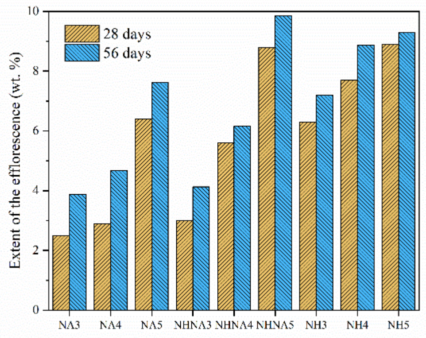

Fig. 7.14 Efflorescence testing of sodium hydroxide and sodium aluminate activated slag and waste glass at 28 and 56 days.

compressive strength. The poor microstructure leads to the strongest tendency towards efflorescence, where free alkali ions can easily transport to the surface of the paste.

7.3.5 Compressive strength

The compressive strength of SAASG pastes is displayed in Fig. 7.15 from 3 days up to 28 days. NA samples group consistently has the highest compressive strength at all ages, followed by the NH group and NHNA group. The high compressive strength of NA pastes can be ascribed to its large amount of C(N)−A−S−H formation, leading to a denser matrix [334,390]. Besides, the NA samples show the lowest efflorescence extent, which means less carbonation. The high carbonation of NH and NHNA groups leads to lower compressive strength as well [42]. The solo activators (NA or NH) show that the higher alkali concentration leads to lower compressive strength. The waste glass particles are attacked by the alkali activator during the dissolution process. It causes a layer to form on the waste glass particles, slowing down the reaction rate and consequently lowering the compressive strength [338]. However, the higher alkali concentration in the hybrid activator increases the compressive strength. It may be associated with a large amount of zeolite Na-P_1 formation consuming mostly the alkali ion and extra $Al(OH)_4^-$. The rest alkali ions are used for the dissolution of silica in the waste glass. And the higher alkalinity is beneficial to the geopolymerization process in NHNA samples.

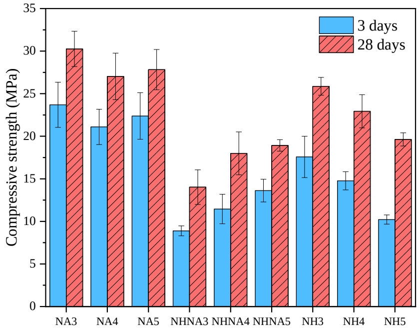

Fig. 7.15 Compressive strength of sodium hydroxide and sodium aluminate activated waste glass pastes at 3 and 28 days.

7.4 Discussion

This study assessed the possibility of using sodium aluminate to control the efflorescence of activated waste glass and slag blends. The $NaAlO_2$ activator transferred the primary reaction products from C−S−H to C(N)−A−S−H inhibiting the intensive efflorescence of alkali activated waste glass (AAWG). Such an application would be an inspiring method to utilize waste glass as a building material with a low risk of efflorescence. The findings showed that the sodium aluminate activated slag and waste glass (SAASG) exhibited a low extent of efflorescence and high mechanical strength. In previous studies, researchers adjusted the Si/Al ratio by supplementing Al-rich precursors, e.g. metakaolin [392] and fly ash [334]. Those studies indicated the high effectiveness of extra alumina in the strength development of glass-based geopolymer. While this chapter attempted to supplement Al resources from waste glass. Because $NaAlO_2$ could provide a large quantity of $Al(OH)_4^-$ for the geopolymerization process leading to an enhanced mechanical property.

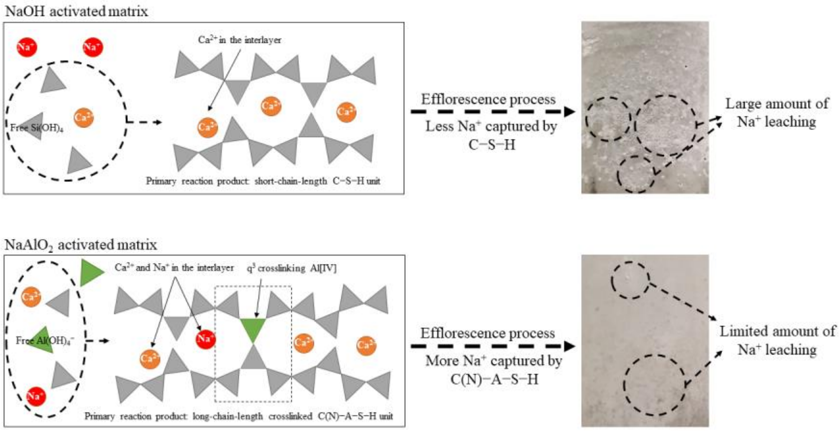

Fig. 7.16 Efflorescence process of NaOH and $NaAlO_2$ activated slag and waste glass.

Fig. 7.16 represents how the primary reaction products influence the efflorescence process of NaOH and $NaAlO_2$ activated slag and waste glass. The $NaAlO_2$ activator provides extra $Al(OH)_4^-$ promoting the geopolymerization process. At the same time, the participation of $Al(OH)_4^-$ monomers at the bridging sites of the silicate chain led to Na^+ adopted by C−A−S−H forming C(N)−A−S−H gels. It was also reported by Richardson [300]. Thus, the $NaAlO_2$ activator effectively stimulates $Al(OH)_4^-$ and Na^+ occupying the silicate and calcium sites, respectively. It results in the crosslinked C(N)−A−S−H gel structure in $NaAlO_2$ activated matrix. Consequently, a large amount of free Na^+ ions are captured by the C(N)−A−S−H gels leading to a high resistance towards efflorescence. While NaOH activated matrix lacks the $Al(OH)_4^-$ monomers, the primary reaction products are C−S−H gels. Relatively, the numerous free Na^+ ions in the pore solution are at risk of leaching. Simultaneously, the high alkalinity of NaOH activated matrix has a higher potential to carbonation. Thereby, the resistance of NaOH activated matrix towards efflorescence is relatively lower than that of $NaAlO_2$ activated matrix.

Nevertheless, sodium aluminate promotes the C(N)−A−S−H gel formation inhibiting the efflorescence process. The C(N)−A−S−H gel content in the matrix is still difficult to determine. Consequently, the quantitative influence of the $NaAlO_2$ activator is hard to conduct. Investigating methods to quantify the C(N)−A−S−H gel formation would be of scientific and practical interest in controlling the efflorescence behavior.

7.5 Conclusions

This chapter utilizes the sodium aluminate to activate the slag (minority) and waste glass (majority) matrix to control the efflorescence behavior. Results show that the sodium aluminate provides extra $Al(OH)_4^-$ promoting C(N)−A−S−H gel formation, which significantly improves the resistance of efflorescence and mechanical properties. Moreover, it expands the application of waste glass as supplementary cementitious materials. The following detailed conclusions can be drawn:

- Sodium aluminate promotes C(N)−A−S−H gels (major product) and zeolite A (secondary product) formation. While the elevated pH (incorporated with NaOH) results in zeolite Na-P_1 as the secondary reaction product. However, the Si-high, Al- and Ca-low gel is the primary reaction product in sodium hydroxides activation.
- Sodium aluminate activation generates longer main-chain-length and highly crosslinked gels. The Al substitution is significantly higher than that of sodium hydroxides activated matrix. The silicate species of NA samples indicate a more complex gel structure than that of NH samples.
- The more and more dissolved Ca^{2+} from slag adopted by amorphous gels transferred the reaction products from Na-rich to Ca-rich C(N)−A−S−H gels with the curing ages. It also results in the shorter main chain length of C(N)−A−S−H gels.
- The extra $Al(OH)_4^-$ from sodium aluminate activator captures more Na^+ to form Na-rich C(N)−A−S−H gels enhancing the resistance of efflorescence. Simultaneously, the sodium aluminate improves the mechanical property by supplementing extra Al resources forming a denser microstructure.

Chapter 8 Conclusions and recommendations

8.1 Conclusions

The most common material used in the construction of structures is cement. The cement industry uses a lot of natural resources and energy. Alkali activation is one method to use supplementary cementitious materials (SCMs) to create a cementless binder. The durability and leaching issue of alkali activated materials (AAMs) are receiving a lot more attention lately as a result of these environmental and sustainability concerns. Layered double hydroxides (LDHs) in binders have the properties for binding heavy metal and anions in their structure. To understand the mechanism of in-situ formation of LDHs in slag systems, the mineralogy, gel structure, microstructure, thermodynamic modelling, mechanical property, and long-term performance have been comprehensively investigated in the research. Furthermore, the superior performance of in-situ formed LDHs via $NaAlO_2$ activation can alleviate the chloride penetration and heavy metal leaching issue. Therefore, municipal solid waste incineration bottom ash (MSWI BA) can be effectively utilized as building materials rather than landfill. This concept, promotion of in-situ formed LDHs, makes it feasible to use solid waste achieving an eco-friendly method to develop new SCMs, e.g. MSWI BA. Another SCMs, waste glass is a Si-rich and Al-low SCM, that faces a severe efflorescence with alkali activation. While the $NaAlO_2$ is the feasible activator for waste glass to lessen the extent of efflorescence, because the extra Al in $NaAlO_2$ changes the gel structure and the microstructure of the matrix. Based on the results, the main conclusions from this thesis and the recommendation for future perspectives are summarized as follows.

8.1.1 In-situ formation of LDHs in AAMs

In Chapters 2 to 5, alkali activated slag, fly ash (FA), and municipal solid waste incineration bottom ash (MSWI BA) are investigated by NaOH, Na_2SiO_3, and $NaAlO_2$ activators. The mechanism has been revealed of the in-situ formation of LDHs. Common activators, e.g. NaOH, and Na_2SiO_3, show that the LDHs are the secondary reaction product with limited contents in phase assemblages. MgO promotes the formation of the in-situ growth of the LDH phase, and the CLDH completes the LDH-reconstruction process in NaOH, Na_2SiO_3 activated fly ash and slag (AAFS). Externally added LDH-NO_3 remains in the AAFS matrix, and $NaAlO_2$ activator provides extra $Al(OH)_4^-$, which lessens the competition between $Si(OH)_4$, and Mg^{2+} capturing $Al(OH)_4^-$. Extra Al promotes the content of in-situ formed LDHs and gels simultaneously. Moreover, the increase of pH value in the pore solution of sodium aluminate activated slag transfers the primary reaction products from C−A−S−H to N−A−S−H. The incorporation of MgO in $NaAlO_2$ activation results in more Mg^{2+} reacting with $Al(OH)_4^-$, reducing the reaction between Ca^{2+} and $Al(OH)_4^-$. Since fewer $Al(OH)_4^-$ reacts with Na^+, this results in less zeolite formation. Mg–Al LDHs tends to be the predominant LDHs (rather than Ca–Al LDHs) in the MgO–$NaAlO_2$ activated system, and, zeolite production is impeded by an aqueous environment rich in Mg^{2+}.

$NaAlO_2$ activated and MgO–$NaAlO_2$ activated slag systems show an improved microstructure over NaOH activated slag systems. This is due to the more $Al(OH)_4^-$ promoting the formation of gel, leading to a denser microstructure. Those is reflected in the mechanical properties and microstructural properties. However, FA and MSWI BA negatively influence the development of microstructure, because of less C(N)–A–S–H formation.

Most importantly, the elevated LDHs enhance the chloride resistance and improve the heavy metal binding capacity in the matrix. With a higher sodium aluminate content, the content of gels in the matrix is promoted. Thereby, the chloride binding capacity is enhanced by the promoted generation of reaction products (LDHs and gels). At the same time, heavy-metal leaching is significantly decreased by the incorporation of MgO, which contributes to more LDHs formation as well. As a result, the leaching of SO_4^{2-} decreased dramatically, since the in-situ-formed LDHs absorbed more SO_4^{2-} than Cl^- with elevated MgO addition, owing to the high affinity of LDHs for SO_4^{2-}.

Thermodynamic modelling results slightly overestimate the phase content compared to experimental results. The predicted heavy metal ions binding capacity of the matrix shows that the uptake of Cu is related to C(N)−A−S−H formation, while the binding capacity of Sb, sulfates, and chlorides increases with the hydrotalcite formation from prolonged curing.

8.1.2 Reuse waste glass in AAMs

In Chapters 6 to 7, alkali activation of slag, fly ash, and waste glass (WG) by NaOH and $NaAlO_2$ are investigated in terms of chloride resistance and efflorescence behavior. The mechanism of how waste glass influences the microstructure and chloride resistance of NaOH activated slag and fly ash is revealed, and the effect of $NaAlO_2$ on waste glass activation has been explored as well. As a silica-rich, aluminum-low material, waste glass plays a role as amorphous silica source to form C(N)−A−S−H gels during alkali activation. In NaOH activated slag and fly ash, the waste glass promotes the formation of the gel, which is due to extra reactive SiO_2 provided by waste glass. In $NaAlO_2$ activated slag and waste glass, $NaAlO_2$ promotes C(N)−A−S−H gels (major product) and zeolite A (secondary product) formation. Furthermore, the elevated pH (associated with NaOH) results in zeolite Na-P_1 as the secondary reaction product. Nonetheless, Si-high, Al- and Ca-low gel is the primary reaction product in sodium hydroxide activation. The effect of $NaAlO_2$ activation is longer main-chain-length and highly crosslinked gels, and Al substitution is significantly higher than that of the NaOH activated matrix.

Moreover, a higher content of waste glass in alkali activated slag and fly ash improves the chloride resistance of the matrix. The waste glass containing AAMs matrix shows both physical and chemical absorption of chloride ions, attributed to mesopores improvement and hydrotalcite phase. $NaAlO_2$ activated slag and waste glass show that extra $Al(OH)_4^-$ from $NaAlO_2$ activator captures more Na^+ to form Na-rich C(N)−A−S−H gels enhancing the resistance to efflorescence.

8.2 Recommendations for future perspectives

This thesis investigates the in-situ formation of LDHs in $NaAlO_2$ activated slag/MSWI BA in terms of chloride resistance and heavy metal binding. Simultaneously, the reuse of waste glass in alkali activated slag/fly ash is evaluated as well. Based on an analysis of mineralogy, microstructure, thermodynamic modelling, mechanical property, and long-term performance, the utilization of these SCMs was comprehensively studied. The presented results can be used for an optimal design of sustainable building materials to achieve properties of excellent durability at low costs. Nevertheless, some open questions remain for future research:

1. Alkalis plays a key role in the activator, the lower pH activation of $NaAlO_2$ activator compared to NaOH shows the feasibility to apply to such low alkaline (low pH) based binders, it can prevent pollution transfer and lower the impact on operation and transport. To effectively quantify and promote the sustainability of the new binder, the basic research about implementation is lacking, that is the actual production, including transport and utilization of specific materials in a given location. Therefore, the environmental impact of low alkaline based binders remains an open debate. The life cycle analysis (LCA) approach can be used to further promote the sustainability of the binder. It can be coupled with experimental data to predict the final environmental impact of the binder. Specifically, the in-situ formation of LDHs can be utilized to predict CO_2 capture along the life cycle of the binder. Because the LDHs show superior CO_2 capture during the curing and use process.

2. Limited knowledge of durability issues like corrosion behavior of reinforced geopolymer concrete impedes the usage of this technology in structural applications. The pH of alkaline activated systems is higher than 13.5, and even 14.5 in some systems, passivation should be achieved directly. However, such a high pH level also may induce the formation of non-stable passivating films on the steel surface. $MgO-NaAlO_2$ activation in this thesis may be the potential approach preventing rebar corrosion by in-situ formed LDHs as an inhibitor and relatively low pH environment to the steel surface. Therefore, the mechanism of the corrosion process of reinforced $MgO-NaAlO_2$ activated slag is vital to be investigated at paste, mortar, and concrete scales.

3. The LDHs also have an excellent capacity to absorb radioactive elements. The in-situ formation of LDHs in $NaAlO_2$ activated slag is successfully achieved in this thesis. Therefore, the $NaAlO_2$ activated slag can be utilized as radiative element absorbent by blending slag with radiative materials from nuclear waste. Furthermore, the environmental impact of blended binders with radiative materials should be evaluated in future research.

4. The application of $NaAlO_2$ activated waste glass and slag reveals that $NaAlO_2$ activator can be utilized to activate Si-rich Al-low raw materials. To effectively evaluate the impact of $Al(OH)_4^-$ from $NaAlO_2$, the gel structure, microstructure, and the long-term performance should be investigated. It offers an opportunity to use low pH and Al-rich activators to develop new Si-rich Al-low SCMs.

References

[1] G. Habert, S.A. Miller, V.M. John, J.L. Provis, A. Favier, A. Horvath, K.L. Scrivener, Environmental impacts and decarbonization strategies in the cement and concrete industries, Nat. Rev. Earth Environ. 1 (2020) 559–573. doi:10.1038/s43017-020-0093-3.

[2] Y. Meng, T.C. Ling, K.H. Mo, W. Tian, Enhancement of high temperature performance of cement blocks via CO 2 curing, Sci. Total Environ. 671 (2019) 827–837. doi:10.1016/j.scitotenv.2019.03.411.

[3] M. Saillio, V. Baroghel-Bouny, S. Pradelle, M. Bertin, J. Vincent, J.B. d'Espinose de Lacaillerie, Effect of supplementary cementitious materials on carbonation of cement pastes, Cem. Concr. Res. 142 (2021). doi:10.1016/j.cemconres.2021.106358.

[4] J. Skibsted, R. Snellings, Reactivity of supplementary cementitious materials (SCMs) in cement blends, Cem. Concr. Res. 124 (2019). doi:10.1016/j.cemconres.2019.105799.

[5] H. Maraghechi, M. Maraghechi, F. Rajabipour, C.G. Pantano, Pozzolanic reactivity of recycled glass powder at elevated temperatures: Reaction stoichiometry, reaction products and effect of alkali activation, Cem. Concr. Compos. 53 (2014) 105–114. doi:10.1016/j.cemconcomp.2014.06.015.

[6] B. Li, T.C. Ling, J.G. Yu, J. Wu, W. Chen, Cement pastes modified with recycled glass and supplementary cementitious materials: Properties at the ambient and high temperatures, J. Clean. Prod. 241 (2019). doi:10.1016/j.jclepro.2019.118155.

[7] H.Y. Zhang, G.H. Qiu, V. Kodur, Z.S. Yuan, Spalling behavior of metakaolin-fly ash based geopolymer concrete under elevated temperature exposure, Cem. Concr. Compos. 106 (2020). doi:10.1016/j.cemconcomp.2019.103483.

[8] M. Nawaz, A. Heitor, M. Sivakumar, Geopolymers in construction - recent developments, Constr. Build. Mater. 260 (2020). doi:10.1016/j.conbuildmat.2020.120472.

[9] O.G. Rivera, W.R. Long, C.A. Weiss, R.D. Moser, B.A. Williams, K. Torres-Cancel, E.R. Gore, P.G. Allison, Effect of elevated temperature on alkali-activated geopolymeric binders compared to portland cement-based binders, Cem. Concr. Res. 90 (2016) 43–51. doi:10.1016/j.cemconres.2016.09.013.

[10] F. Abed. Turkey, S. Bt. Beddu, A. Najah Ahmed, S. Al-Hubboubi, A review – Behaviour of geopolymer concrete to high temperature, Mater. Today Proc. (2021). doi:10.1016/j.matpr.2021.05.489.

[11] C. Shi, X. Wu, M. Tang, Research on alkali-activated cementitious systems in China: A review, Adv. Cem. Res. 5 (1993) 1–7. doi:10.1680/adcr.1993.5.17.1.

[12] K.K. Ramagiri, A. Kar, Effect of high-temperature on the microstructure of alkali-activated binder, Mater. Today Proc. 28 (2019) 1123–1129. doi:10.1016/j.matpr.2020.01.093.

[13] K.K. Ramagiri, A. Kar, Environmental impact assessment of alkali-activated mortar with waste precursors and activators, J. Build. Eng. 44 (2021). doi:10.1016/j.jobe.2021.103391.

[14] S.E. Wallah, B.V. Rangan, Low-calcium fly ash-based geopolymer concrete: Long-term properties, Res. Rep. GC. (2006). http://www.geopolymer.org/fichiers_pdf/curtin_flyash_GC-2.pdf.

[15] J. Zhang, Y. Ma, J. Hu, H. Wang, Z. Zhang, Review on chloride transport in alkali-activated materials: Role of precursors, activators and admixtures, Constr. Build. Mater. 328 (2022). doi:10.1016/j.conbuildmat.2022.127081.

[16] J. Liu, Z. Wang, G. Xie, Z. Li, X. Fan, W. Zhang, F. Xing, L. Tang, J. Ren, Resource utilization of municipal solid waste incineration fly ash - cement and alkali-activated cementitious materials: A review, Sci. Total Environ. 852 (2022). doi:10.1016/j.scitotenv.2022.158254.

[17] F. Pacheco-Torgal, Z. Abdollahnejad, A.F. Camões, M. Jamshidi, Y. Ding, Durability of alkali-activated binders: A clear advantage over Portland cement or an unproven issue?, Constr. Build. Mater. 30 (2012) 400–405. doi:10.1016/j.conbuildmat.2011.12.017.

[18] T. Liu, Q. Yu, H.J.H. Brouwers, In-situ formation of layered double hydroxides (LDHs) in sodium aluminate activated slag: The role of Al-O tetrahedra, Cem. Concr. Res. 153 (2022). doi:10.1016/j.cemconres.2021.106697.

[19] P. Chen, B. Ma, H. Tan, X. Liu, T. Zhang, C. Li, Q. Yang, Z. Luo, Utilization of barium slag to improve chloride-binding ability of cement-based material, J. Clean. Prod. 283 (2021). doi:10.1016/j.jclepro.2020.124612.

[20] T. Yang, Z. Zhang, F. Zhang, Y. Gao, Q. Wu, Chloride and heavy metal binding capacities of hydrotalcite-like phases formed in greener one-part sodium carbonate-activated slag cements, J. Clean. Prod. 253 (2020).

doi:10.1016/j.jclepro.2020.120047.

[21] T. Liu, Y. Chen, Q. Yu, J. Fan, H.J.H. Brouwers, Effect of MgO, Mg-Al-NO3 LDH and calcined LDH-CO3 on chloride resistance of alkali activated fly ash and slag blends, Constr. Build. Mater. 250 (2020). doi:10.1016/j.conbuildmat.2020.118865.

[22] H. Ye, Autogenous formation and smart behaviors of nitrite- and nitrate-intercalated layered double hydroxides (LDHs) in Portland cement-metakaolin-dolomite blends, Cem. Concr. Res. 139 (2021). doi:10.1016/j.cemconres.2020.106267.

[23] J.L. Provis, S.A. Bernal, Geopolymers and Related Alkali-Activated Materials, Annu. Rev. Mater. Res. 44 (2014) 299–327. doi:10.1146/annurev-matsci-070813-113515.

[24] J.L. Provis, J.S.J. Van Deventer, Geopolymers: Structures, processing, properties and industrial applications, Elsevier Ltd, 2009. doi:10.1533/9781845696382.

[25] S.A. Greenberg, T.N. Chang, Investigation of the colloidal hydrated calcium silicates. II. Solubility relationships in the calcium oxide-silica-water system at 25°, J. Phys. Chem. 69 (1965) 182–188. doi:10.1021/j100885a027.

[26] S. Song, D. Sohn, H.M. Jennings, T.O. Mason, Hydration of alkali-activated ground granulated blast furnace slag, J. Mater. Sci. 35 (2000) 249–257. doi:10.1023/A:1004742027117.

[27] Z. Sun, X. Lin, P. Liu, D. Wang, A. Vollpracht, M. Oeser, Study of alkali activated slag as alternative pavement binder, Constr. Build. Mater. 186 (2018) 626–634. doi:10.1016/j.conbuildmat.2018.07.154.

[28] K.H. Yang, A.R. Cho, J.K. Song, Effect of water-binder ratio on the mechanical properties of calcium hydroxide-based alkali-activated slag concrete, Constr. Build. Mater. 29 (2012) 504–511. doi:10.1016/j.conbuildmat.2011.10.062.

[29] X. Ke, S.A. Bernal, J. Provis, Assessing the chloride binding capacity of synthetic cementitious phases in alkali- activated slag simulated pore solution, Ist Int. Conf. Constr. Mater. Sustain. Futur. (2017).

[30] X.H. Zhu, X.J. Kang, K. Yang, C.H. Yang, Effect of graphene oxide on the mechanical properties and the formation of layered double hydroxides (LDHs) in alkali-activated slag cement, Constr. Build. Mater. 132 (2017) 290–295. doi:10.1016/j.conbuildmat.2016.11.059.

[31] H.J. Chen, S.S. Huang, C.W. Tang, M.A. Malek, L.W. Ean, Effect of curing environments on strength, porosity and chloride ingress resistance of blast furnace slag cement concretes: A construction site study, Constr. Build. Mater. 35 (2012) 1063–1070. doi:10.1016/j.conbuildmat.2012.06.052.

[32] S.J. Mills, A.G. Christy, J.-M.R. Génin, T. Kameda, F. Colombo, Nomenclature of the hydrotalcite supergroup: natural layered double hydroxides, Mineral. Mag. 76 (2012) 1289–1336. doi:10.1180/minmag.2012.076.5.10.

[33] S.D. Wang, K.L. Scrivener, P.L. Pratt, Factors affecting the strength of alkali-activated slag, Cem. Concr. Res. 24 (1994) 1033–1043. doi:10.1016/0008-8846(94)90026-4.

[34] J.L. Provis, J.S.J. Van Deventer, Geopolymers: Structures, processing, properties and industrial applications, Geopolymers Struct. Process. Prop. Ind. Appl. (2009) 1–454. doi:10.1533/9781845696382.

[35] T. Luukkonen, H. Sreenivasan, Z. Abdollahnejad, J. Yliniemi, A. Kantola, V.V. Telkki, P. Kinnunen, M. Illikainen, Influence of sodium silicate powder silica modulus for mechanical and chemical properties of dry-mix alkali-activated slag mortar, Constr. Build. Mater. 233 (2020) 117354. doi:10.1016/j.conbuildmat.2019.117354.

[36] C. Ma, G. Long, Y. Shi, Y. Xie, Preparation of cleaner one-part geopolymer by investigating different types of commercial sodium metasilicate in China, J. Clean. Prod. 201 (2018) 636–647. doi:10.1016/j.jclepro.2018.08.060.

[37] B. Yuan, C. Straub, S. Segers, Q.L. Yu, H.J.H. Brouwers, Sodium carbonate activated slag as cement replacement in autoclaved aerated concrete, Ceram. Int. 43 (2017) 6039–6047. doi:10.1016/j.ceramint.2017.01.144.

[38] B. Yuan, Q.L. Yu, H.J.H. Brouwers, Time-dependent characterization of Na 2 CO 3 activated slag, Cem. Concr. Compos. 84 (2017) 188–197. doi:10.1016/j.cemconcomp.2017.09.005.

[39] J. Wang, X.J. Lyu, L. Wang, X. Cao, Q. Liu, H. Zang, Influence of the combination of calcium oxide and sodium carbonate on the hydration reactivity of alkali-activated slag binders, J. Clean. Prod. 171 (2018) 622–629. doi:10.1016/j.jclepro.2017.10.077.

[40] A.M. Rashad, Y. Bai, P.A.M. Basheer, N.B. Milestone, N.C. Collier, Hydration and properties of sodium sulfate activated slag, Cem. Concr. Compos. 37 (2013) 20–29. doi:10.1016/j.cemconcomp.2012.12.010.

[41] H. Tan, X. Deng, X. He, J. Zhang, X. Zhang, Y. Su, J. Yang, Compressive strength and hydration process of

wet-grinded granulated blast-furnace slag activated by sodium sulfate and sodium carbonate, Cem. Concr. Compos. 97 (2019) 387–398. doi:10.1016/j.cemconcomp.2019.01.012.

[42] Z. Shi, C. Shi, S. Wan, N. Li, Z. Zhang, Effect of alkali dosage and silicate modulus on carbonation of alkali-activated slag mortars, Cem. Concr. Res. 113 (2018) 55–64. doi:10.1016/j.cemconres.2018.07.005.

[43] Z. Shi, C. Shi, S. Wan, Z. Zhang, Effects of alkali dosage and silicate modulus on alkali-silica reaction in alkali-activated slag mortars, Cem. Concr. Res. 111 (2018) 104–115. doi:10.1016/j.cemconres.2018.06.005.

[44] G. Möschner, B. Lothenbach, R. Figi, R. Kretzschmar, Influence of slag chemistry on the hydration of alkali-activated blast-furnace slag — Part I: Effect of MgO, Cem. Concr. Res. 39 (2009) 275–282. doi:10.1016/j.cemconres.2009.01.005.

[45] Y. Chen, Z. Shui, W. Chen, Q. Li, G. Chen, Effect of MgO content of synthetic slag on the formation of Mg-Al LDHs and sulfate resistance of slag-fly ash-clinker binder, Constr. Build. Mater. 125 (2016) 766–774. doi:10.1016/j.conbuildmat.2016.08.086.

[46] H.N. Yoon, S.M. Park, H.K. Lee, Effect of MgO on chloride penetration resistance of alkali-activated binder, Constr. Build. Mater. 178 (2018) 584–592. doi:10.1016/j.conbuildmat.2018.05.156.

[47] F. Collins, J.G. Sanjayan, Early age strength and workability of slag pastes activated by NaOH and Na2CO3, Cem. Concr. Res. 28 (1998) 655–664.

[48] Z. Jiao, Y. Wang, W. Zheng, W. Huang, Effect of dosage of sodium carbonate on the strength and drying shrinkage of sodium hydroxide based alkali-activated slag paste, Constr. Build. Mater. 179 (2018) 11–24. doi:10.1016/j.conbuildmat.2018.05.194.

[49] G. Ishwarya, B. Singh, S. Deshwal, S.K. Bhattacharyya, Effect of sodium carbonate/sodium silicate activator on the rheology, geopolymerization and strength of fly ash/slag geopolymer pastes, Cem. Concr. Compos. 97 (2019) 226–238. doi:10.1016/j.cemconcomp.2018.12.007.

[50] H. Ye, Z. Chen, L. Huang, Mechanism of sulfate attack on alkali-activated slag: The role of activator composition, Cem. Concr. Res. 125 (2019) 105868. doi:10.1016/j.cemconres.2019.105868.

[51] S.K. Nath, S. Kumar, Role of alkali concentration on reaction kinetics of fly ash geopolymerization, J. Non. Cryst. Solids. 505 (2019) 241–251. doi:10.1016/j.jnoncrysol.2018.11.007.

[52] F. Winnefeld, A. Leemann, M. Lucuk, P. Svoboda, M. Neuroth, Assessment of phase formation in alkali activated low and high calcium fly ashes in building materials, Constr. Build. Mater. 24 (2010) 1086–1093. doi:10.1016/j.conbuildmat.2009.11.007.

[53] J.S.J. van Deventer, J.L. Provis, P. Duxson, G.C. Lukey, Reaction mechanisms in the geopolymeric conversion of inorganic waste to useful products, J. Hazard. Mater. 139 (2007) 506–513. doi:10.1016/j.jhazmat.2006.02.044.

[54] M. Criado, A. Fernández-Jiménez, A.G. de la Torre, M.A.G. Aranda, A. Palomo, An XRD study of the effect of the SiO2/Na2O ratio on the alkali activation of fly ash, Cem. Concr. Res. 37 (2007) 671–679. doi:10.1016/j.cemconres.2007.01.013.

[55] J.E. Oh, P.J.M. Monteiro, S.S. Jun, S. Choi, S.M. Clark, The evolution of strength and crystalline phases for alkali-activated ground blast furnace slag and fly ash-based geopolymers, Cem. Concr. Res. 40 (2010) 189–196. doi:10.1016/j.cemconres.2009.10.010.

[56] C.A. Rees, J.L. Provis, G.C. Lukey, J.S.J. Van Deventer, Attenuated total reflectance fourier transform infrared analysis of fly ash geopolymer gel aging, Langmuir. 23 (2007) 8170–8179. doi:10.1021/la700713g.

[57] N.R. Rakhimova, R.Z. Rakhimov, Reaction products, structure and properties of alkali-activated metakaolin cements incorporated with supplementary materials - A review, J. Mater. Res. Technol. 8 (2019) 1522–1531. doi:10.1016/j.jmrt.2018.07.006.

[58] C.E. White, J.L. Provis, T. Proffen, J.S.J. van Deventer, Molecular mechanisms responsible for the structural changes occurring during geopolymerization: Multiscale simulation, AIChE J. 58 (2012) 2241–2253. doi:10.1002/aic.12743.

[59] M.L. Granizo, M.T. Blanco-Varela, S. Martínez-Ramírez, Alkali activation of metakaolins: Parameters affecting mechanical, structural and microstructural properties, J. Mater. Sci. 42 (2007) 2934–2943. doi:10.1007/s10853-006-0565-y.

[60] M.L. Granizo, S. Alonso, M.T. Blanco-Varela, A. Palomo, Alkaline Activation of Metakaolin: Effect of Calcium Hydroxide in the Products of Reaction, J. Am. Ceram. Soc. 85 (2004) 225–231. doi:10.1111/j.1151-2916.2002.tb00070.x.

[61] M.L. Granizo, M.T. Blanco-Varela, A. Palomo, Influence of the starting kaolin on alkali-activated materials

based on metakaolin. Study of the reaction parameters by isothermal conduction calorimetry, J. Mater. Sci. 35 (2000) 6309–6315. doi:10.1023/A:1026790924882.

[62] N.K. Lee, H.K. Lee, Reactivity and reaction products of alkali-activated, fly ash/slag paste, Constr. Build. Mater. 81 (2015) 303–312. doi:10.1016/j.conbuildmat.2015.02.022.

[63] S.A. Bernal, J.L. Provis, V. Rose, R. Mejía De Gutierrez, Evolution of binder structure in sodium silicate-activated slag-metakaolin blends, Cem. Concr. Compos. 33 (2011) 46–54. doi:10.1016/j.cemconcomp.2010.09.004.

[64] A. Mobili, A. Belli, C. Giosuè, T. Bellezze, F. Tittarelli, Metakaolin and fly ash alkali-activated mortars compared with cementitious mortars at the same strength class, Cem. Concr. Res. 88 (2016) 198–210. doi:10.1016/j.cemconres.2016.07.004.

[65] H. Alanazi, J. Hu, Y.R. Kim, Effect of slag, silica fume, and metakaolin on properties and performance of alkali-activated fly ash cured at ambient temperature, Constr. Build. Mater. 197 (2019) 747–756. doi:10.1016/j.conbuildmat.2018.11.172.

[66] G. Liu, M.V.A. Florea, H.J.H. Brouwers, Characterization and performance of high volume recycled waste glass and ground granulated blast furnace slag or fly ash blended mortars, J. Clean. Prod. 235 (2019) 461–472. doi:10.1016/j.jclepro.2019.06.334.

[67] S.P. Kang, S.J. Kwon, Effects of red mud and Alkali-Activated Slag Cement on efflorescence in cement mortar, Constr. Build. Mater. 133 (2017) 459–467. doi:10.1016/j.conbuildmat.2016.12.123.

[68] P. Krivenko, O. Kovalchuk, A. Pasko, T. Croymans, M. Hult, G. Lutter, N. Vandevenne, S. Schreurs, W. Schroeyers, Development of alkali activated cements and concrete mixture design with high volumes of red mud, Constr. Build. Mater. 151 (2017) 819–826. doi:10.1016/j.conbuildmat.2017.06.031.

[69] A. Darsanasiri, F. Matalkah, S. Ramli, K. Al-Jalode, A. Balachandra, P. Soroushian, Ternary alkali aluminosilicate cement based on rice husk ash, slag and coal fly ash, J. Build. Eng. 19 (2018) 36–41. doi:10.1016/j.jobe.2018.04.020.

[70] K.T. Tong, R. Vinai, M.N. Soutsos, Use of Vietnamese rice husk ash for the production of sodium silicate as the activator for alkali-activated binders, J. Clean. Prod. 201 (2018) 272–286. doi:10.1016/j.jclepro.2018.08.025.

[71] I. Ismail, S.A. Bernal, J.L. Provis, R. San Nicolas, S. Hamdan, J.S.J. Van Deventer, Modification of phase evolution in alkali-activated blast furnace slag by the incorporation of fly ash, Cem. Concr. Compos. 45 (2014) 125–135. doi:10.1016/j.cemconcomp.2013.09.006.

[72] H. Jiao, S. Wang, A. Wu, H. Shen, J. Wang, Cementitious property of NaAlO2-activated Ge slag as cement supplement, Int. J. Miner. Metall. Mater. 26 (2019) 1594–1603. doi:10.1007/s12613-019-1901-y.

[73] A. Nikolov, H. Nugteren, I. Rostovsky, Optimization of geopolymers based on natural zeolite clinoptilolite by calcination and use of aluminate activators, Constr. Build. Mater. 243 (2020). doi:10.1016/j.conbuildmat.2020.118257.

[74] C. Forano, U. Costantino, V. Prévot, C.T. Gueho, Layered double hydroxides (LDH), 2013. doi:10.1016/B978-0-08-098258-8.00025-0.

[75] C. Tennakoon, A. Shayan, J.G. Sanjayan, A. Xu, Chloride ingress and steel corrosion in geopolymer concrete based on long term tests, Mater. Des. 116 (2017) 287–299. doi:10.1016/j.matdes.2016.12.030.

[76] J. Osio-Norgaard, J.P. Gevaudan, W. V. Srubar, A review of chloride transport in alkali-activated cement paste, mortar, and concrete, Constr. Build. Mater. 186 (2018) 191–206. doi:10.1016/j.conbuildmat.2018.07.119.

[77] G. Koch, Cost of corrosion, Trends Oil Gas Corros. Res. Technol. Prod. Transm. (2017) 3–30. doi:10.1016/B978-0-08-101105-8.00001-2.

[78] G. Li, X. Zhang, J. Sun, A. Zhang, C. Liao, Effective removal of bisphenols from aqueous solution with magnetic hierarchical rattle-like Co/Ni-based LDH, J. Hazard. Mater. 381 (2020) 120985. doi:10.1016/j.jhazmat.2019.120985.

[79] J.L. Provis, J.S.J. Van Deventer, Introduction to geopolymers, Geopolymers Struct. Process. Prop. Ind. Appl. (2009) 1–11. doi:10.1533/9781845696382.1.

[80] D.G. Costa, A.B. Rocha, W.F. Souza, S.S.X. Chiaro, A.A. Leitão, Comparative Structural, thermodynamic and electronic analyses of Zn-Al-A n- hydrotalcite-like compounds (A n-Cl -, F -, Br -, OH -, CO 32- or NO 3-: An ab initio study, Appl. Clay Sci. 56 (2012) 16–22. doi:10.1016/j.clay.2011.11.014.

[81] J. Xu, Y. Song, Y. Zhao, L. Jiang, Y. Mei, P. Chen, Chloride removal and corrosion inhibitions of nitrate, nitrite-intercalated Mg–Al layered double hydroxides on steel in saturated calcium hydroxide solution, Appl.

Clay Sci. 163 (2018) 129–136. doi:10.1016/j.clay.2018.07.023.

[82] M. Chi, Effects of dosage of alkali-activated solution and curing conditions on the properties and durability of alkali-activated slag concrete, Constr. Build. Mater. 35 (2012) 240–245. doi:10.1016/j.conbuildmat.2012.04.005.

[83] S.A. Bernal, R. Mejía De Gutiérrez, J.L. Provis, Engineering and durability properties of concretes based on alkali-activated granulated blast furnace slag/metakaolin blends, Constr. Build. Mater. 33 (2012) 99–108. doi:10.1016/j.conbuildmat.2012.01.017.

[84] K. Behfarnia, M. Rostami, Effects of micro and nanoparticles of SiO2 on the permeability of alkali activated slag concrete, Constr. Build. Mater. 131 (2017) 205–213. doi:10.1016/j.conbuildmat.2016.11.070.

[85] R.J. Thomas, E. Ariyachandra, D. Lezama, S. Peethamparan, Comparison of chloride permeability methods for Alkali-Activated concrete, Constr. Build. Mater. 165 (2018) 104–111. doi:10.1016/j.conbuildmat.2018.01.016.

[86] H.N. Yoon, S.M. Park, H.K. Lee, Effect of MgO on chloride penetration resistance of alkali-activated binder, Constr. Build. Mater. 178 (2018) 584–592. doi:10.1016/j.conbuildmat.2018.05.156.

[87] C. Monticelli, M.E. Natali, A. Balbo, C. Chiavari, F. Zanotto, S. Manzi, M.C. Bignozzi, A study on the corrosion of reinforcing bars in alkali-activated fly ash mortars under wet and dry exposures to chloride solutions, Cem. Concr. Res. 87 (2016) 53–63. doi:10.1016/j.cemconres.2016.05.010.

[88] I. Ismail, S.A. Bernal, J.L. Provis, R. San Nicolas, D.G. Brice, A.R. Kilcullen, S. Hamdan, J.S.J. Van Deventer, Influence of fly ash on the water and chloride permeability of alkali-activated slag mortars and concretes, Constr. Build. Mater. 48 (2013) 1187–1201. doi:10.1016/j.conbuildmat.2013.07.106.

[89] M. Babaee, A. Castel, Chloride diffusivity, chloride threshold, and corrosion initiation in reinforced alkali-activated mortars: Role of calcium, alkali, and silicate content, Cem. Concr. Res. 111 (2018) 56–71. doi:10.1016/j.cemconres.2018.06.009.

[90] A. Noushini, A. Castel, J. Aldred, A. Rawal, Chloride diffusion resistance and chloride binding capacity of fly ash-based geopolymer concrete, Cem. Concr. Compos. (2019) 103290. doi:10.1016/j.cemconcomp.2019.04.006.

[91] P.S. Mangat, O.O. Ojedokun, Bound chloride ingress in alkali activated concrete, Constr. Build. Mater. 212 (2019) 375–387. doi:10.1016/j.conbuildmat.2019.03.302.

[92] D. Bondar, M. Basheer, S. Nanukuttan, Suitability of alkali activated slag/fly ash (AA-GGBS/FA) concretes for chloride environments: Characterisation based on mix design and compliance testing, Constr. Build. Mater. 216 (2019) 612–621. doi:10.1016/j.conbuildmat.2019.05.043.

[93] D. Ravikumar, N. Neithalath, Electrically induced chloride ion transport in alkali activated slag concretes and the influence of microstructure, Cem. Concr. Res. 47 (2013) 31–42. doi:10.1016/j.cemconres.2013.01.007.

[94] X. Ke, S.A. Bernal, O.H. Hussein, J.L. Provis, Chloride binding and mobility in sodium carbonate-activated slag pastes and mortars, Mater. Struct. Constr. 50 (2017). doi:10.1617/s11527-017-1121-8.

[95] X. Hu, C. Shi, Z. Shi, L. Zhang, Compressive strength, pore structure and chloride transport properties of alkali-activated slag/fly ash mortars, Cem. Concr. Compos. 104 (2019). doi:10.1016/j.cemconcomp.2019.01.010.

[96] Z.Y. Qu, Q.L. Yu, H.J.H. Brouwers, Relationship between the particle size and dosage of LDHs and concrete resistance against chloride ingress, Cem. Concr. Res. 105 (2018) 81–90. doi:10.1016/j.cemconres.2018.01.005.

[97] D. Tichit, G. Layrac, C. Gérardin, Synthesis of layered double hydroxides through continuous flow processes: A review, Chem. Eng. J. 369 (2019) 302–332. doi:10.1016/j.cej.2019.03.057.

[98] M. Ben Haha, B. Lothenbach, G. Le Saout, F. Winnefeld, Influence of slag chemistry on the hydration of alkali-activated blast-furnace slag — Part I: Effect of MgO, Cem. Concr. Res. 41 (2011) 955–963. doi:10.1016/j.cemconres.2011.05.002.

[99] Y. Chen, Z. Shui, W. Chen, G. Chen, Chloride binding of synthetic Ca-Al-NO3 LDHs in hardened cement paste, Constr. Build. Mater. 93 (2015) 1051–1058. doi:10.1016/j.conbuildmat.2015.05.047.

[100] L. El Gaini, M. Lakraimi, E. Sebbar, A. Meghea, M. Bakasse, Removal of indigo carmine dye from water to Mg-Al-CO3-calcined layered double hydroxides, J. Hazard. Mater. 161 (2009) 627–632. doi:10.1016/j.jhazmat.2008.04.089.

[101] T. Sato, T. Wakabayashi, M. Shlmada, Adsorption of Various Anions by Magnesium Aluminum Oxide of (Mg0.7Al0.3O1.15), Ind. Eng. Chem. Prod. Res. Dev. 25 (1986) 89–92. doi:10.1021/i300021a020.

[102] X. Ke, S.A. Bernal, J.L. Provis, Controlling the reaction kinetics of sodium carbonate-activated slag cements

using calcined layered double hydroxides, Cem. Concr. Res. 81 (2016) 24–37. doi:10.1016/j.cemconres.2015.11.012.

[103] M.A. Shand, The Chemistry and Technology of Magnesia, Chem. Technol. Magnesia. (2006) 1–266. doi:10.1002/0471980579.

[104] En 196-1, Methods of testing cement - Part 1: Determination of strength, (2005) 1–33.

[105] N. De Belie, J.Kratky, S.Van Vlierberghe, Influence of pozzolans and slag on the microstructure of partially carbonated cement paste by means of water vapour and nitrogen sorption experiments and BET calculations, Cem. Concr. Res. 40 (2010) 1723–1733. doi:10.1016/j.cemconres.2010.08.014.

[106] NORDTEST, NT Build 492, Nordtest. Proj. 1388 (1999) 1–8.

[107] K. Barlos, D. Gatos, J. Kallitsis, G. Papaphotiu, P. Sotiriu, Y. Wenging, W. Schäfer, Geopolymers and geopolymeric materials, Tetrahedron Lett. 30 (1989) 3943–3946. doi:10.1190/segam2013-0137.1.

[108] J. Davidovits, Geopolymers - Inorganic polymeric new materials, J. Therm. Anal. 37 (1991) 1633–1656. doi:10.1007/BF01912193.

[109] M. Ben Haha, B. Lothenbach, G. Le Saout, F. Winnefeld, Influence of slag chemistry on the hydration of alkali-activated blast-furnace slag - Part II: Effect of Al2O3, Cem. Concr. Res. 42 (2012) 74–83. doi:10.1016/j.cemconres.2011.08.005.

[110] X. Ke, S.A. Bernal, J.L. Provis, Uptake of chloride and carbonate by Mg-Al and Ca-Al layered double hydroxides in simulated pore solutions of alkali-activated slag cement, Cem. Concr. Res. 100 (2017) 1–13. doi:10.1016/j.cemconres.2017.05.015.

[111] Z. Ali, I. Khan, I. Ahmad, M.S. Khan, S.J. Asadabadi, Materials Chemistry and Physics, 3 (2015) 1–8. doi:10.1016/j.matchemphys.2015.05.072.

[112] G. Liu, M.V.A. Florea, H.J.H. Brouwers, Waste glass as binder in alkali activated slag–fly ash mortars, Mater. Struct. 52 (2019). doi:10.1617/s11527-019-1404-3.

[113] F. Moghaddam, V. Sirivivatnanon, K. Vessalas, The effect of fly ash fineness on heat of hydration, microstructure, flow and compressive strength of blended cement pastes, Case Stud. Constr. Mater. 10 (2019). doi:10.1016/j.cscm.2019.e00218.

[114] K. Kiattikomol, C. Jaturapitakkul, S. Songpiriyakij, S. Chutubtim, A study of ground coarse fly ashes with different finenesses from various sources as pozzolanic materials, Cem. Concr. Compos. 23 (2001) 335–343. doi:10.1016/S0958-9465(01)00016-6.

[115] F. Jin, K. Gu, A. Al-Tabbaa, Strength and drying shrinkage of reactive MgO modified alkali-activated slag paste, Constr. Build. Mater. 51 (2014) 395–404. doi:10.1016/j.conbuildmat.2013.10.081.

[116] F. Jin, K. Gu, A. Al-Tabbaa, Strength and hydration properties of reactive MgO-activated ground granulated blastfurnace slag paste, Cem. Concr. Compos. 57 (2015) 8–16. doi:10.1016/j.cemconcomp.2014.10.007.

[117] C.L. Hwang, D.H. Vo, V.A. Tran, M.D. Yehualaw, Effect of high MgO content on the performance of alkali-activated fine slag under water and air curing conditions, Constr. Build. Mater. 186 (2018) 503–513. doi:10.1016/j.conbuildmat.2018.07.129.

[118] P. Duan, W. Chen, J. Ma, Z. Shui, Influence of layered double hydroxides on microstructure and carbonation resistance of sulphoaluminate cement concrete, Constr. Build. Mater. 48 (2013) 601–609. doi:10.1016/j.conbuildmat.2013.07.049.

[119] Y. Chen, R. Yu, X. Wang, J. Chen, Z. Shui, Evaluation and optimization of Ultra-High Performance Concrete (UHPC) subjected to harsh ocean environment: Towards an application of Layered Double Hydroxides (LDHs), Constr. Build. Mater. 177 (2018) 51–62. doi:10.1016/j.conbuildmat.2018.03.210.

[120] S.A. Bernal, R. San Nicolas, R.J. Myers, R. Mejía De Gutiérrez, F. Puertas, J.S.J. Van Deventer, J.L. Provis, MgO content of slag controls phase evolution and structural changes induced by accelerated carbonation in alkali-activated binders, Cem. Concr. Res. 57 (2014) 33–43. doi:10.1016/j.cemconres.2013.12.003.

[121] C. Shi, Effect of mixing proportions of concrete on its electrical conductivity and the rapid chloride permeability test (ASTM C1202 or ASSHTO T277) results, Cem. Concr. Res. 34 (2004) 537–545.

[122] J.C. Liu, T.J. Wang, L.C. Sung, P.F. Kao, T.Y. Yang, W.R. Hao, C.C. Chen, Y.P. Hsu, S.Y. Wu, Influenza vaccination reduces hemorrhagic stroke risk in patients with atrial fibrillation: A population-based cohort study, Int. J. Cardiol. 232 (2017) 315–323. doi:10.1016/j.ijcard.2016.12.074.

[123] M. Babaee, A. Castel, Water vapor sorption isotherms, pore structure, and moisture transport characteristics of alkali-activated and Portland cement-based binders, Cem. Concr. Res. 113 (2018) 99–120. doi:10.1016/j.cemconres.2018.07.006.

[124] P. Spiesz, H.J.H. Brouwers, Influence of the applied voltage on the Rapid Chloride Migration (RCM) test, Cem. Concr. Res. 42 (2012) 1072–1082. doi:10.1016/j.cemconres.2012.04.007.

[125] A. Wang, Y. Zheng, Z. Zhang, K. Liu, Y. Li, L. Shi, D. Sun, The Durability of Alkali-Activated Materials in Comparison with Ordinary Portland Cements and Concretes: A Review, Engineering. 6 (2020) 695–706. doi:10.1016/j.eng.2019.08.019.

[126] J. Zhang, C. Shi, Z. Zhang, Z. Ou, Durability of alkali-activated materials in aggressive environments: A review on recent studies, Constr. Build. Mater. 152 (2017) 598–613. doi:10.1016/j.conbuildmat.2017.07.027.

[127] E. Adesanya, P. Perumal, T. Luukkonen, J. Yliniemi, K. Ohenoja, P. Kinnunen, M. Illikainen, Opportunities to improve sustainability of alkali-activated materials: A review of side-stream based activators, J. Clean. Prod. 286 (2021). doi:10.1016/j.jclepro.2020.125558.

[128] X. Ke, S.A. Bernal, O.H. Hussein, J.L. Provis, Chloride binding and mobility in sodium carbonate-activated slag pastes and mortars, Mater. Struct. Constr. 50 (2017). doi:10.1617/s11527-017-1121-8.

[129] Z. Yang, H. Fischer, R. Polder, Laboratory investigation of the influence of two types of modified hydrotalcites on chloride ingress into cement mortar, Cem. Concr. Compos. 58 (2015) 105–113. doi:10.1016/j.cemconcomp.2014.12.016.

[130] X. Ke, S.A. Bernal, J.L. Provis, Uptake of chloride and carbonate by Mg-Al and Ca-Al layered double hydroxides in simulated pore solutions of alkali-activated slag cement, Cem. Concr. Res. 100 (2017) 1–13. doi:10.1016/j.cemconres.2017.05.015.

[131] S. Mundra, D.P. Prentice, S.A. Bernal, J.L. Provis, Modelling chloride transport in alkali-activated slags, Cem. Concr. Res. 130 (2020) 106011. doi:10.1016/j.cemconres.2020.106011.

[132] C. Forano, U. Costantino, V. Prévot, C.T. Gueho, Layered double hydroxides (LDH), Dev. Clay Sci. 5 (2013) 745–782. doi:10.1016/B978-0-08-098258-8.00025-0.

[133] S. Mallakpour, M. Dinari, Intercalation of amino acid containing chiral dicarboxylic acid between Mg-Al layered double hydroxide: Preparation and characterization, J. Therm. Anal. Calorim. 119 (2015) 1123–1130. doi:10.1007/s10973-014-4166-8.

[134] A.A. Ramezanianpour, V.M. Malhotra, Effect of curing on the compressive strength, resistance to chloride-ion penetration and porosity of concretes incorporating slag, fly ash or silica fume, Cem. Concr. Compos. 17 (1995) 125–133. doi:10.1016/0958-9465(95)00005-W.

[135] R. Cao, S. Zhang, N. Banthia, Y. Zhang, Z. Zhang, Interpreting the early-age reaction process of alkali-activated slag by using combined embedded ultrasonic measurement, thermal analysis, XRD, FTIR and SEM, Compos. Part B Eng. 186 (2020) 107840. doi:10.1016/j.compositesb.2020.107840.

[136] D. Ravikumar, N. Neithalath, Electrically induced chloride ion transport in alkali activated slag concretes and the influence of microstructure, Cem. Concr. Res. 47 (2013) 31–42. doi:10.1016/j.cemconres.2013.01.007.

[137] J.L.Provis, S.A.Bernal, Geopolymers and related alkali-activated Materials, Annu. Rev. Mater. Res. 44 (2014) 299–327.

[138] Q. Wan, F. Rao, S. Song, R.E. García, R.M. Estrella, C.L. Patiño, Y. Zhang, Geopolymerization reaction, microstructure and simulation of metakaolin-based geopolymers at extended Si/Al ratios, Cem. Concr. Compos. 79 (2017) 45–52. doi:10.1016/j.cemconcomp.2017.01.014.

[139] EN 196-1, En 196-1, (2005) 1–33.

[140] G. Plusquellec, M.R. Geiker, J. Lindgård, J. Duchesne, B. Fournier, K. De Weerdt, Determination of the pH and the free alkali metal content in the pore solution of concrete: Review and experimental comparison, Cem. Concr. Res. 96 (2017) 13–26. doi:10.1016/j.cemconres.2017.03.002.

[141] K. De Weerdt, G. Plusquellec, A. Belda Revert, M.R. Geiker, B. Lothenbach, Effect of carbonation on the pore solution of mortar, Cem. Concr. Res. 118 (2019) 38–56. doi:10.1016/j.cemconres.2019.02.004.

[142] Z. Jia, R. Cao, C. Chen, Y. Zhang, Using in-situ observation to understand the leaching behavior of Portland cement and alkali-activated slag pastes, Compos. Part B Eng. 177 (2019). doi:10.1016/j.compositesb.2019.107366.

[143] N.T. Dung, T.J.N. Hooper, C. Unluer, Accelerating the reaction kinetics and improving the performance of Na2CO3-activated GGBS mixes, Cem. Concr. Res. 126 (2019). doi:10.1016/j.cemconres.2019.105927.

[144] X. Ke, S.A. Bernal, J.L. Provis, Controlling the reaction kinetics of sodium carbonate-activated slag cements using calcined layered double hydroxides, Cem. Concr. Res. 81 (2016) 24–37. doi:10.1016/j.cemconres.2015.11.012.

[145] A. Fernández-Jiménez, F. Puertas, Setting of alkali-activated slag cement. Influence of activator nature, Adv.

Cem. Res. 13 (2001) 115–121. doi:10.1680/adcr.2001.13.3.115.

[146] S.R. Paudel, M. Yang, Z. Gao, PH Level of Pore Solution in Alkali-Activated Fly-Ash Geopolymer Concrete and Its Effect on ASR of Aggregates with Different Silicate Contents, J. Mater. Civ. Eng. 32 (2020) 04020257. doi:10.1061/(ASCE)MT.1943-5533.0003344.

[147] Yibing Zuo, Marija Nedeljković, Guang Ye, Pore solution composition of alkali-activated slag/fly ash pastes, Cem. Concr. Res. 41 (2019) 1257–1278. https://doi.org/10.1016/j.cemconres.2018.10.010.

[148] P. Li, J. Tang, Y. Bai, X. Chen, J. Chen, Experimental study on the pH for activating ground granulated blast-furnace slag activity at different temperatures, Sadhana - Acad. Proc. Eng. Sci. 44 (2019). doi:10.1007/s12046-019-1204-z.

[149] Q. Li, H. Ma, Y. Tang, W. Chen, Combined effect of NaAlO2 and NaOH on the early age hydration of Portland cement with a high concentration of borate solution, Cem. Concr. Res. 144 (2021). doi:10.1016/j.cemconres.2021.106430.

[150] T. Liu, Y. Chen, Q. Yu, J. Fan, H.J.H. Brouwers, Effect of MgO, Mg-Al-NO3 LDH and calcined LDH-CO3 on chloride resistance of alkali activated fly ash and slag blends, Constr. Build. Mater. (2020). doi:10.1016/j.conbuildmat.2020.118865.

[151] I.G. Richardson, Tobermorite/jennite- and tobermorite/calcium hydroxide-based models for the structure of C-S-H: Applicability to hardened pastes of tricalcium silicate, β-dicalcium silicate, Portland cement, and blends of Portland cement with blast-furnace slag, metakaol, Cem. Concr. Res. 34 (2004) 1733–1777. doi:10.1016/j.cemconres.2004.05.034.

[152] M. Król, P. Rożek, D. Chlebda, W. Mozgawa, ATR/FT-IR studies of zeolite formation during alkali-activation of metakaolin, Solid State Sci. 94 (2019) 114–119. doi:10.1016/j.solidstatesciences.2019.06.004.

[153] G. Liu, M.V.A. Florea, H.J.H. Brouwers, The role of recycled waste glass incorporation on the carbonation behaviour of sodium carbonate activated slag mortar, J. Clean. Prod. 292 (2021). doi:10.1016/j.jclepro.2021.126050.

[154] E.R. McCaslin, C.E. White, A parametric study of accelerated carbonation in alkali-activated slag, Cem. Concr. Res. 145 (2021). doi:10.1016/j.cemconres.2021.106454.

[155] L. Fernández-Carrasco, J. Rius, C. Miravitlles, Supercritical carbonation of calcium aluminate cement, Cem. Concr. Res. 38 (2008) 1033–1037. doi:10.1016/j.cemconres.2008.02.013.

[156] R. Xiao, Y. Zhang, X. Jiang, P. Polaczyk, Y. Ma, B. Huang, Alkali-activated slag supplemented with waste glass powder: Laboratory characterization, thermodynamic modelling and sustainability analysis, J. Clean. Prod. 286 (2021). doi:10.1016/j.jclepro.2020.125554.

[157] I. Perná, M. Šupová, T. Hanzlíček, Gehlenite and anorthite formation from fluid fly ash, J. Mol. Struct. 1157 (2018) 476–481. doi:10.1016/j.molstruc.2017.12.084.

[158] A.M. Rashad, G.M.F. Essa, Effect of ceramic waste powder on alkali-activated slag pastes cured in hot weather after exposure to elevated temperature, Cem. Concr. Compos. 111 (2020). doi:10.1016/j.cemconcomp.2020.103617.

[159] Z. Yan, Z. Sun, J. Yang, H. Yang, Y. Ji, K. Hu, Mechanical performance and reaction mechanism of copper slag activated with sodium silicate or sodium hydroxide, Constr. Build. Mater. 266 (2021). doi:10.1016/j.conbuildmat.2020.120900.

[160] F.B. Reig, J.V.G. Adelantado, M.C.M. Moya Moreno, FTIR quantitative analysis of calcium carbonate (calcite) and silica (quartz) mixtures using the constant ratio method. Application to geological samples, Talanta. 58 (2002) 811–821. doi:10.1016/S0039-9140(02)00372-7.

[161] M. Criado, A. Fernández-Jiménez, A. Palomo, Alkali Activation of fly ash: Effect of the SiO2/Na2O ratio Part I: FTIR study, Microporous Mesoporous Mater. 106 (2007) 180–191.

[162] X. Gao, B. Yuan, Q.L. Yu, H.J.H. Brouwers, Characterization and application of municipal solid waste incineration (MSWI) bottom ash and waste granite powder in alkali activated slag, J. Clean. Prod. 164 (2017) 410–419. doi:10.1016/j.jclepro.2017.06.218.

[163] E. Loginova, K. Schollbach, M. Proskurnin, H.J.H. Brouwers, Municipal solid waste incineration bottom ash fines: Transformation into a minor additional constituent for cements, Resour. Conserv. Recycl. 166 (2021). doi:10.1016/j.resconrec.2020.105354.

[164] X.G. Li, Y. Lv, B.G. Ma, Q. Bin Chen, X.B. Yin, S.W. Jian, Utilization of municipal solid waste incineration bottom ash in blended cement, J. Clean. Prod. 32 (2012) 96–100. doi:10.1016/j.jclepro.2012.03.038.

[165] R. Carvalho, R. V. Silva, J. de Brito, M.F.C. Pereira, Alkali activation of bottom ash from municipal solid

waste incineration: Optimization of NaOH- and Na 2SiO3-based activators, J. Clean. Prod. 291 (2021). doi:10.1016/j.jclepro.2021.125930.

[166] P. H. Brunner, H. Rechberger, Waste to energy – key element for sustainable waste management, Waste Manag. 37 (2015) 3–12. doi: 10.1016/j.wasman.2014.02.003.

[167] Q. Song, Z. Wang, J. Li, Environmental performance of municipal solid waste strategies based on LCA method: A case study of Macau, J. Clean. Prod. 57 (2013) 92–100. doi:10.1016/j.jclepro.2013.04.042.

[168] H. Birgisdóttir, K.A. Pihl, G. Bhander, M.Z. Hauschild, T.H. Christensen, Environmental assessment of roads constructed with and without bottom ash from municipal solid waste incineration, Transp. Res. Part D Transp. Environ. 11 (2006) 358–368. doi:10.1016/j.trd.2006.07.001.

[169] W. Zhu, X. Chen, L.J. Struble, E.H. Yang, Characterization of calcium-containing phases in alkali-activated municipal solid waste incineration bottom ash binder through chemical extraction and deconvoluted Fourier transform infrared spectra, J. Clean. Prod. 192 (2018) 782–789. doi:10.1016/j.jclepro.2018.05.049.

[170] A. Jawad, L. Peng, Z. Liao, Z. Zhou, A. Shahzad, J. Ifthikar, M. Zhao, Z. Chen, Z. Chen, Selective removal of heavy metals by hydrotalcites as adsorbents in diverse wastewater: Different intercalated anions with different mechanisms, J. Clean. Prod. 211 (2019) 1112–1126. doi:10.1016/j.jclepro.2018.11.234.

[171] D. Nordmark, A. Lagerkvist, Controlling the mobility of chromium and molybdenum in MSWI fly ash in a washing process, Waste Manag. 76 (2018) 727–733. doi:10.1016/j.wasman.2018.03.016.

[172] B. Chen, J. Wang, J. Zhao, Effect of Sodium Aluminate Dosage as a Solid Alkaline Activator on the Properties of Alkali-Activated Slag Paste, Adv. Mater. Sci. Eng. 2021 (2021). doi:10.1155/2021/6658588.

[173] J.W. Phair, J.S.J. Van Deventer, Characterization of fly-ash-based geopolymeric binders activated with sodium aluminate, Ind. Eng. Chem. Res. 41 (2002) 4242–4251. doi:10.1021/ie010937o.

[174] Y. Zuo, M. Nedeljković, G. Ye, Coupled thermodynamic modelling and experimental study of sodium hydroxide activated slag, Constr. Build. Mater. 188 (2018) 262–279. doi:10.1016/j.conbuildmat.2018.08.087.

[175] R.J. Myers, S.A. Bernal, J.L. Provis, A thermodynamic model for C-(N-)A-S-H gel: CNASH-ss. Derivation and validation, Cem. Concr. Res. 66 (2014) 27–47. doi:10.1016/j.cemconres.2014.07.005.

[176] R.J. Myers, S.A. Bernal, J.L. Provis, Phase diagrams for alkali-activated slag binders, Cem. Concr. Res. 95 (2017) 30–38. doi:10.1016/j.cemconres.2017.02.006.

[177] H. Ye, A. Radlińska, Quantitative analysis of phase assemblage and chemical shrinkage of Alkali-activated slag, J. Adv. Concr. Technol. 14 (2016) 245–260. doi:10.3151/jact.14.245.

[178] Y. Liu, Q. Chen, M.C. Dalconi, S. Molinari, L. Valentini, Y. Wang, S. Sun, P. Wang, G. Artioli, Retention of phosphorus and fluorine in phosphogypsum for cemented paste backfill: Experimental and numerical simulation studies, Environ. Res. 214 (2022). doi:10.1016/j.envres.2022.113775.

[179] Q. Liu, X. Wang, M. Gao, Y. Guan, C. Wu, Q. Wang, Y. Rao, S. Liu, Heavy metal leaching behaviour and long-term environmental risk assessment of cement-solidified municipal solid waste incineration fly ash in sanitary landfill, Chemosphere. 300 (2022). doi:10.1016/j.chemosphere.2022.134571.

[180] A.A. Coelho, TOPAS and TOPAS-Academic: An optimization program integrating computer algebra and crystallographic objects written in C++: An, J. Appl. Crystallogr. 51 (2018) 210–218. doi:10.1107/S1600576718000183.

[181] Q. Alam, T. Dezaire, F. Gauvin, A.C.A. Delsing, H.J.H. Brouwers, Valorization of bottom ash fines by surface functionalization to reduce leaching of harmful contaminants, J. Environ. Manage. 271 (2020). doi:10.1016/j.jenvman.2020.110884.

[182] R. Cai, T. Wu, C. Fu, H. Ye, Thermal degradation of potassium-activated ternary slag-fly ash-silica fume binders, Constr. Build. Mater. 320 (2022). doi:10.1016/j.conbuildmat.2021.126304.

[183] R. Yamazaki, N. Karyu, M. Noda, S. Fujii, Y. Nakamura, Quantitative measurement of physisorbed silane on a silica particle surface treated with silane coupling agents by thermogravimetric analysis, J. Appl. Polym. Sci. 133 (2016). doi:10.1002/app.43256.

[184] T. Liu, Q. Yu, H.J.H. Brouwers, X. Fan, Utilization of waste glass in alkali activated slag/fly ash blends: reaction process, microstructure, and chloride diffusion behavior, J. Sustain. Cem. Mater. (2022) 1–11. doi:10.1080/21650373.2022.2082577.

[185] M. Bensharada, R. Telford, B. Stern, V. Gaffney, Loss on ignition vs. thermogravimetric analysis: a comparative study to determine organic matter and carbonate content in sediments, J. Paleolimnol. 67 (2022) 191–197. doi:10.1007/s10933-021-00209-6.

[186] Dutch Soil Quality Decree, Regulation of the State Secretary for Housing, Planning and the Environment and

the State Secretary for Transport, Public Works and Water Management, The Netherlands, (2007). https://zoek.officielebekendmakingen.nl/stb-2007-469.html.

[187] F. Jiao, L. Zhang, Z. Dong, T. Namioka, N. Yamada, Y. Ninomiya, Study on the species of heavy metals in MSW incineration fly ash and their leaching behavior, Fuel Process. Technol. 152 (2016) 108–115. doi:10.1016/j.fuproc.2016.06.013.

[188] G. Cornelis, C.A. Johnson, T. Van Gerven, C. Vandecasteele, Leaching mechanisms of oxyanionic metalloid and metal species in alkaline solid wastes: A review, Appl. Geochemistry. 23 (2008) 955–976. doi:10.1016/j.apgeochem.2008.02.001.

[189] G. Okkenhaug, G.D. Breedveld, T. Kirkeng, M. Lægreid, T. Mæhlum, J. Mulder, Treatment of air pollution control residues with iron rich waste sulfuric acid: Does it work for antimony (Sb)?, J. Hazard. Mater. 248–249 (2013) 159–166. doi:10.1016/j.jhazmat.2012.12.041.

[190] M.J. Quina, J.C.M. Bordado, R.M. Quinta-Ferreira, The influence of pH on the leaching behaviour of inorganic components from municipal solid waste APC residues, Waste Manag. 29 (2009) 2483–2493. doi:10.1016/j.wasman.2009.05.012.

[191] BS EN196-1, Methods of testing cement - Part 1: Determination of strength, Eur. Stand. (2005) 1–33.

[192] A.M. Ginstling, B.L. Brounshtein, Concerning the diffusion kinetics of reactions in spherical particles, Appli Chem USSR. 23 (1950) 1327–1338.

[193] P. Bénézeth, D.A. Palmer, L.M. Anovitz, J. Horita, Dawsonite synthesis and reevaluation of its thermodynamic properties from solubility measurements: Implications for mineral trapping of CO2, Geochim. Cosmochim. Acta. 71 (2007) 4438–4455. doi:10.1016/j.gca.2007.07.003.

[194] L. Qiu, V. Murashov, M.A. White, Zeolite 4A: Heat capacity and thermodynamic properties, Solid State Sci. 2 (2000) 841–846. doi:10.1016/S1293-2558(00)01102-X.

[195] R.A. Robie, B.S. Hemingway, P Gillet, B. Reynard, On the entropy of glaucophane Na2Mg3Al2Si8O22(OH)2., Contrib. to Mineral. Petrol. 107 (1991) 484–486. doi:10.1007/BF00310682.

[196] B. Lothenbach, D.A. Kulik, T. Matschei, M. Balonis, L. Baquerizo, B. Dilnesa, G.D. Miron, R.J. Myers, Cemdata18: A chemical thermodynamic database for hydrated Portland cements and alkali-activated materials, Cem. Concr. Res. 115 (2019) 472–506. doi:10.1016/j.cemconres.2018.04.018.

[197] BS EN 12457-2, Characterisation of Waste - Leaching - Compliance Test for Leaching of Granular Waste Materials and Sludges - Part 2: One stage batch test at a liquid to solid ratio of 10 l/kg for materials with particle size below 4 mm (without or with size reduction), BSI Stand. Publ. 3 (2014) 30.

[198] V.A. Reddy, C.H. Solanki, S. Kumar, K.R. Reddy, Y.-J. Du, Pb-Zn Smelter Residue (LZSR) Stabilized Using Low-Carbon, Low-Cost Limestone–Calcined Clay Cement: Leachability, Chemical Speciation, Strength, and Microstructure, J. Hazardous, Toxic, Radioact. Waste. 24 (2020) 04020054. doi:10.1061/(asce)hz.2153-5515.0000552.

[199] R.H. Worden, Dawsonite cement in the Triassic Lam Formation, Shabwa Basin, Yemen: A natural analogue for a potential mineral product of subsurface CO2 storage for greenhouse gas reduction, Mar. Pet. Geol. 23 (2006) 61–77. doi:10.1016/j.marpetgeo.2005.07.001.

[200] P. Rożek, M. Król, W. Mozgawa, Geopolymer-zeolite composites: A review, J. Clean. Prod. 230 (2019) 557–579. doi:10.1016/j.jclepro.2019.05.152.

[201] C.W. Huggins, T.E. Green, Thermal decomposition of dawsonite, Am. Mineral. 58 (1973) 548–550.

[202] M.J. Hernandez, M.A. Ulibarri, J. Cornejo, M.J. Peña, C.J. Serna, Thermal stability of aluminium hydroxycarbonates with monovalent cations, Thermochim. Acta. 94 (1985) 257–266. doi:10.1016/0040-6031(85)85269-2.

[203] F. Lundvall, G.N. Kalantzopoulos, D.S. Wragg, B. Arstad, R. Blom, A.O. Sjåstad, H. Fjellvåg, Characterization and evaluation of synthetic Dawsonites as CO2 sorbents, Fuel. 236 (2019) 747–754. doi:10.1016/j.fuel.2018.09.057.

[204] K.J.D. MacKenzie, J. Temuujin, K. Okada, Thermal decomposition of mechanically activated gibbsite, Thermochim. Acta. 327 (1999) 103–108. doi:10.1016/s0040-6031(98)00609-1.

[205] E. Bernard, W.J. Zucha, B. Lothenbach, U. Mäder, Stability of hydrotalcite (Mg-Al layered double hydroxide) in presence of different anions, Cem. Concr. Res. 152 (2022). doi:10.1016/j.cemconres.2021.106674.

[206] S. Mindess, J.F. Young, D. Darwin, “Concrete Mindess” 2nd Edition, Prentice-Hall, Upper Saddle River, 2003..

[207] Z. Zhang, Y. Zhu, H. Zhu, Y. Zhang, J.L. Provis, H. Wang, Effect of drying procedures on pore structure and phase evolution of alkali-activated cements, Cem. Concr. Compos. 96 (2019) 194–203. doi:10.1016/j.cemconcomp.2018.12.003.

[208] T.H. Tan, K.H. Mo, T.C. Ling, S.H. Lai, Current development of geopolymer as alternative adsorbent for heavy metal removal, Environ. Technol. Innov. 18 (2020). doi:10.1016/j.eti.2020.100684.

[209] T. Liu, S. Li, Y. Chen, H.J.H. Brouwers, Q. Yu, In-situ formation of LDHs in MgO-NaAlO 2 activated GGBS / MSWI BA : The impact of Mg 2 + on reaction mechanism and leaching behavior, Cem. Concr. Compos. (Accepted).

[210] H. Luo, Y. Cheng, D. He, E.H. Yang, Review of leaching behavior of municipal solid waste incineration (MSWI) ash, Sci. Total Environ. 668 (2019) 90–103. doi:10.1016/j.scitotenv.2019.03.004.

[211] R. Mohamed, R. Abd Razak, M.M.A.B. Abdullah, S.Z.A. Abd Rahim, L. Yuan-Li, Subaer, A.V. Sandu, J.J. Wysłocki, Heat evolution of alkali-activated materials: A review on influence factors, Constr. Build. Mater. 314 (2022). doi:10.1016/j.conbuildmat.2021.125651.

[212] Y. Luo, K.M. Klima, H.J.H. Brouwers, Q. Yu, Effects of ladle slag on Class F fly ash geopolymer: Reaction mechanism and high temperature behavior, Cem. Concr. Compos. 129 (2022). doi:10.1016/j.cemconcomp.2022.104468.

[213] H.F.W. Taylor, Cement chemistry, Thomas Telford Publishing, London, 361 (1997). doi:10.1680/cc.25929.

[214] K. Kishi, T., and Maekawa, Thermal and mechanical modeling of young concrete based on hydration process of multi-component cement minerals, RILEM Symp. Therm. Crack. Concr. Early Ages. (1995) 11–18.

[215] A. Baldermann, V. Preissegger, S. Šimić, I. Letofsky-Papst, F. Mittermayr, M. Dietzel, Uptake of aqueous heavy metal ions (Co2+, Cu2+ and Zn2+) by calcium-aluminium-silicate-hydrate gels, Cem. Concr. Res. 147 (2021). doi:10.1016/j.cemconres.2021.106521.

[216] S. Fujii, Y. Sugie, M. Kobune, A. Touno, J. Touji, Uptakes of Cu2+, Pb2+ and Zn2+ on Synthetic Hydrotalcite in Aqueous Solution., Nippon KAGAKU KAISHI. (1992) 1504–1507. doi:10.1246/nikkashi.1992.1504.

[217] J. Li, M. Li, Q. Song, S. Wang, X. Cui, F. Liu, X. Liu, Efficient recovery of Cu(II) by LTA-zeolites with hierarchical pores and their resource utilization in electrochemical denitrification: Environmentally friendly design and reutilization of waste in water, J. Hazard. Mater. 394 (2020). doi:10.1016/j.jhazmat.2020.122554.

[218] S. Ahmari, L. Zhang, Durability and leaching behavior of mine tailings-based geopolymer bricks, Constr. Build. Mater. 44 (2013) 743–750. doi:10.1016/j.conbuildmat.2013.03.075.

[219] X. He, Z. Yuhua, S. Qaidi, H.F. Isleem, O. Zaid, F. Althoey, J. Ahmad, Mine tailings-based geopolymers: A comprehensive review, Ceram. Int. (2022). doi:10.1016/j.ceramint.2022.05.345.

[220] S. Paikaray, M.J. Hendry, J. Essilfie-Dughan, Controls on arsenate, molybdate, and selenate uptake by hydrotalcite-like layered double hydroxides, Chem. Geol. 345 (2013) 130–138. doi:10.1016/j.chemgeo.2013.02.015.

[221] B. Verbinnen, C. Block, D. Hannes, P. Lievens, M. Vaclavikova, K. Stefusova, G. Gallios, C. Vandecasteele, Removal of Molybdate Anions from Water by Adsorption on Zeolite-Supported Magnetite, Water Environ. Res. 84 (2012) 753–760. doi:10.2175/106143012x13373550427318.

[222] T. Luukkonen, H. Runtti, M. Niskanen, E.T. Tolonen, M. Sarkkinen, K. Kemppainen, J. Rämö, U. Lassi, Simultaneous removal of Ni(II), As(III), and Sb(III) from spiked mine effluent with metakaolin and blast-furnace-slag geopolymers, J. Environ. Manage. 166 (2016) 579–588. doi:10.1016/j.jenvman.2015.11.007.

[223] T. Kameda, E. Kondo, T. Yoshioka, Equilibrium and kinetics studies on As(V) and Sb(V) removal by Fe2+-doped Mg-Al layered double hydroxides, J. Environ. Manage. 151 (2015) 303–309. doi:10.1016/j.jenvman.2014.12.050.

[224] R. Dabiri, E. Amiri Shiraz, Evaluating performance of natural sepiolite and zeolite nanoparticles for nickel, antimony, and arsenic removal from synthetic wastewater, J. Min. Environ. 9 (2018) 1049–1064.

[225] W. Cai, Z. Xu, Z. Zhang, J. Hu, H. Huang, Y. Ma, Z. Zhang, H. Wang, S. Yin, J. Wei, C. Shi, Q. Yu, Chloride binding behavior of synthesized reaction products in alkali-activated slag, Compos. Part B Eng. 238 (2022). doi:10.1016/j.compositesb.2022.109919.

[226] G. Zhang, X. Zhang, Q. Ding, D. Hou, K. Liu, Microstructural Evolution Mechanism of C-(A)-S-H Gel in Portland Cement Pastes Affected by Sulfate Ions, J. Wuhan Univ. Technol. Mater. Sci. Ed. 33 (2018) 639–647. doi:10.1007/s11595-018-1872-2.

[227] F.L. Theiss, S.J. Couperthwaite, G.A. Ayoko, R.L. Frost, A review of the removal of anions and oxyanions of the halogen elements from aqueous solution by layered double hydroxides, J. Colloid Interface Sci. 417 (2014)

356–368. doi:10.1016/j.jcis.2013.11.040.

[228] M.T. Rahman, T. Kameda, T. Miura, S. Kumagai, T. Yoshioka, Removal of sulfate from wastewater via synthetic Mg–Al layered double hydroxide: An adsorption, kinetics, and thermodynamic study, J. Indian Chem. Soc. 98 (2021). doi:10.1016/j.jics.2021.100185.

[229] J.M. Newsam, The zeolite cage structure, Science (80-.). 231 (1986) 1093–1099. doi:10.1126/science.231.4742.1093.

[230] Q. Alam, M.V.A. Florea, K. Schollbach, H.J.H. Brouwers, A two-stage treatment for Municipal Solid Waste Incineration (MSWI) bottom ash to remove agglomerated fine particles and leachable contaminants, Waste Manag. 67 (2017) 181–192. doi:10.1016/j.wasman.2017.05.029.

[231] P.H. Brunner, H. Rechberger, Waste to energy - key element for sustainable waste management, Waste Manag. 37 (2015) 3–12. doi:10.1016/j.wasman.2014.02.003.

[232] J.E. Aubert, B. Husson, A. Vaquier, Metallic aluminum in MSWI fly ash: Quantification and influence on the properties of cement-based products, Waste Manag. 24 (2004) 589–596. doi:10.1016/j.wasman.2004.01.005.

[233] C.H.K. Lam, A.W.M. Ip, J.P. Barford, G. McKay, Use of incineration MSW ash: A review, Sustainability. 2 (2010) 1943–1968. doi:10.3390/su2071943.

[234] Z. Ji, Y. Pei, Bibliographic and visualized analysis of geopolymer research and its application in heavy metal immobilization: A review, J. Environ. Manage. 231 (2019) 256–267. doi:10.1016/j.jenvman.2018.10.041.

[235] X. Niu, Y. Elakneswaran, C.R. Islam, J.L. Provis, T. Sato, Adsorption behaviour of simulant radionuclide cations and anions in metakaolin-based geopolymer, J. Hazard. Mater. 429 (2022) 128373. doi:10.1016/j.jhazmat.2022.128373.

[236] J.L. Provis, J.S.J. Van Deventer, Geopolymers and other alkali-activated materials, Lea's Chem. Cem. Concr. (2019) 779–805. doi:10.1016/B978-0-08-100773-0.00016-2.

[237] B. Li, S. Zhang, Q. Li, N. Li, B. Yuan, W. Chen, H.J.H. Brouwers, Q. Yu, Uptake of heavy metal ions in layered double hydroxides and applications in cementitious materials: Experimental evidence and first-principle study, Constr. Build. Mater. 222 (2019) 96–107. doi:10.1016/j.conbuildmat.2019.06.135.

[238] T. Liu, Y. Chen, Q. Yu, J. Fan, H.J.H. Brouwers, Effect of MgO, Mg-Al-NO3 LDH and Calcined LDH-CO3 on chloride resistance of alkali activated fly ash and slag blends, Constr. Build. Mater. 250 (2020) 118865. doi:10.1016/j.conbuildmat.2020.118865.

[239] B. Chen, J. Wang, J. Zhao, Mitigating the drying shrinkage and autogenous shrinkage of alkali-activated slag by NaAlO2, Materials (Basel). 13 (2020). doi:10.3390/MA13163499.

[240] H. Luo, Y. Cheng, D. He, E.H. Yang, Review of leaching behavior of municipal solid waste incineration (MSWI) ash, Sci. Total Environ. 668 (2019) 90–103. doi:10.1016/j.scitotenv.2019.03.004.

[241] M.J. Quina, J.C.M. Bordado, R.M. Quinta-Ferreira, The influence of pH on the leaching behaviour of inorganic components from municipal solid waste APC residues, Waste Manag. 29 (2009) 2483–2493. doi:10.1016/j.wasman.2009.05.012.

[242] J. Yliniemi, B. Walkley, J.L. Provis, P. Kinnunen, M. Illikainen, Influence of activator type on reaction kinetics, setting time, and compressive strength of alkali-activated mineral wools, J. Therm. Anal. Calorim. 144 (2021) 1129–1138. doi:10.1007/s10973-020-09651-6.

[243] Z. Wang, S. Park, H.R. Khalid, H.K. Lee, Hydration properties of alkali-activated fly ash/slag binders modified by MgO with different reactivity, J. Build. Eng. 44 (2021) 103252. doi:10.1016/j.jobe.2021.103252.

[244] S.A. Bernal, R. San Nicolas, R.J. Myers, R. Mejía De Gutiérrez, F. Puertas, J.S.J. Van Deventer, J.L. Provis, MgO content of slag controls phase evolution and structural changes induced by accelerated carbonation in alkali-activated binders, Cem. Concr. Res. 57 (2014) 33–43. doi:10.1016/j.cemconres.2013.12.003.

[245] Y. Zuo, M. Nedeljković, G. Ye, Pore solution composition of alkali-activated slag/fly ash pastes, Cem. Concr. Res. 115 (2019) 230–250. doi:10.1016/j.cemconres.2018.10.010.

[246] X. Ke, S.A. Bernal, J.L. Provis, Uptake of chloride and carbonate by Mg-Al and Ca-Al layered double hydroxides in simulated pore solutions of alkali-activated slag cement, Cem. Concr. Res. 100 (2017) 1–13. doi:10.1016/j.cemconres.2017.05.015.

[247] M. Nedeljković, B. Ghiassi, S. van der Laan, Z. Li, G. Ye, Effect of curing conditions on the pore solution and carbonation resistance of alkali-activated fly ash and slag pastes, Cem. Concr. Res. 116 (2019) 146–158. doi:10.1016/j.cemconres.2018.11.011.

[248] S. Song, H.M. Jennings, Pore solution chemistry of alkali-activated ground granulated blast-furnace slag, Cem. Concr. Res. 29 (1999) 159–170. doi:10.1016/S0008-8846(98)00212-9.

[249] EN196-1, Methods of testing cement - Part 1: Determination of strength, Eur. Stand. (2005) 1–33.

[250] EN 196-1, En 196-1, EN 196-1 Ed. 2015-08-01 Methods Test. Cem. Part 1 Determ. Strength. 1 (2011) 46.

[251] S. Li, O.M. Jensen, Z. Wang, Q. Yu, Influence of micromechanical property on the rate-dependent flexural strength of ultra-high performance concrete containing coarse aggregates (UHPC-CA), Compos. Part B Eng. 227 (2021). doi:10.1016/j.compositesb.2021.109394.

[252] Z. Pi, H. Xiao, R. Liu, M. Liu, H. Li, Effects of brass coating and nano-SiO2 coating on steel fiber–matrix interfacial properties of cement-based composite, Compos. Part B Eng. 189 (2020). doi:10.1016/j.compositesb.2020.107904.

[253] K.C. Newlands, M. Foss, T. Matschei, J. Skibsted, D.E. Macphee, Early stage dissolution characteristics of aluminosilicate glasses with blast furnace slag- and fly-ash-like compositions, J. Am. Ceram. Soc. 100 (2017) 1941–1955. doi:10.1111/jace.14716.

[254] D.A. Vermilyea, The Dissolution of MgO and Mg(OH)[sub 2] in Aqueous Solutions, J. Electrochem. Soc. 116 (1969) 1179. doi:10.1149/1.2412273.

[255] C.L. Wetteland, J. Sanchez, C.A. Silken, N.T. Nguyen, O. Mahmood, H. Liu, Dissociation of magnesium oxide and magnesium hydroxide nanoparticles in physiologically relevant fluids, J. Nanoparticle Res. 20 (2018). doi: 10.1007/s11051-018-4314-3.

[256] T. Matschei, B. Lothenbach, F.G.-C. and C. Research, undefined 2007, Thermodynamic properties of Portland cement hydrates in the system CaO–Al2O3–SiO2–CaSO4–CaCO3–H2O, Elsevier. (n.d.). https://www.sciencedirect.com/science/article/pii/S0008884607001299.

[257] Q. Li, Y. Zhang, Z. Cao, W. Gao, L. Cui, Influence of synthesis parameters on the crystallinity and Si/Al ratio of NaY zeolite synthesized from kaolin, Pet. Sci. 7 (2010) 403–409. doi:10.1007/s12182-010-0085-x.

[258] M. Ben Haha, B. Lothenbach, G. Le Saout, F. Winnefeld, Influence of slag chemistry on the hydration of alkali-activated blast-furnace slag - Part I: Effect of MgO, Cem. Concr. Res. 41 (2011) 955–963. doi:10.1016/j.cemconres.2011.05.002.

[259] S. Berger, C.C.D. Coumes, P. Le Bescop, D. Damidot, Influence of a thermal cycle at early age on the hydration of calcium sulphoaluminate cements with variable gypsum contents, Cem. Concr. Res. 41 (2011) 149–160. doi:10.1016/j.cemconres.2010.10.001.

[260] F. Song, Z. Yu, F. Yang, Y. Liu, Y. Lu, Strätlingite and calcium hemicarboaluminate hydrate in belite-calcium sulphoaluminate cement, Ceram. - Silikaty. 58 (2014) 269–274.

[261] C. Forano, U. Costantino, V. Prévot, C.T. Gueho, Chapter 14.1 - Layered Double Hydroxides (LDH), (2013).

[262] N.M. Musyoka, L.F. Petrik, E. Hums, A. Kuhnt, W. Schwieger, Thermal stability studies of zeolites A and X synthesized from South African coal fly ash, Res. Chem. Intermed. 41 (2015) 575–582. doi:10.1007/s11164-013-1211-3.

[263] E.S. Zhitova, S. V. Krivovichev, I. Pekov, H.C. Greenwell, Crystal chemistry of natural layered double hydroxides. 5. Single-crystal structure refinement of hydrotalcite, [Mg6Al2(OH)16](CO3)(H2O)4, Mineral. Mag. 83 (2019) 269–280. doi:10.1180/mgm.2018.145.

[264] A.E. Morandeau, C.E. White, Role of Magnesium-Stabilized Amorphous Calcium Carbonate in Mitigating the Extent of Carbonation in Alkali-Activated Slag, Chem. Mater. 27 (2015) 6625–6634. doi:10.1021/acs.chemmater.5b02382.

[265] B. Jones, Review of aragonite and calcite crystal morphogenesis in thermal spring systems, Sediment. Geol. 354 (2017) 9–23. doi:10.1016/j.sedgeo.2017.03.012.

[266] L.E. Wasylenki, P.M. Dove, J.J. De Yoreo, Effects of temperature and transport conditions on calcite growth in the presence of Mg2+: Implications for paleothermometry, Geochim. Cosmochim. Acta. 69 (2005) 4227–4236. doi:10.1016/j.gca.2005.04.006.

[267] O. Burciaga-Díaz, I. Betancourt-Castillo, Characterization of novel blast-furnace slag cement pastes and mortars activated with a reactive mixture of MgO-NaOH, Cem. Concr. Res. 105 (2018) 54–63. doi:10.1016/j.cemconres.2018.01.002.

[268] H. Sreenivasan, E. Adesanya, H. Niu, P. Perumal, A.M. Kantola, V.V. Telkki, M. Huttula, W. Cao, J.L. Provis, M. Illikainen, P. Kinnunen, Evidence of formation of an amorphous magnesium silicate (AMS) phase during alkali activation of (Na-Mg) aluminosilicate glasses, Cem. Concr. Res. 145 (2021). doi:10.1016/j.cemconres.2021.106464.

[269] B. Akturk, M. Abolfathi, S. Ulukaya, A.B. Kizilkanat, T.J.N. Hooper, L. Gu, E.H. Yang, C. Unluer, Hydration kinetics and performance of sodium carbonate-activated slag-based systems containing reactive MgO and

metakaolin under carbonation, Cem. Concr. Compos. 132 (2022). doi:10.1016/j.cemconcomp.2022.104617.

[270] B. Li, Q. Li, W. Chen, Spatial zonation of a hydrotalcite-like phase in the inner product of slag: New insights into the hydration mechanism, Cem. Concr. Res. 145 (2021). doi:10.1016/j.cemconres.2021.106460.

[271] Dutch Soil Quality Regulation, (2006). https://rwsenvironment.eu/subjects/soil/legislation-and/soil-quality-decree/.

[272] Y. Zhang, B. Cetin, W.J. Likos, T.B. Edil, Impacts of pH on leaching potential of elements from MSW incineration fly ash, Fuel. 184 (2016) 815–825. doi:10.1016/j.fuel.2016.07.089.

[273] Q. Tian, B. Guo, K. Sasaki, Immobilization mechanism of Se oxyanions in geopolymer: Effects of alkaline activators and calcined hydrotalcite additive, J. Hazard. Mater. 387 (2020). doi:10.1016/j.jhazmat.2019.121994.

[274] X. Huang, C. Xin, J. shan Li, P. Wang, S. Liao, C.S. Poon, Q. Xue, Using hazardous barium slag as a novel admixture for alkali activated slag cement, Cem. Concr. Compos. 125 (2022). doi:10.1016/j.cemconcomp.2021.104332.

[275] F. Jin, K. Gu, A. Al-Tabbaa, Strength and hydration properties of reactive MgO-activated ground granulated blastfurnace slag paste, Cem. Concr. Compos. 57 (2015) 8–16. doi:10.1016/j.cemconcomp.2014.10.007.

[276] S.A. Walling, S.A. Bernal, L.J. Gardner, H. Kinoshita, J.L. Provis, Phase Formation and Evolution in Mg(OH)2-Zeolite Cements, Ind. Eng. Chem. Res. 57 (2018) 2105–2113. doi:10.1021/acs.iecr.7b04201.

[277] Z. Baščarevć, The resistance of alkali-activated cement-based binders to chemical attack, Handb. Alkali-Activated Cem. Mortars Concr. (2015) 373–396. doi:10.1533/9781782422884.3.373.

[278] Z. Giergiczny, Fly ash and slag, Cem. Concr. Res. 124 (2019). doi:10.1016/j.cemconres.2019.105826.

[279] I.B. Topçu, M. Canbaz, Properties of concrete containing waste glass, Cem. Concr. Res. 34 (2004) 267–274. doi:10.1016/j.cemconres.2003.07.003.

[280] H. Du, K.H. Tan, Properties of high volume glass powder concrete, Cem. Concr. Compos. 75 (2017) 22–29. doi:10.1016/j.cemconcomp.2016.10.010.

[281] H. Du, K.H. Tan, Waste glass powder as cement replacement in concrete, J. Adv. Concr. Technol. 12 (2014) 468–477. doi:10.3151/jact.12.468.

[282] S. Zhang, A. Keulen, K. Arbi, G. Ye, Cement and Concrete Research Waste glass as partial mineral precursor in alkali-activated slag / fl y ash system, Cem. Concr. Res. 102 (2017) 29–40. doi:10.1016/j.cemconres.2017.08.012.

[283] M.M. Tashima, L. Soriano, M. V. Borrachero, J. Monzó, C.R. Cheeseman, J. Payá, Alkali activation of vitreous calcium aluminosilicate derived from glass fiber waste, J. Sustain. Cem. Mater. 1 (2012) 83–93. doi:10.1080/21650373.2012.742610.

[284] R. Si, Q. Dai, S. Guo, J. Wang, Mechanical property , nanopore structure and drying shrinkage of metakaolin-based geopolymer with waste glass powder, J. Clean. Prod. 242 (2020) 118502. doi:10.1016/j.jclepro.2019.118502.

[285] F. Torres-Carrasco, M., Tognonvi, M.T., Tagnit-Hamou, A., Puertas, Durability of Alkali-Activated Slag Concretes Prepared Using Waste Glass as Alternative Activator, ACI Mater. J. 112 (2015) 791–800. doi:10.14359/51687903.

[286] G.J. Osborne, Durability of Portland blast-furnace slag cement concrete, Cem. Concr. Compos. 21 (1999) 11–21. doi:10.1016/S0958-9465(98)00032-8.

[287] H.A. Khan, M.S.H. Khan, A. Castel, J. Sunarho, Deterioration of alkali-activated mortars exposed to natural aggressive sewer environment, Constr. Build. Mater. 186 (2018) 577–597. doi:10.1016/j.conbuildmat.2018.07.137.

[288] Y. Yuan, Y. Ji, Modeling corroded section configuration of steel bar in concrete structure, Constr. Build. Mater. 23 (2009) 2461–2466. doi:10.1016/j.conbuildmat.2008.09.026.

[289] C. Monticelli, M.E. Natali, A. Balbo, C. Chiavari, F. Zanotto, S. Manzi, M.C. Bignozzi, Corrosion behavior of steel in alkali-activated fly ash mortars in the light of their microstructural, mechanical and chemical characterization, Cem. Concr. Res. 80 (2016) 60–68. doi:10.1016/j.cemconres.2015.11.001.

[290] D.W. Law, A.A. Adam, T.K. Molyneaux, I. Patnaikuni, Durability assessment of alkali activated slag (AAS) concrete, Mater. Struct. Constr. 45 (2012) 1425–1437. doi:10.1617/s11527-012-9842-1.

[291] F. Puertas, Cement and Concrete Research Use of glass waste as an activator in the preparation of alkali-activated slag . Mechanical strength and paste characterisation, Cem. Concr. Res. 57 (2014) 95–104.

doi:10.1016/j.cemconres.2013.12.005.

[292] H. Yazici, The effect of curing conditions on compressive strength of ultra high strength concrete with high volume mineral admixtures, Build. Environ. 42 (2007) 2083–2089. doi:10.1016/j.buildenv.2006.03.013.

[293] J. Kärger, R. Valiullin, Diffusion in Porous Media, Encycl. Magn. Reson. (2011). doi:10.1002/9780470034590.emrstm0121.pub2.

[294] S.Y. Yi, L.W. Fan, J.H. Fu, X. Xu, Z.T. Yu, Experimental determination of the water vapor diffusion coefficient of autoclaved aerated concrete (AAC) via a transient method: Effects of the porosity and temperature, Int. J. Heat Mass Transf. 103 (2016) 607–610. doi:10.1016/j.ijheatmasstransfer.2016.07.111.

[295] X. Chang, X. Yang, W. Zhou, G. Xie, S. Liu, Influence of Glass Powder on Hydration Kinetics of Composite Cementitious Materials, Adv. Mater. Sci. Eng. 2015 (2015). doi:10.1155/2015/713415.

[296] B. Yin, T. Kang, J. Kang, Y. Chen, L. Wu, M. Du, Investigation of the hydration kinetics and microstructure formation mechanism of fresh fly ash cemented filling materials based on hydration heat and volume resistivity characteristics, Appl. Clay Sci. 166 (2018) 146–158. doi:10.1016/j.clay.2018.09.019.

[297] S. Zhang, A. Keulen, K. Arbi, G. Ye, Waste glass as partial mineral precursor in alkali-activated slag/fly ash system, Cem. Concr. Res. 102 (2017) 29–40. doi:10.1016/j.cemconres.2017.08.012.

[298] G. Bumanis, L. Vitola, D. Bajare, L. Dembovska, I. Pundiene, Impact of reactive SiO2/Al2O3 ratio in precursor on durability of porous alkali activated materials, Ceram. Int. 43 (2017) 5471–5477. doi:10.1016/j.ceramint.2017.01.060.

[299] F. Puertas, Waste glass as a precursor in alkaline activation : Chemical process and hydration products, Constr. Build. Mater. 139 (2017) 342–354. doi:10.1016/j.conbuildmat.2017.02.071.

[300] I.G. Richardson, Tobermorite/jennite- and tobermorite/calcium hydroxide-based models for the structure of C-S-H: Applicability to hardened pastes of tricalcium silicate, β-dicalcium silicate, Portland cement, and blends of Portland cement with blast-furnace slag, metakaol, Cem. Concr. Res. 34 (2004) 1733–1777. doi:10.1016/j.cemconres.2004.05.034.

[301] NORDTEST, Accelerated chloride penetration, NT Build 443, Nordtest. (1995) 1–5.

[302] CEN, Characterisation of waste - Leaching - Compliance test for leaching of granular waste materials and sludges - Part 1, CEN. (2002).

[303] Z. Yang, J. Jiang, X. Jiang, S. Mu, M. Wu, S. Sui, L. Wang, F. Wang, The influence of sodium sulfate and magnesium sulfate on the stability of bound chlorides in cement paste, Constr. Build. Mater. 228 (2019). doi:10.1016/j.conbuildmat.2019.116775.

[304] E.H. Oelkers1, S.R. Gislason, The mechanism, rates and consequences of basaltic glass dissolution: I. An experimental study of the dissolution rates of basaltic glass as a function of aqueous Al, Si and oxalic acid concentration at 25°C and pH _ 3 and 11., Geochim. Cosmochim. Acta,. 65 (2001) 3671–3681.

[305] J.L. Provis, S.A. Bernal, Geopolymers and Related Alkali-Activated Materials, Annual Review of Materials Research (2014) 299–329. doi:10.1146/annurev-matsci-070813-113515.

[306] J. Lu, Z. Lu, C. Peng, X. Li, H. Jiang, In fl uence of particle size on sinterability , crystallisation kinetics and fl exural strength of wollastonite glass-ceramics from waste glass and fl y ash, Mater. Chem. Phys. 148 (2014) 449–456. doi:10.1016/j.matchemphys.2014.08.013.

[307] E.J. Garboczi, K.A. Riding, M. Mirzahosseini, Particle shape effects on particle size measurement for crushed waste glass, Adv. Powder Technol. 28 (2017) 648–657. doi:10.1016/j.apt.2016.12.002.

[308] M. Torres-Carrasco, F. Puertas, Waste glass as a precursor in alkaline activation: Chemical process and hydration products, Constr. Build. Mater. 139 (2017) 342–354. doi:10.1016/j.conbuildmat.2017.02.071.

[309] M. Whittaker, M. Zajac, M. Ben Haha, F. Bullerjahn, L. Black, The role of the alumina content of slag, plus the presence of additional sulfate on the hydration and microstructure of Portland cement-slag blends, Cem. Concr. Res. 66 (2014) 91–101. doi:10.1016/j.cemconres.2014.07.018.

[310] G. Liu, M.V.A. Florea, H.J.H. Brouwers, Performance evaluation of sustainable high strength mortars incorporating high volume waste glass as binder, Constr. Build. Mater. 202 (2019) 574–588. doi:10.1016/j.conbuildmat.2018.12.110.

[311] C.L. Hwang, D.H. Vo, V.A. Tran, M.D. Yehualaw, Effect of high MgO content on the performance of alkali-activated fine slag under water and air curing conditions, Constr. Build. Mater. 186 (2018) 503–513. doi:10.1016/j.conbuildmat.2018.07.129.

[312] Y. Zhang, R. Xiao, X. Jiang, W. Li, X. Zhu, B. Huang, Effect of particle size and curing temperature on mechanical and microstructural properties of waste glass-slag-based and waste glass-fly ash-based

geopolymers, J. Clean. Prod. 273 (2020). doi:10.1016/j.jclepro.2020.122970.

[313] P.Z. Wang, R. Trettin, V. Rudert, Effect of fineness and particle size distribution of granulated blast-furnace slag on the hydraulic reactivity in cement systems, Adv. Cem. Res. 17 (2005) 161–166. doi:10.1680/adcr.2005.17.4.161.

[314] S. Liu, Y. Hao, G. Ma, Approaches to enhance the carbonation resistance of fly ash and slag based alkali-activated mortar- experimental evaluations, J. Clean. Prod. 280 (2021). doi:10.1016/j.jclepro.2020.124321.

[315] M.L. McGlashan, Manual of symbols and terminology for physicochemical quantities and units, Pure Appl. Chem. 21 (1970) 1–44. doi:10.1351/pac197021010001.

[316] L.B. Skinner, S.R. Chae, C.J. Benmore, H.R. Wenk, P.J.M. Monteiro, Nanostructure of calcium silicate hydrates in cements, Phys. Rev. Lett. 104 (2010). doi:10.1103/PhysRevLett.104.195502.

[317] G. Fang, M. Zhang, Multiscale micromechanical analysis of alkali-activated fly ash-slag paste, Cem. Concr. Res. 135 (2020). doi:10.1016/j.cemconres.2020.106141.

[318] C. Shi, Effect of mixing proportions of concrete on its electrical conductivity and the rapid chloride permeability test (ASTM C1202 or ASSHTO T277) results, Cem. Concr. Res. 34 (2004) 537–545. doi:10.1016/j.cemconres.2003.09.007.

[319] A. Noushini, A. Castel, J. Aldred, A. Rawal, Chloride diffusion resistance and chloride binding capacity of fly ash-based geopolymer concrete, Cem. Concr. Compos. 105 (2020). doi:10.1016/j.cemconcomp.2019.04.006.

[320] X. Hu, C. Shi, Z. Shi, L. Zhang, Compressive strength, pore structure and chloride transport properties of alkali-activated slag/fly ash mortars, Cem. Concr. Compos. 104 (2019). doi:10.1016/j.cemconcomp.2019.103392.

[321] M.T. Hasholt, K.U. Christensen, C. Pade, Frost resistance of concrete with high contents of fly ash - A study on how hollow fly ash particles distort the air void analysis, Cem. Concr. Res. 119 (2019) 102–112. doi:10.1016/j.cemconres.2019.02.013.

[322] Q. Zhou, C. Lu, W. Wang, S. Wei, C. Lu, M. Hao, Effect of fly ash and sustained uniaxial compressive loading on chloride diffusion in concrete, J. Build. Eng. 31 (2020). doi:10.1016/j.jobe.2020.101394.

[323] K. Shanmuganathan, C.J. Ellison, Layered Double Hydroxides, Polym. Green Flame Retard. (2014) 675–707. doi:10.1016/b978-0-444-53808-6.00020-2.

[324] D. Hou, T. Li, Q. Han, J. Zhang, Insight on the sodium and chloride ions adsorption mechanism on the ettringite crystal: Structure, dynamics and interfacial interaction, Comput. Mater. Sci. 153 (2018) 479–492. doi:10.1016/j.commatsci.2018.07.021.

[325] T.C. Ling, C.S. Poon, Spent fluorescent lamp glass as a substitute for fine aggregate in cement mortar, J. Clean. Prod. 161 (2017) 646–654. doi:10.1016/j.jclepro.2017.05.173.

[326] T. Liu, Q. Yu, H.J.H. Brouwers, X. Fan, Utilization of waste glass in alkali activated slag/fly ash blends: reaction process, microstructure, and chloride diffusion behavior, J. Sustain. Cem. Mater. (2022). doi:10.1080/21650373.2022.2082577.

[327] N.N.M. Pauzi, R. Hamid, M. Jamil, M.F.M. Zain, The effect of melted-spherical and crushed CRT funnel glass waste as coarse aggregates on concrete performance, J. Build. Eng. 35 (2021). doi:10.1016/j.jobe.2020.102035.

[328] W.C. Wang, B.T. Chen, H.Y. Wang, H.C. Chou, A study of the engineering properties of alkali-activated waste glass material (AAWGM), Constr. Build. Mater. 112 (2016) 962–969. doi:10.1016/j.conbuildmat.2016.03.022.

[329] C.C. Wang, H.Y. Wang, B.T. Chen, Y.C. Peng, Study on the engineering properties and prediction models of an alkali-activated mortar material containing recycled waste glass, Constr. Build. Mater. 132 (2017) 130–141. doi:10.1016/j.conbuildmat.2016.11.103.

[330] M. Mastali, Z. Abdollahnejad, F. Pacheco-Torgal, Performance of waste based alkaline mortars submitted to accelerated carbon dioxide curing, Resour. Conserv. Recycl. 129 (2018) 12–19. doi:10.1016/j.resconrec.2017.10.017.

[331] R. Martinez-Lopez, J. Ivan Escalante-Garcia, Alkali activated composite binders of waste silica soda lime glass and blast furnace slag: Strength as a function of the composition, Constr. Build. Mater. 119 (2016) 119–129. doi:10.1016/j.conbuildmat.2016.05.064.

[332] M. Torres-Carrasco, F. Puertas, Waste glass as a precursor in alkaline activation: Chemical process and hydration products, Constr. Build. Mater. 139 (2017) 342–354. doi:10.1016/j.conbuildmat.2017.02.071.

[333] G. Liang, H. Li, H. Zhu, T. Liu, Q. Chen, H. Guo, Reuse of waste glass powder in alkali-activated

metakaolin/fly ash pastes: Physical properties, reaction kinetics and microstructure, Resour. Conserv. Recycl. 173 (2021). doi:10.1016/j.resconrec.2021.105721.

[334] R. Xiao, Y. Ma, X. Jiang, M. Zhang, Y. Zhang, Y. Wang, B. Huang, Q. He, Strength, microstructure, efflorescence behavior and environmental impacts of waste glass geopolymers cured at ambient temperature, J. Clean. Prod. 252 (2020). doi:10.1016/j.jclepro.2019.119610.

[335] W. Dong W. Li, Z. Tao, A comprehensive review on performance of cementitious and geopolymeric concretes with recycled waste glass as powder, sand or cullet, Resour. Conserv. Recycl. 172 (2021).

[336] E. Najafi Kani, A. Allahverdi, J.L. Provis, Efflorescence control in geopolymer binders based on natural pozzolan, Cem. Concr. Compos. 34 (2012) 25–33. doi:10.1016/j.cemconcomp.2011.07.007.

[337] H. Brocken, T.G. Nijland, White efflorescence on brick masonry and concrete masonry blocks, with special emphasis on sulfate efflorescence on concrete blocks, Constr. Build. Mater. 18 (2004) 315–323. doi:10.1016/j.conbuildmat.2004.02.004.

[338] M. Cyr, R. Idir, T. Poinot, Properties of inorganic polymer (geopolymer) mortars made of glass cullet, J. Mater. Sci. 47 (2012) 2782–2797. doi:10.1007/s10853-011-6107-2.

[339] R. Redden, N. Neithalath, Microstructure, strength, and moisture stability of alkali activated glass powder-based binders, Cem. Concr. Compos. 45 (2014) 46–56. doi:10.1016/j.cemconcomp.2013.09.011.

[340] K. Sun, H.A. Ali, D. Xuan, J. Ban, C.S. Poon, Utilization of APC residues from sewage sludge incineration process as activator of alkali-activated slag/glass powder material, Cem. Concr. Compos. 133 (2022). doi:10.1016/j.cemconcomp.2022.104680.

[341] M. Vafaei, A. Allahverdi, High strength geopolymer binder based on waste-glass powder, Adv. Powder Technol. 28 (2017) 215–222. doi:10.1016/j.apt.2016.09.034.

[342] M. Criado, A. Palomo, A. Fernández-Jiménez, Alkali activation of fly ashes. Part 1: Effect of curing conditions on the carbonation of the reaction products, Fuel. 84 (2005) 2048–2054. doi:10.1016/j.fuel.2005.03.030.

[343] A. Fernández-Jiménez, A. Palomo, I. Sobrados, J. Sanz, The role played by the reactive alumina content in the alkaline activation of fly ashes, Microporous Mesoporous Mater. 91 (2006) 111–119. doi:10.1016/j.micromeso.2005.11.015.

[344] Y. Yan, B. Ma, G.D. Miron, D.A. Kulik, K. Scrivener, B. Lothenbach, Al uptake in calcium silicate hydrate and the effect of alkali hydroxide, Cem. Concr. Res. 162 (2022) 106957. doi:10.1016/j.cemconres.2022.106957.

[345] A. Mendes, W.P. Gates, J.G. Sanjayan, F. Collins, NMR, XRD, IR and synchrotron NEXAFS spectroscopic studies of OPC and OPC/slag cement paste hydrates, Mater. Struct. Constr. 44 (2011) 1773–1791. doi:10.1617/s11527-011-9737-6.

[346] Y.X. Chen, S. Li, B. Mezari, E.J.M. Hensen, R. Yu, K. Schollbach, H.J.H. Brouwers, Q. Yu, Effect of highly dispersed colloidal olivine nano-silica on early age properties of ultra-high performance concrete, Cem. Concr. Compos. 131 (2022). doi:10.1016/j.cemconcomp.2022.104564.

[347] B. Walkley, J.L. Provis, Solid-state nuclear magnetic resonance spectroscopy of cements, Mater. Today Adv. 1 (2019). doi:10.1016/j.mtadv.2019.100007.

[348] J. Skibsted, M.D. Andersen, The effect of alkali ions on the incorporation of aluminum in the calcium silicate hydrate (C-S-H) phase resulting from portland cement hydration studied by 29Si MAS NMR, J. Am. Ceram. Soc. 96 (2013) 651–656. doi:10.1111/jace.12024.

[349] M. Daugaard Andersen, H.J. Jakobsen, Jø. Skibsted, Incorporation of aluminum in the calcium silicate hydrate (C-S-H) of hydrated Portland cements: A high-field 27Al and 29Si MAS NMR investigation, Inorg. Chem. 42 (2003) 2280–2287. doi:10.1021/ic020607b.

[350] G.W. Groves, I.G. Richardson, The structure of the calcium silicate hydrate phases present in hardened pastes of white Portland cement/blast-furnace slag blends, J. Mater. Sci. 32 (1997) 4793–4802.

[351] I.G. Richardson, A.R. Brough, G.W. Groves, C.M. Dobson, The characterization of hardened alkali-activated blast-furnace slag pastes and the nature of the calcium silicate hydrate (C-S-H) phase, Cem. Concr. Res. 24 (1994) 813–829. doi:10.1016/0008-8846(94)90002-7.

[352] D. Tang, C. Yang, Mitigation of efflorescence of alkali-activated slag mortars by incorporating calcium hydroxide, Constr. Build. Mater. 298 (2021). https://www.sciencedirect.com/science/article/pii/S0950061821016330.

[353] M.M. Kumar, H. Jena, Direct single-step synthesis of phase pure zeolite Na–P1, hydroxy sodalite and analcime from coal fly ash and assessment of their Cs+ and Sr2+ removal efficiencies, Microporous Mesoporous Mater.

333 (2022). doi:10.1016/j.micromeso.2022.111738.

[354] A. Jiménez, V. Rives, M.A. Vicente, Thermal study of the hydrocalumite–katoite–calcite system, Thermochim. Acta. 713 (2022) 179242. doi:10.1016/j.tca.2022.179242.

[355] J.W. Kim, H.G. Lee, Thermal and carbothermic decomposition of Na2CO3 and Li2CO3, Metall. Mater. Trans. B Process Metall. Mater. Process. Sci. 32 (2001) 17–24. doi:10.1007/s11663-001-0003-0.

[356] S. Dadsetan, H. Siad, M. Lachemi, O. Mahmoodi, M. Sahmaran, Optimization and characterization of geopolymer binders from ceramic waste, glass waste and sodium glass liquid, J. Clean. Prod. 342 (2022). doi:10.1016/j.jclepro.2022.130931.

[357] W. Mozgawa, M. Król, J. Dyczek, J. Deja, Investigation of the coal fly ashes using IR spectroscopy, Spectrochim. Acta - Part A Mol. Biomol. Spectrosc. 132 (2014) 889–894. doi:10.1016/j.saa.2014.05.052.

[358] B. Walkley, R. San Nicolas, M.A. Sani, G.J. Rees, J. V. Hanna, J.S.J. van Deventer, J.L. Provis, Phase evolution of C-(N)-A-S-H/N-A-S-H gel blends investigated via alkali-activation of synthetic calcium aluminosilicate precursors, Cem. Concr. Res. 89 (2016) 120–135. doi:10.1016/j.cemconres.2016.08.010.

[359] G. Bin Cai, S.F. Chen, L. Liu, J. Jiang, H. Bin Yao, A.W. Xu, S.H. Yu, 1,3-Diamino-2-hydroxypropane-N,N,N′,N′-tetraacetic acid stabilized amorphous calcium carbonate: Nucleation, transformation and crystal growth, CrystEngComm. 12 (2010) 234–241. doi:10.1039/b911426m.

[360] W. Mozgawa, W. Jastrzębski, M. Handke, Vibrational spectra of D4R and D6R structural units, J. Mol. Struct. 744–747 (2005) 663–670. doi:10.1016/j.molstruc.2004.12.051.

[361] Y. Zhan, X. Li, Y. Zhang, L. Han, Y. Chen, Phase and morphology control of LTA/FAU zeolites by adding trace amounts of inorganic ions, Ceram. Int. 39 (2013) 5997–6003. doi:10.1016/j.ceramint.2013.01.005.

[362] M. Sayehi, G. Garbarino, G. Delahay, G. Busca, H. Tounsi, Synthesis of high value-added Na–P1 and Na-FAU zeolites using waste glass from fluorescent tubes and aluminum scraps, Mater. Chem. Phys. 248 (2020). doi:10.1016/j.matchemphys.2020.122903.

[363] Durability of alkali-activated materials with different C–S–H and N-A-S-H gels in acid and alkaline environment, (n.d.).

[364] N. V. Chukanov, Infrared spectra of mineral species: Extended library, Infrared Spectra Miner. Species Ext. Libr. 1 (2014) 21–1701. http://link.springer.com/10.1007/978-94-007-7128-4.

[365] P.J. Schilling, L.G. Butler, A. Roy, H.C. Eaton, 29Si and 27Al MAS-NMR of NaOH-Activated Blast-Furnace Slag, J. Am. Ceram. Soc. 77 (1994) 2363–2368. doi:10.1111/j.1151-2916.1994.tb04606.x.

[366] B. Walkley, X. Ke, J.L. Provis, S.A. Bernal, Activator Anion Influences the Nanostructure of Alkali-Activated Slag Cements, J. Phys. Chem. C. 125 (2021) 20727–20739. doi:10.1021/acs.jpcc.1c07328.

[367] F. Souayfan, E. Rozière, M. Paris, D. Deneele, A. Loukili, C. Justino, 29Si and 27Al MAS NMR spectroscopic studies of activated metakaolin-slag mixtures, Constr. Build. Mater. 322 (2022). doi:10.1016/j.conbuildmat.2022.126415.

[368] L.E. Menchaca-Ballinas, A. V. Gorokhovsky, J.I. Escalante-Garcia, Waste glass as a precursor in sustainable hydraulic cements activated with CaO-NaOH-Na2CO3, Constr. Build. Mater. 302 (2021). doi:10.1016/j.conbuildmat.2021.124099.

[369] F. Puertas, M. Torres-Carrasco, Use of glass waste as an activator in the preparation of alkali-activated slag. Mechanical strength and paste characterisation, Cem. Concr. Res. 57 (2014) 95–104. doi:10.1016/j.cemconres.2013.12.005.

[370] J. Davidovits, Geopolymer Chemistry and Applications. 5-th edition, J. Davidovits.–Saint-Quentin, Fr. (2020) 680.

[371] S.Y. Yang, Y. Yan, B. Lothenbach, J. Skibsted, Incorporation of Sodium and Aluminum in Cementitious Calcium-Alumino-Silicate-Hydrate C-(A)-S-H Phases Studied by 23Na, 27Al, and 29Si MAS NMR Spectroscopy, J. Phys. Chem. C. 125 (2021) 27975–27995. doi:10.1021/acs.jpcc.1c08419.

[372] Y. Chiang, S.W. Chang, Bridging the gap between NMR measured mean silicate chain length and nano-scale silicate polymorphism of calcium silicate hydrates, Cem. Concr. Res. 140 (2021). doi:10.1016/j.cemconres.2020.106268.

[373] S.A. Bernal, J.L. Provis, B. Walkley, R. San Nicolas, J.D. Gehman, D.G. Brice, A.R. Kilcullen, P. Duxson, J.S.J. Van Deventer, Gel nanostructure in alkali-activated binders based on slag and fly ash, and effects of accelerated carbonation, Cem. Concr. Res. 53 (2013) 127–144. doi:10.1016/j.cemconres.2013.06.007.

[374] J. Wang, Z. Hu, Y. Chen, J. Huang, Y. Ma, W. Zhu, J. Liu, Effect of Ca/Si and Al/Si on micromechanical properties of C(-A)-S-H, Cem. Concr. Res. 157 (2022) 106811. doi:10.1016/j.cemconres.2022.106811.

[375] K. Shimoda, Y. Tobu, K. Kanehashi, T. Nemoto, K. Saito, Total understanding of the local structures of an amorphous slag: Perspective from multi-nuclear (29Si, 27Al, 17O, 25Mg, and 43Ca) solid-state NMR, J. Non. Cryst. Solids. 354 (2008) 1036–1043. doi:10.1016/j.jnoncrysol.2007.08.010.

[376] R.J. Myers, S.A. Bernal, J.D. Gehman, J.S.J. Van Deventer, J.L. Provis, The role of al in cross-linking of alkali-Activated slag cements, J. Am. Ceram. Soc. 98 (2015) 996–1004. doi:10.1111/jace.13360.

[377] G.K. Sun, J.F. Young, R.J. Kirkpatrick, The role of Al in C-S-H: NMR, XRD, and compositional results for precipitated samples, Cem. Concr. Res. 36 (2006) 18–29. doi:10.1016/j.cemconres.2005.03.002.

[378] M.D. Andersen, H.J. Jakobsen, J. Skibsted, A new aluminium-hydrate species in hydrated Portland cements characterized by 27Al and 29Si MAS NMR spectroscopy, Cem. Concr. Res. 36 (2006) 3–17. doi:10.1016/j.cemconres.2005.04.010.

[379] J.Z. Hu, C. Wan, A. Vjunov, M. Wang, Z. Zhao, M.Y. Hu, D.M. Camaioni, J.A. Lercher, 27Al MAS NMR Studies of HBEA Zeolite at Low to High Magnetic Fields, J. Phys. Chem. C. 121 (2017) 12849–12854. doi:10.1021/acs.jpcc.7b03517.

[380] X. Pardal, F. Brunet, T. Charpentier, I. Pochard, A. Nonat, 27Al and 29Si solid-state NMR characterization of calcium-aluminosilicate-hydrate, Inorg. Chem. 51 (2012) 1827–1836. doi:10.1021/ic202124x.

[381] K.L. Moran, P.D. Barker, J.E. Readman, P.P. Edwards, R. Dupree, P.A. Anderson, 29Si and 27Al MAS NMR spectra are affected by alkali metal cluster formation in zeolite LTA, Chem. Commun. (2000) 55–56. doi:10.1039/a908027i.

[382] S. Kalirai, P.P. Paalanen, J. Wang, F. Meirer, B.M. Weckhuysen, Visualizing Dealumination of a Single Zeolite Domain in a Real-Life Catalytic Cracking Particle, Angew. Chemie - Int. Ed. 55 (2016) 11134–11138. doi:10.1002/anie.201605215.

[383] E. Pustovgar, R.K. Mishra, M. Palacios, J.B. d'Espinose de Lacaillerie, T. Matschei, A.S. Andreev, H. Heinz, R. Verel, R.J. Flatt, Influence of aluminates on the hydration kinetics of tricalcium silicate, Cem. Concr. Res. 100 (2017) 245–262. doi:10.1016/j.cemconres.2017.06.006.

[384] J. Davidovits, Properties of Geopolymer Cements, First Int. Conf. Alkaline Cem. Concr. (1994) 131–149.

[385] John L. Provis, Susan A. Bernal, Geopolymers and Related Alkali-Activated Materials, Annu. Rev. Mater. Res. (2014) 299–327.

[386] E. Kapeluszna, Ł. Kotwica, A. Różycka, Ł. Gołek, Incorporation of Al in C-A-S-H gels with various Ca/Si and Al/Si ratio: Microstructural and structural characteristics with DTA/TG, XRD, FTIR and TEM analysis, Constr. Build. Mater. 155 (2017) 643–653. doi:10.1016/j.conbuildmat.2017.08.091.

[387] H.F.W. Taylor, Hydrated calcium silicates. Part I. Compound formation at ordinary temperatures, Am. Concr. Institute, ACI Spec. Publ. SP-249 (2008) 67–79.

[388] H.F.W. Taylor, Nanostructure of CSH: Current status, Adv. Cem. Based Mater. 1 (1993) 38–46. doi:10.1016/1065-7355(93)90006-A.

[389] R.R. Lloyd, J.L. Provis, J.S.J. Van Deventer, Pore solution composition and alkali diffusion in inorganic polymer cement, Cem. Concr. Res. 40 (2010) 1386–1392. doi:10.1016/j.cemconres.2010.04.008.

[390] L. Srinivasamurthy, V.S. Chevali, Z. Zhang, M.A. Longhi, T.W. Loh, H. Wang, Mechanical property and microstructure development in alkali activated fly ash slag blends due to efflorescence, Constr. Build. Mater. 332 (2022). doi:10.1016/j.conbuildmat.2022.127273.

[391] L. Srinivasamurthy, V.S. Chevali, Z. Zhang, H. Wang, Phase changes under efflorescence in alkali activated materials with mixed activators, Constr. Build. Mater. 283 (2021). doi:10.1016/j.conbuildmat.2021.122678.

[392] M.U. Christiansen, An Investigation of Waste Glass-Based Geopolymers Supplemented With Alumina, PhD thesis, 2013. http://linkinghub.elsevier.com/retrieve/pii/0040195174900067.

Symbols and abbreviations

Abbreviations

AAMs	Alkali activated materials
AAFS	Alkali activated fly ash and slag blends
AAWG	Alkali activated waste glass
ACPT	Accelerated chloride penetration test
BA	Bottom ash
BET	Nitrogen sorption tests
BJH	Barrett, Joyner, and Halenda method
C−A−S−H	Calcium aluminosilicate hydrates
C−S−H	Calcium silicate hydrates
CLDHs	Calcined layered double hydroxides
CWE	Cold water extraction
D	Diffusion
FA	Fly ash
FTIR	Fourier Transform InfraRed spectroscopy
GGBS	Ground granulated blast furnace slag
GP	Waste glass powder
HCFA	High-calcium fly ash
IC	Ion chromatography
ICP-OES	Inductively coupled plasma-optical emission spectrometry
ITZ	Interfacial transition zone
I	Interactions at phase boundary
LCFA	Low-calcium fly ash
LDHs	Layered double hydroxides
LOI	Loss on ignition
MCL	Mean chain length

MSWI BA	Municipal solid waste incineration bottom ash
MSAASB	MgO–$NaAlO_2$-activated GGBS/BA
MgO	Magnesium oxide
Mg-Al-NO_3 LDH	Nitrate intercalated LDH
MIP	Mercury intrusion porosimetry
MK	Metakaolin
N−A−S−H	Sodium aluminosilicate hydrates
NSSM	Non-steady-state migration
NG	Nucleation and crystal growth
NMR	Nuclear magnetic resonance
OPC	Ordinary Portland Cement
PSD	Particle size distribution
PTEs	Potentially toxic elements
QXRD	Quantification of X-ray diffractometry
SCMs	Supplementary cementitious materials
SEM	Scanning electron microscopy
SEM-EDS	Scanning electron microscopy-energy-dispersive X-ray spectroscopy
SAAS	Sodium aluminate activated slag
SAASB	Sodium aluminate activated slag and bottom ash
SAASG	Sodium aluminate activated slag and waste glass
SAAG	Sodium aluminate activated waste glass
SF	Silica fume
TAH	Third aluminate hydrate
TG	Thermogravimetric test
TRRP	Time to reach the reaction peak
WG	Waste glass
XRD	X-ray diffraction

XRF	X-ray fluorescence

Formulas

Akermanite	$Ca_2Mg[Si_2O_7]$
Calcite	$CaCO_3$
Chabazite	$(Ca,K_2,Na_2,Mg)Al_2Si_4O_{12}\bullet 6H_2O$
Dawsonite	$NaAlCO_3(OH)_2$
Ferro-glaucophane	$Na_2Fe_3Al_2Si_8O_{22}(OH)_2$
Gibbsite	$Al(OH)_3$
Gaylussite	$Na_2Ca(CO_3)_2\cdot 5H_2O$
Hemi-carbonaluminate	$Ca_4Al_2(OH)_{12}[OH(CO_3)_{0.5}]\cdot 5.5H_2O$
Hydrotalcite	$(Mg_{0.67}Al_{0.33}(OH)_2)(CO_3)_{0.165}(H_2O)_{0.48}$
Katoite	$Ca_{2.93}Al_{1.97}$ $(Si_{.64}O_{2.56})$ $(OH)_{9.44}$
Magnetite	Fe_3O_4
Magnesite	$MgCO_3$
Meionite	$Ca_4Al_6Si_6O_{24}CO_3$
Mullite	$2Al_2O_3$ SiO_2
Natrite	Na_2CO_3
Periclase	MgO
Quartz	SiO_2
Wustite	FeO
Zeolite A	$Na_{12}Al_{12}Si_{12}O_{48}$ $27H_2O$
Zeolite Na-P_1	$Na_6Al_6Si_{10}O_{32}\cdot 12H_2O$
Zeolite	$1.08Na_2O\cdot Al_2O_3\cdot 1.68SiO_2\cdot 1.8H_2O$

Appendix A

The pore solution composition data of Ref-NH, NA2, NA2.5, NA3, NA3.5, NA4 are listed in respectively.

Table A1 Ions concentration of NA2 at different function times (mmol/L).

Samples	Na	Ca	Si	Al	B	Cu	Fe	Ga	Li	Mg	Se	V
NA2 3d	422.3280	0.1227	0.8206	90.9544	0.0647	0.0007	0.0454	0.0135	0.0049	0.0008	0.0030	0.0110
NA2 7d	307.2342	0.0385	1.4125	125.4716	0.0660	0.0003	0.0312	0.0129	0.0037	0.0003	0.0024	0.0143
NA2 14d	226.6478	0.0841	1.7661	32.3877	0.1070	0.0002	0.0821	0.0095	0.0030	0.0005	0.0022	0.0193
NA2 28d	90.0473	0.2237	0.7905	2.9636	0.0882	0.0001	0.0127	0.0013	0.0076	0.0002	0.0006	0.0025

Table A2 Ions concentration of NA2.5 at different function times (mmol/L).

Samples	Na	Ca	Si	Al	B	Cu	Fe	Ga	Li	Mg	Se	V
NA2.5 3d	480.1467	0.1209	1.0572	91.0072	0.0757	0.0002	0.0438	0.0154	0.0044	0.0003	0.0032	0.0141
NA2.5 7d	303.1695	0.0790	1.9007	57.7767	0.1152	0.0000	0.0906	0.0121	0.0028	0.0005	0.0025	0.0220
NA2.5 14d	200.0539	0.1447	2.1079	10.0428	0.1597	0.0000	0.0562	0.0071	0.0031	0.0004	0.0015	0.0161
NA2.5 28d	72.4681	0.2527	0.5925	2.2263	0.0574	0.0000	0.0060	0.0008	0.0082	0.0004	0.0005	0.0015

Table A3 Ions concentration of NA3 at different function times (mmol/L).

Samples	Na	Ca	Si	Al	B	Cu	Fe	Ga	Li	Mg	Se	V
NA3 3d	559.2362	0.1537	0.8682	90.2738	0.0927	0.0001	0.0418	0.0175	0.0033	0.0003	0.0037	0.0172
NA3 7d	331.9159	0.0859	2.4244	41.1940	0.1435	0.0001	0.0712	0.0125	0.0028	0.0003	0.0026	0.0267
NA3 14d	99.0634	0.2161	0.8261	2.5922	0.0774	0.0001	0.0132	0.0013	0.0073	0.0004	0.0007	0.0023
NA3 28d	71.4253	0.2521	0.5604	2.0620	0.0519	0.0001	0.0061	0.0008	0.0098	0.0000	0.0005	0.0015

Table A4 Ions concentration of NA3.5 at different function times (mmol/L).

Samples	Na	Ca	Si	Al	B	Cu	Fe	Ga	Li	Mg	Se	V
NA3.5 3d	612.6617	0.1896	0.7509	88.9156	0.1102	0.0001	0.0390	0.0186	0.0029	0.0004	0.0041	0.0196
NA3.5 7d	335.7975	0.1055	2.4191	43.8903	0.1657	0.0001	0.0671	0.0137	0.0026	0.0004	0.0027	0.0300
NA3.5 14d	102.8402	0.2226	0.7378	2.4238	0.0778	0.0002	0.0133	0.0013	0.0092	0.0002	0.0008	0.0023
NA3.5 28d	82.8333	0.2417	0.5455	2.3718	0.0596	0.0001	0.0085	0.0009	0.0137	0.0005	0.0006	0.0014

Table A5 Ions concentration of NA4 at different function times (mmol/L).

Samples	Na	Ca	Si	Al	B	Cu	Fe	Ga	Li	Mg	Se	V
NA4 3d	740.7523	0.2156	0.9378	92.1152	0.1379	0.0000	0.0425	0.0220	0.0026	0.0004	0.0047	0.0239
NA4 7d	400.3221	0.0978	1.6493	88.3565	0.1705	0.0001	0.0642	0.0177	0.0026	0.0003	0.0033	0.0331
NA4 14d	99.1647	0.1923	0.5369	2.6865	0.0712	0.0000	0.0107	0.0014	0.0109	0.0002	0.0008	0.0022
NA4 28d	91.1295	0.2014	0.5889	2.8065	0.0614	0.0000	0.0071	0.0011	0.0174	0.0001	0.0007	0.0014

Table A6 Ions concentration of Ref-NH at different function times (mmol/L).

Samples	Na	Ca	Si	Al	B	Cu	Fe	Ga	Li	Mg	Se	V
Ref-NH 3d	120.2818	0.2354	0.5234	2.7838	0.0750	0.0001	0.0319	0.0001	0.1948	0.0010	0.0028	0.0032
Ref-NH 7d	112.3505	0.2668	0.3265	2.0206	0.0389	0.0002	0.0070	0.0001	0.0922	0.0005	0.0014	0.0012
Ref-NH 14d	111.4816	0.3040	0.2984	2.1557	0.0420	0.0001	0.0077	0.0001	0.1169	0.0001	0.0015	0.0013
Ref-NH 28d	53.7944	0.2689	0.2891	2.0361	0.0363	0.0001	0.0060	0.0001	0.1090	0.0001	0.0014	0.0011

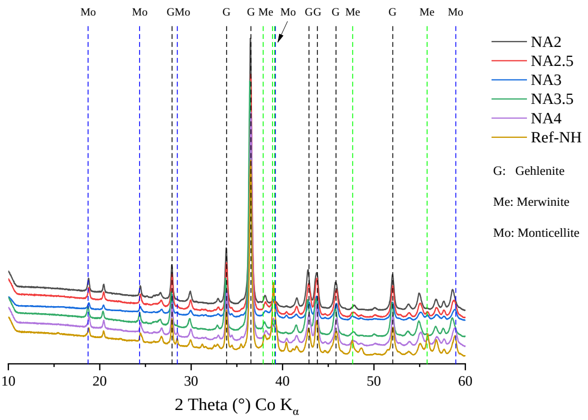

Fig. A1 XRD patterns of the SAAS pastes at 28 days after 1-hour 900℃ heating.

Table A7 5min leaching test of GGBS under different pH values of alkali leaching solution (mmol/L).

pH	Si	Al	Mg
13.5	2.2771	1.1721	0.0001
13	0.0831	0.0004	0.0002
12.5	0.2410	0.0383	0.0002
12	0.4122	0.0335	0.0001

Appendix B

Table B1 Quantification of XRD at 7 days (wt.%).

	Akermanite	Calcite	Dawsonite	Gibbsite	Magnetite	Meionite	Quartz	Wuestite	Amor.
BA0	0	0.88	0.67	1.64	0	0.33	0	0	86.49
BA5	0.47	0.76	0.49	0.84	0	0.54	0.59	0	86.32
BA10	0.58	0.66	0.45	0.8	0.24	0.47	1	0	85.8
BA15	0.96	1.04	0.72	0.97	0.67	0.35	2.48	0	82.81
BA20	0.91	0.78	0.24	0.97	0.79	0.84	3.2	0.62	81.64
BA25	1.09	1.05	0.87	0.01	1.33	0.69	3.5	0	81.45

Table B2 Quantification of XRD at 28 days (wt.%).

	Akermanite	Calcite	Hc	Ferro-glaucophane	Hydrotalcite	Magnetite	Meionite	Quartz	Zeolite A	Amor.
BA0	0.00	2.51	0.83	0.00	1.68	0.00	0.30	0.10	0.94	93.62
BA5	1.26	1.43	0	0.10	1.61	0.33	0	0.32	1.22	93.71
BA10	1.38	1.53	0	0.20	1.59	0.41	0	0.42	1.26	93.21
BA15	1.68	2.74	0	0.37	1.13	0.73	0	0.51	1.46	91.38
BA20	2.13	2.67	0	0.46	0.97	1.66	0	0.44	1.83	89.84
BA25	2.07	3.29	0	0.42	0.76	2.11	0	0.69	1.99	88.67

Table B3 Statistics of t_4, 1/N, and 1/N ln*k* fittings.

	BA20	BA25
t_4 (hours)	697.44	734.71
1/N after t_4	2.9333	-23.637
1/N ln*k* after t_4	3.3018	-26.081

Table B4 Element inputs from raw materials. (Cu, Mo, Sb, Cl^-, SO_4^{2-}) (mg/ g raw materials).

	GGBS	MSWI BA
Cu	0.00002	0.01083
Mo	0.00007	0.00732
Sb	0.00006	0.00401
Cl^-	0.362	33.544
SO_4^{2-}	1.55	73.033

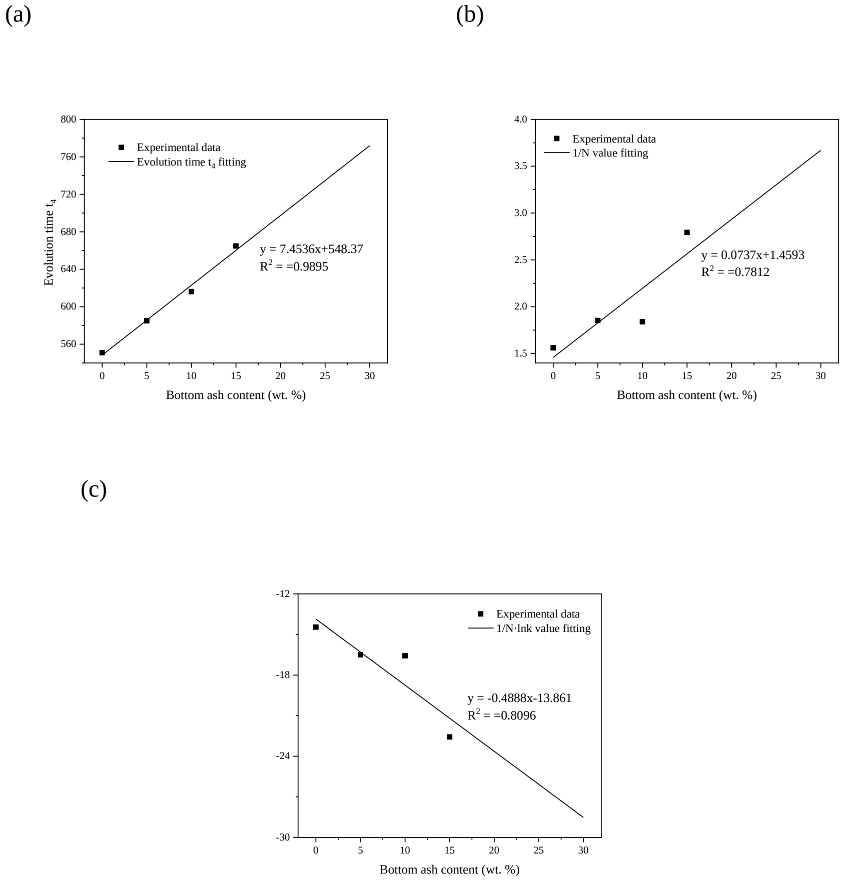

Fig. B1 (a) Evolution time t_4 fitting; (b) 1/N fitting; (c) 1/N lnk fitting.

Appendix C

The pore solution composition data of Al, Si, Mg, Na, and Ca are listed in the following tables, respectively.

Table C1 Concentration of Al (mmol/L).

Sample	Curing days			
	3	7	14	28
NH	2.1234	1.7607	2.2433	2.4057
NA	75.1852	34.9474	16.7144	3.6974
MA0.5	58.1482	33.6204	19.5022	2.7827
MA1	35.0422	27.1274	13.9833	2.6297
MA2	33.6444	20.1656	3.0030	2.6612
MA4	16.6037	1.7040	2.1946	1.8413

Table C2 Concentration of Si (mmol/L).

Sample	Curing days			
	3	7	14	28
NH	0.5837	0.4228	0.4173	0.3853
NA	1.7929	2.7211	0.8193	0.7188
MA0.5	1.7296	2.5118	0.7482	0.6222
MA1	1.8771	2.0111	0.5579	0.6865
MA2	2.1729	0.9918	0.3625	0.6592
MA4	3.1757	0.6452	0.4954	0.4686

Table C3 Concentration of Mg (mmol/L).

Sample	Curing days			
	3	7	14	28
NH	0.0000	0.0001	0.0002	0.0001
NA	0.0023	0.0013	0.0010	0.0001
MA0.5	0.0013	0.0010	0.0009	0.0004
MA1	0.0011	0.0009	0.0010	0.0001
MA2	0.0009	0.0009	0.0018	0.0001
MA4	0.0009	0.0018	0.0037	0.0001

Table C4 Concentration of Na (mmol/L).

Sample	Curing days			
	3	7	14	28
NH	161.4366	103.7492	126.7275	119.8649
NA	452.7518	402.9746	324.2820	118.8610
MA0.5	425.5259	332.6816	311.5509	121.7669
MA1	387.5637	317.4098	285.4848	119.0914
MA2	398.9046	303.4701	160.0295	128.7268
MA4	350.6898	101.6660	113.6112	91.1854

Table C5 Concentration of Ca (mmol/L).

Sample	Curing days			
	3	7	14	28
NH	0.2432	0.2625	0.2299	0.2207
NA	0.0263	0.0567	0.1082	0.1746
MA0.5	0.0551	0.0964	0.1360	0.1921
MA1	0.0743	0.1050	0.1155	0.1985
MA2	0.1209	0.1331	0.1469	0.1889
MA4	0.1544	0.2238	0.2379	0.2458

Table C6 Quantification of XRD results at 7 days (wt. %).

	NH	NA	MA0.5	MA1	MA2	MA4
Akermanite	0.14	0.49	0.27	0.22	0.19	0.44
Aragonite	1.09	1.96	1.43	1.38	0.84	0.66
Calcite	1.48	0.49	0.97	1.07	1.32	2.03
Hemi carbonaluminate	0.09	0.12	0.00	0.00	0.01	0.07
Hydrotalcite	1.47	1.11	1.13	1.34	1.67	2.53
Meionite	0.38	0.09	0.10	0.11	0.19	0.22
Periclase	0.00	0.00	0.32	0.71	1.38	3.70
Quartz	0.28	0.21	0.31	0.26	0.28	0.24
Vaterite	0.12	0.89	1.12	1.56	0.73	0.33
Zeolite A	0.00	0.04	0.02	0.02	0.00	0.00
Amor.	94.94	94.61	94.33	93.33	93.40	89.79

Table C7 Quantification of XRD results at 28 days (wt. %).

	NH	NA	MA0.5	MA1	MA2	MA4
Akermanite	0.21	0.34	0.44	0.47	0.19	0.57
Aragonite	2.37	2.37	2.11	1.82	1.43	0.48
Calcite	2.28	1.47	1.69	1.79	1.77	1.90
Hemi carbonaluminate	0.00	0.00	0.02	0.04	0.00	0.00
Hydrotalcite	1.68	1.61	1.77	2.13	2.33	3.04
Meionite	0.21	0.09	0.09	0.08	0.17	0.20
Periclase	0.00	0.00	0.19	0.44	1.31	2.97
Quartz	0.22	0.36	0.30	0.20	0.28	0.26
Vaterite	1.23	0.67	0.59	0.26	0.66	0.00
Zeolite A	0.00	0.16	0.08	0.02	0.00	0.00
Amor.	91.79	92.93	92.72	92.74	91.87	90.58

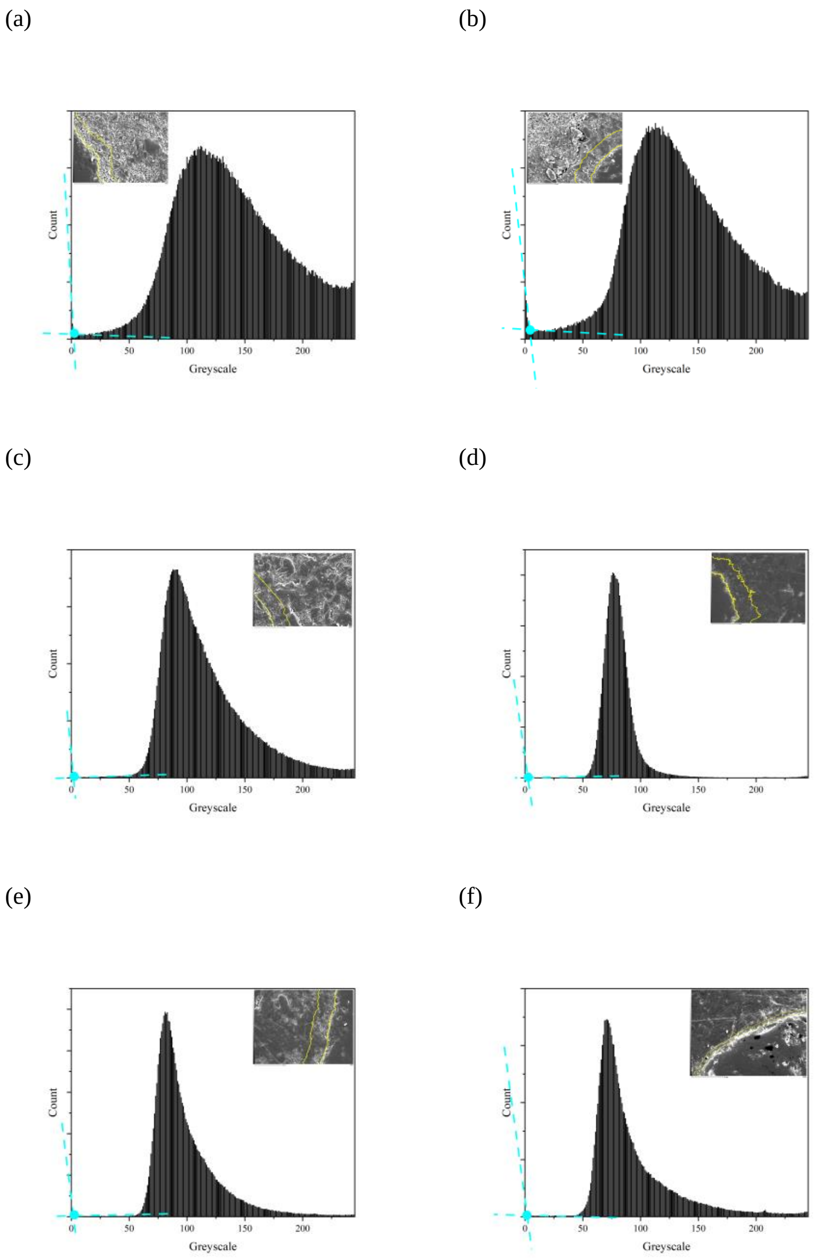

Fig. C1 ITZ determination by grayscale of (a) NH; (b) NA; (c) MA0.5; (d) MA1; (e) MA2; (f) MA4.

Appendix D

Table D1 Quantification of XRD results at 3 days (wt. %).

	NA3-3d	NA4-3d	NA5-3d	NHNA3-3d	NHNA4-3d	NHNA5-3d	NH3-3d	NH4-3d	NH5-3d
Calcite	0.00	0.00	0.00	1.00	1.30	1.53	1.04	1.59	1.38
Hydrotalcite	0.00	0.00	0.00	0.00	0.00	0.00	0.51	0.92	0.66
Katoite	0.00	1.68	1.97	0.88	0.63	0.43	0.00	0.00	0.00
Zeolite Na-P_1	0.00	0.03	0.07	1.12	10.69	16.07	0.00	0.00	0.00
Natrite	0.00	0.61	0.29	0.80	0.49	0.86	2.33	4.39	6.01
Zeolite A	3.04	3.20	3.27	3.56	0.76	0.34	0.00	0.00	0.00
Amor.	96.96	94.47	94.40	92.63	86.12	80.77	96.11	93.10	91.96

Table D2 Quantification of XRD results at 28 days (wt. %).

	NA3-3d	NA4-3d	NA5-3d	NHNA3-3d	NHNA4-3d	NHNA5-3d	NH3-3d	NH4-3d	NH5-3d
Calcite	0.00	0.00	0.00	0.88	2.21	1.93	1.00	1.52	1.94
Hydrotalcite	0.00	0.00	0.00	0.00	0.00	0.00	0.76	0.97	1.34
Katoite	0.00	4.83	6.18	0.48	0.76	0.24	0.00	0.00	0.00
Magnesite	0.00	0.00	0.00	1.51	2.41	1.54	1.66	2.67	3.11
Zeolite Na-P_1	0.00	2.50	0.80	1.11	17.16	20.40	0.00	0.00	0.00
Natrite	0.00	0.00	0.00	0.93	0.92	1.20	0.93	1.58	3.99
Zeolite A	5.34	8.19	8.36	2.79	0.93	0.60	0.00	0.00	0.00
Amor.	94.66	84.49	84.68	92.31	75.61	74.09	95.67	93.28	89.61

NA3

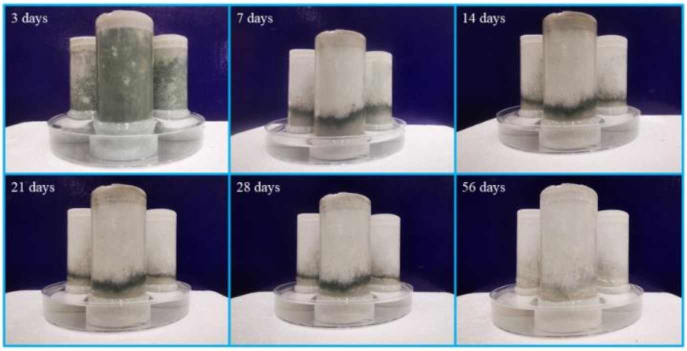
3 days
7 days
14 days
21 days
28 days
56 days

NA4

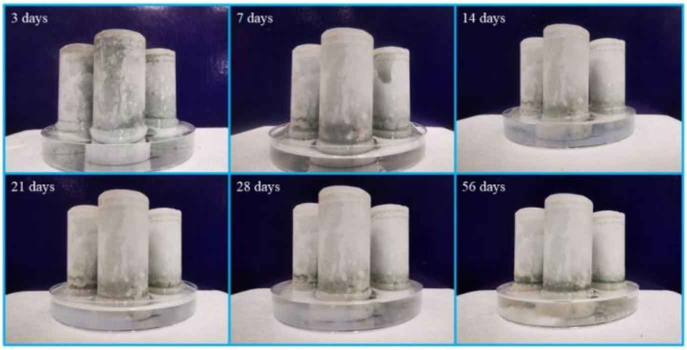
3 days
7 days
14 days
21 days
28 days
56 days

NA5

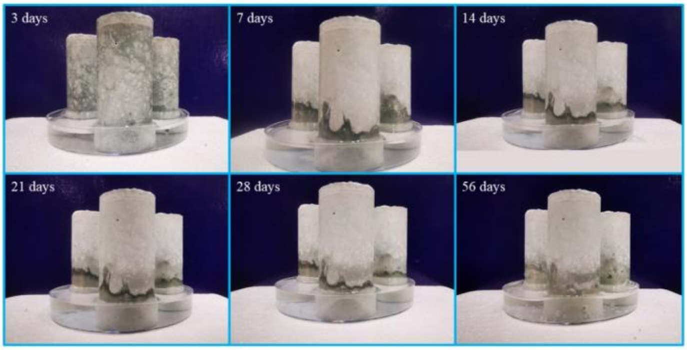
3 days
7 days
14 days
21 days
28 days
56 days

NHNA3

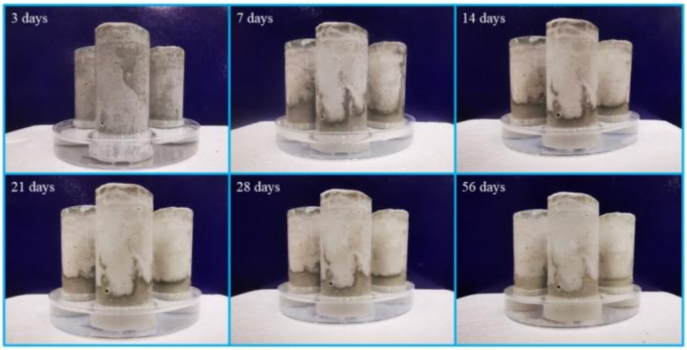

NHNA4

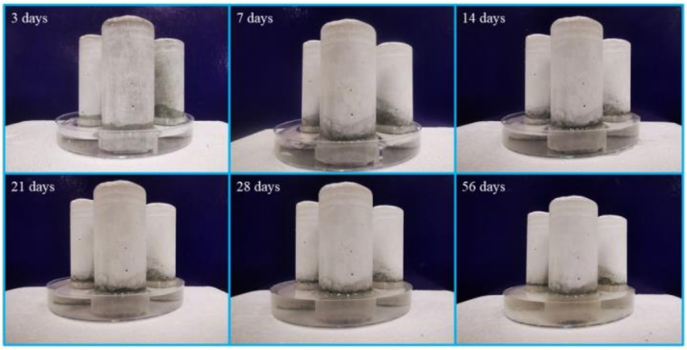

NHNA5

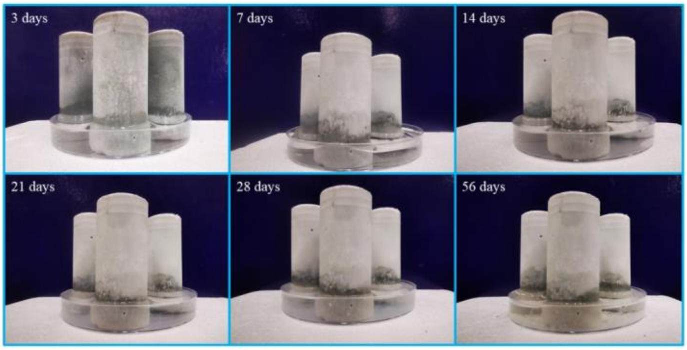

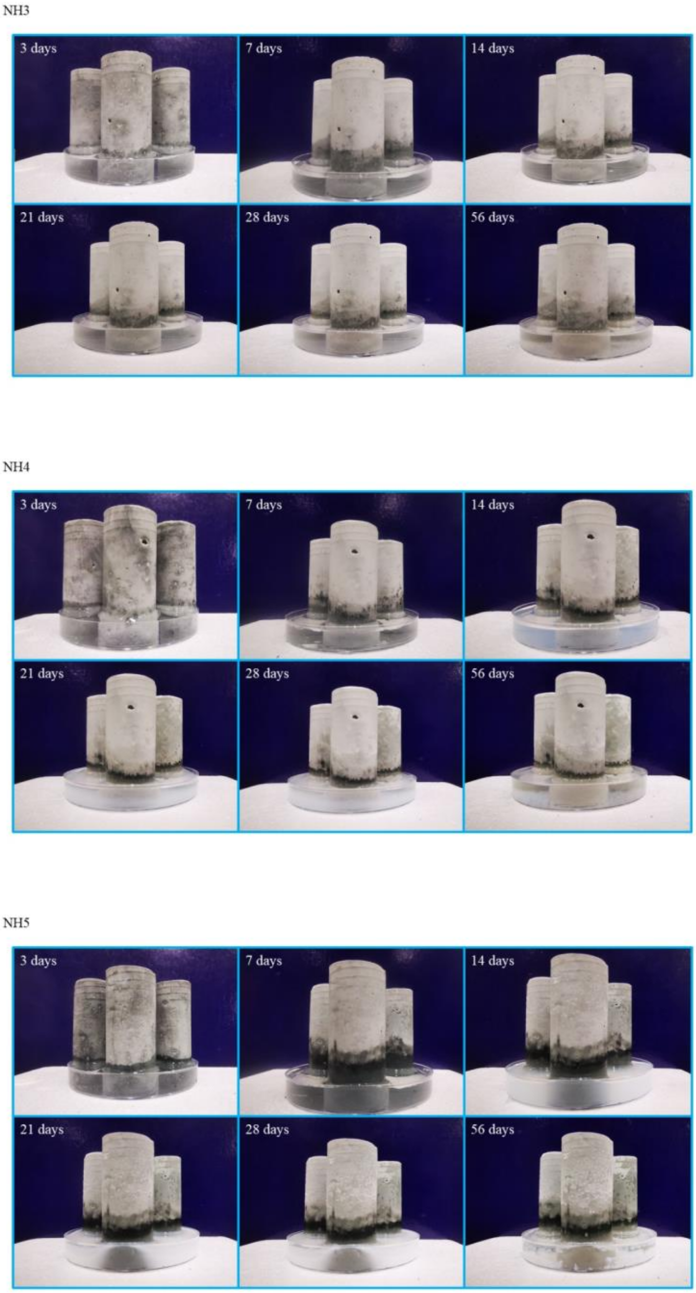

Fig. D1 Visual efflorescence testing of SAASG pastes at different curing ages.

Summary

Supplementary cementitious materials (SCMs) provide a significant contribution to sustainable construction. The use of these materials in concrete production consumes less energy and offers improved efficiency and building performance. Facing the challenges of SCMs utilization, this thesis firstly focuses on the alkali activation of slag, fly ash, waste glass, and municipal solid waste incineration bottom ash (MSWI BA). Simultaneously, the sodium hydroxides, sodium silicate, and sodium aluminate were used as activators aiming to the promotion of in-situ formed layered double hydroxides (LDHs).

Firstly, the different effects of MgO, nitrate intercalated LDH (Mg-Al-NO_3 LDH), and calcined natural LDH-CO_3 on the alkali activated fly ash and slag blends (AAFS) were investigated in terms of chloride resistance (Chapter 2). Then, sodium aluminate-activated slag was investigated to enhance the chloride binding of alkali activated materials (AAMs) to promote the in-situ formation of layered double hydroxides (LDHs) (Chapter 3). Thirdly, the influence of MSWI BA on $NaAlO_2$ activated slag was researched in terms of the reaction process, thermodynamic modelling, and further, leaching behavior (Chapter 4). Subsequently, MgO-$NaAlO_2$ activated slag and MSWI BA was studied to alleviate the leaching issues of MSWI BA via promoted gels and LDHs formation (Chapter 5). Then, this study aims to investigate the chloride diffusion behavior of alkali activated slag and fly ash blends with different contents of waste glass powder (GP) addition (Chapter 6). Finally, the efflorescence behavior of NaOH and $NaAlO_2$ activated waste glass powder was determined (Chapter 7).

The evolution of pore solution (using ICP), reaction products (using XRD, TGA, and FTIR), and microstructure (via BET and MIP) were determined to investigate the dynamic activation process. Furthermore, the thermodynamic modelling of sodium aluminate activation was performed by GEM-selector. Moreover, the mechanical property, chloride resistance, leaching behavior, and efflorescence behavior were tested to evaluate the performance of the final activated matrices.

The results show that sodium aluminate stabilizes the pH environment at around 12.7 during the curing ages. The Mg-Al-LDHs are promoted with higher Al-O tetrahedra and Mg^{2+} contents, enhancing chloride resistance and heavy metal ion binding capacity. Simultaneously, the sodium aluminate activation transfers the reaction products from C−S−H to C(N)−A−S−H, promoting the resistance to efflorescence.

The thesis reveals the effect of extra Al-O tetrahedra and Mg^{2+} on the in-situ formation of LDHs. Based on the results, the mechanism of sodium aluminate activation is proposed. At the same time, the mechanism of how Mg^{2+} influences the reaction products and leaching behavior is proposed as well. Furthermore, thermodynamic modelling gives the prediction of the heavy metal ion binding capacity of activated matrices. The design, modelling, and application of sodium aluminate activation have been comprehensively investigated.

List of publications

Peer-reviewed journal papers

[1] **T. Liu**, Q. Yu, H.J.H. Brouwers, In-situ formation of layered double hydroxides (LDHs) in sodium aluminate activated slag: The role of Al-O tetrahedra. Cement and Concrete Research 153 (2022). doi:10.1016/j.cemconres.2021.106697.

[2] **T. Liu**, Y. Chen, Q. Yu, J. Fan, H.J.H. Brouwers, Effect of MgO, Mg-Al-NO3 LDH and calcined LDH-CO3 on chloride resistance of alkali activated fly ash and slag blends. Construction and Building Materials 250 (2020).doi:10.1016/j.conbuildmat.2020.118865.

[3] **T. Liu**, Q. Yu, H.J.H. Brouwers, Utilization of waste glass in alkali activated slag/fly ash blends: reaction process, microstructure, and chloride diffusion behavior, Journal of Sustainable Cement-Based Materials (2022). doi: 10.1080/21650373.2022.2082577.

[4] **T. Liu**, S. Li, Y. Chen, H.J.H. Brouwers, Q. Yu, In-situ formation of LDHs in MgO-NaAlO2 activated GGBS / MSWI BA: The impact of Mg2+ on reaction mechanism and leaching behavior. Cement and Concrete Composites (Revision submitted).

[5] **T. Liu**, Y. Tang, K. Schollbach, J.L. Stapper, H.J.H. Brouwers, Q. Yu, NaAlO2 activated slag and MSWI bottom ash: Simulation and experimental analysis of leaching behavior (In progress).

[6] **T. Liu**, Y. Chen, G. Liu, B. Yuan, W. Zhuang, H.J.H. Brouwers, Q. Yu, Reaction, microstructure, and efflorescence behavior of NaOH / NaAlO2 activated slag and wastes glass: The transformation from C−S−H to C(N)−A−S–H (In progress).

[7] **T. Liu**, J. He, Q. Yu, H.J.H. Brouwers, Corrosion behavior of steel rebar embedded MgO-NaAlO2 activated slag mortar. (In preparation).

[8] **T. Liu**, Q. Yu, J. Fan, Z. Peng, E. Wang, Concrete spherical joint contact stress distribution and overturning moment of swing bridge. Structures 28 (2020) 1187–1195. doi:10.1016/j.istruc.2020.09.053.

[9] **T. Liu**, J. Fan, Z. Peng, Central load-bearing control in the construction process of the concrete spherical joint Nandu River swing bridge: A case study. Buildings 12 (2022). doi:10.3390/buildings12050511.

[10] **T. Liu**, J. Fan, Z. Peng, Mechanical properties, dry shrinkage, and water penetration of reusing fine and ultrafine recycled concrete aggregate. Materials 15 (2022). doi: 10.3390/ma15248947.

Conferences

[1] **T Liu**, Y Chen, QL Yu, HJH Brouwers, Effect of MgO, nitrate intercalated LDH and Calcined-LDH on chloride resistance of alkali-activated fly ash/slag mortar, PROCEEDINGS ICSBM 2019 VOLUME 2-New cementitious binders, 372, Eindhoven, Netherlands, 2019.

[2] **T Liu**, QL Yu, HJH Brouwers, In-situ LDH Formation of Sodium Aluminate Activated Slag, International Journal of Materials and Metallurgical Engineering 16 (2), 7-11, 2022.

[3] **T Liu**, QL Yu, HJH Brouwers, Effect of Mg/Al on the in-situ formation of LDHs in alkali activated slag, 4th International Conference on the Chemistry of Construction Materials, Karlsruhe Institute of Technology, Germany, 2022. (Poster)

Curriculum vitae

Tao Liu was born in Hefei, Anhui Province, China on March 1st, 1993. After finishing his primary, middle and high school educations in Hefei, he started to study at Anhui University of Science and Technology (AUST) in September 2011. In June 2015, he received his bachelor's degree majoring in Civil Engineering. In September 2015, he started to study at the School of Civil Engineering and Architecture at Wuhan University of Technology (WUT) as a master's student supervised by Prof. Jianfeng Fan, majoring in structural calculation and simulation, and gaining his master's degree in June 2018. His research interests include the concrete spherical joint contact stress distribution of swing bridges and finite element modelling (FEM). In October 2018, he started his Ph.D. study under the supervision of Prof. H.J.H. (Jos) Brouwers and Prof. Qingliang Yu at Eindhoven University of Technology (TU/e), Eindhoven, the Netherlands. His Ph.D. research topic is related to the immobilization potential of alkali activated materials, including mineralogy, thermal dynamic analysis, environmental impact, durability, and modelling.

Bouwstenen is een publicatiereeks van de Faculteit Bouwkunde, Technische Universiteit Eindhoven. Zij presenteert resultaten van onderzoek en andere activiteiten op het vakgebied der Bouwkunde, uitgevoerd in het kader van deze Faculteit.

Bouwstenen en andere proefschriften van de TU/e zijn online beschikbaar via:
https://research.tue.nl/

Reeds verschenen in de serie
Bouwstenen

nr 1
Elan: A Computer Model for Building Energy Design: Theory and Validation
Martin H. de Wit
H.H. Driessen
R.M.M. van der Velden

nr 2
Kwaliteit, Keuzevrijheid en Kosten: Evaluatie van Experiment Klarendal, Arnhem
J. Smeets
C. le Nobel
M. Broos
J. Frenken
A. v.d. Sanden

nr 3
Crooswijk:
Van 'Bijzonder' naar 'Gewoon'
Vincent Smit
Kees Noort

nr 4
Staal in de Woningbouw
Edwin J.F. Delsing

nr 5
Mathematical Theory of Stressed Skin Action in Profiled Sheeting with Various Edge Conditions
Andre W.A.M.J. van den Bogaard

nr 6
Hoe Berekenbaar en Betrouwbaar is de Coëfficiënt k in x-ksigma en x-ks?
K.B. Lub
A.J. Bosch

nr 7
Het Typologisch Gereedschap:
Een Verkennende Studie Omtrent Typologie en Omtrent de Aanpak van Typologisch Onderzoek
J.H. Luiten

nr 8
Informatievoorziening en Beheerprocessen
A. Nauta
Jos Smeets (red.)
Helga Fassbinder (projectleider)
Adrie Proveniers
J. v.d. Moosdijk

nr 9
Strukturering en Verwerking van Tijdgegevens voor de Uitvoering van Bouwwerken
ir. W.F. Schaefer
P.A. Erkelens

nr 10
Stedebouw en de Vorming van een Speciale Wetenschap
K. Doevendans

nr 11
Informatica en Ondersteuning van Ruimtelijke Besluitvorming
G.G. van der Meulen

nr 12
Staal in de Woningbouw, Korrosie-Bescherming van de Begane Grondvloer
Edwin J.F. Delsing

nr 13
Een Thermisch Model voor de Berekening van Staalplaatbetonvloeren onder Brandomstandigheden
A.F. Hamerlinck

nr 14
De Wijkgedachte in Nederland: Gemeenschapsstreven in een Stedebouwkundige Context
K. Doevendans
R. Stolzenburg

nr 15
Diaphragm Effect of Trapezoidally Profiled Steel Sheets:
Experimental Research into the Influence of Force Application
Andre W.A.M.J. van den Bogaard

nr 16
Versterken met Spuit-Ferrocement:
Het Mechanische Gedrag van met Spuit-Ferrocement Versterkte Gewapend Betonbalken
K.B. Lubir
M.C.G. van Wanroy

nr 17
De Tractaten van Jean Nicolas Louis Durand
G. van Zeyl

nr 18
Wonen onder een Plat Dak: Drie Opstellen over Enkele Vooronderstellingen van de Stedebouw
K. Doevendans

nr 19
Supporting Decision Making Processes: A Graphical and Interactive Analysis of Multivariate Data
W. Adams

nr 20
Self-Help Building Productivity: A Method for Improving House Building by Low-Income Groups Applied to Kenya 1990-2000
P. A. Erkelens

nr 21
De Verdeling van Woningen: Een Kwestie van Onderhandelen
Vincent Smit

nr 22
Flexibiliteit en Kosten in het Ontwerpproces: Een Besluitvormingondersteunend Model
M. Prins

nr 23
Spontane Nederzettingen Begeleid: Voorwaarden en Criteria in Sri Lanka
Po Hin Thung

nr 24
Fundamentals of the Design of Bamboo Structures
Oscar Arce-Villalobos

nr 25
Concepten van de Bouwkunde
M.F.Th. Bax (red.)
H.M.G.J. Trum (red.)

nr 26
Meaning of the Site
Xiaodong Li

nr 27
Het Woonmilieu op Begrip Gebracht: Een Speurtocht naar de Betekenis van het Begrip 'Woonmilieu'
Jaap Ketelaar

nr 28
Urban Environment in Developing Countries
editors: Peter A. Erkelens
George G. van der Meulen (red.)

nr 29
Stategische Plannen voor de Stad: Onderzoek en Planning in Drie Steden
prof.dr. H. Fassbinder (red.)
H. Rikhof (red.)

nr 30
Stedebouwkunde en Stadsbestuur
Piet Beekman

nr 31
De Architectuur van Djenné: Een Onderzoek naar de Historische Stad
P.C.M. Maas

nr 32
Conjoint Experiments and Retail Planning
Harmen Oppewal

nr 33
Strukturformen Indonesischer Bautechnik: Entwicklung Methodischer Grundlagen für eine 'Konstruktive Pattern Language' in Indonesien
Heinz Frick arch. SIA

nr 34
Styles of Architectural Designing: Empirical Research on Working Styles and Personality Dispositions
Anton P.M. van Bakel

nr 35
Conjoint Choice Models for Urban Tourism Planning and Marketing
Benedict Dellaert

nr 36
Stedelijke Planvorming als Co-Produktie
Helga Fassbinder (red.)

nr 37
Design Research in the Netherlands
editors: R.M. Oxman
M.F.Th. Bax
H.H. Achten

nr 38
Communication in the Building Industry
Bauke de Vries

nr 39
Optimaal Dimensioneren van Gelaste Plaatliggers
J.B.W. Stark
F. van Pelt
L.F.M. van Gorp
B.W.E.M. van Hove

nr 40
Huisvesting en Overwinning van Armoede
P.H. Thung
P. Beekman (red.)

nr 41
Urban Habitat:
The Environment of Tomorrow
George G. van der Meulen
Peter A. Erkelens

nr 42
A Typology of Joints
John C.M. Olie

nr 43
Modeling Constraints-Based Choices for Leisure Mobility Planning
Marcus P. Stemerding

nr 44
Activity-Based Travel Demand Modeling
Dick Ettema

nr 45
Wind-Induced Pressure Fluctuations on Building Facades
Chris Geurts

nr 46
Generic Representations
Henri Achten

nr 47
Johann Santini Aichel:
Architectuur en Ambiguiteit
Dirk De Meyer

nr 48
Concrete Behaviour in Multiaxial Compression
Erik van Geel

nr 49
Modelling Site Selection
Frank Witlox

nr 50
Ecolemma Model
Ferdinand Beetstra

nr 51
Conjoint Approaches to Developing Activity-Based Models
Donggen Wang

nr 52
On the Effectiveness of Ventilation
Ad Roos

nr 53
Conjoint Modeling Approaches for Residential Group preferences
Eric Molin

nr 54
Modelling Architectural Design Information by Features
Jos van Leeuwen

nr 55
A Spatial Decision Support System for the Planning of Retail and Service Facilities
Theo Arentze

nr 56
Integrated Lighting System Assistant
Ellie de Groot

nr 57
Ontwerpend Leren, Leren Ontwerpen
J.T. Boekholt

nr 58
Temporal Aspects of Theme Park Choice Behavior
Astrid Kemperman

nr 59
Ontwerp van een Geïndustrialiseerde Funderingswijze
Faas Moonen

nr 60
Merlin: A Decision Support System for Outdoor Leisure Planning
Manon van Middelkoop

nr 61
The Aura of Modernity
Jos Bosman

nr 62
Urban Form and Activity-Travel Patterns
Daniëlle Snellen

nr 63
Design Research in the Netherlands 2000
Henri Achten

nr 64
Computer Aided Dimensional Control in Building Construction
Rui Wu

nr 65
Beyond Sustainable Building
editors: Peter A. Erkelens
Sander de Jonge
August A.M. van Vliet
co-editor: Ruth J.G. Verhagen

nr 66
Das Globalrecyclingfähige Haus
Hans Löfflad

nr 67
Cool Schools for Hot Suburbs
René J. Dierkx

nr 68
A Bamboo Building Design Decision Support Tool
Fitri Mardjono

nr 69
Driving Rain on Building Envelopes
Fabien van Mook

nr 70
Heating Monumental Churches
Henk Schellen

nr 71
Van Woningverhuurder naar Aanbieder van Woongenot
Patrick Dogge

nr 72
Moisture Transfer Properties of Coated Gypsum
Emile Goossens

nr 73
Plybamboo Wall-Panels for Housing
Guillermo E. González-Beltrán

nr 74
The Future Site-Proceedings
Ger Maas
Frans van Gassel

nr 75
Radon transport in Autoclaved Aerated Concrete
Michel van der Pal

nr 76
The Reliability and Validity of Interactive Virtual Reality Computer Experiments
Amy Tan

nr 77
Measuring Housing Preferences Using Virtual Reality and Belief Networks
Maciej A. Orzechowski

nr 78
Computational Representations of Words and Associations in Architectural Design
Nicole Segers

nr 79
Measuring and Predicting Adaptation in Multidimensional Activity-Travel Patterns
Chang-Hyeon Joh

nr 80
Strategic Briefing
Fayez Al Hassan

nr 81
Well Being in Hospitals
Simona Di Cicco

nr 82
Solares Bauen:
Implementierungs- und Umsetzungs-Aspekte in der Hochschulausbildung in Österreich
Gerhard Schuster

nr 83
Supporting Strategic Design of Workplace Environments with Case-Based Reasoning
Shauna Mallory-Hill

nr 84
ACCEL: A Tool for Supporting Concept Generation in the Early Design Phase
Maxim Ivashkov

nr 85
Brick-Mortar Interaction in Masonry under Compression
Ad Vermeltfoort

nr 86
Zelfredzaam Wonen
Guus van Vliet

nr 87
Een Ensemble met Grootstedelijke Allure
Jos Bosman
Hans Schippers

nr 88
On the Computation of Well-Structured Graphic Representations in Architectural Design
Henri Achten

nr 89
De Evolutie van een West-Afrikaanse Vernaculaire Architectuur
Wolf Schijns

nr 90
ROMBO Tactiek
Christoph Maria Ravesloot

nr 91
External Coupling between Building Energy Simulation and Computational Fluid Dynamics
Ery Djunaedy

nr 92
Design Research in the Netherlands 2005
editors: Henri Achten
Kees Dorst
Pieter Jan Stappers
Bauke de Vries

nr 93
Ein Modell zur Baulichen Transformation
Jalil H. Saber Zaimian

nr 94
Human Lighting Demands: Healthy Lighting in an Office Environment
Myriam Aries

nr 95
A Spatial Decision Support System for the Provision and Monitoring of Urban Greenspace
Claudia Pelizaro

nr 96
Leren Creëren
Adri Proveniers

nr 97
Simlandscape
Rob de Waard

nr 98
Design Team Communication
Ad den Otter

nr 99
Humaan-Ecologisch Georiënteerde Woningbouw
Juri Czabanowski

nr 100
Hambase
Martin de Wit

nr 101
Sound Transmission through Pipe Systems and into Building Structures
Susanne Bron-van der Jagt

nr 102
Het Bouwkundig Contrapunt
Jan Francis Boelen

nr 103
A Framework for a Multi-Agent Planning Support System
Dick Saarloos

nr 104
Bracing Steel Frames with Calcium Silicate Element Walls
Bright Mweene Ng'andu

nr 105
Naar een Nieuwe Houtskeletbouw
F.N.G. De Medts

nr 106 and 107
Niet gepubliceerd

nr 108
Geborgenheid
T.E.L. van Pinxteren

nr 109
Modelling Strategic Behaviour in Anticipation of Congestion
Qi Han

nr 110
Reflecties op het Woondomein
Fred Sanders

nr 111
On Assessment of Wind Comfort by Sand Erosion
Gábor Dezsö

nr 112
Bench Heating in Monumental Churches
Dionne Limpens-Neilen

nr 113
RE. Architecture
Ana Pereira Roders

nr 114
Toward Applicable Green Architecture
Usama El Fiky

nr 115
Knowledge Representation under Inherent Uncertainty in a Multi-Agent System for Land Use Planning
Liying Ma

nr 116
Integrated Heat Air and Moisture Modeling and Simulation
Jos van Schijndel

nr 117
Concrete Behaviour in Multiaxial Compression
J.P.W. Bongers

nr 118
The Image of the Urban Landscape
Ana Moya Pellitero

nr 119
The Self-Organizing City in Vietnam
Stephanie Geertman

nr 120
A Multi-Agent Planning Support System for Assessing Externalities of Urban Form Scenarios
Rachel Katoshevski-Cavari

nr 121
Den Schulbau Neu Denken, Fühlen und Wollen
Urs Christian Maurer-Dietrich

nr 122
Peter Eisenman Theories and Practices
Bernhard Kormoss

nr 123
User Simulation of Space Utilisation
Vincent Tabak

nr 125
In Search of a Complex System Model
Oswald Devisch

nr 126
Lighting at Work:
Environmental Study of Direct Effects of Lighting Level and Spectrum on Psycho-Physiological Variables
Grazyna Górnicka

nr 127
Flanking Sound Transmission through Lightweight Framed Double Leaf Walls
Stefan Schoenwald

nr 128
Bounded Rationality and Spatio-Temporal Pedestrian Shopping Behavior
Wei Zhu

nr 129
Travel Information:
Impact on Activity Travel Pattern
Zhongwei Sun

nr 130
Co-Simulation for Performance Prediction of Innovative Integrated Mechanical Energy Systems in Buildings
Marija Trčka

nr 131
Niet gepubliceerd

nr 132
Architectural Cue Model in Evacuation Simulation for Underground Space Design
Chengyu Sun

nr 133
Uncertainty and Sensitivity Analysis in Building Performance Simulation for Decision Support and Design Optimization
Christina Hopfe

nr 134
Facilitating Distributed Collaboration in the AEC/FM Sector Using Semantic Web Technologies
Jacob Beetz

nr 135
Circumferentially Adhesive Bonded Glass Panes for Bracing Steel Frame in Façades
Edwin Huveners

nr 136
Influence of Temperature on Concrete Beams Strengthened in Flexure with CFRP
Ernst-Lucas Klamer

nr 137
Sturen op Klantwaarde
Jos Smeets

nr 139
Lateral Behavior of Steel Frames with Discretely Connected Precast Concrete Infill Panels
Paul Teewen

nr 140
Integral Design Method in the Context of Sustainable Building Design
Perica Savanović

nr 141
Household Activity-Travel Behavior: Implementation of Within-Household Interactions
Renni Anggraini

nr 142
Design Research in the Netherlands 2010
Henri Achten

nr 143
Modelling Life Trajectories and Transport Mode Choice Using Bayesian Belief Networks
Marloes Verhoeven

nr 144
Assessing Construction Project Performance in Ghana
William Gyadu-Asiedu

nr 145
Empowering Seniors through Domotic Homes
Masi Mohammadi

nr 146
An Integral Design Concept for Ecological Self-Compacting Concrete
Martin Hunger

nr 147
Governing Multi-Actor Decision Processes in Dutch Industrial Area Redevelopment
Erik Blokhuis

nr 148
A Multifunctional Design Approach for Sustainable Concrete
Götz Hüsken

nr 149
Quality Monitoring in Infrastructural Design-Build Projects
Ruben Favié

nr 150
Assessment Matrix for Conservation of Valuable Timber Structures
Michael Abels

nr 151
Co-simulation of Building Energy Simulation and Computational Fluid Dynamics for Whole-Building Heat, Air and Moisture Engineering
Mohammad Mirsadeghi

nr 152
External Coupling of Building Energy Simulation and Building Element Heat, Air and Moisture Simulation
Daniel Cóstola

nr 153
Adaptive Decision Making In Multi-Stakeholder Retail Planning
Ingrid Janssen

nr 154
Landscape Generator
Kymo Slager

nr 155
Constraint Specification in Architecture
Remco Niemeijer

nr 156
A Need-Based Approach to Dynamic Activity Generation
Linda Nijland

nr 157
Modeling Office Firm Dynamics in an Agent-Based Micro Simulation Framework
Gustavo Garcia Manzato

nr 158
Lightweight Floor System for Vibration Comfort
Sander Zegers

nr 159
Aanpasbaarheid van de Draagstructuur
Roel Gijsbers

nr 160
'Village in the City' in Guangzhou, China
Yanliu Lin

nr 161
Climate Risk Assessment in Museums
Marco Martens

nr 162
Social Activity-Travel Patterns
Pauline van den Berg

nr 163
Sound Concentration Caused by Curved Surfaces
Martijn Vercammen

nr 164
Design of Environmentally Friendly Calcium Sulfate-Based Building Materials: Towards an Improved Indoor Air Quality
Qingliang Yu

nr 165
Beyond Uniform Thermal Comfort on the Effects of Non-Uniformity and Individual Physiology
Lisje Schellen

nr 166
Sustainable Residential Districts
Gaby Abdalla

nr 167
Towards a Performance Assessment Methodology using Computational Simulation for Air Distribution System Designs in Operating Rooms
Mônica do Amaral Melhado

nr 168
Strategic Decision Modeling in Brownfield Redevelopment
Brano Glumac

nr 169
Pamela: A Parking Analysis Model for Predicting Effects in Local Areas
Peter van der Waerden

nr 170
A Vision Driven Wayfinding Simulation-System Based on the Architectural Features Perceived in the Office Environment
Qunli Chen

nr 171
Measuring Mental Representations Underlying Activity-Travel Choices
Oliver Horeni

nr 172
Modelling the Effects of Social Networks on Activity and Travel Behaviour
Nicole Ronald

nr 173
Uncertainty Propagation and Sensitivity Analysis Techniques in Building Performance Simulation to Support Conceptual Building and System Design
Christian Struck

nr 174
Numerical Modeling of Micro-Scale Wind-Induced Pollutant Dispersion in the Built Environment
Pierre Gousseau

nr 175
Modeling Recreation Choices
over the Family Lifecycle
Anna Beatriz Grigolon

nr 176
Experimental and Numerical Analysis of
Mixing Ventilation at Laminar, Transitional
and Turbulent Slot Reynolds Numbers
Twan van Hooff

nr 177
Collaborative Design Support:
Workshops to Stimulate Interaction and
Knowledge Exchange Between Practitioners
Emile M.C.J. Quanjel

nr 178
Future-Proof Platforms for Aging-in-Place
Michiel Brink

nr 179
Motivate:
A Context-Aware Mobile Application for
Physical Activity Promotion
Yuzhong Lin

nr 180
Experience the City:
Analysis of Space-Time Behaviour and
Spatial Learning
Anastasia Moiseeva

nr 181
Unbonded Post-Tensioned Shear Walls of
Calcium Silicate Element Masonry
Lex van der Meer

nr 182
Construction and Demolition Waste
Recycling into Innovative Building Materials
for Sustainable Construction in Tanzania
Mwita M. Sabai

nr 183
Durability of Concrete
with Emphasis on Chloride Migration
Przemysław Spiesz

nr 184
Computational Modeling of Urban
Wind Flow and Natural Ventilation Potential
of Buildings
Rubina Ramponi

nr 185
A Distributed Dynamic Simulation
Mechanism for Buildings Automation
and Control Systems
Azzedine Yahiaoui

nr 186
Modeling Cognitive Learning of Urban
Networks in Daily Activity-Travel Behavior
Şehnaz Cenani Durmazoğlu

nr 187
Functionality and Adaptability of Design
Solutions for Public Apartment Buildings
in Ghana
Stephen Agyefi-Mensah

nr 188
A Construction Waste Generation Model
for Developing Countries
Lilliana Abarca-Guerrero

nr 189
Synchronizing Networks:
The Modeling of Supernetworks for
Activity-Travel Behavior
Feixiong Liao

nr 190
Time and Money Allocation Decisions
in Out-of-Home Leisure Activity Choices
Gamze Zeynep Dane

nr 191
How to Measure Added Value of CRE and
Building Design
Rianne Appel-Meulenbroek

nr 192
Secondary Materials in Cement-Based
Products:
Treatment, Modeling and Environmental
Interaction
Miruna Florea

nr 193
Concepts for the Robustness Improvement
of Self-Compacting Concrete:
Effects of Admixtures and Mixture
Components on the Rheology and Early
Hydration at Varying Temperatures
Wolfram Schmidt

nr 194
Modelling and Simulation of Virtual Natural Lighting Solutions in Buildings
Rizki A. Mangkuto

nr 195
Nano-Silica Production at Low Temperatures from the Dissolution of Olivine - Synthesis, Tailoring and Modelling
Alberto Lazaro Garcia

nr 196
Building Energy Simulation Based Assessment of Industrial Halls for Design Support
Bruno Lee

nr 197
Computational Performance Prediction of the Potential of Hybrid Adaptable Thermal Storage Concepts for Lightweight Low-Energy Houses
Pieter-Jan Hoes

nr 198
Application of Nano-Silica in Concrete
George Quercia Bianchi

nr 199
Dynamics of Social Networks and Activity Travel Behaviour
Fariya Sharmeen

nr 200
Building Structural Design Generation and Optimisation including Spatial Modification
Juan Manuel Davila Delgado

nr 201
Hydration and Thermal Decomposition of Cement/Calcium-Sulphate Based Materials
Ariën de Korte

nr 202
Republiek van Beelden:
De Politieke Werkingen van het Ontwerp in Regionale Planvorming
Bart de Zwart

nr 203
Effects of Energy Price Increases on Individual Activity-Travel Repertoires and Energy Consumption
Dujuan Yang

nr 204
Geometry and Ventilation:
Evaluation of the Leeward Sawtooth Roof Potential in the Natural Ventilation of Buildings
Jorge Isaac Perén Montero

nr 205
Computational Modelling of Evaporative Cooling as a Climate Change Adaptation Measure at the Spatial Scale of Buildings and Streets
Hamid Montazeri

nr 206
Local Buckling of Aluminium Beams in Fire Conditions
Ronald van der Meulen

nr 207
Historic Urban Landscapes:
Framing the Integration of Urban and Heritage Planning in Multilevel Governance
Loes Veldpaus

nr 208
Sustainable Transformation of the Cities:
Urban Design Pragmatics to Achieve a Sustainable City
Ernesto Antonio Zumelzu Scheel

nr 209
Development of Sustainable Protective Ultra-High Performance Fibre Reinforced Concrete (UHPFRC):
Design, Assessment and Modeling
Rui Yu

nr 210
Uncertainty in Modeling Activity-Travel Demand in Complex Uban Systems
Soora Rasouli

nr 211
Simulation-based Performance Assessment of Climate Adaptive Greenhouse Shells
Chul-sung Lee

nr 212
Green Cities:
Modelling the Spatial Transformation of the Urban Environment using Renewable Energy Technologies
Saleh Mohammadi

nr 213
A Bounded Rationality Model of Short and Long-Term Dynamics of Activity-Travel Behavior
Ifigeneia Psarra

nr 214
Effects of Pricing Strategies on Dynamic Repertoires of Activity-Travel Behaviour
Elaheh Khademi

nr 215
Handstorm Principles for Creative and Collaborative Working
Frans van Gassel

nr 216
Light Conditions in Nursing Homes:
Visual Comfort and Visual Functioning of Residents
Marianne M. Sinoo

nr 217
Woonsporen:
De Sociale en Ruimtelijke Biografie van een Stedelijk Bouwblok in de Amsterdamse Transvaalbuurt
Hüseyin Hüsnü Yegenoglu

nr 218
Studies on User Control in Ambient Intelligent Systems
Berent Willem Meerbeek

nr 219
Daily Livings in a Smart Home:
Users' Living Preference Modeling of Smart Homes
Erfaneh Allameh

nr 220
Smart Home Design:
Spatial Preference Modeling of Smart Homes
Mohammadali Heidari Jozam

nr 221
Wonen:
Discoursen, Praktijken, Perspectieven
Jos Smeets

nr 222
Personal Control over Indoor Climate in Offices:
Impact on Comfort, Health and Productivity
Atze Christiaan Boerstra

nr 223
Personalized Route Finding in Multimodal Transportation Networks
Jianwe Zhang

nr 224
The Design of an Adaptive Healing Room for Stroke Patients
Elke Daemen

nr 225
Experimental and Numerical Analysis of Climate Change Induced Risks to Historic Buildings and Collections
Zara Huijbregts

nr 226
Wind Flow Modeling in Urban Areas Through Experimental and Numerical Techniques
Alessio Ricci

nr 227
Clever Climate Control for Culture:
Energy Efficient Indoor Climate Control Strategies for Museums Respecting Collection Preservation and Thermal Comfort of Visitors
Rick Kramer

nr 228
Fatigue Life Estimation of Metal Structures Based on Damage Modeling
Sarmediran Silitonga

nr 229
A multi-agents and occupancy based strategy for energy management and process control on the room-level
Timilehin Moses Labeodan

nr 230
Environmental assessment of Building Integrated Photovoltaics:
Numerical and Experimental Carrying Capacity Based Approach
Michiel Ritzen

nr 231
Performance of Admixture and Secondary Minerals in Alkali Activated Concrete:
Sustaining a Concrete Future
Arno Keulen

nr 232
World Heritage Cities and Sustainable Urban Development:
Bridging Global and Local Levels in Monitoring the Sustainable Urban Development of World Heritage Cities
Paloma C. Guzman Molina

nr 233
Stage Acoustics and Sound Exposure in Performance and Rehearsal Spaces for Orchestras:
Methods for Physical Measurements
Remy Wenmaekers

nr 234
Municipal Solid Waste Incineration (MSWI) Bottom Ash:
From Waste to Value Characterization, Treatments and Application
Pei Tang

nr 235
Large Eddy Simulations Applied to Wind Loading and Pollutant Dispersion
Mattia Ricci

nr 236
Alkali Activated Slag-Fly Ash Binders:
Design, Modeling and Application
Xu Gao

nr 237
Sodium Carbonate Activated Slag:
Reaction Analysis, Microstructural Modification & Engineering Application
Bo Yuan

nr 238
Shopping Behavior in Malls
Widiyani

nr 239
Smart Grid-Building Energy Interactions:
Demand Side Power Flexibility in Office Buildings
Kennedy Otieno Aduda

nr 240
Modeling Taxis Dynamic Behavior in Uncertain Urban Environments
Zheng Zhong

nr 241
Gap-Theoretical Analyses of Residential Satisfaction and Intention to Move
Wen Jiang

nr 242
Travel Satisfaction and Subjective Well-Being:
A Behavioral Modeling Perspective
Yanan Gao

nr 243
Building Energy Modelling to Support the Commissioning of Holistic Data Centre Operation
Vojtech Zavrel

nr 244
Regret-Based Travel Behavior Modeling:
An Extended Framework
Sunghoon Jang

nr 245
Towards Robust Low-Energy Houses:
A Computational Approach for Performance Robustness Assessment using Scenario Analysis
Rajesh Reddy Kotireddy

nr 246
Development of sustainable and functionalized inorganic binder-biofiber composites
Guillaume Doudart de la Grée

nr 247
A Multiscale Analysis of the Urban Heat Island Effect: From City Averaged Temperatures to the Energy Demand of Individual Buildings
Yasin Toparlar

nr 248
Design Method for Adaptive Daylight Systems for buildings covered by large (span) roofs
Florian Heinzelmann

nr 249
Hardening, high-temperature resistance and acid resistance of one-part geopolymers
Patrick Sturm

nr 250
Effects of the built environment on dynamic repertoires of activity-travel behaviour
Aida Pontes de Aquino

nr 251
Modeling for auralization of urban environments: Incorporation of directivity in sound propagation and analysis of a framework for auralizing a car pass-by
Fotis Georgiou

nr 252
Wind Loads on Heliostats and Photovoltaic Trackers
Andreas Pfahl

nr 253
Approaches for computational performance optimization of innovative adaptive façade concepts
Roel Loonen

nr 254
Multi-scale FEM-DEM Model for Granular Materials: Micro-scale boundary conditions, Statics, and Dynamics
Jiadun Liu

nr 255
Bending Moment - Shear Force Interaction of Rolled I-Shaped Steel Sections
Rianne Willie Adriana Dekker

nr 256
Paralympic tandem cycling and handcycling: Computational and wind tunnel analysis of aerodynamic performance
Paul Fionn Mannion

nr 257
Experimental characterization and numerical modelling of 3D printed concrete: Controlling structural behaviour in the fresh and hardened state
Robert Johannes Maria Wolfs

nr 258
Requirement checking in the building industry: Enabling modularized and extensible requirement checking systems based on semantic web technologies
Chi Zhang

nr 259
A Sustainable Industrial Site Redevelopment Planning Support System
Tong Wang

nr 260
Efficient storage and retrieval of detailed building models: Multi-disciplinary and long-term use of geometric and semantic construction information
Thomas Ferdinand Krijnen

nr 261
The users' value of business center concepts for knowledge sharing and networking behavior within and between organizations
Minou Weijs-Perrée

nr 262
Characterization and improvement of aerodynamic performance of vertical axis wind turbines using computational fluid dynamics (CFD)
Abdolrahim Rezaeiha

nr 263
In-situ characterization of the acoustic impedance of vegetated roofs
Chang Liu

nr 264
Occupancy-based lighting control: Developing an energy saving strategy that ensures office workers' comfort
Christel de Bakker

nr 265
Stakeholders-Oriented Spatial Decision Support System
Cahyono Susetyo

nr 266
Climate-induced damage in oak museum objects
Rianne Aleida Luimes

nr 267
Towards individual thermal comfort: Model predictive personalized control of heating systems
Katarina Katic

nr 268
Modelling and Measuring Quality of Urban Life: Housing, Neighborhood, Transport and Job
Lida Aminian

nr 269
Optimization of an aquifer thermal energy storage system through integrated modelling of aquifer, HVAC systems and building
Basar Bozkaya

nr 270
Numerical modeling for urban sound propagation: developments in wave-based and energy-based methods
Raúl Pagán Muñoz

nr 271
Lighting in multi-user office environments: improving employee wellbeing through personal control
Sanae van der Vleuten-Chraibi

nr 272
A strategy for fit-for-purpose occupant behavior modelling in building energy and comfort performance simulation
Isabella I. Gaetani dell'Aquila d'Aragona

nr 273
Een architectuurhistorische waardestelling van naoorlogse woonwijken in Nederland: Het voorbeeld van de Westelijke Tuinsteden in Amsterdam
Eleonore Henriette Marie Mens

nr 274
Job-Housing Co-Dependent Mobility Decisions in Life Trajectories
Jia Guo

nr 275
A user-oriented focus to create healthcare facilities: decision making on strategic values
Emilia Rosalia Catharina Maria Huisman

nr 276
Dynamics of plane impinging jets at moderate Reynolds numbers – with applications to air curtains
Adelya Khayrullina

nr 277
Valorization of Municipal Solid Waste Incineration Bottom Ash - Chemical Nature, Leachability and Treatments of Hazardous Elements
Qadeer Alam

nr 278
Treatments and valorization of MSWI bottom ash - application in cement-based materials
Veronica Caprai

nr 279
Personal lighting conditions of office workers - input for intelligent systems to optimize subjective alertness
Juliëtte van Duijnhoven

nr 280
Social influence effects in tourism travel: air trip itinerary and destination choices
Xiaofeng Pan

nr 281
Advancing Post-War Housing: Integrating Heritage Impact, Environmental Impact, Hygrothermal Risk and Costs in Renovation Design Decisions
Lisanne Claartje Havinga

nr 282
Impact resistant ultra-high performance fibre reinforced concrete: materials, components and properties
Peipeng Li

nr 283
Demand-driven Science Parks: The Perceived Benefits and Trade-offs of Tenant Firms with regard to Science Park Attributes
Wei Keat Benny Ng

nr 284
Raise the lantern; how light can help to maintain a healthy and safe hospital environment focusing on nurses
Maria Petronella Johanna Aarts

nr 285
Modelling Learning and Dynamic Route and Parking Choice Behaviour under Uncertainty
Elaine Cristina Schneider de Carvalho

nr 286
Identifying indoor local microclimates for safekeeping of cultural heritage
Karin Kompatscher

nr 287
Probabilistic modeling of fatigue resistance for welded and riveted bridge details. Resistance models and estimation of uncertainty.
Davide Leonetti

nr 288
Performance of Layered UHPFRC under Static and Dynamic Loads: Effects of steel fibers, coarse aggregates and layered structures
Yangyueye Cao

nr 289
Photocatalytic abatement of the nitrogen oxide pollution: synthesis, application and long-term evaluation of titania-silica composites
Yuri Hendrix

nr 290
Assessing knowledge adoption in post-disaster reconstruction: Understanding the impact of hazard-resistant construction knowledge on reconstruction processes of self-recovering communities in Nepal and the Philippines
Eefje Hendriks

nr 291
Locating electric vehicle charging stations: A multi-agent based dynamic simulation
Seheon Kim

nr 292
De invloed van Lean Management op de beheersing van het bouwproces
Wim van den Bouwhuijsen

nr 293
Neighborhood Environment and Physical Activity of Older Adults
Zhengying Liu

nr 294
Practical and continuous luminance distribution measurements for lighting quality
Thijs Willem Kruisselbrink

nr 295
Auditory Distraction in Open-Plan Study Environments in Higher Education
Pieternella Elizabeth Braat-Eggen

nr 296
Exploring the effect of the sound environment on nurses' task performance: an applied approach focusing on prospective memory
Jikke Reinten

nr 297
Design and performance of water resistant cementitious materials– Mechanisms, evaluation and applications
Zhengyao Qu

nr 298
Design Optimization of Seasonal Thermal Energy Storage Integrated District Heating and Cooling System: A Modeling and Simulation Approach
Luyi Xu

nr 299
Land use and transport: Integrated approaches for planning and management
Zhongqi Wang

nr 300
Multi-disciplinary optimization of building spatial designs: co-evolutionary design process simulations, evolutionary algorithms, hybrid approaches
Sjonnie Boonstra

nr 301
Modeling the spatial and temporal relation between urban land use, temperature, and energy demand
Hung-Chu Chen

nr 302
Seismic retrofitting of masonry walls with flexible deep mounted CFRP strips
Ömer Serhat Türkmen

nr 303
Coupled Aerostructural Shape and Topology Optimization of Horizontal-Axis Wind Turbine Rotor Blades
Zhijun Wang

nr 304
Valorization of Recycled Waste Glass and Converter Steel Slag as Ingredients for Building Materials: Hydration and Carbonation Studies
Gang Liu

nr 305
Low-Carbon City Development based on Land Use Planning
Gengzhe Wang

nr 306
Sustainable energy transition scenario analysis for buildings and neighborhoods - Data driven optimization
Shalika Saubhagya Wickramarachchi Walker

nr 307
In-between living and manufactured: an exploratory study on biobuilding components for building design
Berrak Kirbas Akyurek

nr 308
Development of alternative cementitious binders and functionalized materials: design, performance and durability
Anna Monika Kaja

nr 309
Development a morphological approach for interactive kinetic façade design: Improving multiple occupants' visual comfort
Seyed Morteza Hosseini

nr 310
PV in urban context: modeling and simulation strategies for analyzing the performance of shaded PV systems
Ádám Bognár

nr 311
Life Trajectory, Household Car Ownership Dynamics and Home Renewable Energy Equipment Adoption
Gaofeng Gu

nr 312
Impact of Street-Scale Built Environment on Walking/Cycling around Metro Stations
Yanan Liu

nr 313
Advances in Urban Traffic Network Equilibrium Models and Algorithms
Dong Wang

nr 314
Development of an uncertainty analysis framework for model-based consequential life cycle assessment: application to activity-based modelling and life cycle assessment of multimodal mobility
Paul Martin Baustert

nr 315
Variable stiffness and damping structural joints for semi-active vibration control
Qinyu Wang

nr 316
Understanding Carsharing-Facilitating Neighborhood Preferences
Juan Wang

nr 317
Dynamic alignment of Corporate Real Estate to business strategies: An empirical analysis using historical data and in-depth modelling of decision making
Howard Cooke

nr 318
Local People Matter: Towards participatory governance of cultural heritage in China
Ji Li

nr 319
Walkability and Walkable Healthy Neighborhoods
Bojing Liao

nr 320
Light directionality in design of healthy offices: exploration of two methods
Parisa Khademagha

nr 321
Room acoustic modeling with the time-domain discontinuous Galerkin method
Huiqing Wang

nr 322
Sustainable insulating lightweight materials for enhancing indoor building performance: miscanthus, aerogel and nano-silica
Yuxuan Chen

nr 323
Computational analysis of the impact of façade geometrical details on wind flow and pollutant dispersion
Xing Zheng

nr 324
Analysis of urban wind energy potential around high-rise buildings in close proximity using computational fluid dynamics
Yu-Hsuan Jang

nr 325
A new approach to automated energy performance and fault detection and diagnosis of HVAC systems: Development of the 4S3F method
Arie Taal

nr 326
Innovative Admixtures for Modifying Viscosity and Volume Change of Cement Composites
Hossein Karimi

nr 327
Towards houses with low grid dependency: A simulation-based design optimization approach
Zahra Mohammadi

nr 328
Activation of demand flexibility for heating systems in buildings: Real-life demonstration of optimal control for power-to-heat and thermal energy storage
Christian Finck

nr 329
A computational framework for analysis and optimisation of automated solar shading systems
Samuel B. de Vries

nr 330
Challenges and potential solutions for cultural heritage adaptive reuse:
a comparative study employing the Historic Urban Landscape approach
Nadia Pintossi

nr 331
Shared control in office lighting systems
Tatiana Aleksandrovna Lashina

nr 332
Comfort in Urban Public Spaces
You Peng

nr 333
Numerical modelling of metal soap formation in historical oil paintings
Gerardus Johannes Anna Maria Eumelen

nr 334
A transdisciplinary decision-making approach to food-water-energy nexus: A guide towards sustainable development
Maryam Ghodsvali

nr 335
Numerical modelling of transient low-frequency sound propagation and vibration in buildings
Indra Sihar

nr 336
Characterization of impact sound from lightweight joist floors
Yi Qin

nr 337
Cities for Children: Supporting Children and Caregivers in Participatory Urban Planning
Özlemnur Ataol

nr 338
Engaging the unengaged: Exploring citizen participation in nature-based solutions in China
Li Dai

nr 339
Municipal Solid Waste Incineration Residues: analysis, treatments, and applications
Ekaterina Loginova

nr 340
Enhancing the Uptake of Nature-Based Solutions in Urban Settings: An Information Systems Approach
Shahryar Ershad Sarabi

nr 341
Work Schedule Arrangements in Two-Adult Households with Children
Bilin Han

nr 342
Increasing awareness of urban cultural heritage using digital technologies: empirical design and analysis of a new multi-media web platform
Benshuo Wang

nr 343
Mechanical and physical properties of fibre-cement composites using alternative natural fibres
Katerina Kochova

nr 344
Numerical and experimental investigation of urban microclimate in a real compact heterogeneous urban area
Nestoras Antoniou

nr 345
Higher education classrooms' indoor environmental conditions: Input for the development of guidelines for higher education
Henk W. Brink

nr 346
High-temperature resistant geopolymers: composition, microstructure and performance
Kinga Malgorzata Klima

nr 347
Individual and household decision-making in shared parking
Qianqian Yan

Supplementary cementitious materials (SCMs) provide a significant contribution to sustainable construction. The use of these materials in concrete production consumes less energy and offers improved efficiency and building performance. Facing the challenges of SCMs utilization, this thesis firstly focuses on the alkali activation of slag, fly ash, waste glass, and municipal solid waste incineration bottom ash (MSWI BA). Simultaneously, the sodium hydroxides, sodium silicate, and sodium aluminate were used as activators aiming to the promotion of in-situ formed layered double hydroxides (LDHs).

DEPARTMENT OF THE BUILT ENVIRONMENT

TU/e EINDHOVEN
UNIVERSITY OF
TECHNOLOGY